UNIVERSITAT DE BARCELONA

Synthesis and characterization of multilayer graphene nanostructures

Arevik Musheghyan Avetisyan

ADVERTIMENT. La consulta d'aquesta tesi queda condicionada a l'acceptació de les següents condicions d'ús: La difusió d'aquesta tesi per mitjà del servei TDX (**www.tdx.cat**) i a través del Dipòsit Digital de la UB (**diposit.ub.edu**) ha estat autoritzada pels titulars dels drets de propietat intel·lectual únicament per a usos privats emmarcats en activitats d'investigació i docència. No s'autoritza la seva reproducció amb finalitats de lucre ni la seva difusió i posada a disposició des d'un lloc aliè al servei TDX ni al Dipòsit Digital de la UB. No s'autoritza la presentació del seu contingut en una finestra o marc aliè a TDX o al Dipòsit Digital de la UB (framing). Aquesta reserva de drets afecta tant al resum de presentació de la tesi com als seus continguts. En la utilització o cita de parts de la tesi és obligat indicar el nom de la persona autora.

ADVERTENCIA. La consulta de esta tesis queda condicionada a la aceptación de las siguientes condiciones de uso: La difusión de esta tesis por medio del servicio TDR (**www.tdx.cat**) y a través del Repositorio Digital de la UB (**diposit.ub.edu**) ha sido autorizada por los titulares de los derechos de propiedad intelectual únicamente para usos privados enmarcados en actividades de investigación y docencia. No se autoriza su reproducción con finalidades de lucro ni su difusión y puesta a disposición desde un sitio ajeno al servicio TDR o al Repositorio Digital de la UB. No se autoriza la presentación de su contenido en una ventana o marco ajeno a TDR o al Repositorio Digital de la UB (framing). Esta reserva de derechos afecta tanto al resumen de presentación de la tesis como a sus contenidos. En la utilización o cita de partes de la tesis es obligado indicar el nombre de la persona autora.

WARNING. On having consulted this thesis you're accepting the following use conditions: Spreading this thesis by the TDX (**www.tdx.cat**) service and by the UB Digital Repository (**diposit.ub.edu**) has been authorized by the titular of the intellectual property rights only for private uses placed in investigation and teaching activities. Reproduction with lucrative aims is not authorized nor its spreading and availability from a site foreign to the TDX service or to the UB Digital Repository. Introducing its content in a window or frame foreign to the TDX service or to the UB Digital Repository is not authorized (framing). Those rights affect to the presentation summary of the thesis as well as to its contents. In the using or citation of parts of the thesis it's obliged to indicate the name of the author.

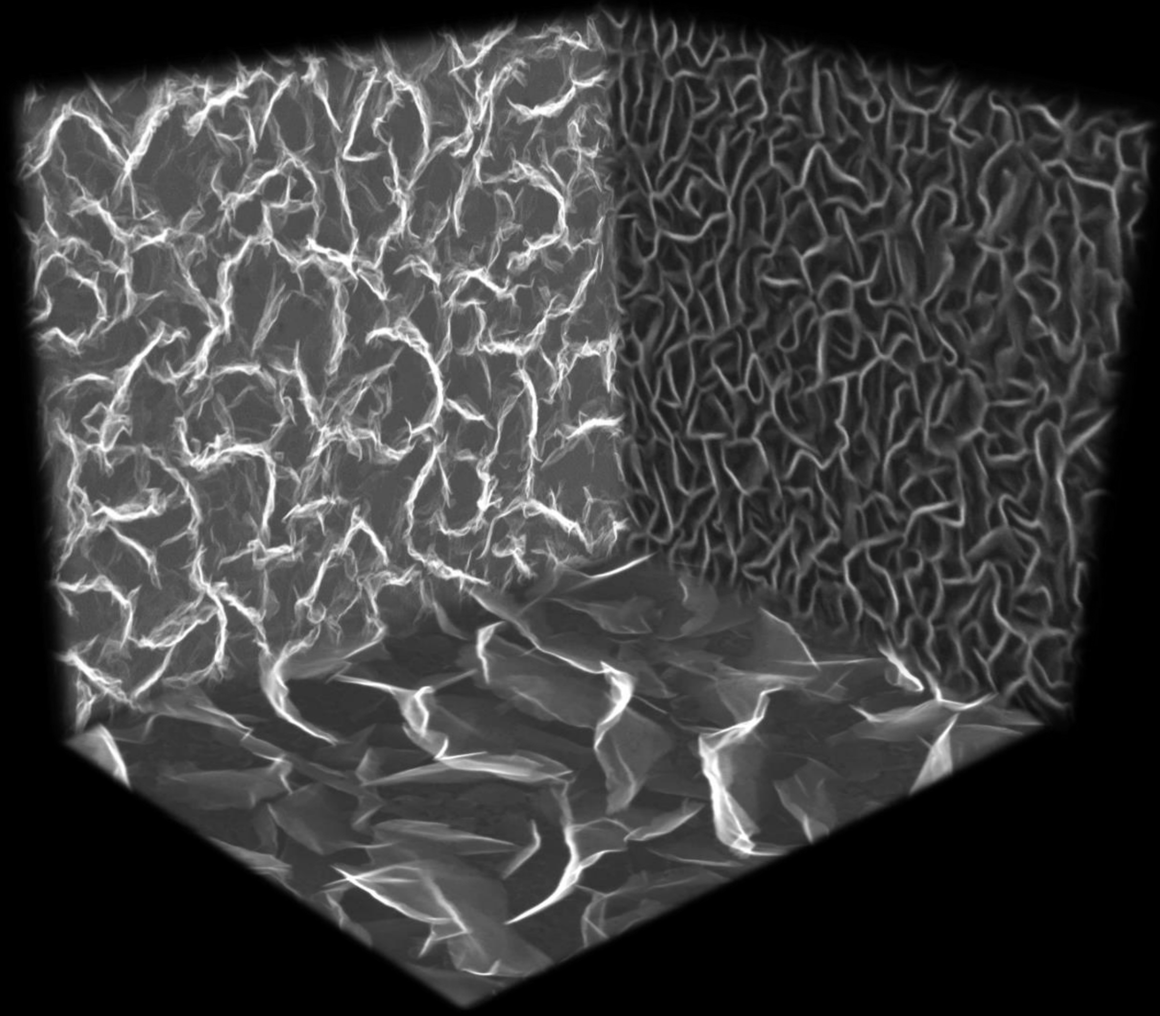

Synthesis and characterization of multilayer graphene nanostructures

Arevik Musheghyan Avetisyan

Doctoral thesis

Synthesis and characterization of multilayer graphene nanostructures

Autora: Arevik Musheghyan Avetisyan

Director: Enric Bertran Serra

UNIVERSITAT DE BARCELONA

Síntesi i caracterització de nanoestructures de grafè multicapa

Memòria presentada per optar al grau de doctor
per la Universitat de Barcelona

Programa de doctorat en Nanociències

Autora: Arevik Musheghyan Avetisyan
Director i tutor: Prof. Enric Bertran Serra

UNIVERSITAT DE BARCELONA

Dedicated to my loving Mother,
Husband and Son.

¨Science never solves a problem
without creating ten more¨
George Bernard Shaw

This research work has been carried out in the lab of the ENPHOCAMAT(FEMAN) research group, Department of Applied Physics, Faculty of Physics, University of Barcelona Spain. During writing master theses for the program of official university master degree in Nanoscience and Nanotechnology author already acquired some basic knowledge about the graphene growth mechanism, sputtering, PECVD and characterization technique. After completion of the master degree in July 2013, in September 2014 the author was officially enrolled in the PhD program of Nanoscience, University of Barcelona. The presented work has been supervised by Prof. Enric Bertran in the framework of the project,ENE2014-56109-C3-1-R and ENE2017-89210-C2-2-R, and 2014SGR0985 and 2017SGR1086 from the AGAUR of Generalitat de Catalunya.

Acknowledgements

Foremost, I would like to express my sincere gratitude to my research director Professor Dr. Enric Bertran Serra for the continuous support of my PhD study and research, for his patience, motivation, enthusiasm, and immense knowledge. His guidance helped me during all the time of the research and writing of this thesis. I would never imagine having a better advisor and mentor for my PhD study. I have been extremely lucky to have a supervisor who cared so much about my work, and tried to guide me to enhance the quality of this work and present it in the best possible way. He was always nice and calm and he taught me how to be always optimistic, even in the dark. Thank you very much!

Numerous thanks go to the rest of the professors of the FEMAN group, Prof. Dr. Jose Luis Andujar and Prof. Dr. Esther Pascual and Dr. Roger Amade, who helped me with advice during the whole study. I consider myself very fortunate for being able to work with very considerate and encouraging professors like them.

I also acknowledge the help of the scientific staff of the Scientific-Technical Services of the UB (CCTiUB), without them most of the results described in this thesis would not have been obtained. Special thanks go to Tariq for Raman analyses, Eva Prats Miralles and David Artiaga Torres for SEM measurements, Luis López for TEM analyses and Lorenzo Calvo for XPS analyses. Special thanks go to Frank Güel for Photoluminescence analysis.

I am also deeply thankful to the secretarial team of the Department, Ms. Maria Teresa Fraile Sanchez, Mr. Jordi Sola Antolin and Ms. Cristina Egusquiza. They have been always organizing everything in the best possible way.

I am grateful to all those with whom I have had the pleasure to work during writing this thesis. My special words of thanks for cooperation, motivation and support should also go to my past and present group members Victor, Shahzad, Stefanos, Fernando, Joan, Islam. I would like to thank my former roommates Marta and Laura for their friendship and support.

It's my fortune to gratefully acknowledge the support of my friends, Armine, Ani, Aksana, Mariam, Armina for their support and generous care throughout the research tenure. They were always beside me during the happy and hard moments to encourage and motivate me.

Last but not the least I would like to thank my family members for their constant inspiration and encouragement. A very special word of thanks goes to my lovely Mother, Karine, for her unconditional support, encouragement and love, and without which I would not have come this far. Finally, I have to thank my husband and love of my life, Andranik, whose unconditional love, patience, and continued support of my academic endeavours over the past several years enabled me to complete this thesis. The last word goes for Mark, my baby boy, who has been the light of my life for the last four years and who has given me the extra strength and motivation to get things done.

Outline and Objective of this thesis

The goal of the present investigation is to examine the processing-structure-property relationships of multilayer graphene nanowall materials. Various plasma enhanced chemical vapor deposition (PECVD) processing parameters were altered to control the structure and morphology of the material. Growth parameters and substrate material were the major structural features studied, and these were characterized by spectroscopic techniques. Additionally, we have obtained a 3D hybrid structure by using CNTs as a substrate material for MLGNWs growth. The presence of MLGNWs improved the specific surface area of carbon nanowalls, and by this way make them useful for a large number of applications, such as energy storage, supercapacitor and building blocks composite.

In recent years, many theoretical and experimental studies have been carried out to develop one of the most interesting aspects of the science and nanotechnology which is called carbon-related nanomaterials. Carbon nanomaterials are formed in various structural features using several different processing methods and they find application in different nanotechnology platforms. Two-dimensional carbon nanostructures with vertical orientation were discovered more than 20 years ago, during fabrication of carbon nanotubes in 1997, but the discovery of graphene in 2004 was followed by an intense study of this new material. However, recently, attention has been focused on graphene nanowalls, which possess high mobility for carriers and large sustainable current density, which make them one of the most promising carbon structures used for nanoscale electronic devices.

This PhD thesis was carried out since October 2014 when I officially started my PhD Thesis. It took place in the Department of Applied Physics of the University of Barcelona (UB).

Before it, the academic year 2011-2013, I carried out my Master studies in the University of Barcelona in the field of Nanoscience and Nanotechnology. My collaboration with ENPHOCAMAT(FEMAN) group and Prof. E. Bertran started since then, within the framework of my master thesis research. My Master thesis was entitled ¨Carbon based self-assembled and nanostructured surfaces¨. This work was supported by AGAUR of Generalitat de Catalunya, project ENE2014-56109-C3-1-R and ENE2017 89210 C2-2-R, and 2014SGR0985 and 2017SGR1086.

The experimental part of this thesis was done by the author in the *Departament de Física Aplicada* of the *Universitat de Barcelona* (UB). All substantial part of the characterization of the samples was done in the *Centres Cientifics i Tecnològics de la UB* (CCiT-UB).

The goal of the thesis has different tasks consisting of:

a) The design and construction of a new inductively coupled plasma remote chemical vapor deposition reactor in the PECVD-FEMAN laboratory of the *Universitat de Barcelona*.
b) Fabrication of vertical graphene nanostructures at low temperature on different conductive and nonconductive substrates.
c) Characterization of the vertical graphene obtained through different synthesis parameters in order to optimize their physical and surface properties; such as structural and morphological studies by Raman spectroscopy, SEM and TEM.
d) Functionalization of MLGNWs by MnO nanoparticles for hybrid supercapacitor systems.

The thesis is divided in four main parts:

Part I Introduction

Chapter 1 –Carbon materials. This chapter provides a brief introduction of carbon materials, history, state of art, properties and applications.

Chapter 2 –Graphene and graphene nanowalls. In this chapter the graphene and graphene nanowalls will be introduced as a novel material and their history, outstanding properties, discovery, and all the technologies that prompted their development during these years until the first application. Moreover, in this chapter the methods for the synthesis of carbon nanostructures and brief explanation of the fundamentals of each technique will be explained.

Part II Experimental description

Chapter 3 – MLGNWs characterization techniques. In this chapter, the concepts and technologies of plasma, plasma enhanced chemical vapor deposition (PECVD) and PECVD related techniques are exposed**.** Moreover, in this chapter a deposition reactor designed by us will be described, where all experiments carried out during this thesis took place**.** The second part of this chapter is related to the basics and work principles of different characterization techniques. The characterization of thin films and MLGNWs involves various, spectroscopic, X-ray and photoluminescence techniques.

Chapter 4 – Production technology and proposed growth mechanism. In this chapter, the introduction of microwave and radio frequency plasma enhanced chemical vapor deposition

(PECVD) have been described. Also, in this chapter we propose a growth mechanism of MLGNWs by plasma enhanced chemical vapor deposition (PECVD).

Part III Results

Chapter 5 – Functional study of tubular reactor for production of multilayer graphene nanowalls. This chapter discusses the study of growing material along the entire length of the tube. The importance of sample location inside a tubular quartz reactor has been demonstrated. The microstructure and morphology of the grown film were investigated using field emission scanning electron microscopy (FESEM), transmission electron microscopy (TEM) and high resolution TEM (HRTEM). The chemical characteristics of as grown structures were studied by Raman spectroscopy, X-ray photoelectron spectroscopy (XPS) and Fourier transform infrared (FTIR) spectrometer. The hydrogen and carbon contents in grown samples were determined by elemental analysis (EA). To study the photoluminescent properties of the carbon structure grown in the whole length of the tubular reactor, the room temperature PL spectra were conducted. In addition, the chemical reactions inside the tube under plasma deposition were controlled by optical emission spectroscopy (OES).

Chapter 6 – Effects of different parameters on MLGNWs growth. This is the chapter of the main results. This chapter discusses the successful growth parameters for MLGNWs synthesis. The influence of the substrate material, growth time and growth temperature on the MLGNWs growth process have been discussed. FESEM, TEM, HRTEM, Raman and XPS techniques were performed to examine the change in morphology, structure and chemical state of the MLGNWs synthesized at different growth parameters. The importance of influence of number of radicals on the MLGNWs structure has been explained in details by OES.

Chapter 7–MLGNWs/CNTs hybrid structure. Morphology and electrochemical characterizations. This chapter discusses the growth of MLGNWs on the CNTs substrate, obtained by water assisted CVD (WA-CVD) process. The goal of MLGNWs/CNTs hybrid structure is increased chemical activity of CNTs. The morphological and structural characterization was carried out using Scanning Electron microscope, High resolution transmission electron microscope and Raman scattering analysis. Electrochemical properties of transferred MLGNWs/CNTs were studied by CV and charge/discharge measurements. Furthermore, this chapter provides information about MLGNWs synthesis on water patterned CNTs substrate. Electrochemical properties and structural characteristics of these structures are presented in this chapter.

Chapter 8 –Supercapacitive performance of manganese dioxide/ graphene nanowalls electrodes deposited on stainless steel current collectors and annealing temperature effect. In this chapter preparation of MLGNWs/MnO_2 composite electrode by anodic deposition of MnO_2. Composite electrodes MLGNWs/MnO_2 were characterized by field emission scanning electron microscopy (FESEM) and Raman shift spectroscopy. The electrochemical properties of the MLGNWs/MnO_2 for supercapacitor applications were investigated by cyclic voltammetry (CV), charge/discharge and electrochemical impedance spectroscopy (EIS). The influence of annealing temperature on the electrochemical performance has been studied as well.

Part IV Conclusions

Resumen en castellano

La Nanotecnología se define como el campo de las ciencias aplicadas dedicado al control y manipulación de la materia a una escala menor que un micrómetro (1-1000 nm), es decir, a nivel de varios átomos y/o moléculas hasta partículas por debajo del micrómetro. La Nanociencia y Nanotecnología ofrecen un gran potencial para el desarrollo de nuestros conocimientos de una manera sostenible y han experimentado un enorme crecimiento en pocos años. Actualmente ya se encuentran algunas aplicaciones prácticas de la Nanotecnología y se prevé que habrá muchas más, por lo cual es necesario evaluar el impacto que puedan tener en un futuro próximo. La importancia de la Nanotecnología radica en que, en el mundo nanométrico los materiales pueden adquirir o realzar propiedades diferentes a las que los materiales poseen a escala macroscópica. La Nanotecnología se divide en dos tipificaciones, según la técnica de aplicación: técnicas de arriba hacia abajo (*top-down*) y técnicas de abajo hacia arriba (*bottom-up*). En el caso de la Nanotecnología *top-down*, se trata de diseñar y miniaturizar el tamaño de estructuras para obtener a nanoescala sistemas funcionales en el caso de la producción de nanoelectrónica (miniaturización de sistemas electrónicos). Y en el caso de la Nanotecnología tipo *bottom-up*, se centra en la construcción de estructuras y objetos más grandes a partir de sus componentes atómicos y moleculares. Estos dos procesos se entienden como el enfoque principal de la Nanotecnología ya que permiten un control muy preciso de los materiales.

En una conferencia del 29 de diciembre del año 1959, en el Auditorio de Caltech de la Universidad Tecnológica de California, el físico Richard Feynmann dijo: ¨*En el mundo de lo muy, muy pequeño, muchas cosas nuevas podrán suceder, porque los átomos se comportan de manera distinta a como lo hacen los objetos a mayor escala, pues deben satisfacer las leyes de la mecánica cuántica. Si nos reducimos y comenzamos a juguetear con los átomos allá abajo, estaremos sometidos a unas leyes diferentes, y podremos hacer cosas diferentes. A nivel atómico, aparecen nuevos tipos de fuerzas, nuevas posibilidades, nuevos efectos*¨ (Feynmann R., 1959)

El grafeno, como material basado en el carbono, es un logro del desarrollo y los avances de la Nanotecnología; siendo el grafeno un componente estructural del grafito, posee propiedades tan sorprendentes que lo ha convertido en un potencial sustituto del silicio en el diseño y fabricación de nuevos circuitos integrados. Hasta el año 2004, no se creía posible la existencia de una estructura como la del grafeno como entidad aislada. Se suponía que los cristales estrictamente bidimensionales eran termodinámicamente inestables, debido a fluctuaciones térmicas en redes cristalinas que teóricamente producirían desplazamientos atómicos dando lugar a una estructura en tres dimensiones. Sin embargo, en el año 2004 dos científicos de la Universidad de Manchester, Andre Geim y Konstantin Novoselov fueron capaces de obtener e identificar por vez primera láminas individuales de grafeno de espesor monoatómico junto con otros cristales

bidimensionales. El grafeno con propiedades extraordinarias se ha integrado rápidamente en el área de la Nanotecnología. Sus presentes y futuras aplicaciones, han hecho posible que este material pase de ser un sueño académico a ser una promisoria realidad. Este material delgado con un espesor de 3,35 Å conduce la electricidad tan bien como el cobre: su conductividad eléctrica es $0{,}96\times10^{8}$ S/m, mientras que la del cobre es $0{,}60\times10^{8}$ S/m y la del silicio de $4{,}5\times10^{-4}$ S/m. A demás, la conductividad térmica del grafeno se encuentra en un valor de aproximadamente $5000\ \mathrm{W\cdot m^{-1}\cdot K^{-1}}$, que es el más elevado comparado con la conductividad térmica de todos los materiales conocidos. El grafeno es el material más resistente desde un punto de vista mecánico (resistencia mecánica de 42 N/m) con excelentes características ópticas y muchas más propiedades extraordinarias. Sin embargo, el grafeno presenta en estos momentos un gran problema, su fabricación es muy costosa a nivel económico y poco escalable. Uno de los problemas a los que se enfrenta el grafeno es la posibilidad de que pueda resultar peligroso para la salud y para el medio ambiente, por lo que será necesario continuar con su investigación e introducir las medidas de seguridad necesarias en su producción y comercialización. Además, uno de los principales problemas que impiden la utilización del grafeno, es que la producción de muestras grandes es limitada. Las técnicas más utilizadas para fabricar grafeno son:

- Exfoliación con cinta adhesiva: "*Scotch tape*"
- Deposición desde la fase vapor: "C*hemical vapor deposition (CVD*)"
- Exfoliación con disolventes: "*Liquid phase exfoliation*"
- Mediante descarga de arco eléctrico y generación de plasma
- Oxidación-reducción

Entre ellos, la CVD térmica es la técnica más popular para superar las limitaciones de escalabilidad. Sin embargo, el grafeno fabricado mediante CVD tiene que ser transferido a un sustrato dieléctrico antes de poder ser aplicado en los dispositivos. El proceso de transferencia inevitablemente introduce impurezas y degrada la calidad del grafeno. La síntesis directa de grafeno sin catálisis sobre sustratos dieléctricos, compatible con la tecnología de los semiconductores complementarios de óxido metálico, es una tarea estimulante pero compleja. Recientemente, se ha obtenido el grafeno crecido directamente sobre sustrato dieléctrico con la técnica CVD térmica pero a temperaturas elevadas. La técnica PECVD, que es CVD activado mediante plasma, permite la fabricación de nanoestructuras de carbono a temperaturas más bajas. Por otra parte, el plasma acelera el crecimiento a la vez que no requiere sustratos catalizadores. Como la técnica CVD térmica, los procesos PECVD son ideales para grandes superficies uniformes y recubrimientos homogéneos. Dependiendo del generador utilizado, los procesos PECVD se puede clasificar en varias modalidades o técnicas: microondas (MWCVD), descargas DC (DC-PECVD), plasma acoplado inductivamente (ICP-PECVD o ICP-CVD) y sistemas de chorro con plasma térmico (*thermal plasma jet systems*). El procesado por CVD mediante plasma acoplado inductivamente (ICP-CVD) es el método principal utilizado en esta tesis.

El objetivo de esta tesis es la síntesis y optimización de nanoparedes verticales de grafeno y su posible extensión a aplicaciones en sistemas que requieran superficies macroscópicas. Para ello, se han realizado diferentes tareas:

a) Se ha diseñado y construido un reactor prototipo con plasma remoto en el laboratorio PECVD-FEMAN de la Facultad de Física (Universidad de Barcelona) con el fin último de crecer grafeno en forma de paredes/tabiques verticales nanométricos mediante la técnica PECVD. El reactor incorpora los siguientes elementos:
    - Un tubo de cuarzo como cámara donde se lleva a cabo la reacción con longitud 100 cm y 45 mm de diámetro. El tubo atraviesa axialmente un horno cilíndrico con resistencias de hilo de *Kantal*® que alcanza los 1000 °C y posteriormente una bobina de hilo de tubo de cobre de ¼" que forma un resonador $\lambda/4$ a la frecuencia de 13,56 MHz.
    - Un sistema de gestión de gases controla el flujo másico de tres líneas de gas independientes.
    - Un sistema de vacío con bomba mecánica y control de la presión mediante válvula de conductancia variable.
    - Dos termopares, uno instalado entre el tubo de cuarzo y el horno y otro alojado en el brazo-soporte para transferir el substrato hacia el interior del tubo de cuarzo y controlar la temperatura directamente en la zona del crecimiento.
    - Una fuente de alimentación de radiofrecuencia (RF) de 13,56 MHz de frecuencia de trabajo y 50 Ω de impedancia de salida conectada mediante una línea de transmisión coaxial de 50 Ω de impedancia característica para alta potencia, con dieléctrico de PTFE y conectores de tipo N, con capacidad para proporcionar potencias de hasta 555 W.
    - Un sistema de diagnosis del plasma consistente en un espectroscopio de emisión óptica (OES) para determinar las especies emisoras en tiempo real presentes en el plasma.

b) Se ha desarrollado un proceso PECVD modificado con el fin de mejorar los resultados actuales en términos de: 1) el tiempo de crecimiento (inicialmente del orden de horas), 2) la temperatura (inicialmente del orden de 1000 °C), 3) la naturaleza del substrato, 4) la presión (~50 Pa), y 5) la cantidad de gas precursor (del orden de 10 sccm de flujo másico constante) para crecer grafeno vertical. Las muestras obtenidas fueron caracterizadas mediante microscopía TEM, SEM, XPS, XRD y mayormente mediante espectroscopia Raman, con el objetivo de optimizar el proceso y las propiedades físico-químicas y del grafeno vertical.

c) Se ha desarrollado una estructura híbrida con nanoparedes y nanotubos de carbono. Para ello, se utilizaron tres equipos: el reactor “PEDRO” para la preparación del substrato, el reactor “CNTs” para el crecimiento de nanotubos de carbono y el reactor ICP-CVD para el crecimiento de nanoparedes de grafeno. En esta tesis se investigaron las caracterizaciones morfológicas y electroquímicas, pero aún se necesitan más estudios para confirmar posibles futuras aplicaciones.

d) Para mejorar las propiedades de los supercapacitores basados en los electrodos desarrolladas con nanoparedes de grafeno i acero inoxidable, se ha realizado el crecimiento de capas delgadas de MnO_2 mediante el método de electrodeposición. El efecto de la temperatura de recocido (*annealing*) en las propiedades electroquímicas de las muestras se ha estudiado en el rango de 70° C a 650° C.

Conclusiones:

- El mecanismo de crecimiento del grafeno vertical fue uno de los principales objetivos de esta tesis. Es un proceso complejo, que contiene diferentes pasos. Se ha investigado paso a paso todo el proceso de crecimiento durante el plasma mediante espectroscopia de emisión óptica. Este análisis *in situ* nos da información sobre la evolución de las especies activas y las reacciones en la fase gaseosa. Por otro parte, el grafeno vertical sintetizado en diferentes pasos de crecimiento se caracterizó mediante microscopía electrónica SEM y TEM. Las observaciones con TEM muestran la presencia de maclas de grafeno, que aparece en la segunda fase de crecimiento, debido a la temperatura y el estrés relativamente elevados en las nanoestructuras. Por otra parte, se investigaron las muestras obtenidas en toda la longitud del tubo. Para este investigación se utilizado una cinta de acero inoxidable, que tenía la misma longitud que el tubo de cuarzo. Las estructuras de carbono depositado en diferentes partes del tubo presentaron distintas estructuras y propiedades. Para las zonas con temperaturas relativamente bajas se obtuvieron microestructuras a diferencia de las zonas con temperaturas altas, donde se obtuvieron nanostructuras. Además, las características fotoluminiscentes de las estructuras de carbono obtenidas eran muy diferentes dependiendo de la posición de la muestra. El estudio de las propiedades fotoluminiscentes, asociadas a las distintas morfologías obtenidas en un mismo experimento de crecimiento utilizando ICP-CVD, ha proporcionado diversos resultados que muestran que el origen de la fotoluminiscencia (PL) está asociado a las micro y nanoestructuras que contienen hidrógeno. Las medidas de PL proporcionaron una banda de emisión brillante y muy amplia en el rango visible de 450 a 750 nm, a temperatura ambiente, para muestras obtenidas a temperaturas entre 50ºC y 750ºC. La espectroscopia FTIR y el análisis XPS de estas muestras evidenciaron la presencia de oxígeno (probablemente debido a la posterior oxidación de las estructuras de carbono al ser expuestas a la atmósfera) C-O = C y C = O y un alto contenido de hidrógeno en forma de -CH, -CH_n y enlaces de carbono C-C, C = C. En contraste, las nanoestructuras de carbono obtenidas a la temperaturas más elevadas (750ºC) muestran características diferentes: (1) presencia de nanoparedes con defectos en los bordes (evidenciado a partir del espectro Raman), (2) elevada cristalinidad (a partir de las imágenes TEM y SAED), (3) contenidos muy bajos de hidrógeno y oxígeno, confirmado mediante espectroscopia FTIR y (4) débil PL. El análisis detallado de las estructuras de carbono crecidas en diferentes condiciones durante un único experimento sugiere que las diversas bandas de emisión de PL obtenidas pueden relacionarse con el contenido de H que proviene del plasma de CH_4. Los resultados de esta investigación muestran la diversidad de estructuras de carbono obtenidas, con propiedades fotoluminiscentes muy variadas que dependen fundamentalmente no sólo de la temperatura, sino también de otras condiciones, como la composición del gas y la densidad de las especies en fase gas en cada posición del reactor tubular de cuarzo. Para obtener estructuras particulares, tuvimos que controlar con precisión los parámetros tecnológicos del plasma. Además, las estructuras de carbono obtenidas a temperaturas relativamente bajas con una elevada eficiencia fotoluminiscente pueden promover el desarrollo de una tecnología simplificada para producir dispositivos optoelectrónicos. Por otro lado, las nanoestructuras "no dopadas" de carbono, que tienen una baja emisión de PL, proporcionan una nueva posibilidad para dopar fácilmente las nanoestructuras básicas de carbono durante la fase gaseosa (mediante N_2, NH_3, H_2O, H_2) para mejorar la emisión de PL, que puede ser útil para diversas aplicaciones optoelectrónicas.

- En la investigación del uso de diferentes materiales como sustrato, demostramos que el crecimiento de grafeno vertical era casi independiente de la naturaleza del sustrato. Se ha demostrado que la técnica PECVD es un enfoque versátil para obtener nanoestructuras de grafeno vertical de alta calidad sobre diferentes sustratos. En nuestros experimentos, las nanoestructuras de grafeno crecieron verticalmente en diferentes sustratos con catalizador y sin catalizador. Estas nanoparedes tienen estructuras policristalinas compuestas por nano-hojas de grafeno de pocas capas. Morfologías y estructuras similares obtenidas en el mismo proceso de preparación sobre diferentes sustratos revelaron que el crecimiento de las nanoestructuras sobre paredes de grafeno verticales no es demasiado sensible al tipo de sustrato. Estas nanoestructuras verticales sobre diferentes sustratos pueden tener diversas aplicaciones en supercapacitores, baterías de iones de litio, células solares y biosensores.
- La nanoestructura en forma de paredes verticales de grafeno se puede controlar mediante el tiempo de procesado y la temperatura de crecimiento. Para obtener grafeno en nanoparedes verticales de alta calidad, se realizó un estudio del efecto del tiempo de

procesado mediante Raman, TEM y SEM, el cual permitió confirmar la elevada calidad y la morfología del grafeno verticalmente nanoestructurado. Con microscopia SEM hemos observado las nanoestructuras verticales a partir de 10 min y 5 min de crecimiento para substratos de sílice y acero inoxidable, respectivamente. Dependiendo de las propiedades del sustrato, el crecimiento puede retrasarse o acelerarse. En el análisis mediante espectroscopia Raman hemos observado la formación de carbono amorfo durante los primeros minutos de crecimiento, y con tiempos más largos la formación de carbono cristalino o policristalino. El tiempo para la formación de estructuras ordenadas también puede variar dependiendo del sustrato. La estructura policristalina del grafeno vertical fue confirmada mediante SAED. Además, con el tiempo de crecimiento, el número de capas disminuye, tal como se confirmó mediante TEM y Raman. De los resultados del estudio con diferentes técnicas del grafeno verticalmente nanoestructurado crecido en distintos tiempos hemos concluido que el tiempo de crecimiento óptimo es de 40 minutos. El grafeno verticalmente nanoestructurado crecido durante 40 min presenta nanoparedes bien orientadas con una densidad no muy alta, lo cual facilita la funcionalización de la nanoestructura. Sin embargo, dada la variada morfología que presentan, las nanoestructuras crecidas a diferentes tiempos de crecimiento pueden ser útiles en diversas aplicaciones. Por otra parte, hemos controlado todo el proceso de crecimiento de grafeno verticalmente nanoestructurado en tiempo real mediante OES, lo cual ha permitido determinar la evolución de las reacciones químicas durante el procesado por plasma. Los espectros de OES muestran la evolución de las especies activas como H_α, H_2, C_2 y CH. Se ha demostrado que los radicales CH aumentan linealmente su concentración a lo largo del proceso de crecimiento del grafeno verticalmente nanoestructurado.

- La temperatura es el otro parámetro importante para la síntesis de grafeno vertical. El estudio de temperatura del grafeno vertical muestra que el proceso exitoso de crecimiento de grafeno vertical es a partir de 650°C y las estructuras de grafeno vertical no se forman si la temperatura del sustrato es inferior a 650°C. Las propiedades morfológicas de las muestras de grafeno vertical crecidas sobre diferentes sustratos, alcanzan una mayor densidad y altura al aumentar la temperatura de crecimiento. Los nanoestructuras de grafeno se caracterizaron mediante Raman y SEM. En el proceso de PECVD, y a energías suficientemente altas, el metano se descompone en gas de hidrógeno y en diversos hidruros y otros radicales de carbono, los cuales dan lugar a varios grupos químicamente activos. La variación de la temperatura de crecimiento conduce a diferentes tasas de deposición sobre el sustrato. Una menor energía térmica tiende a disminuir la velocidad de deposición, lo que a su vez reduce la posibilidad de crecimiento vertical. A medida que aumenta la temperatura obtenemos una mayor tasa de deposición en los bordes de las islas de grafeno en lugar de un crecimiento capa a capa, lo cual da lugar al crecimiento vertical cuando las islas de grafeno llegan a tocarse. Las imágenes SEM muestran la ausencia de estructuras verticales para temperaturas por debajo de 600ºC. Con el aumento de la temperatura, la densidad de este crecimiento vertical comienza a aumentar rápidamente, cubriendo toda la superficie cuando la temperatura de crecimiento alcanza los 650°C. También se produce un incremento del número de capas de grafeno tal como se confirma en los espectros Raman. La formación de grafeno vertical a diferentes temperaturas depende de las densidades de los radicales, iones y otras especies activas formadas durante el proceso de plasma. La diagnosis del plasma mediante la emisión óptica espectral nos muestra que la intensidad de las especies activas CH y H es muy baja a baja temperatura, pero para temperaturas relativamente elevadas, la intensidad de la emisión asociada a las especies activa aumenta y provoca el crecimiento de grafeno vertical.

- En el capítulo dedicado a las estructuras híbridas de grafeno vertical y nanotubos de carbono, demostramos que el crecimiento selectivo del grafeno vertical es posible mediante un patrón basado en nanotubos de carbono. El tratamiento con agua de los nanotubos de carbono verticalmente alineados es una forma sencilla de modelarlo basada en las fuerzas capilares. El desarrollo de estas técnicas permiten ampliar el campo de la aplicación de las nanoparedes y las nanotubos de carbono. El patrón en forma de panal (honeycomb) es una estructura abierta cuyas paredes están formadas por nanotubos de carbono. Esa estructura facilita el recubrimiento a todo lo largo de los nanotubos con bordes activos de MLGNWs, lo que hace aumentar la suerficie específica y por tanto la actividad química de los CNTs en diversas aplicaciones (sensores en biomedicina, catálisis, electrodos en procesos electroquímicos como supercondensadores o baterías). En este sentido, se han estudiado las propiedades electroquímicas de las estructuras híbridas, pero los resultados son preliminares y no han sido concluyentes. Uno de los problemas encontrados en el estudio de las propiedades electroquímicas fue la escasa mojabilidad de las estructuras 3D, que limita su uso en ambientes húmedos. Sin embargo, este problema se pudo solucionar sometiendo las estructuras a un breve tratamiento con plasma de oxígeno. El ángulo de contacto después de 20 s de plasma de oxígeno descendió de 126º a 26º.
- Con el fin de mejorar las propiedades electroquímicas de las nanoestructuras de paredes verticales de grafeno, crecimos sobre acero inoxidable flexible y conductor eléctrico utilizando el método ICP-CVD. La electrodeposición galvanostática de MnO_2 aumentó la capacidad específica (SC) de las muestras hasta 356 $F\cdot g^{-1}$ en rampas de 10 $mV\cdot s^{-1}$ para la muestra sin tratamiento térmico. Sin embargo, después de un recocido suave a 70°C, el nanocompuesto de MnO_2/MLGNW exhibió una disminución drástica en la resistencia

a la transferencia de carga, una mayor estabilidad de los ciclos de trabajo y una SC incluso a altas tasas de carga/descarga, lo cual está relacionado con el contacto óptimo entre MLGNWs y MnO_2 y reacciones redox rápidas de superficie. Las muestras recocidas por encima de 200°C muestran una baja SC y poca estabilidad debido a la reducción de la porosidad, a la eliminación del agua ligada del óxido de manganeso y, presumiblemente, a la aparición de reacciones faradaicas o cambios de fase descritos por una resistencia asociada a una pequeña corriente de fuga en los espectros de impedancia electroquímica (EIS).

Contents

Part I
Introduction

Chapter 1

Carbon materials

1.1 Carbon allotropes

Carbon with chemical element symbol C, atomic number 6 and electron configuration [He]$2s^2 2p^2$, is one of the most important elements in the Earth's crust, the second most abundant element in the human body by mass (about 18.5%) and the fourth most abundant element in the universe by mass after hydrogen, helium, and oxygen. The word carbon is derived from the Latin word "carbo," which to the Romans meant charcoal or ember. In modern society carbon holds a much richer and complex meaning [Landau LD, 1980]. This common material plays a singular role in chemical science and materials science. Carbon possesses a very large sphere of application, from drugs to synthetic materials. Specific industrial applications include areas such as oil and natural gas, food, pharmaceuticals, water treatment, hydrometallurgy, gold recovery and carbon-in-pulp process, which are widely used [Stillahn JA, 2008]. The main feature of carbon is its ability to form a variety of allotropes and ability to combine with other elements. Carbon allotropes can be classified in terms of their spatial dimensionality: zero-dimensional are fullerenes, one dimensional are carbon nanotubes, three dimensional are graphite and diamond, two dimensional is graphene. The basic difference between 2D and 3D is considered by the number of layers of atoms. For example, a single layer of an atomic crystal is considered as 2D carbon, whereas 100 layers of carbon form the 3D graphite material [Wu Y, 2004]. For a long time elemental carbon existed only in two natural allotropes, diamond and graphite. Both allotropes show unique thermal and electrical properties. In 1985 Kroto et al. discovered the new

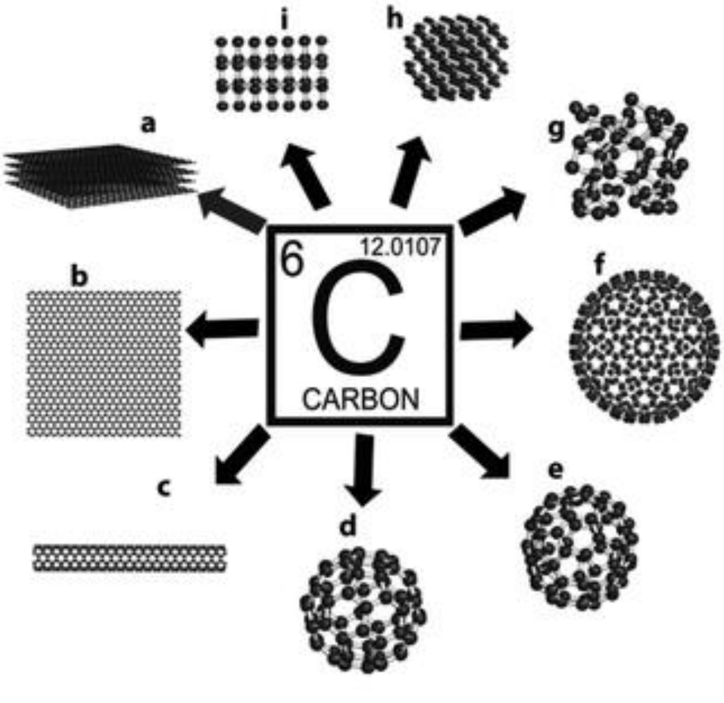

Figure 1.1 Different allotropes of carbon: (a) graphite; (b) graphene; (c) carbon nanotube; (d) C_{60} (Buckminsterfullerene); (e) C_{70} (Fulleren); (f) C_{540}(Fullerite); (g) amorphous carbon; (h) lonsdaleite and (i) diamond [Ravula S, 2015]

form of the carbon fullerenes [Kroto HW, 1985]. After this discovery a new era of synthetic carbon allotropes started, in 1991 synthesis of carbon nanotubes was discovered [Iijima S, 1991] and in 2004, graphene was rediscovered [Novoselov KS, 2004]. At present, more than 9 carbon modifications are known (Fig. 1.1). Below we summarize some of the most important carbon allotropes.

1.1.1 Zero dimensional allotropes (Fullerenes)

History and structure

Fullerenes which are composed entirely of carbon were discovered in 1985 at Rice University by a group of scientists consisting of Richard Smalley, Robert Curl and Harry Kroto. For this discovery, they shared a Nobel Prize in 1996 [Kroto HW, 1985]. The fullerene molecule is the fundamental building block of the crystalline phase. In addition, through doping and chemical reactions, they form the basis of a large family of materials with interesting properties. Fullerenes have many structural variations, it can be found in spherical, elliptical tubes and many other shapes (Fig. 1.2). Spherical form, so-called Buckminsterfullerene (C_{60}) consists of 60 carbon atoms, organized in 12 pentagons and 20 hexagons, in the same way as a soccer ball (Fig. 1.3). The C_{60} fullerene is the best known example of an ideal zero-dimensional structure. In the C_{60} molecule each carbon atom is bonded to three others by two longer bonds (length 0.145 nm) and one shorter bond (bond length 0.14 nm). They are conventionally referred to in the Fullerene's literature as two C-C single bonds, which link a hexagon to a pentagon and one C=C double bond, which lies between two hexagons. It follows that there is bonding anisotropy in the C_{60} molecule since bonds around a pentagon are all single bonds and bonds around a hexagon are alternately single bonds and double bonds. It appears, therefore that the bonding in C_{60} is mainly sp^2 with delocalised π electrons, but with some sp^3 character resulting from the curvature of the C-C bonds [Dresselhaus MS, 1996].

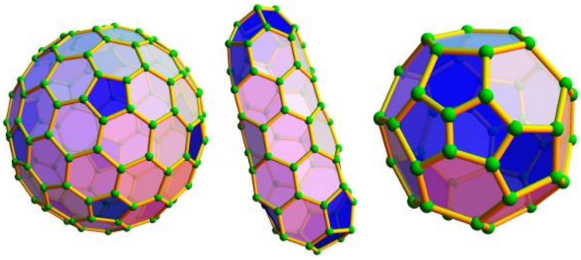

Figure 1.2 Left: A larger, icosahedrally-symmetric fullerene with 140 vertices and 72 faces. Middle: A tube-like fullerene with 66 vertices and 35 faces centres, of which are formed with a long spiral of hexagons. Right: a highly asymmetric fullerene with 44 vertices and 24 faces[1]

---

[1] http://blog.zacharyabel.com/tag/fullerenes/

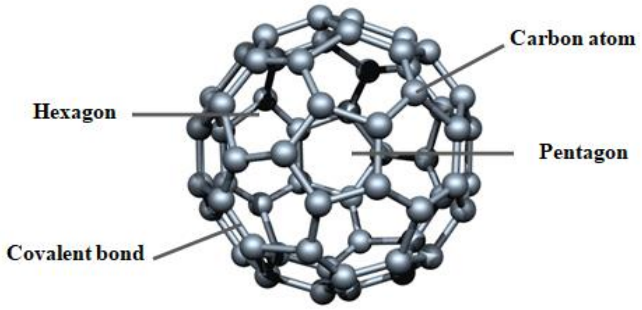

Figure 1.3 The structure of C_{60} “Buckminsterfullerene" [2]

Properties and applications

If the C_{60} molecule were the size of a soccer ball, then the soccer ball in its turn would be about the size of the Earth [Yadav BC, 2008]. It is shown in Fig. 1.4. Fullerenes are extremely strong molecules, they are harder than steel and diamond. The effective bulk modulus of C_{60} is 688 GPa. Some experiments show that fullerenes can withstand collisions of up to 15,000 mph against stainless steel and preserve their shape, thus indicating high stability of the fullerenes molecules. Fullerenes also have attractive chemical and optical properties. The soccer ball shaped C_{60} is not "superaromatic" as it tends to avoid double bonds in the pentagonal rings, resulting in poor electron delocalization. As a result, it behaves more like an electron deficient alkene, and readily reacts with electron-rich species. Geodesic and electronic bonding factors in the structure account for the stability of the molecule [Dresselhaus MS, 1996]. Fullerenes are also found to be soluble in common solvents such as benzene, toluene or chloroform. After shaking some fullerene soot

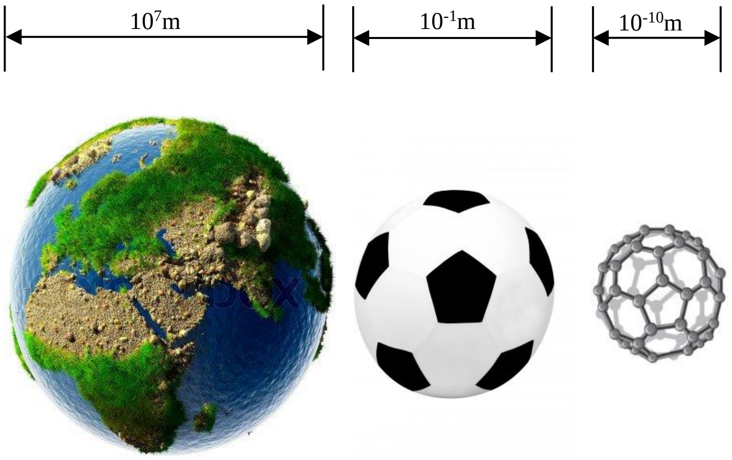

Figure 1.4 Comparison of C_{60} molecule with size of a soccer ball and earth

---

[2] https://phys.org/news/2015-07-scientists-advance-tunable-carbon-capture-materials.html

with toluene and filtering the mixture, one obtains a red solution. As the solvent evaporates, crystals of pure carbon appear [Yadav BC, 2008].

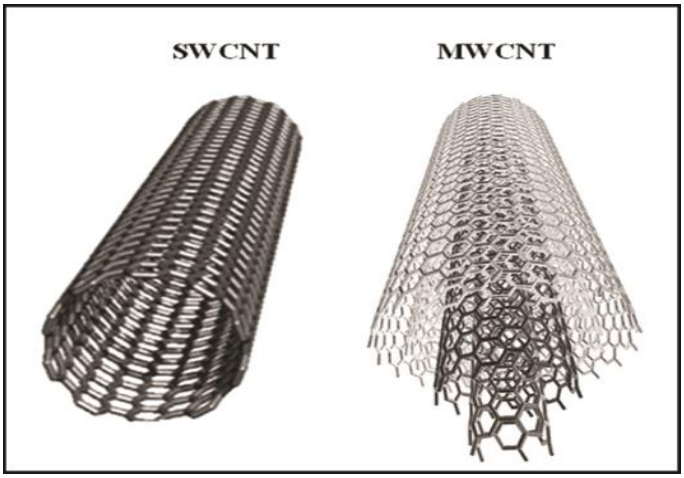

Figure 1.5 Schematic diagrams of single-wall carbon nanotube (SWCNT) and multi-wall carbon nanotube (MWCNT) [Choudhary V, 2011]

Nowadays fullerenes have a large area of application and they are considered like a hot topic in nanotechnology. Fullerenes can be used as photo resistant in certain photolithographic processes, in preparation of super-conductors, in electronic, microelectronic and optical devices, in batteries as charge conies, etc. [Ulloa E, 2013] Fullerenes are very useful materials in medical applications. In future it may be used in the delivery of drugs in small amounts for slow release (cancer treatment). Recently application of fullerene C_{60} and its derivates in cosmetics have been intensively tested. Biological activity permits fullerene to be suitable active compounds in the preparation of skin rejuvenation cosmetic formulations [Lens M, 2009].

1.1.2 One-dimensional Allotropes (Carbon nanotubes)

History and structure

Fullerenes have made significant progress in the area of nanotechnology since 1991, when cylindrical fullerenes (nanotubes) were discovered. These structures, both the so called carbon nanotubes (CNTs) and the buckyballs, are completely composed of carbon, but in a tubular shape and they represent one-dimensional allotrope of carbon. CNTs are usually up to few tens of nm wide and lengths that can range from few hundreds of nm to a few cm. They can have closed or open ends. The structures of tubular fullerenes have aroused great interest in the research community due to the extraordinary electrical and mechanical properties.

There are many different types of carbon nanotubes, but they can be classified into two main types: single-wall carbon nanotubes (SWCNTs) consisting of a unique cylindrical structure and multi-wall carbon nanotubes (MWCNTs) consisting of coaxial cylinders (Fig. 1.5). MWCNTs can range from one outer and one inner tube (a double-walled nanotube) to as many as 100 tubes (walls) or more (multi-walled nanotubes) having interlayer spacing close to that of the interlayer distance in graphite (0.34 nm) [Choudhary V, 2011]. Depending on the number of layers, the inner diameter of MWCNTs diverges from 0.4 nm up to a few nanometers and the outer diameter varies characteristically from 2 nm up to 20 to 30 nm. Both tips of MWCNT are usually closed and the ends of the tubes are covered by a dome-shaped half-fullerene molecules (pentagonal defects), and axial size differs from 1 μm up to a few centimetres. The role of the half-fullerene molecules (pentagonal ring defect) is to help close the tube at two ends [Ajayan PM, 1997]. Unlike in multiwall nanotubes (MWNTs) a single-wall carbon nanotube can be described as a graphene sheet rolled into a cylindrical shape. High quality and large quantities of CNTs can be prepared using three methods, which include arc discharge, laser ablation and chemical vapor deposition (CVD). Most of these processes take place in vacuum or with process gases. CVD growth of CNTs can occur under vacuum or at atmospheric pressure [Choudhary V, 2011].

Properties and applications

Among others CNTs exhibit extraordinary properties in terms of strength, electrical and thermal conductivity. However, directly measuring the properties of these nanoparticles is very difficult by conventional methods. Hence, several properties have been first evaluated by using theoretical studies. The strongest and stiffest nature of CNTs materials were discovered in terms of tensile strength and elastic modulus respectively. This strength results from the covalent sp^2 bonds formed between the individual carbon atoms. Quantum mechanics calculations predict that defect-free single-walled carbon nanotubes possess Young's modulus values of 1 TPa, tensile strengths of 100 GPa, and multiwalled carbon nanotubes with a mean fracture strength higher than 100 GPa [Peng B, 2008]. When exposed to great axial compressive forces, nanotubes can bend, twist, kink, and finally buckle. The tubes, however, do not break under the compressive loads, as shown in Fig. 1.6. Under great axial compression, nanotubes appear to behave consistent with the Euler limit. The Euler limit specifies the point at which a straight tube will buckle. Since

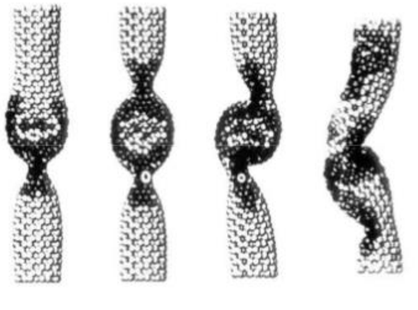

Figure 1.6 Elastic buckling mechanisms of SWNT [Yakobson, 1995]

the deformation in nanotubes is elastic, the tubes return to its original shape when a load is removed [Yakobson, 1995]. Moreover, CNTs have high thermal conductivity along the tube and are insulator laterally to the tube axis. The thermal conductivity of CNTs is determined by phonons [Hone J, 1999]. The results of the experimental measurements show that, thermal conductivity on individual MWNTs reaches up to 3300 W/(m·K), which is about twice as high as diamond [Kim P, 2001]. In addition, CNTs are thermally stable up to 2800°C in vacuum and up to 700°C under air [Belin T, 2005]. CNTs also possess extraordinary electronic properties, which are dependent on the molecular structure (chirality) of CNTs [Thostenson ET, 2001]. The chemical reactivity of one dimensional carbon allotrope, as compared with a two dimensional, is enhanced as a direct result of the surface curvature of the CNT. Carbon nanotube reactivity is directly related to the π-orbital mismatch caused by an increased kink. Therefore, a distinction must be made between the sidewall and the end caps of a nanotube. For the same reason, a smaller nanotube diameter results in an increased reactivity [Sarangdevot K, 2015]. Carbon nanotubes and CNT composites have been emerging as perspective absorbing materials due to their lightweight, large flexibility, high mechanical strength and superior electrical properties. Therefore, CNTs turn out as an ideal candidate for use in filtration of gas, air and water [Rashid H, 2017].

For all these extraordinary properties, nanotubes find application in any field beginning of cancer treatment and ending in hydrogen cars. In the area of nanoelectronics CNTs demonstrate wide range of applications, such as energy storage (supercapacitor) devices [Chen T, 2013]; energy conversion devices that include thermoelectric and photovoltaic devices; field emission displays and radiation sources; nanometer semiconductor transistors, nanoelectromechanical systems (NEMS), electrostatic discharge (ESD) protection[3], interconnections, and passives [Park S, 2013]. These structures of carbon may be tiny—a nanotube's diameter is about 10,000 times smaller than a human hair—but their impact on science and technology is enormous. In the near future billions of carbon nanotubes may be on our desks and in our pockets.

1.1.3 Three dimensional allotropes (Graphite, Diamond and Amorphous carbon)

Graphite

History and structure

Graphite is the most common allotrope of carbon. The origin of the word "graphite" comes from the Greek word "γράψει", meaning "to write". Indeed, graphite has been used to write (and draw) since the dawn of history and the first pencils were manufactured in England in the 15th century. In the 18th century, it was demonstrated that graphite actually is an allotrope of carbon

---

[3] http://www.hyperioncatalysis.com/

[Kelly BT, 1981]. There are two forms of graphite natural (flake, vein, microcrystalline graphite) and synthetic (Primary synthetic, Secondary synthetic graphite and graphite fibers).

Graphite has a layered and planar structure, where each layer is interacting with other layers by weak van der Waals interactions, and carbon atoms are only bonded in two dimensions (the angle between two bonds is 120°). In each layer, the carbon atoms are arranged in a hexagonal lattice in the stacking sequence ABABAB with separation of 0.142 nm, and distance between planes is 0.34 nm (Fig. 1.7). The basis of the crystal structure of graphite is the graphene plane or carbon layer plane. The not perfectly stacked graphene layers often form faults (meaning departures from the ABAB stacking order). This lead to a small increase in the interlayer distance from the value 0.3354 in 3D graphite up to a value of about 0.3440 nm. For this interplanar distance, the stacking of the individual carbon layers become uncorrelated with essentially no site bonding between the carbon atoms of both layers. The resulting structure is called turbostratic graphite [Dresselhaus MS, 2001]. They are two know forms of graphite: hexagonal (*alpha*) and rhombohedral (*beta*). These two structures have very similar physical properties, except that in *beta* form graphene layers stack in a slightly different form. Between these two forms can be a transformation. The *alpha* form can be converted to the *beta* form through mechanical treatment, and the *beta* form reverts to the *alpha* form when it is heated above 1300°C [Dresselhaus MS, 2001].

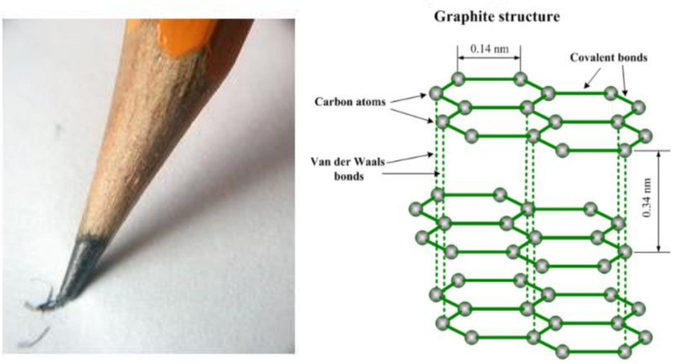

Figure 1.7 Crystal structure of graphite /www.substech.com/

Properties and applications

Graphite materials are distinguished within the group of corrosion-resistant materials by their excellent chemical and corrosion resistance. Graphite has a high temperature resistance and oxidation occurs from 600^{0}C. In case of non-oxidizing atmosphere, the temperature resistance of graphite is determined by the temperature treatment during the production process and it is about 1000°C [Chung DDL, 2002]. Due to the high temperature stability graphite is a one of the used material in the manufacturing of refractory bricks and in production of “Mag-carbon” refractory bricks (Mg-C). Structural strength at a high temperature, thermal shock resistance, high thermal conductivity, low thermal expansion and high chemical resistance makes graphite suitable material for production of iron. There are many high temperature uses of graphite in chemical industry. For example in production of halogens, phosphorus and calcium carbide in arc furnaces. Graphite has low tensile and flexural strength, but a higher compressive strength. In contrast to plastics or metallic materials, in graphite the strength increases as temperature increases, but its resistance to thermal shock is maintained [Burchell TD, 1999]. Also graphite has low density (28% of steel), low hardness, low friction and self-lubrication, low wettability by liquid metals, machinability, high stiffness (modulus of elasticity) and many more attractive properties, which make this material promising in many spheres of application. Table 1.1 list of graphite key properties.

New green energy and technology applications demand new materials with attractive properties, like graphite, for using in different areas such as Li-ion batteries, solar power, nuclear power, supercapacitors (fuel cells) and much more. The demand for graphite in different applications is increasing year by year and is expected to increase as electric vehicles and lithium battery technology are adopted. Almost all portable consumer devices such as laptops, cell phones, MP3 players and cameras use Li-ion batteries and they are now rapidly moving into power tools. Li-ion mega-factories are either in construction or are expanding, which will increase the production capacity of batteries to about 521% by 2020. Li batteries are a very promising devices for developing of new green energy and technology area such as hybrid electric vehicles (“HEV”), plugin electric vehicles (“PEV”) and all electric vehicles (“EV”) [Lowe M, 2010; Tarascon JM,2001]

Table 1.1 Key properties of graphite[4]

Property	Commercial graphite ranges
Bulk density (g/cm^3)	1.3-1.95
Porosity (%)	0.7-53
Modulus of elasticity (GPa)	8-15
Compressive strength (MPa)	20-200
Flexural strength (MPa)	6.9-100
Coefficient of thermal expansion (×10^{-6} K^{-1})	1.2-8.2
Thermal conductivity (W/m·K)	25-470
Specific heat capacity (J/kg·K)	710-830
Electrical resistivity (Ω·m)	5×10^{-6}-30×10^{-6}

---

[4] https://www.azom.com/article.aspx?ArticleID=1630

Diamond

History and structure

Diamonds are thought to have been first recognized and mined in India, where significant alluvial deposits of the stone could be found many centuries ago along the rivers Penner, Krishna and Godavari. Diamonds have been known in India for at least 3,000 years but most likely 6,000 years [Hershey W, 1940]. Crystals of diamond are formed at 150 kilometers inside the ground. At that depth, the temperature is high and the rocks are subject to high pressures. Diamond except for the natural form also can be found from several sources:

- Synthetic single crystal of diamond produced by the high-pressure and high temperature (HPHT) method. The price of this diamond is lower than natural diamond.
- Polycrystalline diamonds are formed usually by either cementing diamond grains together using metal as a bonding agent or sintering using boron carbide as a sintering aid.
- Vapor phase deposition can be used for producing thin films of diamond by means of chemical vapor deposition (CVD) or by physical vapor phase deposition methods (PVD). Diamond produced by these methods is several times more expensive, than natural one.

But, from the point of view of the application, the use of vapor phase deposition of diamond can be justified economically as they are used in the form of thin film and they make a significant difference to the component properties [Ashfold MNR, 1994].

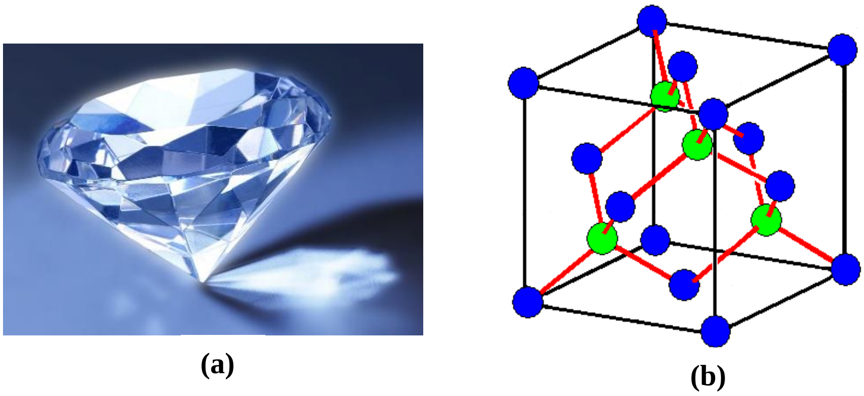
(a) **(b)**

Figure 1.8 (a) Diamond[5] ; (b) A diamond crystal structure[6]

Diamond is a metastable allotrope of tetragonal σ bonding carbon atoms, where each carbon atom is bonded covalently with other surrounding four carbon atoms and are arranged in a variation of

---

[5] https://www.businesstoday.in/markets/stocks/diamond-futures-exchange-reliance-adag-anil-ambani/story/259159.html

[6] https://www.tf.uni-kiel.de/matwis/amat/iss/kap_4/illustr/i4_2_1.html

the face centered cubic (fcc) crystal structure called a diamond lattice (Figure 1.8). In Figure 1.8b the blue circles show the carbon atoms in the lattice points and these atoms forming C-C bonds (sp^3) (0.154 nm long). As compared with graphite, diamond structure it is a bit longer and weaker than graphite (sp^2) and, in case of diamond, the crystallographic structure consists of two superimposed fcc lattices shifted by one-quarter of the cube diagonal. Carbon atoms are shown with a green color in Fig.1.8b, they are outside the lattice points. The red lines symbolize very strong bonds between carbon atoms and such bonds confer extreme hardness to diamond network. The black lines are simply to make the crystalline structure more visual[7].

Properties and applications of diamond

Probably, more than any other gemstone, diamonds feature more predominantly in the history and cultural heritage of the human race. They have been prized for their scarcity for centuries, and still remain a symbol of wealth and prestige up to these days. Apart from their appeal as gemstones, diamonds possess a remarkable range of physical properties. The name diamond is derived from the ancient Greek αδάμας that means unbreakable. Diamond is harder than any known material (metal, alloy, semiconductor, ceramic, glass and any other compound). It is so hard that can only be cut with another diamond. Another amazing property of diamond is its high thermal conductivity (six times that of copper), which is the highest compared with any other bulk material [Raman CV, 1943]. That is why a diamond, in contrast to glass, feels cold when you touch it. It conducts the heat out of the body very efficiently to the surrounding. Also diamond provides high electrical resistivity (10^{11} to 10^{18} $\Omega \cdot m$), high strength, broad optical transparency from ultraviolet to infrared and it is biologically compatible [Raman CV, 1968]. A unique combination of extreme properties makes diamond particularly well suited for high speed, high power, and high temperature applications.

Diamond can be used in different applications such as gem diamond production, mechanical (surgical diamond blades, single point diamond turning (SPDT) blanks, milling tool blanks, etc.), optical (UV, IR, MW, X-ray windows, laser optics components), semiconductors (heat spreaders and heat sinks, sub-mounts for high-power IC & laser diodes), Electronics (high energy particle (HEP) radiation detectors, beam condition monitors, RF diodes, FET, MEMS, radiotherapy dosimeter, etc.)[8]

---

[7] https://www.tf.uni-kiel.de/matwis/amat/iss/kap_4/illustr/i4_2_1.html

[8] http://sekidiamond.com/diamond-seeds-substrates/

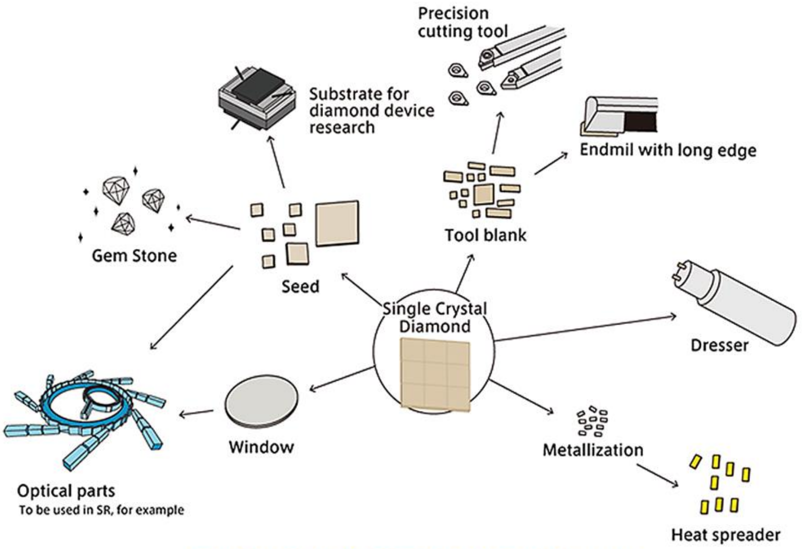

Figure 1.9 Applications for Diamond seeds and substrates[7]

Amorphous carbon

History and structure

Amorphous carbons form another big class of carbon allotropes. As the name suggests, this type of structure has high degree of disorder (non-crystallinity). Fig. 1.10 shows a typical structure of amorphous carbon, where black atoms represent sp^3-bonded carbon atoms whereas grey atoms represent sp^2-bonded carbon atoms in a disordered network [McCulloch DG, 2000]. Amorphous carbon films deposited on a substrate with composition of sp^2 mixture and sp^3 bonding with little evidence of sp^1 bonding being present [Robertson J, 1986]. These carbon structures can indicate some character of sp^2 carbon structure (graphite) or sp^3 (diamond) depending on their sp^2/sp^3 fractions. In addition, hydrogenated amorphous carbon can be synthesized, depending on deposition conditions, due to the hydrogen content during synthesis.

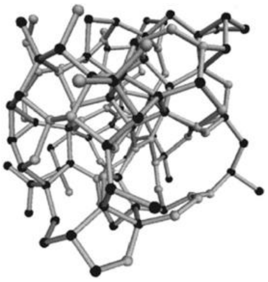

Figure 1.10 Typical structure of amorphous carbon [McCulloch DG, 2000]

Figure 1.11 shows the ternary phase diagram of the amorphous carbon-hydrogen system, where, in each side of the diagram is represented the percentage of sp^2 carbon, sp^3 carbon and hydrogen contents. The entire left side of the phase diagram shows the variation of sp^2C/sp^3C content for films with 0% hydrogen, known as non-hydrogenated amorphous carbon films (a-C). At the bottom left part of the phase diagram, with 100% of sp^2 C bonding, corresponds to the graphitic carbon such as char and soot.

The properties of this type of carbon are similar to graphite, as well as glassy carbon. When the sp^3 C bonding increases, the structure provides diamond-like character. This type of amorphous carbon (a-C) structures, containing significant amount of sp^3 carbon bonds, is called diamond-like carbon (DLC), which exhibits relatively high hardness and mass density and a relatively low electrical conductivity [Ferrari AC, 2004]. If the concentration of sp^3 content in the film increases further to ~70–90%, and the carbon atoms become tetrahedrally bonded in an sp^3 network, then a fundamental change in the structure occurs as the essentially layered material progressively changes into the dense isotropic network structure of tetrahedral amorphous carbon (ta-C) [McKenzie DR, 1996].

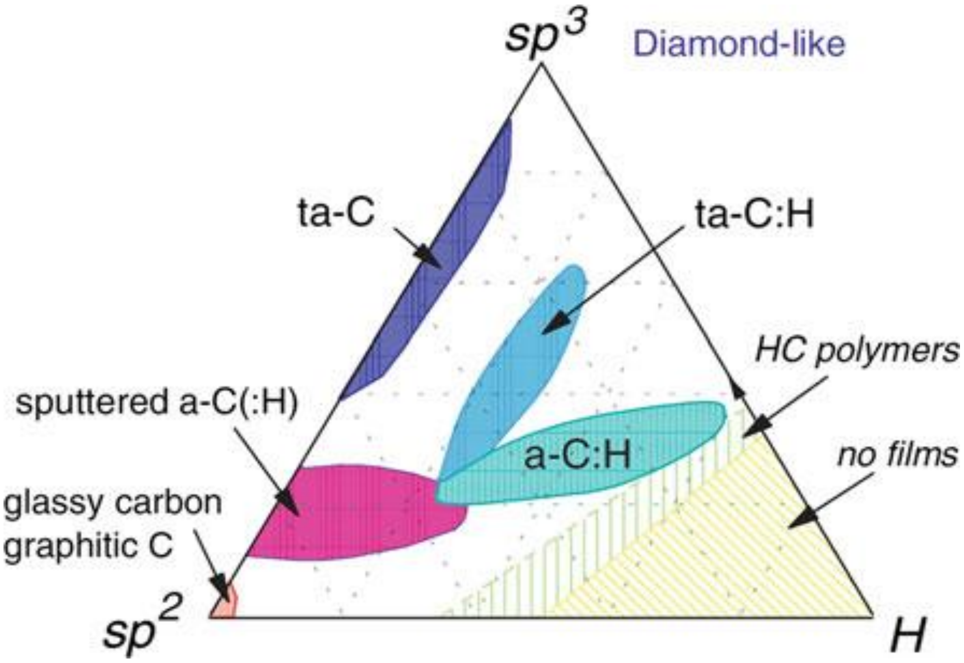

Figure 1.11 Ternary phase diagram of the amorphous carbon-hydrogen system [Robertson, 2002]

With incorporation of hydrogen atoms in carbon network, hydrogenated amorphous carbon can be formed (a-C:H). These types of carbon films can be done by physical vapor deposition of carbon films in a hydrogen atmosphere, or by using hydrocarbon source as a precursor for film growth in chemical vapor deposition processes [Holland L, 1976; Marchon B, 1991] Softer a-C:H films can be obtained with 40–60% of H content, which are known as polymer-like a-C:H (PLCH) films. a-C:H films with intermediate hydrogen content (20–40%) possess relatively higher sp^3 C-C bonding than PLCH films and, hence, better mechanical properties [Heitz T,1999].

Properties and applications of amorphous carbon

Amorphous carbon (a-C) and hydrogenated amorphous carbon (a-C:H) have high mechanical hardness, high optical transparency in the visible and close infrared range, high thermal conductivity, low friction coefficient, and chemical inertness to some corrosive agents [Bubenzer A, 1983; Theye ML, 2002; Zhu H, 2009]. The properties of amorphous carbon strongly depend on the technique and on deposition conditions. For example, amorphous carbon deposited via sputtering usually has a high concentration of sp^2 hybridized carbon (sp^2C) and a very low bandgap, resembling properties of graphite. Properties of amorphous carbon films deposited by chemical vapor deposition (PECVD) depend on the applied bias voltage: when it is lower than 40V the films are very soft and have a high bandgap (> 2.5 eV), a low mechanical stress, and a high concentration of hydrogen (40–60 at. %) bonded to sp^3 hybridized carbon (sp^3C). These films are called polymeric-like carbon. When the bias voltage is -50V to 300V the deposited films are hard with intermediate bandgap (1–2 eV), relatively high stress (1–3 GPa), high hardness (10-30 GPa) and an intermediate content of sp^3 sites (20–60%).These films are called diamond-like carbon (DLC). Finally, films deposited at a higher bias voltage are referred to as graphite-like carbon (GLC) and have an even lower fraction of sp^3 sites and present a very narrow gap. Having in mind all these extraordinary properties, amorphous carbon and hydrogenated amorphous carbon are a class of materials that can be used in several applications. They have been extensively proposed and used in a large variety of applications as protective tribological coating, radiation protection, electron field emitters, and in biomedicine [Popov C, 2006; Neuville S, 2007; Goncalves RGF, 2011; Lifshitz Y, 1999; Grill A, 1999].

Chapter 2

Graphene and graphene nanowalls

2.1 Graphene

2.1.1 History

Graphene is a two-dimensional allotrope of carbon, which serves as building block in the formation of carbon nanowalls based on the experimental results presented in this thesis. Perfect graphene consists exclusively of two-dimensional network of hexagonal cells as shown below in Figure 2.1. The story of graphene goes back to 160 years ago, when in 1859, Sir Benjamin Collins Brodie described the highly lamellar structure of thermally reduced graphite oxide. Theoretically, the existence of graphene was considered in 1947 for P. R. Wallace.

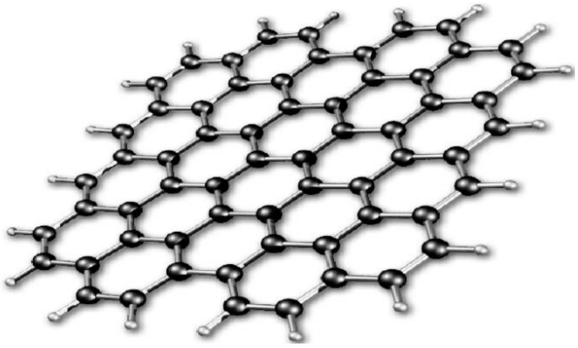

Figure 2.1 Schematic diagram of graphene lattice [Choudhary V, 2012]

The name 'graphene' was first mentioned in 1987 to describe the graphite layers that had various compounds inserted between them. In 1948, with the advent of the first electron microscopy[9], images of several layers of graphite were first observed, followed by the observation of single graphene layers by Ruess and Vogt. Since then, pursuit of "isolating graphene" started, and in 2004 two scientists from University of Manchester Prof. Andre Geim and Prof. Constantine Novoselov for the first time isolated a single atomic layer of carbon (graphene) layers from graphite. They noticed some flakes to be thinner than others. By separating the graphite fragments repeatedly they managed to create flakes which were just one atom thick. They played with graphite cubes and Scotch tape, for pulling flakes of graphite.

They did this again and again with the flaked-off graphite, separating it into thinner and thinner flakes (after ten or twenty or a hundred iterations), until they ended up with graphite flakes with

---

[9] http://www.cealtech.com/2017/05/09/the-history-of-graphene/

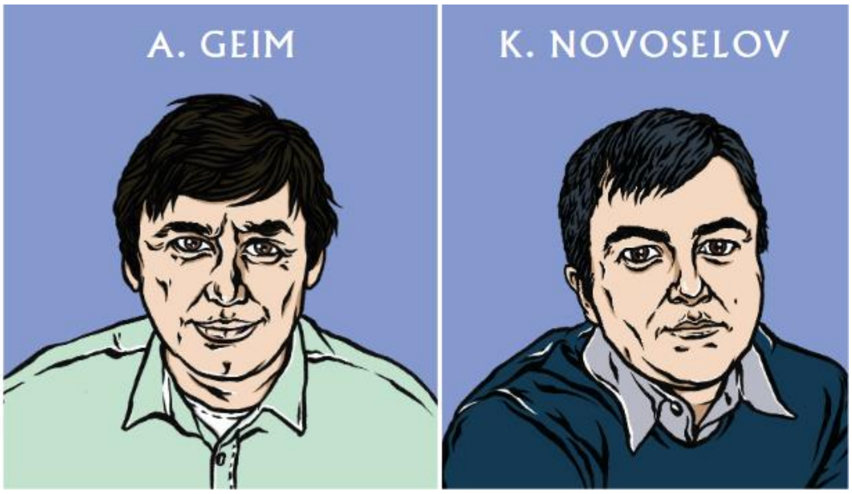

Figure 2.2 Andre Geim and Kontstantin Novoselov, University of Manchester, UK[10]

only one atom thick. The materials could not be thinned more than one atom thick, so this stuff was as close to the two-dimensional system as physically possible. Geim and Novoselov had invented Wallace's graphene. The ¨scotch tape¨ method was so simple and effective, that this area of science grew extremely quickly and nowadays many research institutes around the world use this technique for investigation of graphene, because it doesn't require large investments or complicated equipment [Novoselov KS, 2004]. In 2010 Andre Geim and Konstantin Novoselov were awarded Nobel Prize in physics for this work, becoming the 24th and 25th Nobel Laureates in history of the University's [Geim A, 2010].

2.1.2 Graphene structure

Everyone is familiar with diamond and graphite, which are bulk crystals that are formed purely from carbon atoms. These two bulk crystals are easily understood materials that have been in use for millennia, but interest in graphene has been shown in the past decades because its singular structure and properties.

Graphene is a single layer of carbon packed in a hexagonal (honeycomb) lattice, with a carbon-carbon distance of 0.142 nm that mimics a honeycomb structure. Out of graphene plane, the non-completely filled π orbitals forms weak π bonds and they are responsible for conductive properties. Its extended honeycomb network is the basic building block of other important allotropes; it can be stacked to form 3D graphite, rolled to form 1D nanotubes, and wrapped to form 0D fullerenes. Graphene sheets can stack in three main different ways: hexagonal (Order, AA), bernal (AB), and rhombohedral (ABC) stacking (Fig. 2.3). In Order stacking all the carbon atoms of each layer are well-aligned. For AB and ABC stacking, a cycle period is constituted by

---

[10] http://hebergement.upsud.fr/supraconductivite/histoires%20quantiques/pdf/posters%20ENG%20complet.pdf

two layers and three layers of a non-aligned graphene, respectively [Jhang SH, 2011; Koshino M, 2010; Lui CH, 2010]. In Order stacking, all the carbon atoms of each layer are well aligned. For AB and ABC stacking, a cycle period is constituted by two layers and three layers of a non-aligned graphene, respectively. A highly symmetrical structure occurs in Order stacking, while the structure in ABC stacking is relatively complicated.

Graphene possesses many extraordinary properties and has been the subject of intense scientific interest. One of the interesting features of graphene is the edge effect. Graphene edges are typically far from ideal and suffer from atomic-scale defects, structural distortion and unintended chemical functionalization, leading to unpredictable properties. The presence of edges strongly affects the electronic structure depending on their edge shape (zigzag and armchair edges). Depending on the direction of the cutting line of a graphene sheet, there can be two types of edges created, as shown in figure 2.4, namely armchair edges and zigzag edges [Enoki T, 2007]. Manipulation of graphene edges at atomic level is very promising for exploiting graphene recognized potential in the next generation of electronic, optical, mechanical and chemical devices.

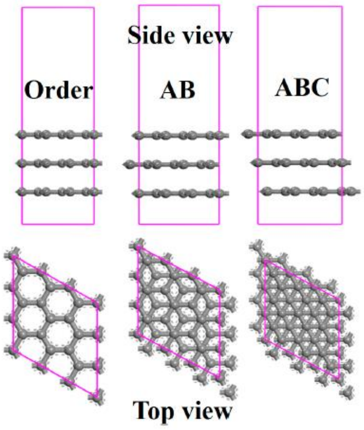

Figure 2.3 The side and top views of the stacked graphene layers with Order, AB, and ABC pattern [Yang N, 2018]

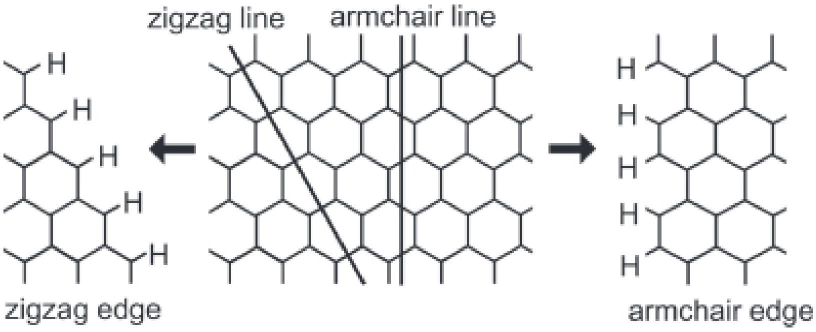

Figure 2.4 Zigzag and armchair lines and hydrogen-terminated zigzag and armchair edges in a graphene sheet [Enoki T, 2007]

The unique plane structure and geometry of monolayer graphene contribute its super properties, including high Young’s modulus (~1100 GPa), high fracture strength (~125 GPa), excellent electrical (~10^6 S/cm) and thermal conductivity (~5000 W/(m·K)), fast mobility of charge carriers (2×10^5 $cm^2/(V\cdot s)$) and large specific surface area (theoretically calculated value, 2630 m^2/g) [Meyer J, 2009; Pan Y, 2012]

2.1.3 Graphene properties

Electrical properties

Most of the experimental researches on graphene focus on the electronic properties. Unique and extreme electrical characteristics are related to the electronic structure of graphene. Most of the properties of graphene are related to the electronic band structure [Castro-Neto AH, 2009] as it is plotted in figure 2.5. As the sixth element in the periodic table, carbon has a $1s^2 2s^2 2p^2$ ground state electron configuration. From the point of view of carbon electronic configuration, the two 1s electrons do not participate in the conduction process. The other four $2s^2 2p^2$ valence electrons

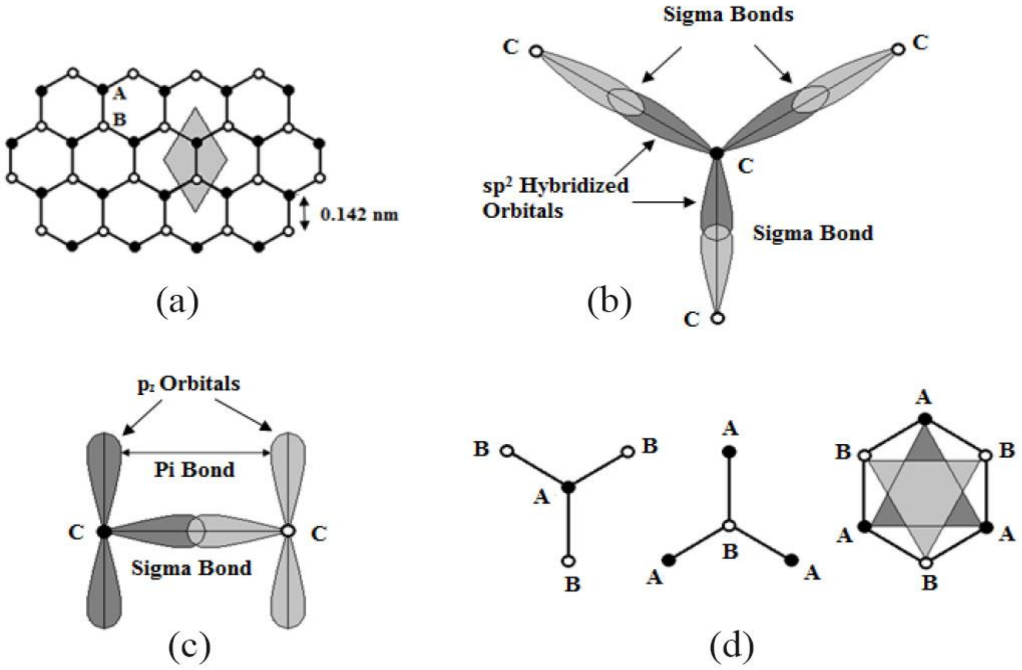

Figure 2.5 Structure of graphene **(a)** honeycomb lattice of carbon atoms, the dark circles and the unfilled circles represent carbon atoms at two different sites designated respectively as A and B, the shaded region indicates a unit cell; **(b)** sp^2 hybridized orbitals of carbon atoms symmetrically distributed in the molecular plane at angles of 120º forming three σ-bonds with those of the three nearest neighbors; **(c)** orbitals of the remaining electrons distributed perpendicularly to the molecular plane form π-bonds with those of one of the nearest neighbor, assigning four bonds to each carbon atoms; **(d)** two different orientations of the arrangement of carbon atoms at lattice sites A and B, the honeycomb lattice can be viewed as two interpenetrating triangular lattices of A and B carbon atoms [Dash GN, 2014]

are responsible for all the properties of graphene, redistribute among themselves with one electron in each of the four orbitals, s, p_x, p_y and p_z. The s, p_x and p_y electrons combine together and form three sp^2 hybridized orbitals. They are symmetrically apart from each other at angles of 120º and form three σ -bonds (Figure 2.5b). These bonds are responsible for the lattice stability and for the elastic properties of graphene. The p_z electrons, which are oriented perpendicularly to the graphene plane, form π-bonds with the nearest carbon atoms (Figure 2.5c). These bonds can have two different orientations and graphene structure can be viewed as two interpenetrating triangular sublattices A and B (Figure 2.5d) with two atoms per unit cell (Figure 2.5a) [Dash GN, 2014]. The first account of this band structure calculation was given by Wallace in 1947. In the calculation lattice structure of graphene, was made out of two interpenetrating triangular lattices A and B, by using a tight binding Hamiltonian. The energy bands derived from this Hamiltonian have the following form [Sarma D, 2011]:

$$\epsilon^{\pm}(\vec{k}) = \pm t\sqrt{3 + f(\vec{k})} - t' f(\vec{k}) \tag{2.1}$$

$$f(\vec{k}) = 2\cos(\sqrt{3}k_y a) + 4\cos\left(\frac{\sqrt{3}k_y a}{2}\right) \cdot \cos\left(\frac{3k_x a}{2}\right) \tag{2.2}$$

k_x and k_y are components of wave vector $\vec{k}$

a is the nearest carbon-carbon interatomic distance and is equal to 1.42 Å

$t \cong$ 2.8 eV is the nearest neighbor hopping energy

$t' \cong$ 0.1eV is the next nearest neighbor hopping energy.

It is possible to represent this equation via 3D plot (Fig. 2.6a). Fig. 2.6a shows that the cone-like conduction band for the π^* electrons and the inverted cone-like valence band for the π-electrons touch at six points in the Brillouin zone, of two different equivalences, named *K* and *K'*, the so-called Dirac points (Fig. 2.6b). The energy dispersion close to the Dirac points is linear with the momentum, being described as a linear dispersion by the equation $\epsilon^{\pm}(\vec{k}) = \hbar \cdot \overrightarrow{V_F} \cdot \vec{k}$, where $\overrightarrow{V_F}$ is the Fermi velocity, $\hbar$ is the Plank constant and $\vec{k}$ is the electron wave vector. The value of the $\overrightarrow{V_F}$ close to the Dirac points is 10^6 m/s (faster than any other material), it means that the electrons in graphene behave like massless Dirac fermions moving with an effective velocity of light, equal to the Fermi velocity and a carrier charge density in order of 10^{13} cm^{-2} [Novoselov KS, 2005a]. This explains the very high mobility predicted of 2.53×10^5 $cm^2 V^{-1} \cdot s^{-1}$. These electrons and holes at a room temperature can travel at a micrometer scale without scattering. This property implies that graphene acts as if it were a semiconductor of zero-gap and like a semimetal, a metal with a negligible density of states at the Fermi level, where the mass of carriers is regarded as zero (Dirac fermion) [González J, 2010].

The description of quasi particles and the Dirac equation describe better the system than the Schrödinger equation, since the electron and holes behave like relativistic particles. The energy band varies with the number of graphene layers. As pointed out above, in graphene nanoribbons the band structure depends on the edge geometry and type of termination: armchair or zig-zag.

Thermal properties

The strong and anisotropic bonding and the low mass of the carbon atoms give graphene and related materials unique thermal properties. Therefore, recently, there has appeared a strong motivation to investigate thermal properties of graphene and related composite materials from the positions of practical applications. From the point of view of performance and reliability of new technologies, such as modern electronic, optoelectronic, photonic devices and systems, the efficient heat removal it is an important issue, which can be resolved by using optimal thermal interface materials (TIMs) between heat sources and heat sinks. Conventional TIMs filled with thermally conductive particles require high volume of fractions filler (f ~ 50%) to achieve thermal conductivity K of the composite in the range of ~1-5 W/(m·K) at a room temperature (RT) [Shahil KMF, 2012]. There is a great demand of TIMs for electronic used in information processing and

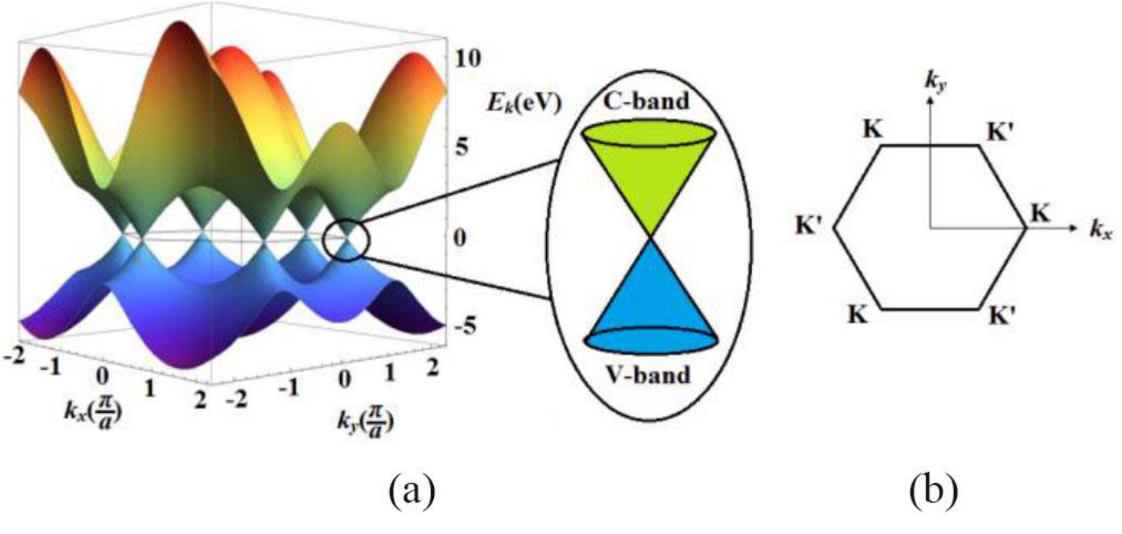

Figure 2.6 Dispersion relation of graphene (a) 3-D view indicating six cones for the conduction band and six inverted cones for the valence band touching at six points (referred to as Dirac points) in the Brillouin zone leaving no bandgap in between[11]; (b) Six Dirac points in k-space, symmetry insists that the six points are not all different reducing them into two equivalent points *K* and *K'* [Dash GN, 2014]

---

[11] Figure reprinted from "The Nobel Prize in Physics 2010—Advanced Information," http://www.nobelprize.org/nobel_prizes/physics/laureates/2010/advanced.html with permission from the Royal Swedish Academy of Sciences _c 2010

communications and also for used in the ¨green¨ technology (Photovoltaic solar cells) revolution. Graphene is great material for using in TEMs. It is demonstrated in different researches that thermal conductivity of TIMs with enhanced graphene elements may lead to revolutionary increase in device and system performance not only in electronics but also in optoelectronics and renewable energy generation. In 2008, it was discovered that graphene has extremely high intrinsic thermal conductivity (K_i), which can exceed that of carbon nanotubes (CNTs) [Balandin AA, 2008; Balandin AA, 2011]. The extraordinary thermal properties were discovered at the University of California—Riverside [Nika DL, 2012].

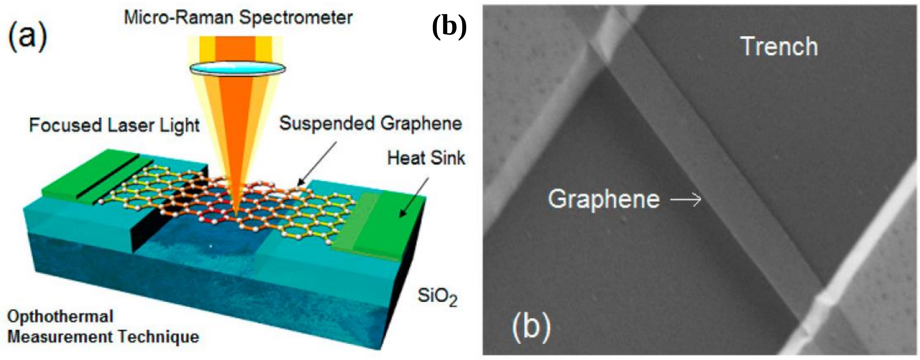

Figure 2.7 Schematic structure of the suspended grapheme used for measurements of the thermal conductivity. Graphene was heated with the laser light focused in the middle of the suspended part. The temperature rise was determined from the shift of the G peak position in graphene Raman spectrum; (**b**) Scanning electron image of the bilayer graphene ribbon suspended across the 3-μm trench in Si/SiO_2 wafer for optothermal measurements [Balandin AA, 2011]

Original non-contact optothermal technique was used for experiment based on Raman spectroscopy (Fig. 2.7). In this experiment the graphene layer was obtained by mechanical exfoliation from high quality bulk graphite. This technique was developed only for measuring thermal conductivity of the atomically thin materials. The value of *K* was found between 3000 W/(m·K) to 5300 W/(m·K), depending on the size of the graphene flakes, at a near room temperature. This number is among the highest of any known material. This result is clearly above the bulk graphite limit of 2000 W/(m·K) [Balandin, AA, 2008] and it exceeds the record values of diamond and carbon nanotubes, about 2000–4000 $W \cdot m^{-1} \cdot K^{-1}$ for freely suspended samples [Balandin, AA, 2011; Chen S, 2012]. This attractive thermal conductivity of graphene makes this material beneficial for electronic applications and establishes graphene as an excellent material for thermal management.

Optical properties

In the research work of Navaselov et al. in 2004, it was demonstrated that graphene exhibits measureable reflection changes as compared to the substrate when deposited on an interferometer. However, in 2007 an article was published where it was reported that number of graphene layers could be identified and counted using SiO_2 interferometer, based on the sensitivity of the optical reflection measurements [Ni ZH, 2007a]. The optical response of graphene is remarkably high for a monoatomic layer (≈ 2% absorption), it absorbs and reflects a tiny portion of the light, for this reason, the graphene layer appears as almost transparent. Absorbance depends on the layers of graphene, it is the result of multiplying $\pi\alpha$ by the number of graphene layers, where $\alpha = e^2/(\hbar \cdot c)$ is the fine-structure constant. Its reflectance increases from 0.1 to about 2% with the increase of the layers number from 1 to 10 [Nair RR, 2008] (Fig. 2.8). These optical properties make graphene useful for applications in optoelectronic and photonic devices, also in photodetectors, touch screens, smart windows, saturable absorbers and optical limiters.

Graphene like other allotropes of carbon possess remarkable nonlinear optical (NLO) properties, which promote design and fabrication of nano and nano-scale optoelectronic and photonic devices [Avouris P, 2008]. All these nano-carbons exhibit diverse NLO properties. For example, carbon black suspensions show strong thermally-induced nonlinear scattering (NLS) effect and hence optical limiting (OL) for intense ns laser pulses [Mansour KM, 1992]; fullerenes show large third-order optical nonlinearity and reverse saturable absorption (RSA) at certain wavelength band [Tutt LW, 1992]; CNTs show ultrafast second- and third order nonlinearities and saturable absorption (SA) in the near infrared (NIR) region (Hasan T, 2009); and graphenes show an ultra-fast relaxation time of charge carriers and an ultra-broad-band resonance NLO response [Bonaccorso F, 2010]. Graphene application in the development of viable nano-carbon OL

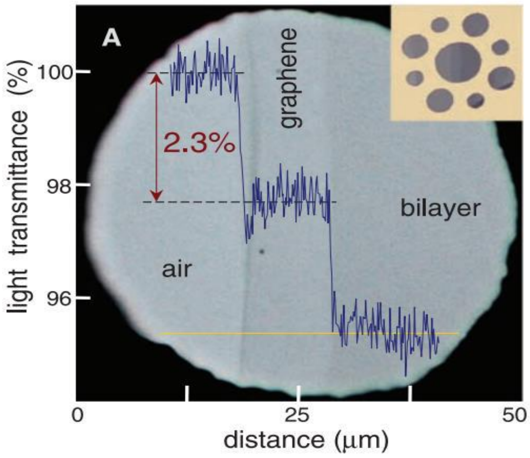

Figure 2.8 Photograph of a 50-mm aperture partially covered by graphene and its bilayer. The line scan profile shows the intensity of transmitted white light along the yellow line. On the inset the metal support with several apertures for the graphene placement [Nair RR, 2008]

devices has limitation, which depends on the difficulty of existing stably in many organic solvents [Wang J, 2009]. So, it is very significant to design and synthesize a graphene-based solution-processed organic/polymeric materials.

So, optical limiting is an important NLO phenomenon, which can be utilized to protect delicate optical instruments from intense laser beams, especially for treating the human eye, [Tutt LW,1993].

Mechanical properties

Graphene, "the mother of all graphitic forms of carbon", is one of the strongest materials in the world, it presents a tensile strength of 130 GPa and is one of the stiffest known materials characterized by a remarkably high Young's modulus of ~ 1 TPa. In general, mechanical properties of a crystalline solid are controlled by characteristics of its pristine crystal lattice and structural defects such as dislocations and grain boundaries [Hirth JP, 1982; Veprek S, 2007]. In the case of graphene, the reason for the exceptional mechanical properties lies in the stability of the sp^2 bonds that form the hexagonal lattice and oppose a variety of in-plane deformations [Lee C, 2008]. For the first time, mechanical measurements of free-standing monolayer graphene were carried out by using nanoindentation in an AFM [Lee C, 2008] (Fig. 2.9). For measuring the mechanical properties of graphene it was deposited onto a substrate with arrays of circular wells and loaded by a tip of an atomic force microscope.

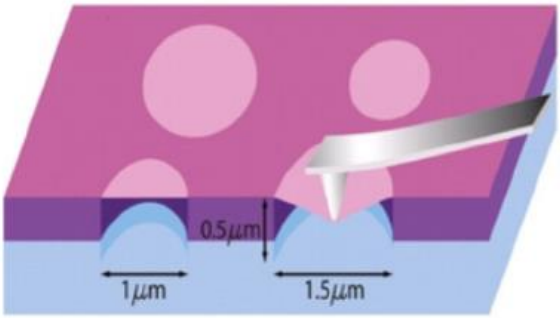

Figure 2.9 Mechanical testing of graphene. Schematic of nanoindentation on suspended graphene membrane [Lee C,2008]

The force-displacement behavior was interpreted within a framework of nonlinear elastic stress-strain response, and yields second- and third-order elastic stiffnesses of 340 $N \cdot m^{-1}$ and -690$N \cdot m^{-1}$, respectively. The breaking strength is 42 Nm^{-1} and represents the intrinsic strength of a defect-free sheet. These quantities correspond to a Young's modulus of E = 1.0 TPa, third-order elastic stiffness of D = -2.0 TPa, and intrinsic strength of σ_{int} = 130 GPa for bulk graphite. After these measurements Hone and coworkers established graphene as ''the strongest material ever measured", citation is in their words[12]. They also show that atomically perfect nanoscale materials can be mechanically tested to deformations, which are well beyond the linear regime [Lee C,2008].

Then, graphene has strength 300 times more than that of steel. However, concept of the strength is something general, there are different types of strength: strength in tension, compression, hardness, toughness and fatigue just to name a few. Some researchers have estimated the sample with elephant poised atop a pencil on a paper from experiments in which they indented a sample of graphene with an atomic force microscope probe (Fig. 2.10). They determined that a sheet with the thickness of Saran wrap would support an elephant poised atop a pencil.

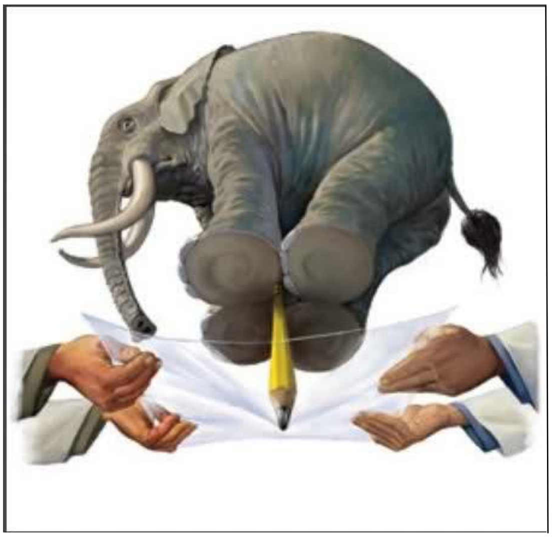

Figure 2.10 Elephant balanced on a pencil to break through a sheet of graphene[13]

There was another famous example with cat sitting on a hammock: one square meter hammock would weigh less than a cat's whisker, but would hold the weight of the cat[14] (Fig. 2.11).

So, nowadays graphene with all of these extraordinary properties is one of the hot topics. The scale up of the production of high-quality graphene is a major issue which is always going to be reflected on the ultimate properties of the materials. Getting this kind of performance out of graphene is a little easier said than done.

---

[12] https://cen.acs.org/articles/86/i29/Graphene-Strongest-Material.html

[13] https://www.extremetech.com/extreme/147456-researchers-successfully-grow-defect-free-graphene-commercial-uses-now-in-sight

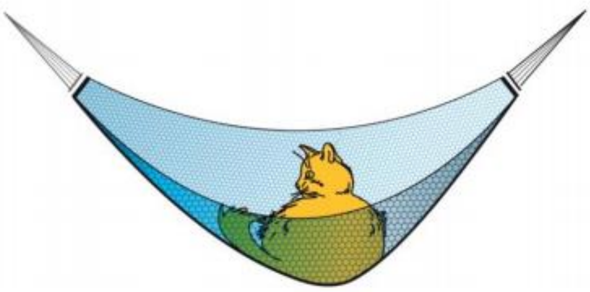

Figure 2.11 A monolayer graphene hammocks placing a cat before breaking[14]

2.1.4 Production technology

In view of the many attractive properties of graphene, it can be used for commercial and strategic applications. Scientists from all over the world are intensively pursuing research activities to develop a variety of technique for graphene synthesis. There are three important challenges for producing graphene, make bigger (mass production), cheaper and of high quality. Currently, there are many techniques for producing graphene, however, one can broadly classify them into two main categories, i.e. bottom-up (e.g., CVD, epitaxial growth on SiC, arc discharge, chemical synthesis etc.) and top-down (e.g., exfoliation methods) processes. In the top-down approach they intend to use natural or synthetic graphite and in various ways to peel off single graphene sheets from graphite (e.g., exfoliation methods). In the bottom up approach it is necessary to synthesize graphene directly on top of substrate using different technique (e.g., CVD, PECVD, epitaxial growth on SiC, arc discharge and chemical synthesis, among others) [Sivudu KS, 2012]. The quality of graphene play important role in the large area of applications. The graphene sheet with the presence of defects, impurities, grain boundaries, multiple domains, structural disorders and wrinkles can have an adverse effect on its electronic and optical properties. In addition, electronic applications require large sample of graphene that is possible to obtain by chemical vapor deposition (CVD), but it should be noted that this method also has some difficulty to produce high quality and single crystalline graphene thin films possessing very high electrical and thermal conductivity along with excellent optical transparency.

---

[14] https://www.nobelprize.org/uploads/2018/06/advanced-physicsprize2010.pdf

CVD graphene can be used in a variety of exciting applications, from touch layers to transistors and sensors. For many years, CVD has been a high cost production process and CVD graphene is still mostly used in research projects in academic and research institutes, but prices are gradually dropping, to the point where commercial applications start to appear in the market (Fig. 2.12). One of the bigger Spanish CVD graphene producing company ¨Graphenea¨ since 2015 until 2017 decreased the price of high-end CVD graphene samples[15].

Figure 2.12 Graphenea monolayer CVD graphene sample price since 2015 to 2017 [8]

Micromechanical exfoliation

Micromechanical exfoliation or so called “scotch tape method” is a very fast and easy graphene preparing method, where a piece of tape is used to peel off graphene flakes from a chunk of graphite. It is necessary to use only scotch tape for exfoliation from natural graphite and also SiO_2/Si wafers for visualization of graphene. After the first peeling off the graphite, on top of adhesive scotch remains multilayer graphene. By repeating the process it is possible to reach single layer graphene flakes. Afterwards, the tape is attached to the substrate by a gentle pressing of the tape, and after the glue is solved, e.g. with acetone, in order to detach the tape (Figure 2.13). Finally, on top of the substrate, the graphene nanostructures remain [Novoselov KS, 2005]. This method involves manual searching for single graphene sheets. The morphology of thin graphite films (graphene) is easily mapped by optical microscope according to the refraction principle of light (Fig. 2.14). The choice of substrate for transferring the exfoliated film is very important, because the single-layer graphene has absorption rate of 2% and for this case SiO_2/Si it is a compatible substrate, due to the interface effect in the interference maxima of reflectance, which will be permit to see graphene flakes with an optical microscope. In Figure 2.13 the optical image of exfoliated graphene on top of SiO_2 substrate is shown, with different layers of graphene [Blake P, 2007]. Exfoliated thin films consist of different films with various thickness values identified by the different color tones in the image. For exfoliated film characterization and number of layers checked with Raman technique and atomic force microscopy (AFM).

---

[15] https://www.graphene-info.com/cvd-graphene-prices-continue-drop-commercial-applications-start-enter-market

Scotch tape exfoliation was used by Andre Geim and Konstantin Novoselov from University of Manchester (UK) for isolating 1-carbon atom thick graphene sheets. This technique is easy and low cost, but in case of mass production it is not useful. The graphene flakes obtained with this method have high quality, almost no defects and could be useful for fundamental studies to characterize chemical and physical properties of graphene. It is difficult to obtain larger amounts of graphene by this method, not even taking into account lack of controllability. The complexity of this method is basically low, nevertheless the graphene flakes need to be found on the substrate surface, which is a time consuming labor.

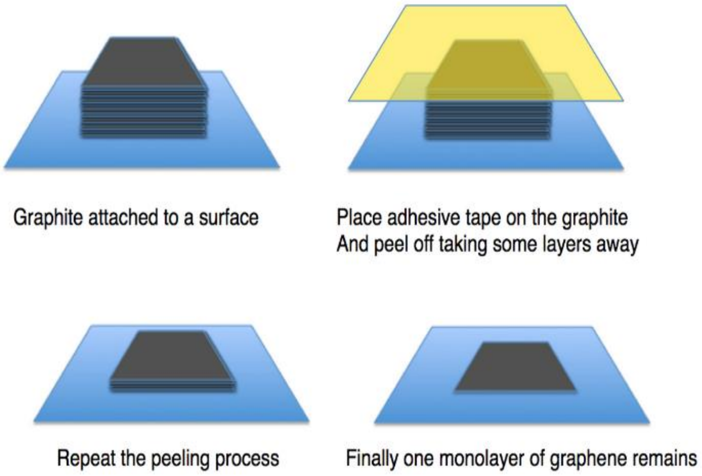

Figure 2.13 Scotch Tape Technique[16]

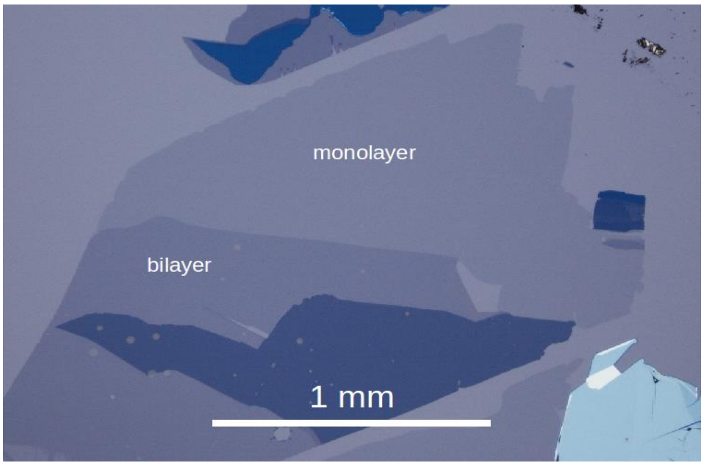

Figure 2.14 Optical image of a graphene flake, obtained from the exfoliation of graphite, with an area of $\lesssim$1 mm^2, on top of a silicon oxide wafer[17]

---

[16] https://investorintel.com/sectors/technology-metals/technology-metals-intel/understanding-graphene-part-2/

[17] courtesy of P. Blake, https://arxiv.org/pdf/1007.2849.pdf

Electrochemical exfoliation

This is another cost effective and simple approach to production of high quality graphene. Here, the synthesis route is based on electrochemical exfoliation of graphite. Graphite is used as a sacrificial electrode and the exfoliated material is being collected from the electrolyte material. In this method, strong acids, surfactants or alkaline solution (KOH dissolved in water) can be used as electrolyte (Fig. 2.15). In case of using surfactants attached to the graphite layers, they induce repulsive double electronic layers that result in a stable colloidal graphene suspension. In case of acids, graphene nanosheets were produced with large lateral size, ranging from several micrometers to tens of micrometers. Disadvantages of this technique are uneven films, slight oxidation and inhomogeneous flake [Parvez K, 2014]. However, electrochemical synthesis is considered as cheaper and greener method potentially capable of mass production of few-layer graphene (FLG).

The main advantage of this method is high output that makes it economically competitive and conjointly convenient to manipulate. This process is versatile because it is a low-cost solution-phase method. It is scalable and would be capable of depositing graphene on a wide variety of substrates, which is not possible using other processes. In addition, this method can be extended to produce graphene-based composites and films, which are key requirements for special applications, such as thin-film transistors, transparent conductive electrodes, etc. [Kumar P,2017].

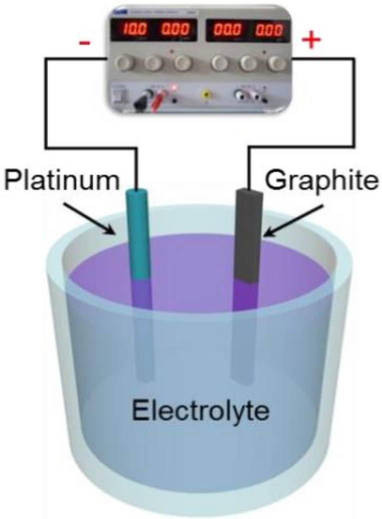

Figure 2.15 Schematic illustration of electrochemical exfoliation of graphite [Parvez K, 2014]

Epitaxial growth

The term epitaxy comes from the Greek and it can be translated as "arranging upon". Epitaxial growth is a substrate-based method, where isolated monolayer of graphene is grown on a single-crystal silicon carbide (c-SiC) by vacuum graphitization. When bulk SiC is heated to around 1500°C some of the silicon sublimates, leaving a layer of carbon on the surface [Berger C, 2004]. The obtained result is in the form of a very thin layer of graphite which under appropriate conditions produces graphene monolayers (Fig. 2.16). During expitaxial growth process, if the epitaxial layer is the same material as the substrate, this type of epitaxy is called homoepitaxy, in other case is called heteroepitaxy. Homoepitaxy is a convenient technique for producing large quantities of the same material with high purity. The graphene growth on the SiC substrate is a homoepitaxy process. Heteroepitaxy, such as metal-semiconductor and insulator-semiconductor epitaxy, has been used in microelectronics integration processes [First PN, 2010]. Furthermore, epitaxial graphene on SiC does not require transfer for the device processing and the size of the graphene sheet can be as large as the substrate, which is another benefit for device processing [Yazdi GZ, 2016]. Epitaxial graphene growth on SiC by the sublimation method is a promising technique for quality graphene growth. They possess interesting physical characteristics such as ballistic transport in nanoribbons [Baringhaus J, 2014], high frequency transistors [Lin YM, 2010; Guo Z, 2013], quantum Hall resistance standard for metrology [Tzalenchuk A, 2010], and half-eV bandgap structures [Hicks J, 2013].

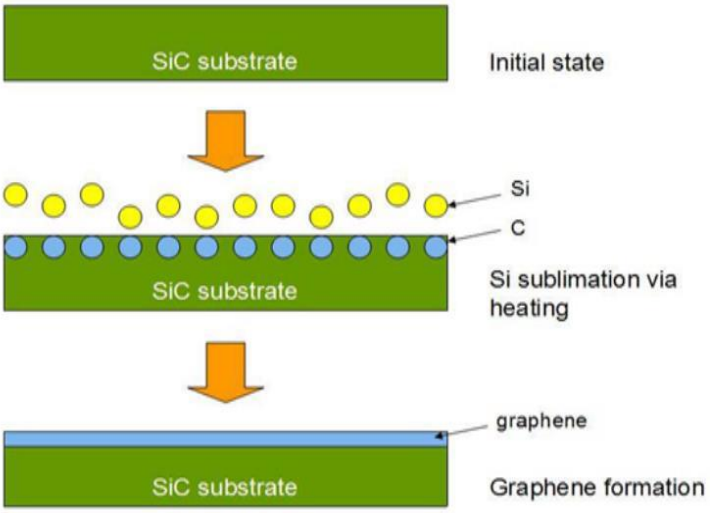

Figure 2.16 Illustration of an epitaxial growth on a SiC substrate after the sublimation of silicon, carbon remains on the surface where it would become graphene later [Hass J, 2008]

Molecular beam epitaxy (MBE) is a well-known method for development of semiconductor technology, but it has recently been used for growing graphene on SiC, Si and sapphire substrates [Al-Temimy A, 2009; Hackley J, 2009; Maeda F, 2010]. In the MBE technique, the graphene layer is formed on a metal substrate by means a carbon molecular beam produced by sublimation from a hot filament of graphite. The carbon atoms travel under conditions of ultra-high vacuum and reach the substrate forming an epitaxial layer [Vignaud D, 2013]. Epitaxy method is one of the most important technique to fabricate various 'state of the art' electronic and optical devices. Films obtained by the epitaxial technique are determined by purity, structural perfection and homogeneity. Epitaxial crystal growth resulting in epitaxial layer perfection, surface flatness and interface abruptness depend on number of factors like: the epitaxial layer growth method, the interfacial energy between substrate and epitaxial film, as well as the growth parameters – thermodynamic driving force, substrate and layer misfit, substrate misalignment, growth temperature and surface mobility.

Chemical Vapor Deposition

The most promising, inexpensive and readily accessible approach for deposition of reasonably high quality graphene is chemical vapor deposition (CVD) onto transition metal substrates. In CVD is necessary for obtaining large-area high quality graphene and for developing a process, ready to be integrated to the existent semiconductor industry. The transition metal are Ni, Pd, Ru, Ir, Cu and each of this metals found its application in different areas of science. These devices on top of the Cu have excellent characteristics such as mobility of up to 7350 $cm^2V^{-1}s^{-1}$ at low temperature and large area of growth (up to 30 square inches) [Li XS, 2009].

There are two phenomena involved in the formation of graphitic layers during CVD, diffusion and segregation of carbon impurities on the metal surface during the annealing and cooling process. At high temperature, hydrocarbons thermally decompose and, depending on carbon-metal solubility for graphene, the surface absorption/desorption or segregation of carbon can occur. For catalyst substrate, absorption/desorption of carbon atoms can occur differently, depending on carbon solubility on transition metal surface. Also in the grain boundaries, the crystallographic orientation of grain can significantly influence the absorption/desorption or segregation of carbon atoms, which can lead to diverse morphologies of graphene on different metal catalysts.

Figure 2.17 shows a schematic graphene growth model on top of a highly carbon soluble Ni (Fig. 2.17a) and on a low carbon soluble Cu catalyst (Fig. 2.17b). The growth of graphene on Ni substrates results in graphene layers with a high density of microstructural defects due to multiple nucleation and in an unpredictable amount of segregated carbon compared to the growth on Cu substrates [Kalita G, 2017].

In the case of Cu catalyst substrates, the enclosure of the 2D shell structure causes a decrease in carbon solubility and reduces the absorption of hydrocarbons on the Cu surface. [Nie S, 2011;

Bhaviripudi S, 2010; Hwang C, 2011]. In addition, there is a difference between graphene grown on a sputtered Cu film and a Cu foil. Graphene growth on top of Cu foil has some advantages, like high purity copper foil used as a substrate is available in different thicknesses and sizes, from one square centimeter pieces to one square meter sheets. On the other hand, Cu deposited on SiO_2 is more controllable in the crystallographic context and cost-effective due to the fact that usually its thickness ranges between 200 and 500 nm. In addition, the grain size for sputtered Cu films is much smaller than for Cu foil, which on a macro-scale can affect the transferred graphene films. It is possible to efficiently transfer monolayer graphene film on top of sputtered Cu and it is easily implemented in mass production [Bae S, 2010; Reina A,2008].

The advantage of CVD method is the production of large graphene domains and easily transferring process due to the etching transition metal by acid solutions. Nowadays there has been huge number of research conducted on the growth mechanism of graphene in a CVD process. Disadvantages of using CVD to create material coatings are that the gaseous by-products of the process are usually very toxic, but they are removed from reaction chamber by gas flow to be disposed of properly. The precursor gases used must be highly volatile in order to react with the substrate, but not so volatile that it is difficult to deliver them to the reaction chamber[18].

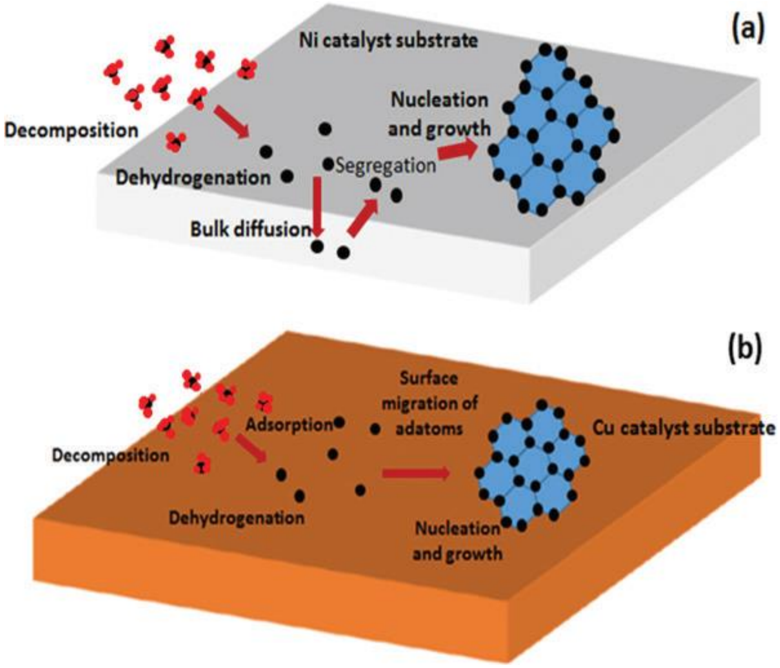

Figure 2.17 (a) Graphene growth process on highly carbon soluble metal substrate (e. g., Ni). Decomposition, dehydrogenation, bulk diffusion, and segregation process determined the graphene nucleation and growth; (b) graphene growth process on a low carbon soluble metal substrate (e.g., Cu). Decomposition, dehydrogenation, and surface adsorption/desorption process determined the graphene nucleation and growth [Kalita G, 2017]

---

[18] https://www.graphenea.com/pages/graphene-uses-applications

Plasma Enhanced Chemical Vapor Deposition (PECVD)

As it can be seen from above, the CVD process requires a high temperature, and that limits their application for coating on temperature sensitive materials. In the case of PECVD, energy required for reaction comes from plasma, rather than from temperature. PECVD allows reducing the temperature of process because plasma facilitates the gas-phase ionization and decomposition giving place to reactive radicals, which react to form a thin solid film on the substrate (Fig. 2.18) [Carey P, 1989]. This process is widely applied in surface engineering. Graphene layers with customized properties can be deposited quickly by PECVD and their cost is lower than using other technologies.

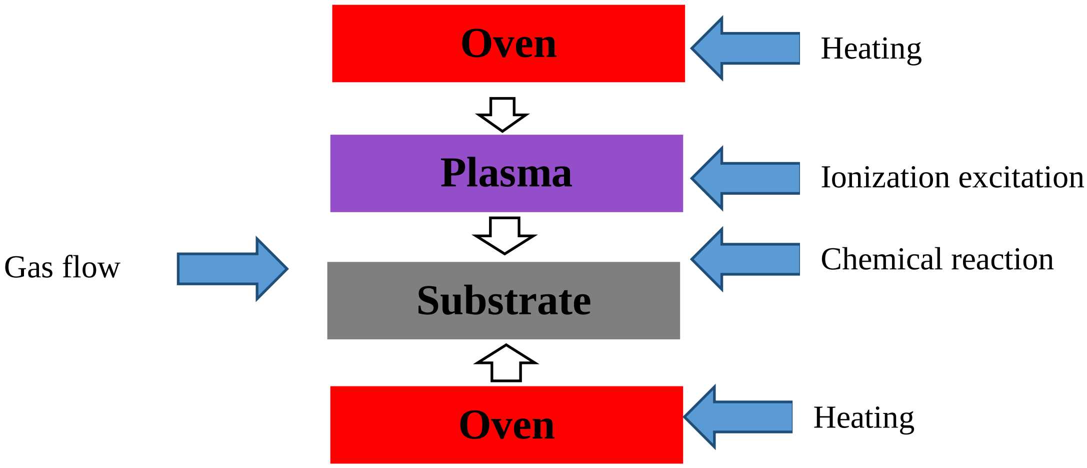

Figure 2.18 Schematic illustration of plasma enhanced chemical vapor deposition method

In a laboratory PECVD process, the energy is transferred to the free electrons (with densities in the range 1010 to 1013 m^{-3}) after ionization in a low-temperature plasma. The electron energy becomes larger than of ions or neutral particles (they are at room temperature) and there is no thermodynamic equilibrium. Electrons can collide with neutrals (with densities in the range 1020 to 1023 m^{-3}) to produce diverse possible reactions: mainly excitation, decomposition and ionization. The mixture of free electrons, ions and neutrals form a plasma, in which reactive radicals appear at lower temperatures if compared to thermal CVD processes. PECVD process requires control of many variables, such as power, total pressure, reactant partial pressure, gas flow rate, sample temperature, pumping speed.

Plasma enhanced chemical vapor deposition is the main method used and investigated in this thesis to grow multilayer graphene nanowalls. This technology will be discussed in detail in chapter 3.

2.2 Graphene nanowalls

Graphene nanowalls (CNWs) are two-dimensional carbon nanostructures consisting of walls that are constructed of aligned graphene layers on different substrates. Vertical graphene (VG) is intrinsically graphene with unique structural features, being arranged perpendicularly to the substrate surface (Fig.2.19). Individual VG nanostructure usually has lateral and vertical dimensions of 0.1 to tens of micrometers and a thickness of only few nanometers [Kondo S, 2008; Ni ZH, 2007]. As compared with the horizontally oriented graphene this type of graphene nanostructures attract attention due to its high surface-area-to-volume ratio. The most important features of MLGNWs are high aspect ratio, large surface area and sharp edges [Ni ZH, 2007].

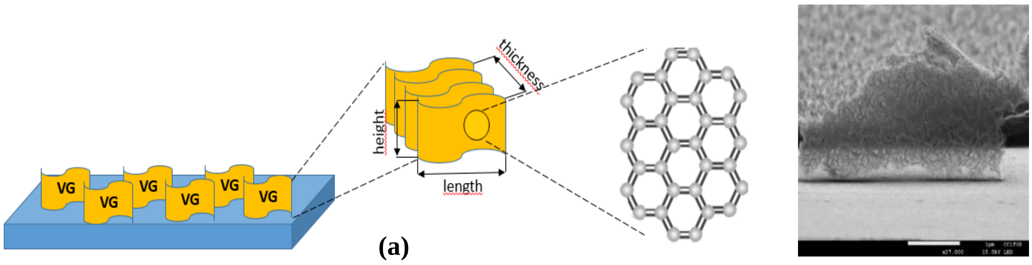

(a)

(b)

Figure 2.19 (a) Schematic image of MLGNWs on top of substrate; (b) SEM image of MLGNWs on top of Si substrate [Musheghyan-Avetisyan A, 2017]

MLGNWs were first discovered in 2001 by Prof. Yihong Wu. The vertical structure was found during the growth of carbon nanotubes in a microwave PECVD process. MLGNWs first deposit was carried out over NiFe (40 nm) coated sapphire substrate, under CH_4 and H_2 gas flow in the 650°C-700°C temperature range. Since then, a number of reports has been published using a variety of growth parameters for MLGNWs synthesis. For vertically oriented graphene growth, the plasma state has an essential role, as compared with planar graphene, which can be synthesized by mechanical and chemical exfoliation, thermal decomposition of carbon-terminated silicon carbide, epitaxial growth and chemical vapor deposition (CVD) [Wu YH, 2002]. Many researchers have used different types of plasma enhanced chemical vapor deposition methods (PECVD), such as DC, RF and microwave plasma discharges in a variety of configurations (Fig. 2.20). PECVD technique has high probability to be a promising technique for new generation technologies, due to its feasibility and potentiality for large-area production with reasonable growth rates at relatively low temperatures. This method as compared with CVD has advantages such as low operating temperature, full step coverage and generally, high growth rate, high plasma density and reactive radical density. It also offers a better control of nanostructure ordering/patterning, due to the presence of energetic electrons, excited molecules and atoms, free radicals, photons and other active species in the plasma region, where occurs MLGNWs deposition [Droes SR, 1997]. Plasma enhanced chemical vapor deposition is the main method used and investigated in this thesis and it will be deeply discussed in chapter 3.

The precursor gases used in these PECVD processes may vary. Many researcher groups used CH_4, C_2H_2, C_2H_4, C_2F_6 and CO_2 as precursor gas [Kondo S, 2009; Chatei H, 2006; Vizireanu S, 2009]. Moreover, etchant and diluent gases, such as H_2, O_2, N_2, NH_3, H_2O, as well as, noble gases He, Ne, Ar and Kr were used [Vizireanu S, 2009; Teii K, 2009; Zhu W, 1990]. For the MLGNWs growth, a broad number of substrates such as conductor, semiconductor, and insulator, was used [Wu YH, 2004; Malesevic A, 2008].

Vertical graphene was discovered in 2001, but there is still no specific description of the growth mechanism. Numerous researchers have proposed growth mechanisms for MLGNWs based on experiments performed in the early stages of deposition [Hiramatsu M, 2006; Kondo S, 2009; Teii K, 2009; Malesevic A, 2008; French BL, 2006]. In this thesis, the new proposed growth mechanisms will be presented.

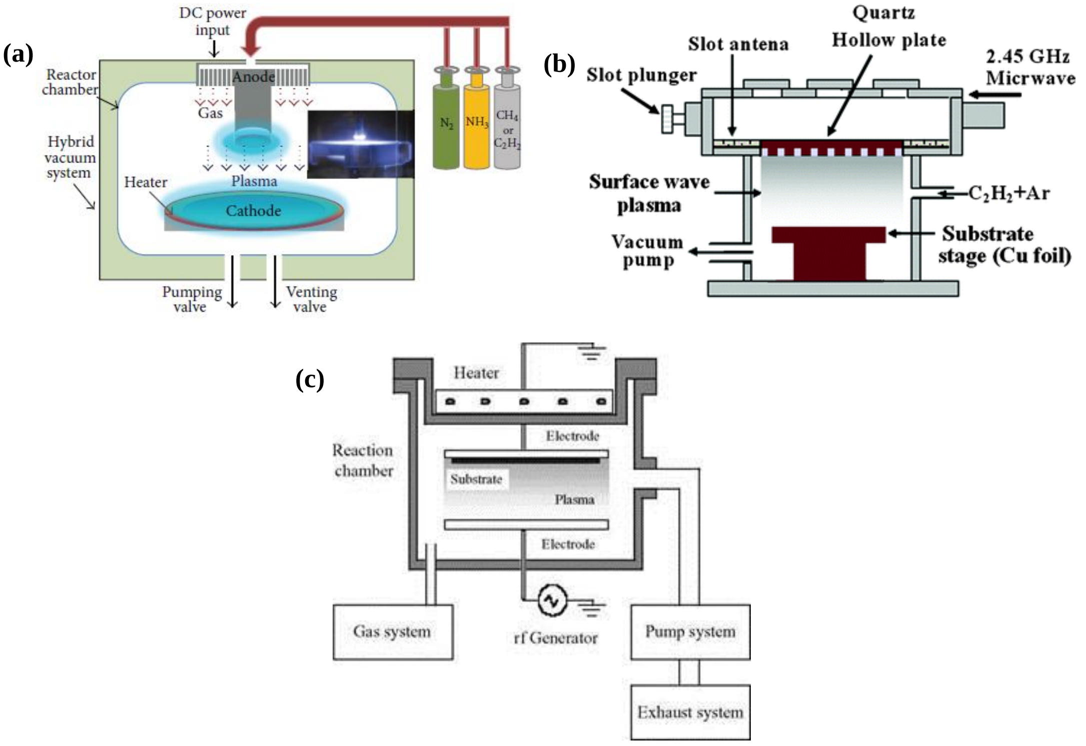

Figure 2.20 Schematic diagrams of various PECVD systems for MLGNWs growth: (a) DC [Jung HK, 2014]; (b) microwave (MW) [Kalita G, 2012] and (c) radio frequency (RF)[19]

---

[19] energyprofessionalsymposium.com/?p=17719

Vertically oriented graphene nanowalls possess a number of unique mechanical, chemical, electronic, electrochemical and optoelectronic properties that could benefit their potential use in a wide range of applications. Many applications have already been described in literature, such as field electron emitters, catalyst supports/templates, and hydrophobic coating (due to the H or F terminations) [Hiramatsu M, 2010] (Fig. 2.21). MLGNWs due to the very low reflectance, high specific absorbance in thin transparent films has possibility of using as dark coating for a bolometer absorber [Krivchenko V, 2013]. The ability to tailor the band gap of CNWs opens new doors to their usage for the design and evolution in modern nano-electronic devices. On the other hand, the carrier concentration and mobility; the band gap inside the individual monolithic graphene nanowall sheets are also of great interest for realizing nanographene devices [Hiramatsu M, 2010]. This unique three-dimensional graphene structure possesses high hydrophobicity and outstanding electron conductivity. The in-situ one step growth method indicates the great potential of using VG in supercapacitors. Also MLGNWs can be used in flexible photovoltaic devices, field-effect transistors (FETs), sensors, charge trapping memory (CNT) [Liu XSJ, 2014]. In addition, MLGNWs is an elegible candidate for using in biocompatible scaffolds for osteoblast culture and tissue engineering [Ion R, 2016]. Electrophoretic deposition can be used to fabricate composite MLGNWs/graphite electrodes for electrochemical detection of DNA sequences with estimated zeptomolar LODs [Akhavan O, 2012]. For each application, high-quality MLGNWs should be grown on suitable substrate. For example, MLGNWs grown on Cu foil becomes an excellent electrode for supercapacitors, meanwhile, MLGNWs on dielectric (SiO_2) substrate could be used to fabricate gas or bio-sensors, also MLGNWs on semiconductor substrates could be used rather for potential application of solar cells [Li M, 2016].

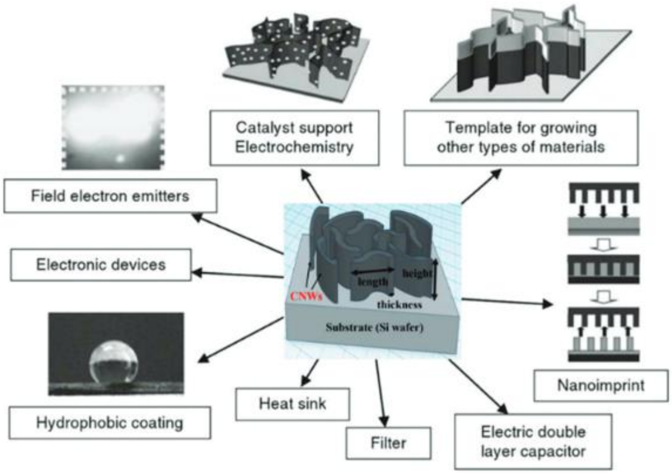

Figure 2.21 Schematic representations of the potential applications of MLGNWs [Hiramatsu M, 2010]

The controllable synthesis of vertical graphene nanosheets growing by PECVD method with different morphologies and structures benefits the improvement in device performance. In the future, systematic studies are required toward better controllability. Research to exploit the potential of graphene nanowalls and to develop next-generation electron devices by using vertical graphene has just begun.

Part II

Experimental Description

Chapter 3

MLGNWs characterization techniques

3.1 Electron microscopy

3.1.1 Scanning electron microscope (SEM)

The scanning electron microscope (SEM) is one of the principal and more common microscopic techniques for the observation of the specimen surface. This instrument differs from all other conventional microscopes, using light or electrons, in forming its image progressively (scanning) and not all at once. The electron source used in the SEM can be a tungsten filament, Lanthanum hexaboride (LaB_6) and Field-emission electron gun (FEG). LaB_6 has advantages over tungsten guns such as larger maximum beam current and longer lifetime.

The principle of SEM is following: when the specimen is irradiated with a fine electron beam, the primary electrons accelerate and strike the sample, producing secondary electrons and these secondary electrons are collected by a positively charged electron detector and that in its turn gives a 3 dimensional image of the sample. As compared with optical microscopes, the basic principle of SEM is based on electron beams to form an image instead of light, SEM can magnify a specimen from about 10 – 300,000 times. The SEM has a high field depth more than 300 times as compared to light microscopes.

SEM microscope consists of the following parts (Fig. 3.1):

- The microscope (electron) column,
- Scanning system,
- Detector (s),
- Display,
- Specimen chamber,
- Vacuum system,
- Electronic controls.

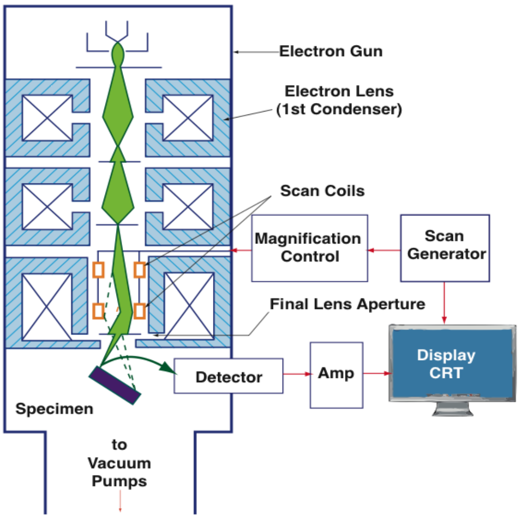

Figure 3.1 Structure of the scanning electron microscope[20]

---

[20] https://cfamm.ucr.edu/documents/sem-intro.pdf

Microscope column consists of the Electron gun, it produces an electron beam, it works normally at voltages from 5 to 30 kV;a seriess of condenser and objective lenses, which act to control the diameter of the beam and focus it on the specimen; scan coils are responsible for rastering that focus beam across the specimen surface.

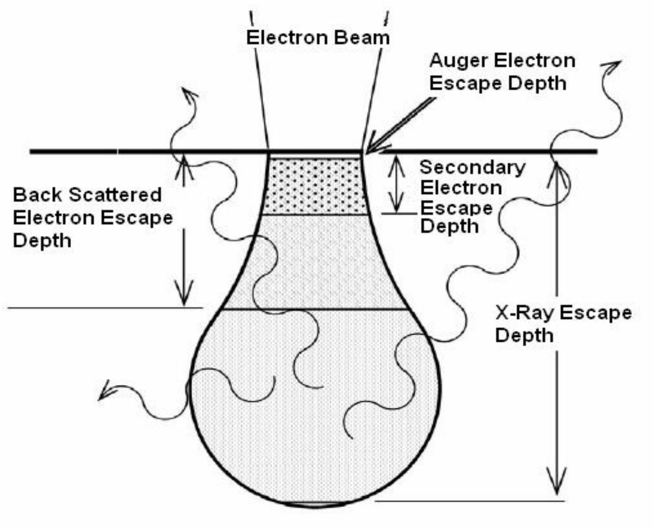

Figure 3.2 Scheme of electron-beam interaction [Hafner B, 2007]

The resolution of SEM images depends on the size and characteristics of the interaction volume. Interaction volume is the region where the incident electrons interact with the sample. As a result of electron-matter interaction, some signals are generated: backscattered electrons, secondary electrons, X-Rays, Auger electrons, cathadoluminescence [Hafner B, 2007]. The SEM utilizes these signals to form images. Penetration of the accelerated beam electrons inside specimen is about 1 μm. Each wave has different escape depth, for example, secondary and backscattered due to the different energy, have different escape depth, of the Secondary electrons is 5-50nm approximately, of the backscattered electrons is a hundred times greater, of the X-rays is even greater (Figure 3.2). The interaction volume plays an important role in the operation of the SEM analysis and determines the nature of SEM imaging. The shape and dimension of the interaction volume depend on the following parameters: accelerating voltage, atomic number and tilt. Interaction volume increases when acceleration voltage increases and decreases with increasing atomic number[21]. Sometimes during SEM analysis, we have damaged some areas of the sample with an electron beam. Loss of the electron beam energy in a specimen and occurs mostly in the form of heat generated at the irradiated point. In case of the thin films hot conductivity can be decreased. With the purpose of avoiding these damages we have decreased the electron beam intensity and exposure time, we also imaged large scanning area with low magnifications. Scanning Electron Microscope is not only for observation of morphology, it is a useful microscope for performing elemental analysis and state analysis.

---

[21] https://www.jeol.co.jp/en/applications/pdf/sm/sem_atoz_all.pdf

In this thesis, SEM was used to characterize the prepared substrate surfaces (graphene nanowalls, carbon nanotubes, MLGNWs/CNTs hybrid structure). With this microscope, it is possible to check the height, thickness and density of MLGNWs and related structures, also the growth parameters influence on the MLGNWs morphology. Field Emission Hitachi S2300 (S4100) was preferentially used for nanometric resolution images by using usual operation voltages 15 and 20 kV. In a Field Emission SEM (FESEM), the electron source consists of an extremely fine tungsten point from which electrons are drawn by a strong electric field. The SEM microscope, which was used during this thesis is located in the CCiTUB (Barcelona).

3.1.2 Transmission electron microscope (TEM)

Transmission electron microscope (TEM) is an analytic tool permitting visualization and analysation of specimens range of microspace to nanospace. High-resolution transmission electron microscopy (HRTEM) is an imaging mode of the transmission electron microscope (TEM) that allows for direct imaging of the atomic structure of the specimen. TEMs were developed because of the limited image resolution in light microscopes which is imposed by the wavelength of visible light. However, after using TEM in large areas of the science, many other reasons were discovered for using electrons most of which are utilized to some extent in a modern TEM. Nowadays, TEMs can reach an atomic resolution using voltages of 200 kV and higher. The wavelength of electrons is a 100,000 times shorter than that of visible light. The image resolution with an electron microscope is much better than with optical, it was determined at the atomic level. At a maximum potential magnification of 1 nanometer, TEMs are the most powerful microscopes. The inner morphology of the nanowalls structures discussed in this thesis and their structural morphology were imaged by such a high-resolution TEM. An image is formed from the interaction of the electrons transmitted through the specimen has dark and light parts. The light parts represent the places where a greater number of electrons were able to pass through the sample and the dark parts reflect dense areas of the object. With these differences it is possible to characterize the sample (texture, shape, structure, size) [Williams D, 2009].

With number of advantages TEM has some disadvantages like high cost, the samples have some limitations (they must be electronically transparent, be able to tolerate the vacuum chamber and be small enough to fit in the chamber). Electron microscopes are sensitive to vibration and electromagnetic fields and must be housed in an area that isolates them from possible exposure[22].

---

[22] http://www.ammrf.org.au/myscope/pdfs/tem.pdf

The components of TEM analytic tools are (Fig. 3.3):

Electron gun: The electrons are generated and accelerated to the required high energy.

Condenser system: The first lens is a condenser that focuses the beam of electrons on the section.

Objective lenses: Most electrons reach the objective lens which forms the first intermediate image, which is then projected through other magnifying lenses.

Diffraction/intermediate lens: This type of lenses make a role of switches between imaging and diffraction mode.

Projective lenses: Because the human eye is not sensitive to electrons, the image is finally projected on a fluorescent screen or is registered by photographic plates or a CCD camera.

Vacuum system: TEM system requires high vacuum, without gas particles, due to the strong interaction of the electron with the matter.

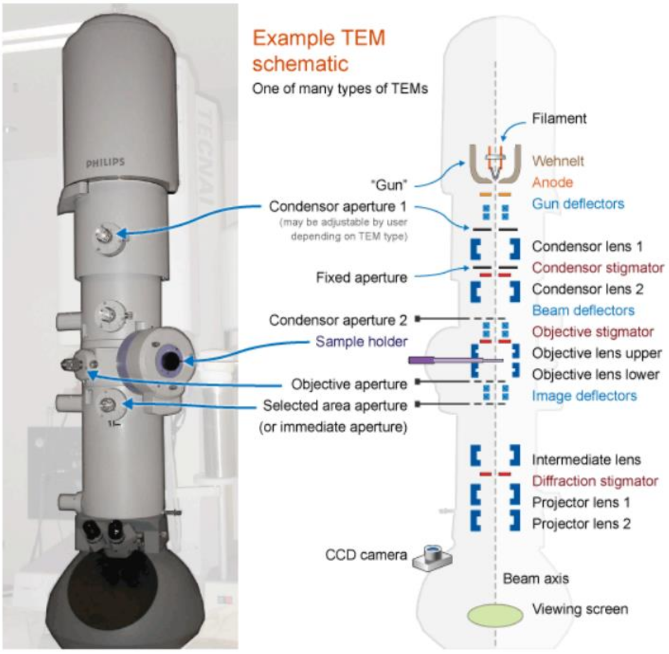

Figure 3.3 Basic components of a TEM system[23]

The working principle of TEM microscope is as follows: electrons, which are produced by the electron gun, pass through the electromagnetic lenses in evacuated column and arrive to the specimen. When the electrons encounter the specimen, one of the three things may happen. They may pass through it unimpeded. They may be scattered without loss of energy (elastic scattering). Or they may be inelastically scattered; this involves an exchange of energy between the electron beam and the specimen, and may cause emission from the specimen of secondary electrons or X-rays. After one of these three electron specimen interaction the transmitted electrons form an image on the CCD camera or phosphorescent screen. Image contrast in the TEM depends on preventing the inelastically scattered electrons from contributing to the image. When an electron

---

[23] http://www.ammrf.org.au/myscope/pdfs/tem.pdf

beam encounters a crystalline structure a diffraction will occur. Conditions for diffractions are given by Bragg by the following equation:

$$n\lambda = 2dsin\theta \qquad (3.1)$$

where λ is the electron wavelength, d is the spacing of the diffracting planes, and θ is the angle between the planes and electron beam [Williams DB, 1996].

Selected area electron diffraction (SAED)

TEM is very useful technique for investigation of the morphology, structure, and local chemistry of materials. It also enables the investigation of crystal structures (Selected area electron diffraction (SAED)), orientations and chemical compositions of phases, precipitates and contaminants through a diffraction pattern, characteristic X-ray, and electron energy loss analysis. SEAD is a crystallographic experimental technique, which is installed inside TEM. They used a diffraction pattern for phase identification, determination of crystal orientation and structural analysis. The image of SAED is a series of spots and each spot corresponds to a satisfied diffraction condition of the sample crystal structure. ED spotting patterns are collected sequentially with an ultra-fast optical CCD camera while an area on the sample is simultaneously being scanned by the TEM focused electron beam, which is at the same time being processed around the direction of incidence at each point. Depending on the orientation of the sample (tilt angle) different diffraction conditions can be activated, no matter whether or not the crystal remains under illumination, the spot can appear and disappear respectively. The technique is called selected area diffraction, because the user can select the area for obtaining the diffraction pattern. This technique is not only capable to identify the crystal structure but also to examine crystal defects. SAED as compared with the similar X-ray diffraction system, has several

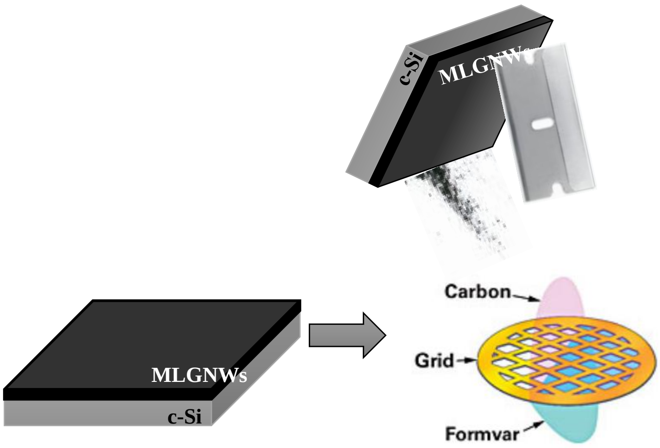

Figure 3.4 Illustration of the MLGNWs transfer on C/Cu grid

hundred nm area, whereas X-ray diffraction typically samples areas of several centimetres in size [Williams DB, 1996].

For this thesis a High-resolution transmission electron microscope (HRTEM) mode and SAED was used. MLGNWs which were grown by the inductively plasma enhanced chemical vapor deposition (ICP-CVD) technique was scratched from the silicon wafer on the Cu/C grid, such as shown in Fig. 3.4. HRTEM JEOL 2100 microscope, which I used during my thesis located in the CCiTUB (Barcelona).

3.2 Techniques of analysis

3.2.1 Fourier transform infrared spectroscopy

Fourier-transform infrared spectroscopy (FTIR) is a technique used to obtain an infrared spectrum of absorption or emission of a solid, liquid or gas. In infrared spectroscopy, IR radiation passes through a sample. Some of the infrared radiation is absorbed by the sample and some of it is reflected (opaque samples) and is transmitted in no opaque samples. The goal of any absorption spectroscopy is to measure sample absorption of IR radiation at each wavelength. In FTIR spectroscopy, a detector measures the intensity of IR radiation at each frequency that passes through a sample and the results represented on a spectrum, which is a plot of intensity vs. wavenumber (Fig. 3.5). The resulting spectrum represents the molecular absorption and transmission, thus creating a molecular fingerprint of the sample.

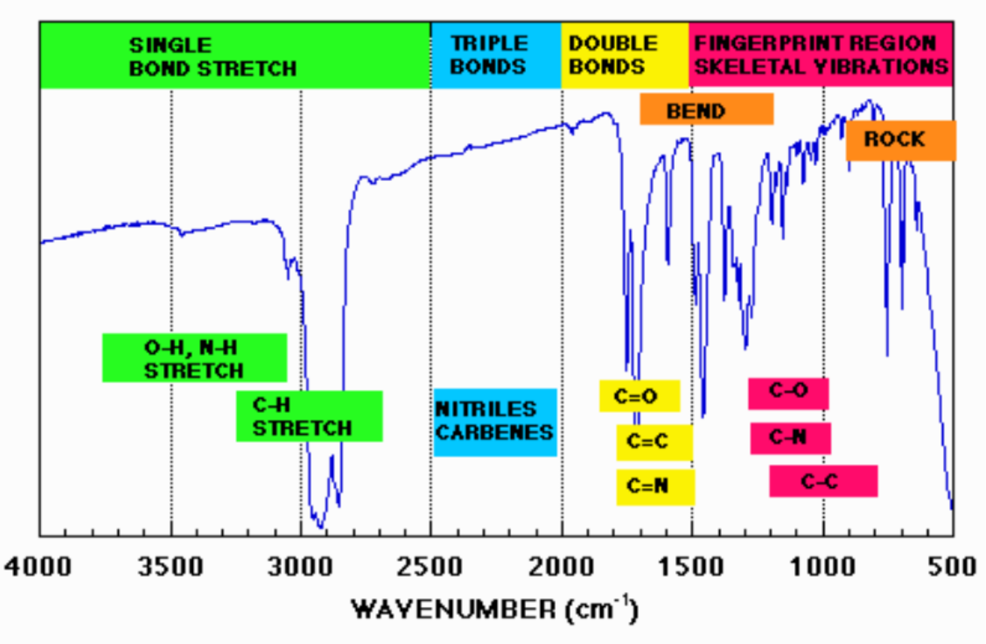

Figure 3.5 FTIR spectrum[24]

---

[24] http://photometrics.net/PhotoMetrics/fourier-transform-infrared-ftir-spectroscopy/

The working principle of FTIR spectroscopy based on molecular bond vibrations at various frequencies depends on the elements and the type of bonds. For any given bond, it can vibrate at several specific frequencies. According to quantum mechanics, these frequencies correspond to the ground state (lowest frequency) and several excited states (higher frequencies). For increasing the frequency of a molecular vibration, it is necessary to excite the bond by absorbing light energy. For any given transition between two states, the light energy (determined by the wavelength) must be exactly equal to the difference in the energy between the ground state and the first excited state [Griffiths PR, 2007]. Fig. 3.6 shows the schematic image of FTIR spectroscopy.

Radiation from the source strikes the beam splitter and separates into two beams. The fixed and moving mirrors reflect each of the beam back to the beam splitter, where the two beams recombine into one and fall on the detector. The two beams combine constructively or destructively, varying as the optical path difference, when the moving mirror is moved. If the radiation beams are in phase, the beams will constructively interfere and the resulting amplitude will be twice as high. If the radiation beams are out of phase, the beams will destructively interfere and cancel each other. When the combined beam is transmitted through the sample, it is detected as an interferogram, which contains all infrared information on the sample. Then, the infrared spectrum can be obtained from the interferogram by the mathematical process of Fourier transformation [Brault JW, 1996].

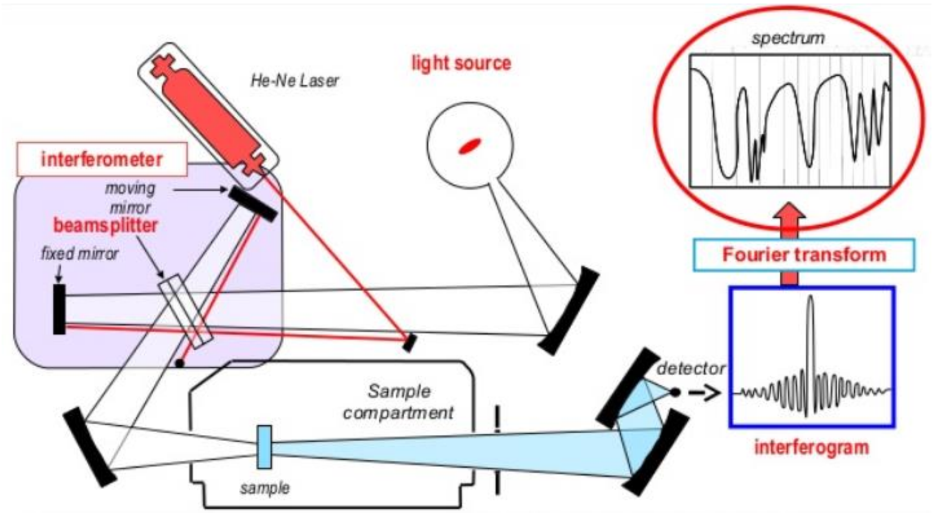

Figure 3.6 Schematic image of FTIR spectroscopy[25]

FTIR spectroscopy is able to identify unknown materials, determine the quality or consistency of a sample and determine the amount of components in a mixture. Fourier transform infrared spectroscopy is preferred over dispersive or filter methods of infrared spectral analysis, due to the high sensitivity, high velocity, mechanical simplicity with only one moving part, also it has a

---

[25] https://www.slideshare.net/muttaqinpapasafira/principles-of-ftir

greater optical throughput and does not require calibration by the user, due to the HeNe laser as an internal wavelength calibration standard.

For this thesis, the composition of MLGNWs was measured by a Thermo SCIENTIFIC NICOLET iZ10 Fourier transform infrared (FTIR) spectrometer with a spectral resolution of 4 cm^{-1}.

3.2.2 Raman spectroscopy

Raman spectroscopy was discovered in 1928 by Prof. Chandrasekhar Venkata Raman, and he won the Nobel Prize for his work. Raman spectroscopy is a spectroscopic technique based on inelastic scattering of monochromatic light, usually from a laser source. They are widely used to provide information on chemical structures and physical forms, to identify substances from the characteristic spectral patterns (‘fingerprinting’), and to determine quantitatively or semi-quantitatively the amount of a substance in a sample [Smith E, 2005]. Raman spectroscopy instruments of nowadays are small, portable and simple for using regularly by people who are neither specialists in spectroscopy nor analysts.

The principle of the Raman spectroscopy is based on the interaction of a monochromatic radiation with a sample in which it can be scattered (less than 10^{-5} of the intensity of the exciting source), reflected and absorbed. Information about the molecular structure of the substrate can be determined from the scattering of the radiation and Raman technique is mainly based on the scattering. The irradiation occurred from the coherent source (in our research, we used laser of 514.5 nm). Most part of the radiation (99% of the dispersed radiation) is elastically scattered, it means that the scattering process occurred without a change of frequency and this scattering mode is called Rayleigh scatter. The process, when a change in the frequency (wavelength) of the light is called not elastic scattering or Raman scattering. Raman scattering can occur with a change in vibrational, rotational or electronic energy of a molecule. Numerically, the Raman shift in wave numbers (cm^{-1}), can be calculated with the following equation:

$$\bar{\upsilon} = \frac{1}{\lambda_{incident}} - \frac{1}{\lambda_{scattered}} \qquad (3.2)$$

where λ_i and λ_s are the wavelengths (in cm) of the incident and Raman scattered photons, respectively [Smith E,2005]. The energy difference between the incident and scattered photons are described in the Fig. 3.7 by the arrows of different lengths, which can easily explain the Raman scattering process: a photon of energy hυ_0 colliding with a molecule can either be scattered elastically (Rayleigh) or inelastically (Raman). In the latter case, the collision with photons induces the molecule to undergo a transition between two vibrational energy levels of the molecule, and the resulting scattered radiation has a different frequency than that of the incident photon. If during the collision, the molecule gains some energy $h\upsilon_{vib}$, the photon will be scattered at the frequency $h\upsilon_0$-$h\upsilon_{vib}$, which is referred to as Stokes Raman scattering. Conversely, if the molecule loses some energy by relaxing from an excited vibrational level to the ground state, then the scattered energy will be at $h\upsilon_0$+$h\upsilon_{vib}$, i.e. anti-Stokes Raman scattering. Raman spectra are usually represented in wavenumbers shift (υ_{vib},), relative to the excitation line. The advantage of using such a shifted scale is that it allows working with a spectrum that gives directly the frequency of the molecular vibrations [Dahlberg T, 2016].

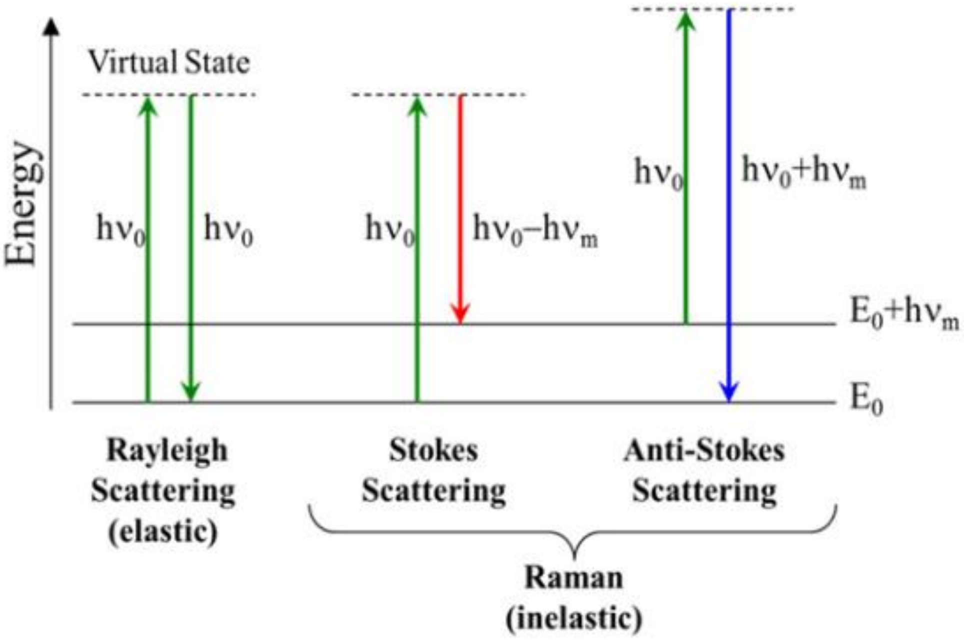

Figure 3.7 Illustration of Rayleigh and Raman scattering processes for photons [26]

The Raman spectroscopy consists of a laser, a Rayleigh filter, a few lenses, a spectrograph (with a triple monochromator and band filters) and a detector (CCD or photomultiplier). Raman spectroscopy offers the possibility to select the optimal laser excitation wavelength for the best Raman information. Raman technique permits to use several laser lines from UV (down to 200 nm) up to infrared (1.064μm Nd:YAG laser line), from μW up to several W [Jawhari T, 2012]. For Raman analyses, three different wavelengths of laser are commonly used for sample excitation (Table 3.1). The Raman shift is directly on the vibrational structure of the sample (Figure 3.7) and it is independent of the excitation wavelength. However, choosing a more appropriate excitation laser wavelength can optimize experimental efficiency.

---

[26] http://bwtek.com/raman-theory-of-raman-scattering/

Table 3.1 Comparative between the most common three laser wavelengths used in Raman spectroscopy

	532 (nm)	**785 (nm)**	**1064 (nm)**
Excitation efficiency	high	medium	low
Fluorescence	high	medium	low
Heat absorption	low	medium	high

Raman scattering efficiency is proportional to λ^{-4}, where λ is the wavelength of the laser light. As an example, the scattering efficiency for a sample excited by a 532 nm laser beam will be ~5 times more efficient than exciting by a 785 nm laser, and 16 times more efficient as compared with 1064 nm laser. In order to achieve the same signal for the same sample excited by two different lasers (1064 nm and 532 nm) it is necessary to acquire a scan 16 times longer when using a 1064 nm laser as compared to a 532 nm laser. Thus, from the point of view of excitation efficiency, shorter wavelength lasers are better. The *fluorescence* is another phenomenon to take into account for choosing the wavelength of laser excitation. In contrast to Raman scattering, in fluorescence, the photon is completely absorbed and causing the molecule to jump to a higher electronic state. Fluorescence occurs due to real electronic transitions, there is no excited state in Raman scattering, therefore the process is almost instantaneous, whereas fluorescence has a characteristic lifetime of nanoseconds.

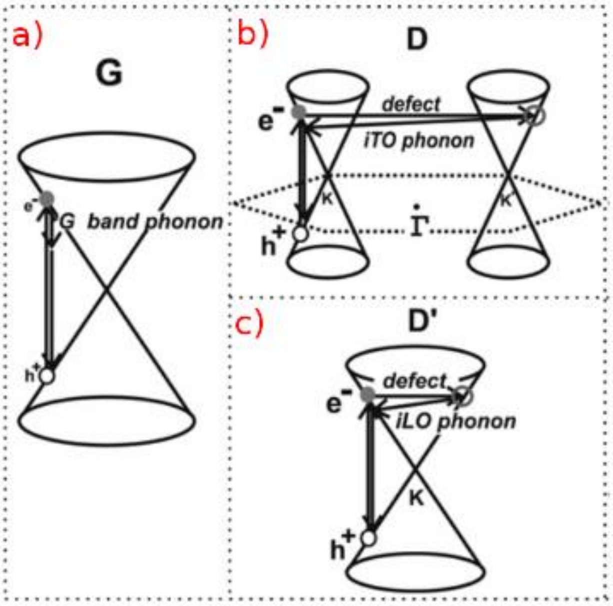

Figure 3.8 Illustration of Raman processes of different bands where the cones show the shape of the electron dispersion relationship close to the Dirac points of graphene a) G band; b) D band; c) D´ band [Jorio A, 2011]

Raman spectroscopy is an important tool for carbon materials identification and characterization. It is particularly well suited to molecular morphology characterization of carbon materials. Raman spectroscopy has become a key technique for classification of the carbon allotropes ranging from highly oriented pyrolytic graphite (HOPG), graphene, carbon nanotubes, pyro-carbons or carbon black. Every band in the Raman spectrum directly corresponds to a specific vibrational frequency of a bond within the molecule. The vibrational frequency and hence the position of the Raman band is very sensitive to the orientation of the bands and weight of the atoms at either end of the bond. In the carbon system, the spectra appear deceivingly simple: just a couple of very intense bands in the 1000–2000 cm^{-1} region and few other second-order modulations. However, the shape, intensity and positions allow distinguishing a hard amorphous carbon, from a crystalline, giving as much information as that obtained by a combination of other lengthy and destructive approaches [Ferrari AC, 2004a]. The peculiar dispersion of the π electrons in graphene is the fundamental reason why Raman spectroscopy in carbons is always resonant and, thus, a powerful and efficient probe of their electronic properties, not only of their vibrations. Vibration modes in the graphene material are described through their respective location in the electron band structure, as can be seen in Fig. 3.8, where “L” and “T” stand for lateral or transverse vibrations and “i-”or “o” stand for in a plane or out of the plane, and “O” stand for optical (three branches) phonon branches [Merlen A, 2017].

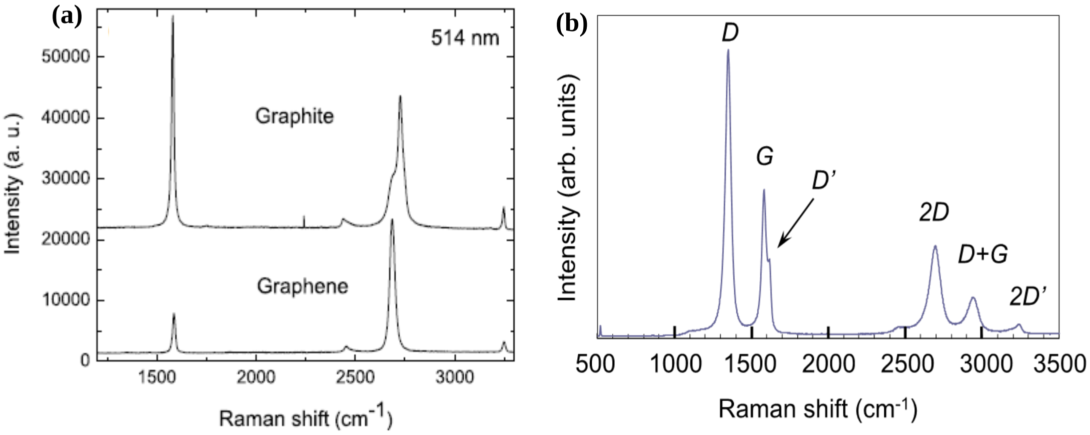

Figure 3.9 (a) Raman spectra of bulk graphite and graphene at 514 nm excitation [Ferrari AC, 2006]; (b) Typical Raman spectrum of MLGNWs measured using the 514.5 nm line of an Ar laser [Hiramatsu M,2012]

In graphene, the Stokes phonon energy shift caused by laser excitation creates two main peaks in the Raman spectrum: *G* (1580 cm^{-1}), a primary in-plane vibrational mode (tangential elongation), and *2D* (2690 cm^{-1}), a second-order overtone of a different in-plane vibration, *D* (1350 cm^{-1}) [Saito, R, 2011]. The main features in the Raman spectra of carbons are these two peaks. *2D* and *D* peak position are depending on the laser excitation energy.

Single, double, and multi-layer graphene have also been differentiated by their Raman fingerprints. Raman spectrum can give information about the disorder, edge and grain boundaries, thickness, doping, strain and thermal conductivity of graphene. Fig.3.9 (a) shows the typical

Raman spectra of graphene and bulk graphite. Raman spectra of graphite as well as graphene exhibit a relatively simple structure, they consist of three main bands *G* band at 1580 cm^{-1}, *D* band at 1350cm^{-1}, which is known as the disorder band and make Raman spectroscopy one of the most sensitive technique to characterize disorder in sp^2 carbon materials. *G* band indicated the formation of graphitized structure and give information about the number of graphene layers. In case of graphene nanowalls *G* peak is accompanied by a shoulder peak at 1620 cm^{-1}, which is associated with finite-size graphite crystals and graphene edges (Fig.3.9b) [Kurita S, 2005; Ferrari AC, 2006]. 2D band for graphene appear at 2700 cm^{-1} and this is one of the main peaks for the determination of graphene layers. However, the determination method from 2D peak is more complex than the G band position method, because by 2D band the determination of the number of the layers depends not only on band position but also on band shape (Fig. 3.10) [Lancelot E, 2013]. The differences in this band between single, bilayer graphene and graphite can be seen in Figure 3.10. For single layer graphene the 2D band is observed to be a single symmetric peak with a full width at half maximum (FWHM) of ~30 cm^{-1}. With an increase in the number of graphene layers, the 2D band split into several overlapping modes. The band splitting of the 2D band going from single layer graphene to multilayer graphene arises from the symmetry lowering that takes place when increasing the layers of graphene in the sample. While a graphene monolayer can be fitted by a single Lorentzian peak, a bi-layer requires four Lorentzians, which are related to the four possible double resonance scattering processes when only one is possible for the monolayer. When the number of layers increases, the number of double resonance processes also increases and the spectral shape converges to that of graphite, where only two peaks are observed. The 2D band is resonant and it exhibits strong dispersive behaviour so the position and shape of the band can be significantly different with different excitation laser frequencies, and it is important to use the same excitation laser frequency for all measurements when doing characterization with the 2D band. Moreover, single layer graphene can also be identified by analysing the peak intensity ratio of the 2D and G bands. The ratio I_{2D}/I_G of these bands for high quality (defect free) single layer graphene will be seen to be equal to 2 [Dresselhau MS, 2010].

Finally, in perfect graphene structure (single layer with no defects), D band is absent, but in MLGNWs the peak intensity of D band is twice as high as that of G band, which is associated with the disorder induced by the plasma process.

Raman Spectroscopy is a great tool not only for determining the number of the layers of graphene but also for determining the doping concentration, the crystallographic orientation, the surface functionalization and other physical properties in graphene. The variation of the intensity or the position of the peaks in the spectrum, together with the appearance of new peaks, indicate modification of the mentioned physical properties [Das A, 2008].

The Raman results of this thesis were mainly characterized by a Jobin Yvon LabRam HR 800, with a 532 nm laser under micro-Raman conditions (100X objective). Generally, the used incident power was 3.3 mW at most, and the size of the spot is 2 µm; the diffraction grating used was 600-1800 lines/mm. This equipment is installed in the CCiT-UB (Barcelona).

3.2.3 X-ray photoelectron spectroscopy

The theoretical foundations of X-ray photoelectron spectroscopy (XPS) originate from Albert Einstein's photoelectric effect experiment. This experiment displayed how a radiation of low intensity and high frequency ejects electrons from certain materials, while lower frequency radiation fails to produce any electrons regardless of the intensity. The equation derived by Einstein for an explanation of the photoelectric effect is the basis of modern XPS analysis, and it is as follows:

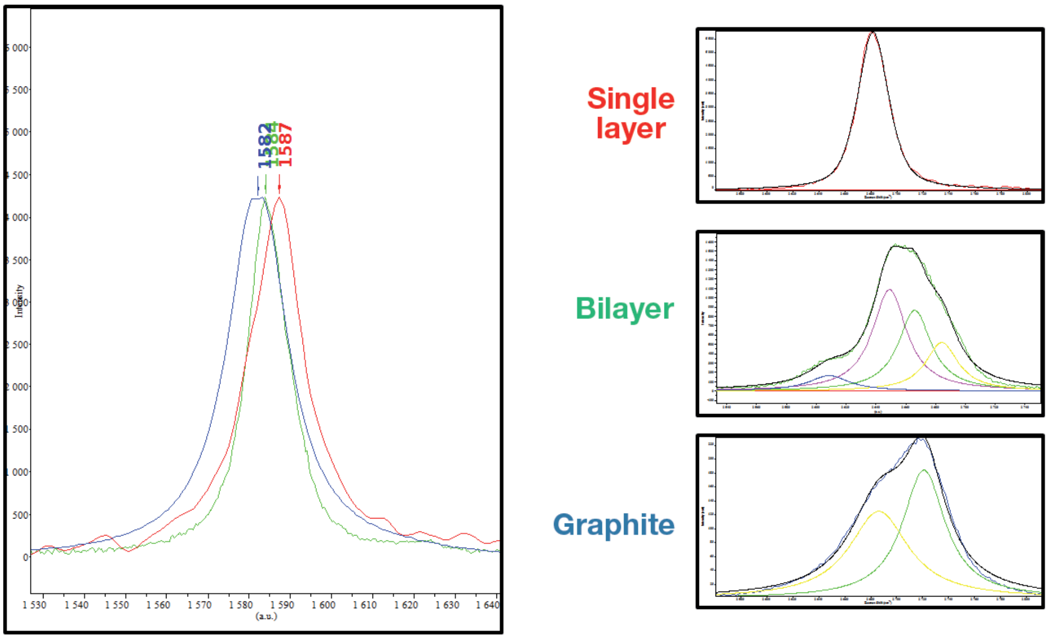

Figure 3.10 G band and 2D band are commonly used to determine the number of graphene layers [Eloïse Lancelot, 2013]

$$\frac{1}{2}m\vartheta_e^2 = h\vartheta - E_b \tag{3.3}$$

where $h\vartheta$ is the energy of the incoming photon, E_b is the binding energy of the electron in matter and ½ $m\vartheta_e^2$ is the kinetic energy of the ejected electron. X-ray radiation is commonly not exactly monochromatic. The photoelectron emission can also be excited by continuous X-rays, which are commonly associated with characteristic X-ray radiation. Such photoelectron emission generates a background in the low binding energy of the spectrum. Therefore, the binding energy is a direct measure of the energy required to remove the electron from material and is specific to the orbital of the element from which it came. This is what gives XPS the power to measure not only elemental information, but to relate the peak intensity to the amount of this element within the sample. The exact binding energy can be dependent upon both oxidation states and the local chemical and visible environment. Atoms of the higher oxidation state exhibit a higher binding energy due to the extra coulomb interaction between the photo-emitted electron and the ion core. This ability to discriminate between different oxidation states and chemical environments is one of the major strengths of the XPS technique.

XPS is the most widely used surface analysis technique because of its relative simplicity in use and data interpretation. XPS analyses chamber requires ultrahigh vacuum (UHV) conditions to remove as much adsorbed gas from the sample surface as possible prior to analysis and keep a clear a path for ejecting electrons to reach the detector. Thus, the operating pressure in the main chamber on the XPS machine should be ~1×10^{-9} mbar. So, to reach this pressure, the sample must move into the main chamber through various vacuum chambers to ensure the sample to be fully evacuated, in order to preserve the vacuum in the main analysis chamber. When an X-ray photon is incident on a solid surface, it has a limited penetration depth in the order of one to ten microns.

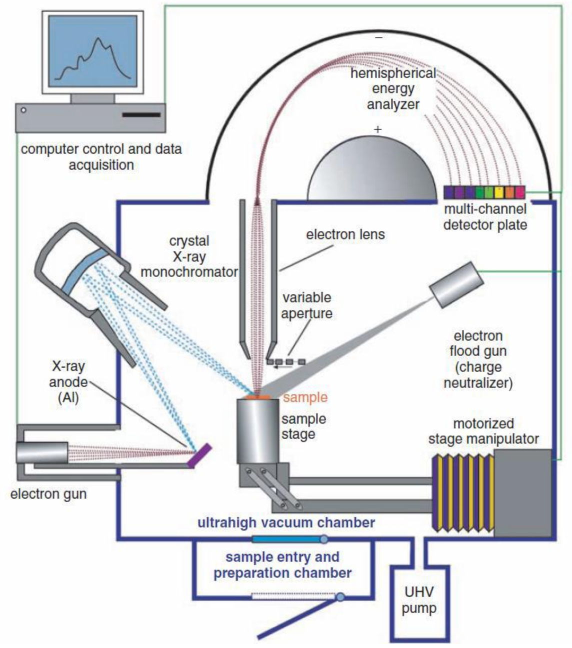

Figure 3.11 Schematic view of the XPS instrumentation [Vickerman JC, 2009]

Within this penetration depth, the photon ionizes the atoms into solid. The electrons ejected during these ionizing interactions have a much greater probability of interacting with the solid than the X-ray photons. Thus, while ionization occurs to a depth of a few microns, only the electrons which originate within a few tens of angstroms below the solid surface can leave the surface without energy loss [Moulder JF, 1995]. The material is analysed by means the ejected electrons due to the characteristic photoelectron peaks in the XPS spectrum. The emission of electrons only from the region near the surface makes the XPS a sensitive technique to the surface. The typical XPS instrumentation (Figure 3.11) consists of a vacuum system, an X-ray source, an electron energy analyzer and data system. X-rays are created usually by impinging a high-energy (~10 keV) electron beam against an anode Mg or Al, resulting in X-rays with energies of 1.4866 and 1.2536 keV. Photoelectrons that have a sufficient energy to escape from the irradiated sample into the vacuum chamber are then separated and counted by the energy dispersive analyzer. When this X-ray flux is illuminating a sample, the spectrometer operation and data acquisition are controlled by the computer programs and are analyzed by software tools. XPS analyses are demanded for many industrial applications where surface composition is a critical factor, such as photovoltaics, electronics devices and EEE parts, packing systems, display technology, magnetic media, corrosion (oxidation) [Vickerman JC, 2009]

The energy measured by XPS analyses is the kinetic energy (KE) of the ejected photoelectrons. The binding energy of the photoelectrons, which are ejected from the conducting sample, are calculated afterwards. In order to calculate it accurately, it is necessary to place it in electrical contact with the XPS spectrometer [Reinert F, 2005].

As shown in Figure 3.12, the Fermi level (E_F) of the sample and the spectrometer are placed at the same energy level, thus BE refers to the EF and is presented as follows:

$$E_b = h\vartheta - E_k - \phi_s \qquad (3.4)$$

where ϕ_s is the work function of the spectrometer and E_k is the measured kinetic energy of the ejected photoelectron. X-ray photoelectron spectroscopy is an accessible and effective method for determining relative concentrations of the various constituents in a sample by interpreting the

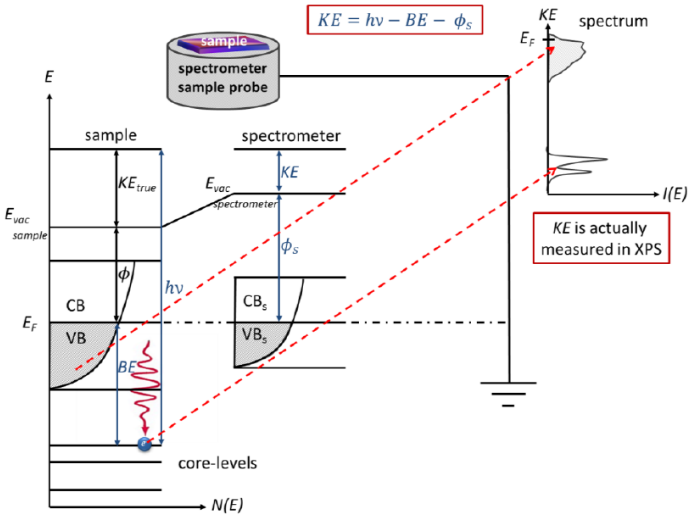

Figure 3.12 Energy level diagram with a schematic view of the photoemission process of the electrically conducting sample placed in electrical contact with the spectrometer [Reinert F, 2005; Vickerman JC, 2009]

peak areas in terms of a peak sensitivity factor. As a quantitative method, it gives the relative ratios of detectable elements on the surface of the material. For a homogeneous sample, the number of photoelectrons ejected per second in a specific peak is given by the following equation:

$$I = nf\sigma\theta y\lambda AT \tag{3.5}$$

where n is the number of atoms of the element (cm^{-3}), f is the X-ray flux (photons/(s-cm^{3})), σ is the photoelectric cross-section for the atomic orbital [cm^{2}], θ is an angular efficiency factor, y is the efficiency of the photoelectric process, λ is the mean-free-path of photoelectrons in the sample, A is the sample area of the probe and T is the detection efficiency. From the Equation 3.5:

$$n = \frac{I}{f\sigma\theta y\lambda AT} \tag{3.6}$$

where the denominator is defined as the atomic sensitivity factor, S. Thus, to determine the atomic fraction of any constituent in a sample, C_x:

$$C_x = \frac{n_x}{\sum n_i} = \frac{I_x/S_x}{\sum I_i\,/S_i} \tag{3.7}$$

where values of S for the different elements can be found in a number of references and peak fitting which allow for elemental quantification of most samples [Moulder JF, 1995].

In this thesis, the main material that has been analyzed by different methods is carbon. Hybridization, bonding, functionalities, and reaction progress are among the characteristics that can be inferred using XPS. All XPS results were obtained using the CasaXPS software. The application of XPS to carbon nanomaterials provides much information about the material, particularly the first few atomic layers, which are most important for the properties and uses of carbon nanomaterials. The peak location of carbon (C1s) is about 284.4 eV, which is mostly present in the sp^{2} hybridization state [Bar-Tow D, 1999]. The broad C1s peak at ~286 eV can be attributed to carbon in C–O group [Liu H, 2011]. The 285 eV is the binding energy corresponding to the sp^{3}-hybridized carbon atoms. Other peak with higher binding energies about 287.6 - 287.3 eV corresponds to carbon atoms attached to different oxygen containing moieties [Kim S, 2014].

3.2.4 X-ray diffraction

X-ray diffraction is a non destructive, and most effective technique to determine the crystal structure of materials. This technique is also useful for the quantitative phase analysis subsequent to the identification. X-ray diffraction technique is superior in elucidating the three-dimensional atomic structure of crystalline solids. The basic phenomena of this technique is the interference of the incident X-ray beam with the reflected beam after its interaction with matter.

There are three different types of interaction in the relevant energy range: (1) electrons may be liberated from their bound atomic states in the process of photoionization, (2) the incoming X-ray beam may undergo, which is termed Compton scattering, and (3) X-rays may be scattered elastically by electrons, which is named Thomson scattering [Birkholz M, 2006]. X-rays are beams of electromagnetic radiation with short-wavelength and high photon energy. X-rays are produced when accelerated electrons collide with the target. The loss of energy of the electrons due to impact is manifested as X-rays. Rapid deceleration of electrons in the target enables the kinetic energy of electrons to be converted to the energy of X-ray radiation. However, most of the kinetic energy is converted into heat, less than 1% being transformed in X-rays. The wavelength of X-ray radiation can be determined from the following equation:

$$E_k = eV = \frac{1}{2}mv^2 \qquad (3.8)$$

where e is the electron charge (1.6×10^{-19}C), E_k the kinetic energy, m the mass of the electrons ($9.11\text{x}\ 10^{-31}$ kg) and v the electron velocity (m/s).

The wavelength of X-ray radiation λ is related to the acceleration voltage of electrons V as shown in the equation:

$$\lambda = \frac{1.2398 \times 10^3}{V} (nm) \qquad (3.9)$$

X-ray belongs to the short-wavelength in the range of 10^{-8} m to 10^{-11} m, high-frequency end of the electromagnetic spectrum, between the γ and the ultraviolet radiation in the order of 3×10^{16} Hz to 3×10^{19} Hz and energies in the range of 100 eV to 100 keV.

There are two types ofX-ray, softt with photon energies below 10keV and hard with photon energies above 10 keV. Due to their penetrating ability, hard X-rays are widely used to image the inside of objects, e.g., in medical radiography and airport security. In contrast to hard X-rays, soft X-rays are easily absorbed in the air and this technology has significant advanced over the past decades, as a result of improvements in X-ray optics and the increased availability of third generation synchrotron sources.

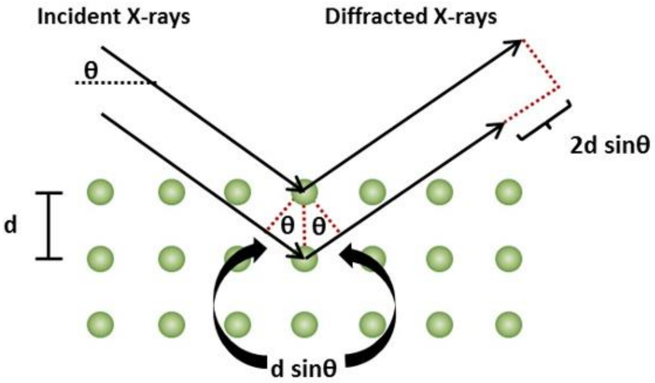

Figure 3.13 Schematic representation of the Bragg equation[27]

Diffraction of an X-ray beam by a crystalline solid is analogous to the diffraction of light by droplets of water, producing the familiar rainbow. X-rays are diffracted by each material differently, depending on what atoms make up the crystal lattice and how these atoms are arranged. When an X-ray beam hits a sample and is diffracted, we can measure the distances between the planes of the atoms that constitute the sample by applying the Bragg's Law, which is one of the keystones in understanding X-ray diffraction (Fig. 3.13):

$$n\lambda = 2dsin\theta \qquad (3.10)$$

where n is an integer, λ is the characteristic wavelength of the X-rays impinging on the crystallize sample, d is the interplanar spacing between rows of atoms, and θ is the angle of the X-ray beam with respect to these planes. As the wavelength in XRD experiments is known and the angles at which constructive interference occurs are measured, the use of the Bragg equation allows determining the distance between the lattice planes of the material.

The measurement results are presented by a diffractogramm. This is a plot of X-ray intensity on the y-axis versus the angle 2θ (2θ is defined as the angle between the incident and the diffracted beam) on the x-axis.

---

[27] https://wiki.anton-paar.com/en/x-ray-diffraction-xrd/

The number of layers in different graphene samples can be obtained by Lorentzian fitting of the (002) reflection making the use of the Scherrer formula [Scherrer P, 1918; Patterson A, 1939]:

$$\tau = \frac{K\lambda}{\beta \cos\theta} \tag{3.11}$$

where:

τ is the mean size of the ordered (crystalline) domains, which may be smaller or equal to the grain size;

K is a dimensionless shape factor, with a value close to unity. The shape factor has a typical value of about 0.9, but varies with the actual shape of the crystallite

β is the line broadening at half the maximum intensity (FWHM), after subtracting the instrumental line broadening, in radians. This quantity is also sometimes denoted as $\Delta(2\theta)$

θ is the Bragg angle

λ is the X-ray wavelength

3.2.5 CHNS elemental analysis

CHNS analyzer is an elemental analysis technique dedicated to the simultaneous determination of the percentage (%) composition of Carbon, Hydrogen, Nitrogen, Sulphur contained in organic, inorganic and polymeric materials and in substances of different nature and origin i.e. solid or liquid samples. This instrument uses combustion to oxidize the sample into simple compounds, which are then detected by thermal conductivity detection or infrared spectroscopy. The principles of elemental analysis are very simple. They rely on the tendency that all atoms prefer to be in their oxidation states. In pure oxygen, at high temperatures, all available carbon will easily burn

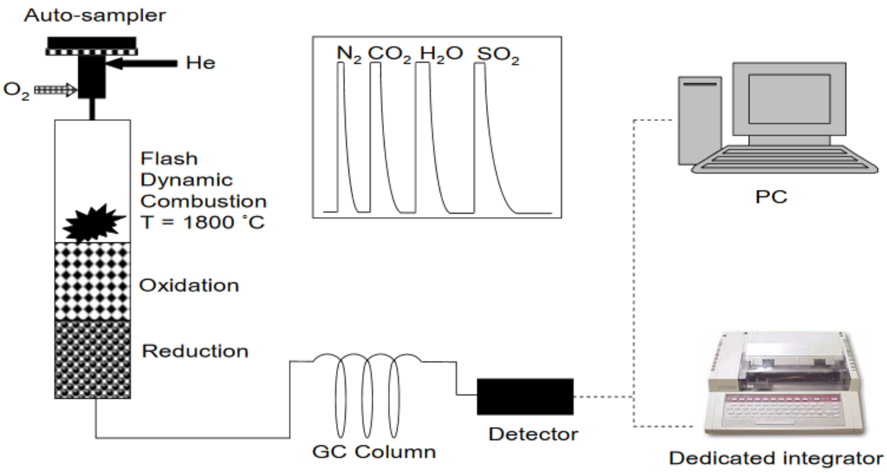

Figure 3.14 A schematic image of CHNS elemental analyzer [Thompson M, 2008]

to become carbon dioxide, all hydrogen will burn to become water and all nitrogen will become various nitric oxides. These fundamentals are enough for determining any components relative percentages of carbon hydrogen and nitrogen. The high temperature combustion in an oxygen-rich environment is based on the classical Pregl-Dumas method. This combustion can be carried out under both static conditions, i.e. the introduction of a set volume of oxygen or dynamic conditions, i.e. a constant flow of oxygen for a set period of time. In addition, it is often the catalyst used during the CHNS analysis process to promote conversion [Thompson M, 2008].

Key components of CHNS analyser are auto sampler, combustion reactors, chromatographic column, and T.C.D. detector (Fig. 3.14). Control of the instrument is established through a computer module, which is used to set up the program of work, report instrument diagnostics, and manage the calibration procedures.

3.2.6 BET surface analysis

The BET theory was developed by Stephen **B**runauer, Paul **E**mmett and Edward **T**eller in 1938 [Brunauer S, 1938]. It is based on the Langmuir theory, developed by Irving Langmuir in 1916. It is the first method to measure the specific surface of finely divided and porous solids. BET analysis refers to the adsorption by assuming an adsorbate behaves as an ideal gas at isothermal conditions. Langmuir theory is based on the following assumptions [Brame J, 2016]:

- All the vacant sites are of equal size and shape on the surface of adsorbent
- There are no interactions between adsorbate molecules on adjacent sites
- Adsorbates form a monolayer.
- Activity of adsorbate is directly proportional to its concentration.
- Each active site can be occupied only by one particle.

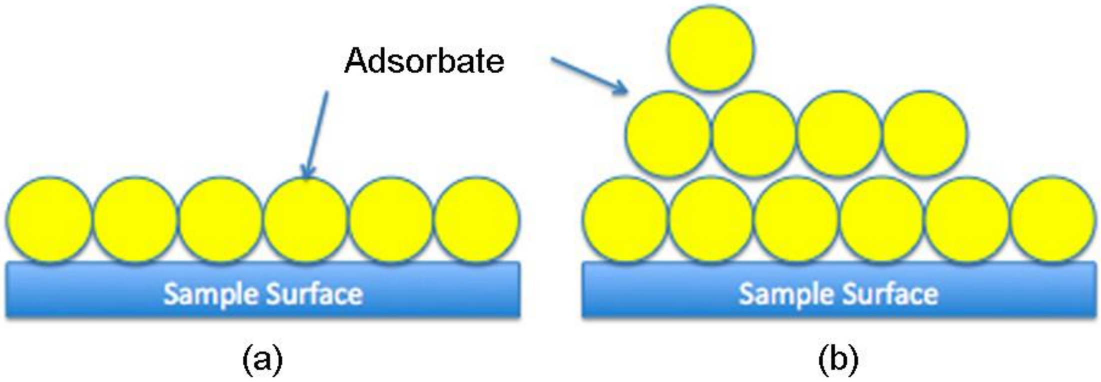

Figure 3.15 Schematic of the adsorption of gas molecules onto the surface of a sample showing (a) thermonolayer adsorption model assumed by the Langmuir theory and (b) multilayer adsorption model assumed by the BET theory [Hwang N, 2011]

In the Figure 3.15 show two models of adsorption single layer and multilayer adsorption. BET theory corresponding to the Langmuir theory to multilayer adsorption (Figure 3.31(b)). As compared with Langmur theory BET has some common assumption and three different, which are presented below [Hwang N, 2011]:

- gas molecules only interact with adjacent layers, it means, that there is no interaction between the different adsorption layers.
- gas molecules physically adsorb on a solid in layers infinitely
- the Langmuir theory can be applied to each layer.

TriStar 3000 system, which was used during this thesis for measuring the specific surface of the graphene nanowalls, composed of the TriStar Automated gas adsorption analyser, vacuum pump, and a control module for entering analysis and reporting options[28] (Fig. 3.16) .

BET analysis requires the following steps:

- Careful measurement of sample mass
- Degassing the sample using heat, vacuum
- Measuring adsorption
- analysing measurement

Figure 3.16 TriStar 3000 Analyser[29]

For BET analysis, samples must be clean, dry and pure. For best results, samples can be left in a desiccator or oven at low temperature, for removing a possible humidity. When the sample is ready for analysis, it is necessary to measure the mass of the sample in the glass tube, which used as a sample holder with rod inserts for reducing the total volume of the tube. The value of the mass is important for the calculation of the BET surface area. The next step is a degassing of sample overnight, before starting the analysis. The degassing step is required to evacuate any moisture in the sample, which would negatively impact on the surface interaction with the N_2 gas during the analysis. The main part of the surface analysis is the nitrogen adsorption test, which lasts 2-3 hours. The test is carried out by introducing pure nitrogen into the tube while recording the pressure ratio (P/P_0) on a graph that provides the BET surface area. Nitrogen is usually used because of its availability in high purity and its strong interaction with most solids. The value of the BET surface area can be calculated from following equation [Brunauer S, 1938]:

---

[28] http://www.micromeritics.com/repository/files/tristar_3000_operators_manual_v6.08.pdf

[29] http://business.magnasardo.com/products/micromeriticsinstruments/physisorption/103-tristar-ii-series

$$\frac{1}{v[(p_0/p)-1]} = \frac{1}{v_m c} + \frac{(C-1)}{v_m C} \cdot \frac{p}{p_0} \qquad (3.12)$$

where p and p_0 are the equilibrium and the saturation pressure of adsorbates respectively, at the temperature of adsorption, $\boldsymbol{v}$ is the adsorbed gas quantity, $\boldsymbol{v}_{\mathbf{m}}$ is the monolayer adsorbed gas quantity and c is the BET constant, which can determine from the following equation:

$$c = exp\left(\frac{E_1 - E_L}{RT}\right)$$

E_1 is the heat of adsorption for the first layer, E_L is the heat of adsorption for the second and higher layers and is equal to the heat of liquefaction.

BET analysis is an important and useful method for determining the total effective surface and the specific surface of porous or nanostructured materials. The total and specific surface can be calculated by the following equations:

$$S_{total} = \frac{v_m N s}{V} \qquad (3.14)$$

$$S_{BET} = \frac{S_{total}}{a} \qquad (3.15)$$

where v_m is in units of volume, which are also the units of the monolayer volume of the adsorbate gas, N is the number of Avogadro, s is the adsorption cross section of the adsorbing species, V is the molar volume of the adsorbate gas and a is the mass of the solid sample or adsorbent.

Disadvantages of BET technique are that it requires a lot of time for the adsorption of gas molecules to occur and a lot of manual preparation is required.

3.2.7 Optical emission spectroscopy

Optical emission spectroscopy (OES) is a sensitive and non-evasive plasma in-situ diagnostic technique which provides useful information on different excited states in the plasma at real-time characterization, without interfering with the plasma [Bashir M, 2014]. Spectroscopic methods for plasma diagnostics are the least perturbative, and for the evolution of the plasma parameters, they study the emitted, absorbed or dispersed radiation. In plasma gas phase, species are promoted to excited electronic states by collisions with energetic electrons. Light is emitted when the excited species go through de-excitation processes as a means of conserving energy. Fig. 3.17 shows the electron impact excitation of the ground state of the atom A to an excited state A^*, followed by the subsequent emission of a photon at frequency ω to reduce the energy of the atom to some lower state A_f.

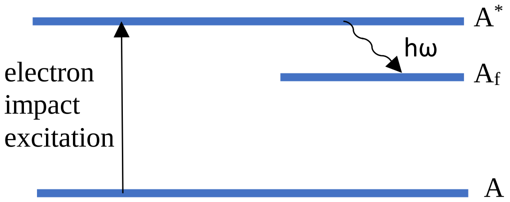

Figure 3.17 Schematic of electron impact excitation followed by a radiative de-excitation process

The emission wavelength can be represented by the following equation.

$$\lambda = \frac{2\pi c}{\omega} \tag{3.16}$$

where

$$\hbar\omega = e\left(E_{A^*} - E_f\right) \tag{3.17}$$

Light emitted by a laboratory plasma is associated with the electronic transitions and they usually fall within the UV-visible wavelength range of the electromagnetic spectrum. The wavelength of emission line depends on the difference in energy between the initial (excited) and final (de-excited) state of the atom and in analytical plasmas it is largely unaffected by plasma. The intensity of emission line is proportional to the number of atoms in an excited state. All atoms and molecules have their own unique energy states with distinct energy differences between the allowed transitions, which enables OES to provide insight into the nature of the chemical species generated within the plasma [Liao Y, 2000].

Plasma radiation is emitted from atoms in discrete quanta, called photon, whose energy ΔE can be described by the following equation:

$$\Delta E = E_i - E_f = \hbar\nu \tag{3.18}$$

where E_i and E_f are the energy of the initial and stationary states of the atom, respectively, $\hbar$ the constant of Planck and ν is the frequency.

The hydrocarbon ICP is the main studied plasma within this thesis. All types of plasma emit radiation depending on their gas composition and plasma parameters. Plasma plays an important role in the deposited material structure.

As an illustration, Fig. 3.18 shows the emission spectrum of methane plasma formed in a region with nitrogen at atmospheric pressure using a micro-plasma jet. The main species producing emission are summarized in Table 3.3. From OES it is evident that the main features of lines in the wavelength range from 300 nm to 800 nm are three known systems of CH located near at 431, 387 and 314 nm. Also The $H_α$ line is visually observed at 656.3 nm, the other lines of the Balmer system, $H_β$ line and $H_γ$ line, were not detected, or the intensities of the two lines were too weak to be distinguished from the noise signal. Moreover, the Swan band system, which is represented by C_2 carbon dimmers and the Fulcher band system of H_2 were also visualized in the spectrum. The absence of the CH_3 and CH_2 depends on long lifetime (about several milliseconds) and short lifetime of radicals, respectively [Liberman MA, 1994; Babayan SE,1998]. Thus, CH_2 radical was immediately converted into CH radical through the following reaction:

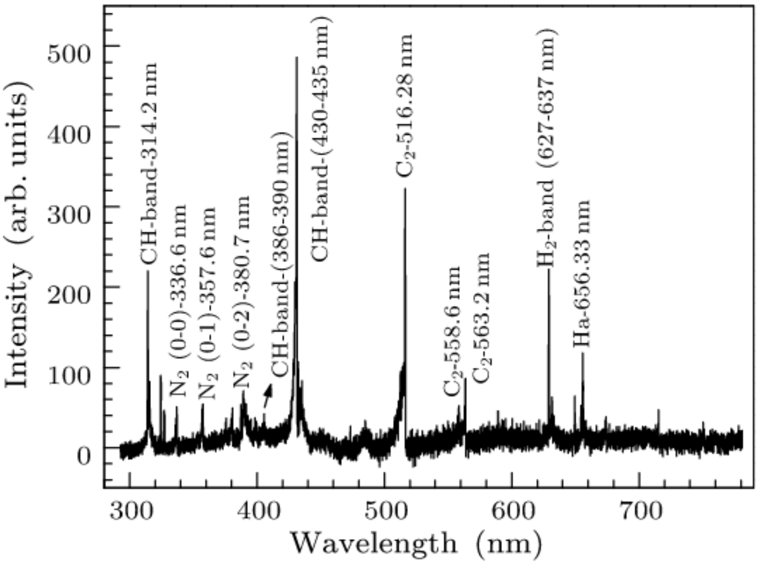

Figure 3.18 Optical emission spectra of methane plasma formed in atmospheric pressure micro-plasma jet

$$CH_2 \rightarrow CH + H$$

The possible pathway for the methane decomposition and the new species formations are:

$$CH_4 + e^* \rightarrow CH_3 + H + e$$

$$CH_3 + e^* \rightarrow CH_2 + H + e$$

$$CH_2 + e^* \rightarrow CH + H + e$$

$$CH_4 + e^* \rightarrow CH_2 + H_2 + e$$

$$CH_3 + e^* \rightarrow CH + H_2 + e$$

$$2CH_4 \xrightarrow{-H_2} C_2H_6 \xrightarrow{-H_2} C_2H_4 \xrightarrow{-H_2} C_2H_2$$

In this thesis, the used optical emission spectroscope has a very simple and compact design. The synthesis chamber equipped with view ports for the in-situ process visualization and characterization. Optical emission spectroscopy (OES) experiment was conducted at different growth conditions using a fiber coupled spectrometer (BLACK-Comet UV-VIS) and collecting optics. BLACK-Comet UV-VIS spectrometer is powered directly from a PC’s USB port. A single strand fiber optic cable assembly delivers input via standard SMA 905 fiber optic. Each emission spectrum was recorded in a time-integrated manner by using SpectraWiz software.

For the measurements of OES along the entire length of the quartz tube in a particular experiment comparing the composition of plasma at different positions, several ¨windows¨ were made in the part of the resonator. In addition, for the oven part, we opened it just a little bit for measure OES with our collecting optical fiber. OES measurements were taken from each part of the tube from a distance of 5 cm (Fig. 3.19).

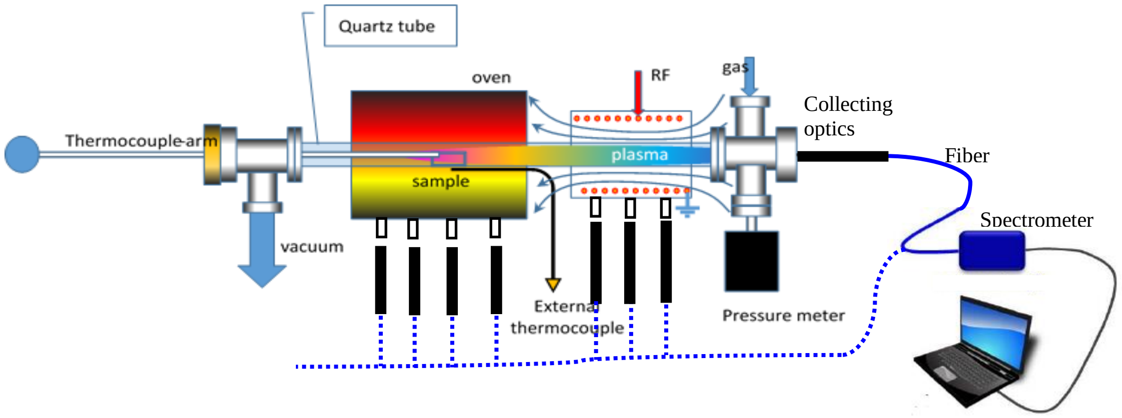

Figure 3.19 Schematic diagram of RF inductively coupled plasma aperture with mobile OES

3.3 Other characterization techniques

3.3.1 Contact angle

The contact angle is the angle, conventionally measured through the liquid, where a liquid/vapor interface meets a solid surface. It indicates the degree of wetting when a solid and liquid interact. Small contact angles (<<90°) correspond to high wettability (hydrophilic), while large contact angles (>>90°) correspond to low wettability (hydrophobic) (Fig. 3.20). The variation of wettability can be defined by the mechanical equilibrium of the drop under the action of three interfacial tensions:

$$\gamma_{lv} cos\theta = \gamma_{sv} + \gamma_{sl} \qquad (3.19)$$

where γ_{lv}, γ_{sv}, γ_{sl} are liquid-vapor, solid-vapor, and solid-liquid interfacial tensions, respectively, and $cos\theta$ is the contact angle. Equation 3.19 called as Young's equation, and $cos\theta$ is Young's contact angle.

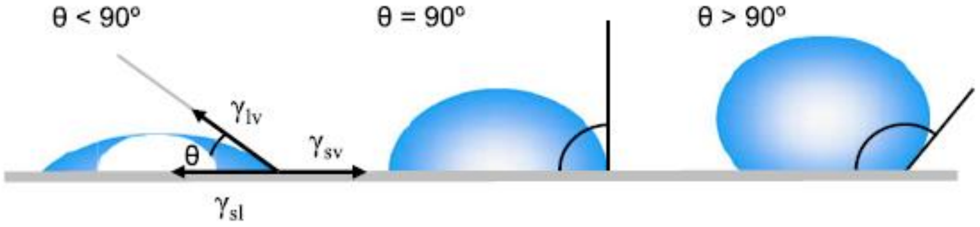

Figure 3.20 Illustration of contact angles formed by sessile liquid drops on a smooth homogeneous solid surface [Yuan Y, 2013]

The wettability of the MLGNWs surface is an important property for the future electrical applications. MLGNWs, governed by chemical composition and by the geometrical microstructure of the contact surface, have hydrophobic properties, which is an obstacle for electrochemical analysis, due to the lower wettability. The contact angle of the substrate can be changed by the post-treatment with oxygen plasma. We measured the static contact angle by using the device CAM200 to check the surface properties of MLGNWs [Corbella CR, 2005].

3.3.2 Photoluminescence spectroscopy

The phenomena which involve absorption of energy and subsequent emission of light are classified generically under the term luminescence. Luminescence covers photoluminescence, electro luminescence, chemiluminescence, cathodoluminescence, among others. Photoluminescence (PL) is light emission from any form of matter after absorption of photons (electromagnetic radiation). Fig. 3.21 shows the principle of photoluminescence transitions.

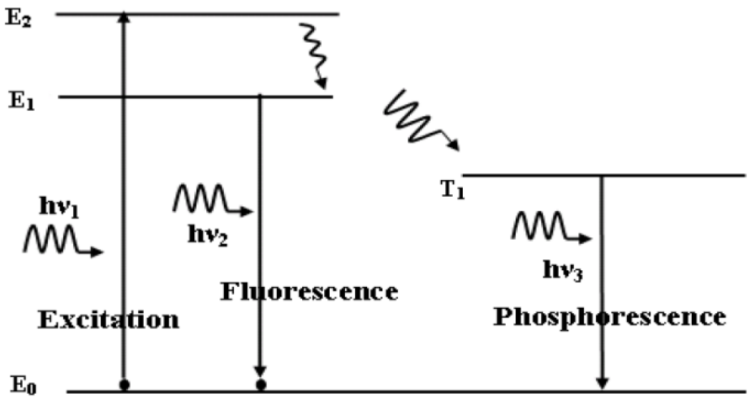

Figure 3.21 Principle of photoluminescence transitions [Alaoui IM, 2008]

Photoluminescence is divided into two categories: fluorescence and phosphorescence. Fluorescence is the absorption of energy by atoms or molecules followed by immediate emission or light or electromagnetic radiation. In fluorescence the excited atoms have comparatively short lifetime before its transition to low energy state (10^{-5}–10^{-8} s). The absorption process occurs over a short time interval and it involves the transition from ground state to singled excited state and it does not change the direction of the spin. The emitted photon (light) has lower energy that the absorbed photon and emission occurs at a longer wavelength than the incident light. In case of phosphorescence, the absorption of energy by atoms or molecules is followed by delaying emission of electromagnetic radiation and the excited atom has comparatively long lifetime before its transition into a low energy state. Phosphorescence involves the transition from the single ground energy state to an excited triplet state, thus involving a change of a spin state. Phosphorescent materials appear to ¨glow in the dark¨, because of the slow emission of light over time [Williams ATR, 1981].

A schematic of a basic design for measuring fluorescence is shown in Fig. 3.22. The requirements for PL spectroscopy are a source of radiation, means of selecting a narrow band of radiation, and a detector. A simple fluorimeter consists of a source of excitation, which can be a lamp or laser (usually a xenon lamp), an excitation monochromator, a cuvette where the sample is placed, an emission monochromator (which reduces passing of light through an undesired wavelength), emission monochromator, a photon detector, and a recorder.

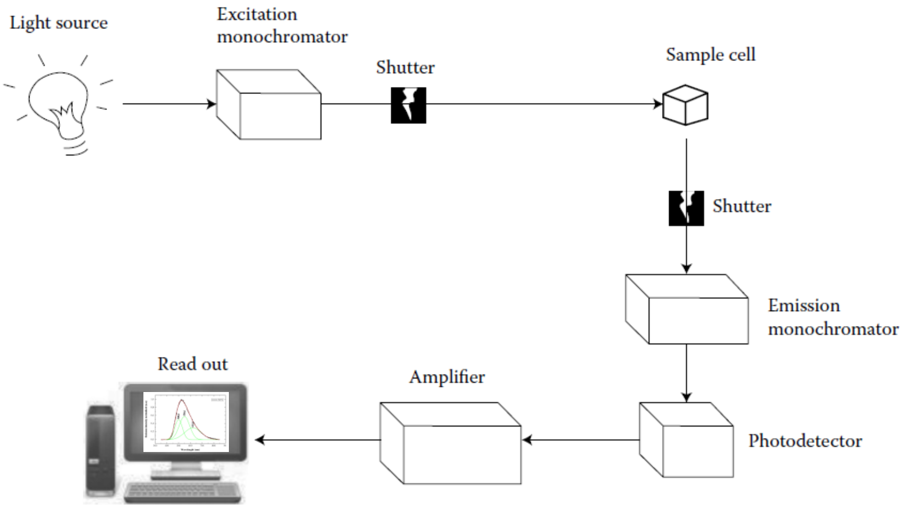

Figure 3.22 A schematic image of PL spectroscopy

PL spectra can be recorded in two ways: by measuring the intensity of emitted radiation as a function of the excitation wavelength, or by measuring the emitted radiation as a function of the emission wavelength. In an excitation spectrum, a fixed wavelength is used to monitor emission while the excitation wavelength is varied. An excitation spectrum is nearly identical to a sample absorbance spectrum. In an emission spectrum, a fixed wavelength is used to excite the sample and the intensity of the emitted radiation is monitored as a function of the wavelength [Shinde KN, 2012].

In this thesis, we have used a room-temperature PL spectroscope. PL spectra were recorded with a chopped Kimmon IK Series He-Cd laser (325 nm and 40 mW). Fluorescence was dispersed through a SpectraPro 2750 (focal length 750 mm) f/9.8 monochromator, detected with a Hamamatsu H8259-02 photomultiplier, and amplified through a Stanford Research Systems SR830 DSP lock-in amplifier. A 360 nm filter was used for filtering the stray light. All spectra were corrected for the response function of the setups.

Chapter 4

Production technology and proposed growth mechanism

4.1 MLGNWs production technology

4.1.1 Plasma state

When a solid is sufficiently heated so that the thermal motion of the atoms break the crystal lattice structure apart, usually a liquid is formed. When a liquid is heated enough so that atoms vaporize off the surface faster than they recondense, gas is formed. When a gas is heated enough so that the atoms collide with each other and knock their electrons off in the process, plasma is formed: the so-called fourth state of matter (Fig. 4.1). Plasma is defined as a quasineutral collection of electrons, ions, photons and neutral gaseous species. Plasmas are often viewed as "electrical fluids" because these charged particles respond to fields collectively. Laboratory plasmas are produced by using electric fields to pull the electrons from gasses rather than the thermal energy used to change between the other states of matter. Electron density, electron energy, degree of ionization are essential factors for description of plasma. The wide range of plasma parameters creates a subdivision for various types of plasmas, including those in thermal equilibrium and those in non-thermal equilibrium. The laboratory plasma is produced when a small amount of gas is heated or ionized by an electric current through the ionized gas or by emitting radio waves in the gas.

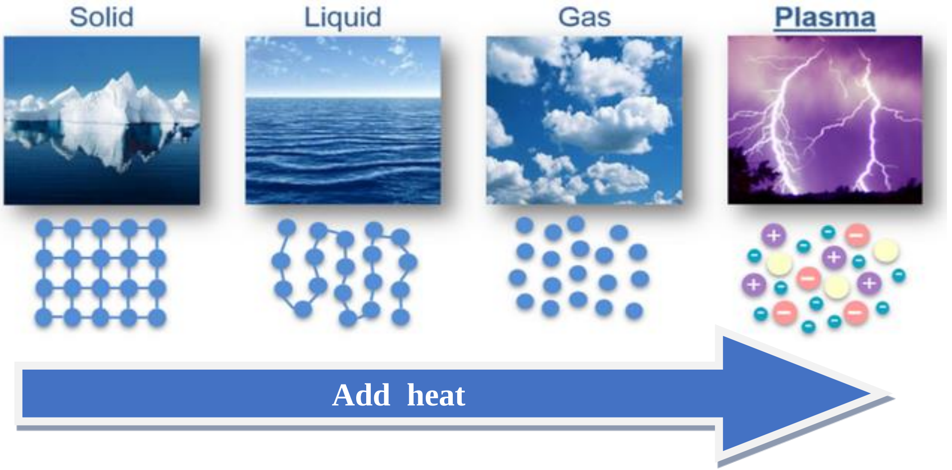

Figure 4.1 Description of plasma as the fourth state of matter[30]

Laboratory plasmas are usually non-thermal equilibrium plasmas where the ion and neutral gas temperatures remain around the room temperature, while the electrons rise to energies corresponding to tens-of-thousands degrees [Goldston RJ, 1995].

Fig. 4.2 shows the parameters of natural and laboratory plasma. From these parameters we can assume that, the plasma state spans enormous ranges in scale-length, density of particles and

---

[30] Image from GRINP: https://thesullivancorp.com/news/tag/ions/

temperature. Plasma improves the thin film deposition technique. Some advantages offered by this plasma coating technique are [Ojha SM, 1982; Ostrikov K, 2007]:

- ✓ ability to deposit a variety of materials on the substrate or workpiece to confer specific properties
- ✓ operation at low a temperature, which is suitable for heat-sensitive substrates
- ✓ thin films of high quality, uniform thickness and resistance to cracking
- ✓ hard adhesion of the film to the substrate
- ✓ ability to coat even complex geometry parts
- ✓ high rates of deposition

Plasma enhanced CVD is the main deposition technique used in this thesis.

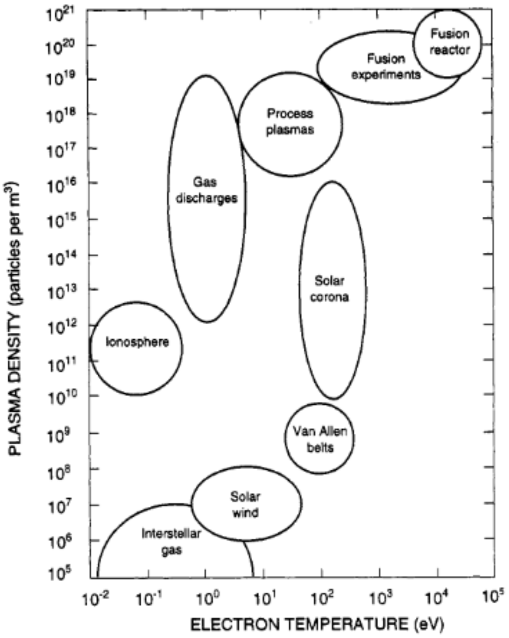

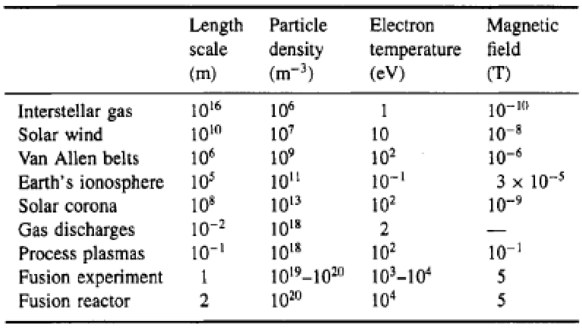

	Length scale (m)	Particle density (m^{-3})	Electron temperature (eV)	Magnetic field (T)
Interstellar gas	10^{16}	10^6	1	10^{-10}
Solar wind	10^{10}	10^7	10	10^{-8}
Van Allen belts	10^6	10^9	10^2	10^{-6}
Earth's ionosphere	10^5	10^{11}	10^{-1}	3×10^{-5}
Solar corona	10^8	10^{13}	10^2	10^{-9}
Gas discharges	10^{-2}	10^{18}	2	—
Process plasmas	10^{-1}	10^{18}	10^2	10^{-1}
Fusion experiment	1	10^{19}–10^{20}	10^3–10^4	5
Fusion reactor	2	10^{20}	10^4	5

Figure 4.2 Typical parameters of naturally occurring and laboratory plasma [Goldston RJ, 1995]

4.1.2 MLGNWs fabrication technologies

As we have commented above, plasma is an important factor for vertical graphene synthesis. MLGNWs synthesis methods are similar to the diamond films and CNTs. For the growth of MLGNWs, high density plasma is necessary for the efficient decomposition of H_2 molecules. MLGNWs can be produced by the following deposition methods:

- Microwave plasma (MW),
- Radio frequency inductively coupled plasma (ICP)
- RF capacitive coupled plasma assisted by H radical injection (CCP)
- Helicon wave plasma
- Electron beam excitation plasma
- Hot filament CVD
- Sputtering of graphite target

MLGNWs growth by PECVD compared with CVD offers advantages, such as a lower substrate temperature, higher growth selectivity, and better control in nanostructure ordering/patterning [Dikonimos T, 2007; Vizireanu S, 2010; Ostrikov K, 2007] due to the presence of energetic electrons, excited molecules and atoms, free radicals, photons, and other active species in the plasma region, which make PECVD a popular method for vertical graphene growth. In addition, PECVD is a complex process as compared to CVD and the morphology of vertical growth structures depend on the plasma source and a series of operation parameters [Ostrikov K, 2008]. The common methods for MLGNWs growth is a PECVD method with different power frequencies of the plasma source: MW plasma (f = 0.5–10 GHz; commonly 2.45 GHz) [Mori T, 2008; Chuang ATH, 2006; Shang NG, 2008; Zhang Y, 2012], radio frequency plasma (f =1–500 MHz; commonly 13.56 MHz) [Jain HG, 2011; Hiramatsu M, 2004], DC plasma [Yu K, 2011; Tanaike O, 2009; Obraztsov AN, 2002] and their combinations [Kondo S, 2008; Takeuchi W, 2008]. So, before going on to describe various methods of plasma deposition, we briefly describe the state of plasma.

4.1.3 Microwave PECVD

MW plasma is a type of electrodeless gas discharge plasma with high frequency electromagnetic radiation in the GHz range. The interaction between the electromagnetic field and the plasma in MW discharges is quasi-optical. MW can be classified into two types: transverse electric (TE) mode and transverse magnetic (TM) mode, referred to as the electric field and magnetic field perpendicular to the direction of wave travel, respectively (Fig. 4.3). The geometrical structure of these two reactors is different.

TE-MW PECVD system composed of the cylindrical quartz tube, where 2.45 GHz MW source is coupled via a traverse rectangular cavity waveguide. The incident electromagnetic wave formed in the waveguide interacts with the plasma generated in the discharge and due to the interaction forms partial dissipation, partial transmission and reflection of the electromagnetic wave [Kobashi K, 1988]. TE-MW PECVD is one of the easy MLGNWs synthesis setups. However, this system has disadvantages, such as limited substrate temperature and possible introduction of contamination from the outside container, since the wave is directly coupled to the quartz tube with a surface wave plasma mode. Moreover, the high operation temperature and MW power of this setup can promote damages of the quartz tube and vacuum system. In addition, the growth efficiency and uniformity of the GNW films is low for the TE-MW PECVD system. For improving these disadvantages a TM-MW PECVD system was designed, where the dominant wave is converted from the TE mode in a rectangular waveguide to the TM mode in a cylindrical waveguide. Fig. 4.3b shows the schematic image of TM-MW PECVD system, where the antenna is positioned in the top of the reactor, a cylindrical cavity, through a coaxial port, to produce a more intense electric field on the central part of the substrate where a plasma is clearly lighting. In this system, the sample is located outside the plasma, which leads to a control of the temperature of the substrate. TM-MW PECVD systems avoids overheating and thus allows using high operation power (2-3 kW) and pressure (several tens of HPa) [Chuang ATH, 2006].

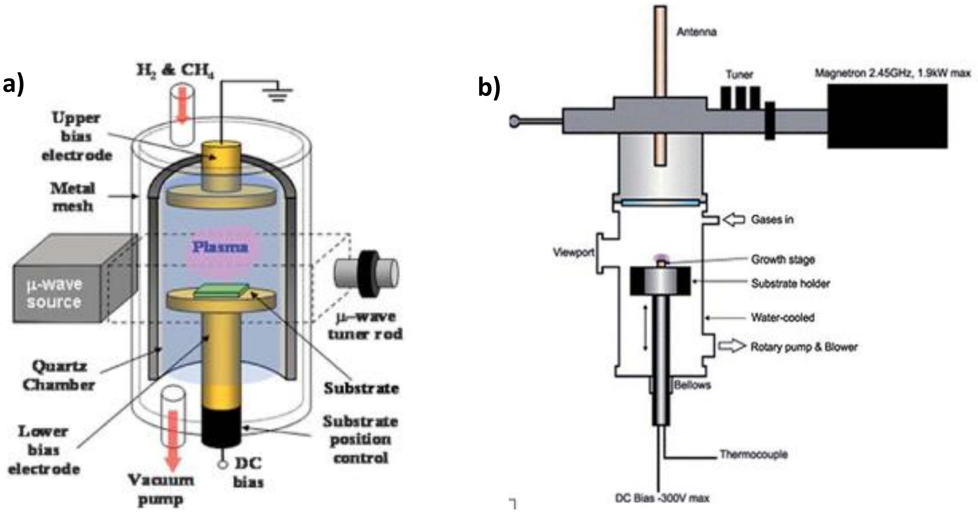

Figure 4.3 Schematic diagrams of MW PECVD systems (a) TE-MW [Wu YH, 2010] and (b) TM-MW [Chuang ATH, 2006]

4.1.4 Radio frequency plasma CVD

One of the most popular sources of plasma for MLGNWs growth is radio frequency plasma (RF). Both microwave and radio-frequency (RF) generators are used to produce high frequency plasmas. The large electromagnetic wave of the RF discharge leads to the reasonably homogeneous plasma generation over large areas [Eliasson B, 1991]. RF frequency plasma is a promising method for synthesizing vertical graphene (Fig. 4.4).

At typical RF frequencies, the electrons and ions behave in drastically different manners due to the large difference between their masses. The mass of electrons is lighter than ions (m_{p+}/m_{e-} = 1836) and can follow the instantaneous electric fields produced by the applied RF voltage. The characteristic frequency of electrons in a plasma (ω_{pe}) is calculated by the following equation:

$$\omega_{pe} = \sqrt{\frac{n_e e^2}{m_e \varepsilon_0}} \qquad (4.1)$$

where n_e is the electron density in cm^{-3}, e is the electron charge, m_e is the mass of one electron and ε_o is the permittivity of free space [Lieberman MA, 2005]. The ions also have a characteristic frequency, which can be determined from the similar relationship of the electrons. However, in typical laboratory plasmas, the electron frequency is in the GHz range while the ion frequency is in the MHz range due to the different masses between the electrons and ions. So, in the RF frequency range above one MHz, the heavy ions will only follow time averaged electric fields, while electrons can follow the instantaneous fields produced by the generator [Lieberman MA, 2005].

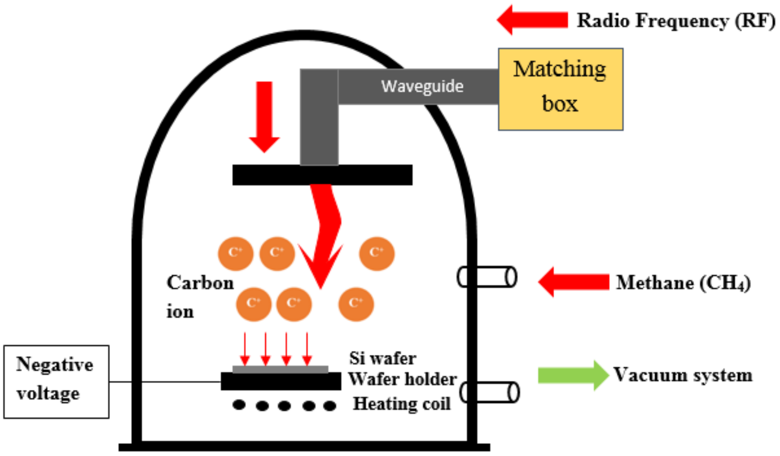

Figure 4.4 Schematic image of PECVD system

There are three main modes to couple the energy of an RF generator to the plasmas: the evanescent electromagnetic (H) mode, the propagating wave (W) mode, and the electrostatic (E) mode [Chabert P, 2011].

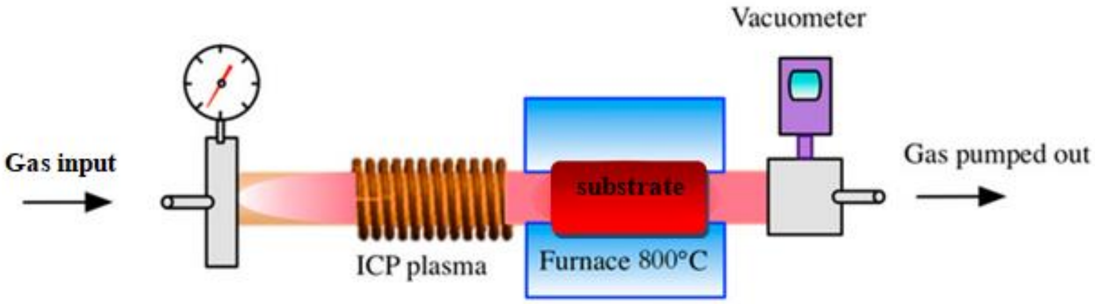

Figure 4.5 Schematic image of ICP-CVD system [Wu A, 2017]

The working principal of evanescent electromagnetic or so-calling ICP mode based on the principle that the energy from the RF power is coupled with an inductive circuit element adjacent to or immersed in the discharge region (Fig. 4.5). The inductive coil stimulates the magnetic field in ICP discharges.

The inductively coupled plasma is a high-density plasma, which operates at a relatively low pressure (10 Pa), below 100 mbar that is typically used in other plasma technologies. Plasma is located inside a chamber which is surrounded by an inductive coil antenna. ICP system can serve in two geometric forms - cylindrical and planar. In the planar geometry, the coil antenna of flat metal wound in spiral works like an electrode. In cylindrical geometry, the antenna is wound like a helical spring. The cylindrical ICP-CVD is the main technique used in this thesis.

The electrostatic E-mode or so-called capacitively coupled (CCP) plasma mode can be produced by a pair of parallel plane electrodes separated by a small distance, with one electrode connected to the power supply while the other is grounded. CCP as compared with ICP has high operating pressure. However, CCP for MLGNWs synthesis process has disadvantages, due to the relatively lower electron density and higher electron energy. The measurements by Langmuir probe showed that the typical electron density was 10^9 to 10^{10} cm^{-3} for CCP and 10^{10} to 10^{12} cm^{-3} for microwave and ICP plasmas [Hopwood J, 1993; Lieberman M, 2005]. In the other hand, the high sheath potential of CCP could possibly destroy the surface bonds and prevent the growth of high quality crystals [Lieberman M, 2005]. For improving these disadvantages the CCP can be combined with expanding RF plasma with a magnetron sputtering setup, as shown in Fig. 4.6.

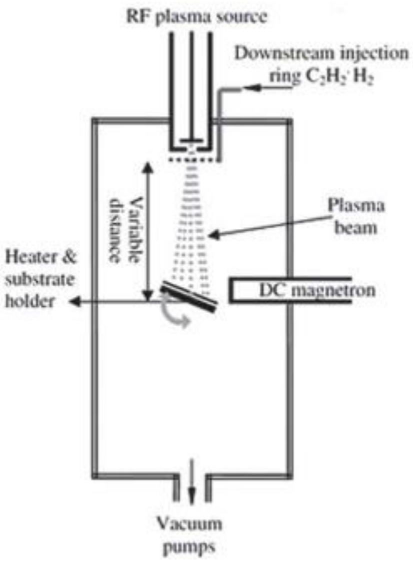

Figure 4.6 Schematic image of expanding CCP system [Vizireanu S, 2010]

4.2 Plasma deposition reactor

A half of the time of the whole PhD thesis was dedicated to the design and construction of a new remote ICP-CVDreactor, which would be placed in the PECVD-FEMAN Laboratory of the Physics Faculty of *Universitat de Barcelona*. One of the goals of this reactor construction was growing vertically oriented graphene nanostructure at relatively low temperature and without catalyst. It was built using a tubular furnace with the possibility to heat samples at low pressure. The main parts of the reactor were a quartz tube, a double shell tubular oven with capability to heat up to 1100°C and a vacuum system. The basic idea was to mount a RF coil (Ø 80 mm)

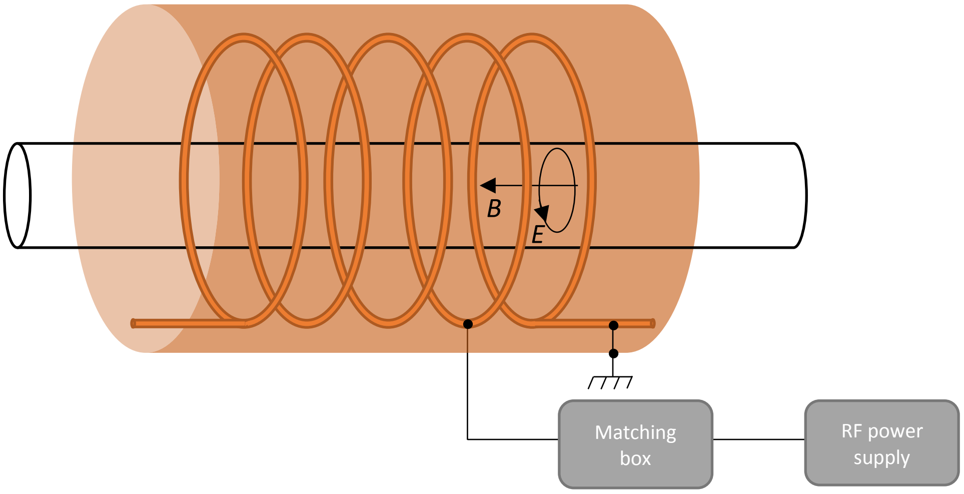

Figure 4.7 Scheme of inductively coupled plasmas with helical antenna

coaxially surrounding a l_{coil} = 100 cm long quartz tube. RF power was applied to the coil antenna and plasma was generated in the chamber. Coil antenna consists of a copper helicoidal tube (6 mm of external diameter) with a total length of $\lambda/4$ (5.527 m), being (λ the wavelength of the electromagnetic wave of 13.56 MHz frequency propagating in the air. One of the main parameters of the coil antenna is the inductance, which depends on the number of turns, the loop diameter, wire diameter, and the permeability of the medium[31]:

$$L_{coil} \approx N^2 \mu_0 \mu_r (\mathrm{D}/2) \left[\ln\left(\frac{8D}{d}\right) - 2\right] \qquad (4.2)$$

Where:

L_{coil} = inductance of the coil in Henry (H)

N = number of turns

μ_0 = permeability of free space = $4\pi\times10^{-7}$ H/m

μ_r = relative permeability

D = loops diameter

d = wire diameter

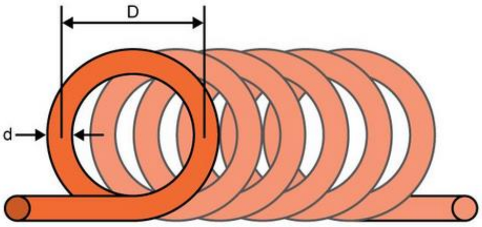

According to this equation, we have designed a coil antenna with 22 turns, wire diameter 0.6 cm and loop diameter 8cm, having a self-inductance, L_{coil} = 65 µH.

The helicoidal $\lambda/4$ resonator with a diameter of 8 cm was wrapped on the tube and creates an axial magnetic field $B_z = B_0(z)\cdot\cos(\omega t)$ (Fig.4.7). Then, an azimuthal electric field, E_φ of near 40kV/m, for a RF power of 400W, is induced inside the quartz tube producing a strong ionization of the gas. From the results obtained, we have seen that the pressure and temperature of the gas play an important role in the formation of MLGNWs and, for this reason, it is necessary that all the technological parameters are controlled externally by a set of electronic instruments. One recommendable thing to operate with an ICP-CVD reactor is to shield the resonator to avoid that the RF signal interferes with the electronic instruments that surround the reactor. Also, we ground all the cables connecting the reactor with electronic devices. In order to keep a stable gas pressure during the entire deposition process, we installed a control valve between the quartz tube and the vacuum system to regulate the pressure in a small range.

The reactor is doted by an optical emission spectrometer (OES) to monitor the chemical composition of the plasma in real time. The quartz fiber that collects the light emitted by the plasma in the radial direction could be displaced along the quartz tube to determine the active species in different parts of the tubular reactor. After four or five MLGNWs deposition sessions, the quartz chamber was cleaned with oxygen plasma during 15 min to ensure the quartz

---

[31] https://www.allaboutcircuits.com/tools/coil-inductance-calculator/

transparency for OES measurements. In addition, to monitor the deposition temperature in the growth zone, we have designed a substrate support arm with a thermocouple to place the sample inside the reactor.

The details of the reactor are described as follows (Figure 4.8):

- Vacuum quartz tube has an internal diameter of 40 mm and 1000 mm long. The quartz tube is surrounded by a cylindrical electric oven, with a Ni-Cr resistance, which allows reaching temperatures up to 1100 °C.
- Plasma generator is the core of the PECVD reactor and based on a cylindrical coil-resonator antenna above described (Fig.4.7) working on a radio frequency (RF) of 13.56 MHz and connected to a RF power supply RFPP5 of 550W by a RG393 PTFE coaxial transmission line of 50 Ω of characteristic impedance and N-type connectors, through a manual impedance matching-box.
- Thermocouple-arm system permits a fast introduction of samples and temperature monitoring in the deposition zone during the process. For the fragile substrates, we developed a molybdenum holder, which hangs on the tip of the thermocouple (Fig. 4.9).
- The gas management system consists of five gas flow controllers for N_2, Ar, O_2 (with a full scale of 200 sccm) and H_2 (with a full scale 0f 50 sccm) and for precursor gases CH_4 and C_2H_2 with a full scale of 10 sccm. The system permits an independent control of the gas rate of three different lines at the same time. The pressure corresponding to the total mass flow (gas mixture) is regulated by an independent variable conductance valve installed in the outlet line, before the vacuum pump (LEYBOLD D8), which has two stages and a pumping speed of 8 m^3/h. All the system is manually controlled.

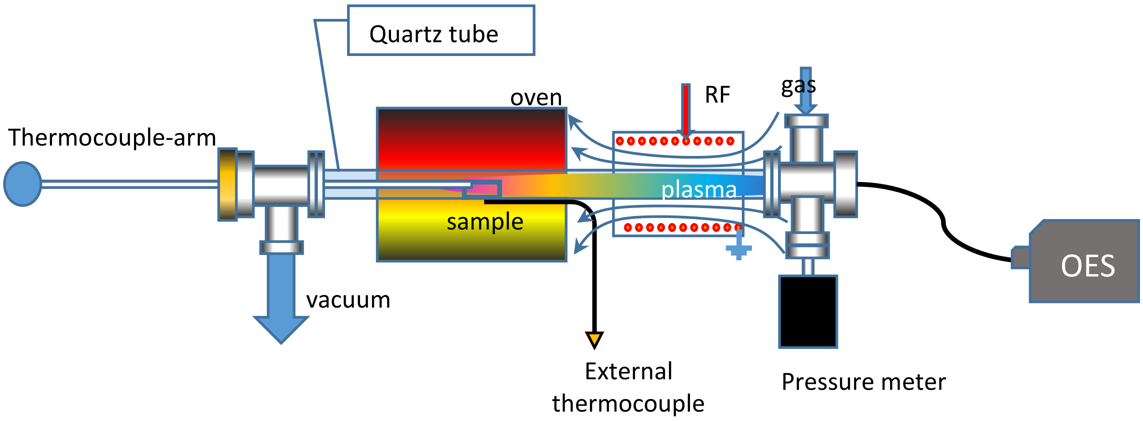

Figure 4.8 Schematic image of ICP-CVD reactor

One of the main advantages of this reactor is the possibility of generating a RF plasma without electrodes inside the quartz tube. This reduces the effects of highly energetic bombardment common to dielectric barrier discharges (DBD) and capacitively coupled plasmas (CCP). ICP plasma system at a frequency of 13.56 MHz allows heating the sample and placing the substrate far from the plasma generator, with a low energetic bombardment. ICP system is very useful for high density plasma applications. In our system, all gases enter through the plasma zone and, travels through the hot zone, the active species generated by plasma interact with the hot sample, and that leads to the formation of a nanostructured carbon layer.

Figure 4.9 Vacuum feedthrough with linear movement, stainless steel blind, 3mm Ø, k-type thermocouple-arm and molybdenum holder (right end)

4.3 Growth mechanism

Plasma enhanced chemical vapour deposition is a common method for the production of MLGNWs. The growth mechanism of graphene nanowalls (MLGNWs) strictly depends on the plasma type. In case of vertical nanostructure fabrication, it is important to elucidate the specific species, such as carbon and hydrogen contained radicals, which are responsible for the successful growth of nanowalls. The growth mechanism of vertical free-standing nanostructures has not been discussed much compared to various techniques for thin film deposition, which have been developed earlier. There are various hypotheses about the GNW growth process. However, there is no unified theory to unveil the growth mechanism. In this chapter, we propose a mechanism for the growth of vertical graphene by plasma-enhanced vapor deposition.

The surface reactions in vapor deposition processes are controlled by nucleation and growth stages, and high performance can be achieved by (1) the selective production of specific reactive species crucial for the film growth and nucleation, (2) the efficient transport of essential species onto the growing surface, and (3) the control of surface reaction for both, nucleation and subsequent growth.

Plasma is an essential factor for the vertical growth of carbon and graphene. The reactions under plasma activated by remote ICP, used to minimize the orientational effect of the plasma electrical fields during the catalyst-free growth of graphene nano-sheets [Cuxart, 2017]: (a) warrant for a low graphene defect density via low plasma kinetics (low energy species during our ICP-CVD processes), (b) decouple the dissociation process of the gas from the growth process of graphene on the substrate (because the remote plasma, in our process), (c) tune the precursor gas chemistry (high presence of C-C dimers in our processes) in view of improving the graphene growth, and (d) reduce the growth temperature as compared to conventional chemical vapor deposition (CVD). In particular ICP is a relatively economical processes and simply way for producing a significant variety of carbon micro and nanostructures, like graphene and graphene nanowalls. The ICP configuration has a number of advantages, such as high energy density, larger plasma volume and, consequently, high growth rate [Hiramatsu M, 2013]. The growth process of vertical graphene is affected by the diverse parameters, such as the type of precursor gas, temperature, pressure, deposition time, substrate materials and plasma power. Also, catalysis-free direct synthesis of MLGNWs in suitable substrate is an additional characteristic of the random oriented nanostructures. Therefore, vertical structures need to be characterized and analyzed at various stages of growth, including the nucleation, vertical growth, and completion of the free-standing vertical nanostructures.

We have carried out a series of experiments for each step of growth and the corresponding *in situ* diagnosis by optical emission spectroscopy (OES) and morphological and structural analysis of the resulting samples, using Raman spectroscopy, scanning electron microscopy and transmission electron microscopy technique in order to understand step by step the MLGNWs growth process by ICP-CVD technique.

4.3.1 Experimental procedure

The vertical carbon nanostructures were grown by a remote cylindrical ICP-CVD reactor, described before (§3.2). The plasma is transferred inside the tube to the oven zone (remote plasma) because the gas flow drags the ions, electrons and other species formed inside the resonator.

An n-type c-Si (100) wafer was used as a substrate, which was positioned directly on the middle of the oven without using any holder. Methane gas was used as a carbon precursor. The plasma was generated by the helicoidal $\lambda/4$ resonator fed with 440 W of RF power at a fixed temperature 750ºC. The deposition time ranged from 1 min to 5 min at growth pressures between 45-50 Pa.

The as-grown samples were described by a field emission scanning electron microscope (FESEM) operated at 15 kV and field emission transmission electron microscopy (FETEM) operated at 200 kV. Also, we have conducted an analysis by Raman scattering at different steps of the deposition process. In addition, MLGNWs growth was in-situ and real-time measured through the optical emission of atoms, molecules and radicals present in the plasma by optical emission spectroscopy (OES). Next, there is a description of these results.

4.3.2 Results and discussion

The ICP-CVD method usually proceeds at a lower temperature than CVD and has better control in nanostructure ordering and higher purity which can easily produce very dense carbon nanostructures [Wang JJ, 2004a; Bo Z, 2013a]. Ions and neutrals are the main source of graphene nanowalls synthesis in ICP synthesis. Optical emission spectra provide peaks due to radicals from dissociation of CH_4. Electron-neutral collision and the dehydrogenation dissociations are the two primary mechanisms for the dissociation of CH_4. The in-situ monitoring of the ICP-CVD is required for detailed analyses of the growth of MLGNWs. Thus, the study of the evolution of active species during the plasma process is essential for understanding the primary mechanism of MLGNWs growth. During the growth of these vertically oriented graphene nanostructures, CH_4 is decomposed by the action of the plasma into the hydrocarbon radicals and atomic hydrogen, where monoatomic hydrogen [H] has a high activity [Denysenko IB, 2004]:

$$CH_4 \rightarrow CH_3 + [H]$$

$$CH_3 + [H] \rightarrow C + 2H_2$$

According to Denysenko et al., the carbon containing molecules, such as CH_4 and C_2H_y (y = 2, 4, 6) are not considered the primary contributors to film growth. Instead, the main growth precursors are the radical species, including C_x (x = 1, 2,3) and CH_x (x = 1, 2, 3). Fig. 4.10a shows the optical emission spectra from our CH_4 gas plasma process, at different growing times, during a single experiment. These spectra evidence that, CH and atomic hydrogen are dominant in the optical emission spectra of pure methane plasma. The observed emission bands of figure 4.1a correspond to the following wavelengths 314, 387, 431, 601, 612, 619, 655 nm.

The emission peaks at 314, 387, 431, 601,612, 619 and 655 nm, are attributed to CH ($C^2\Sigma \rightarrow X\,^2\Pi$),) CH ($B^2\Sigma^- \rightarrow X\,^2\Pi$), CH ($A^2\,\Delta \rightarrow X\,^2\Pi$), H_2(590-640 nm band) and atomic hydrogen transitions (H_α at 655nm), respectively [Terasawa T, 2012; Krivchenko VA, 2013].

Fig. 4.10b shows the evolution of CH, C_2 and H_α radicals versus the deposition time. In methane plasma the high intensity of hydrogen species is due to the high hydrogen content in the precursor gas. Fig. 4.10b evidences that, the density of the CH radicals (assuming that the density of radicals is approximately proportional to the emission counts for each corresponding peak of Fig.4.10a increases along the growing process, while the density of the monoatomic H only shows a moderate increase after the first minute of plasma establishment.

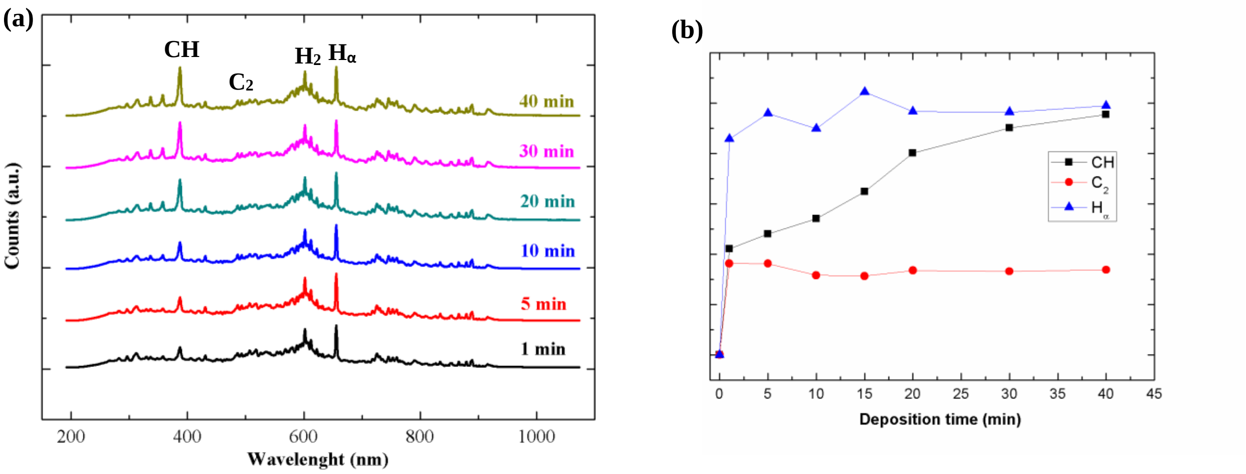

Figure 4.10 (a) Plasma emission spectra measured from the middle of the oven at different time range (17J2601); (b) Deposition time dependence of H_α , C_2 and CH radicals

Fig. 4.10b also shows the maintenance of the values of concentration of C_2 radicals during the studied 40 minutes of discharge. In addition, CH radicals show two clear phases of the increase process of radicals concentration at 0-15 min and 15-40 min.

Associated with the evolution of the radicals concentration with time, we present the drawings and SEM images of Fig.4.11 and Fig.4.12a and b, which illustrate the first phase of growth (buffer layer formation) consisting of a smooth growth of carbon structures at 5 and 10 min: (1) sp^2+sp^3 deposition and (2) sp^2 intermediate buffer layer formation (Fig.4.11).

The hydrocarbon radicals and active hydrogen atoms move, dragged by the gas flowing from the inlet part of the quartz tube, to the hot part of the reactor, where the substrate is positioned. In the range of pressure used during the growth process (50 Pa), hydrocarbon radicals can react in the gas phase to form polymeric structures, which can form the high hydrogenated carbon deposited on the cold surfaces of the tubular reactor, but also can react mutually on the substrate surface located in the hot region inside the tubular oven. Thus, the sp^2 + sp^3 first buffer layer is formed due to the interaction between active carbon species from the gas phase and hot sample surface. This first buffer layer appears very disordered and dehydrogenated due to the low energetic species involved in the growth process. However, the growth conditions facilitate the nucleation of bi-dimensional sp^2 structures (Fig. 4.12a), which block the possibility of 3D growth (only possible with the presence of sp^3 hybridization), being that the growth over the open surface of 2D structures is not possible unless there are defects, which would act as ulterior nucleation centers. Therefore, sp^2 islands (graphene islands) can only grow from their edges (Fig. 4.12b) and, consequently, cover the first buffer layer.

When the entire surface of the substrate becomes covered by sp^2 carbon atoms, due to the absence of crystalline matching compressive strain, nanosheets squeezing one to the other and horizontally graphene growth continuous in vertical direction such as shown in Fig.4.11. Once

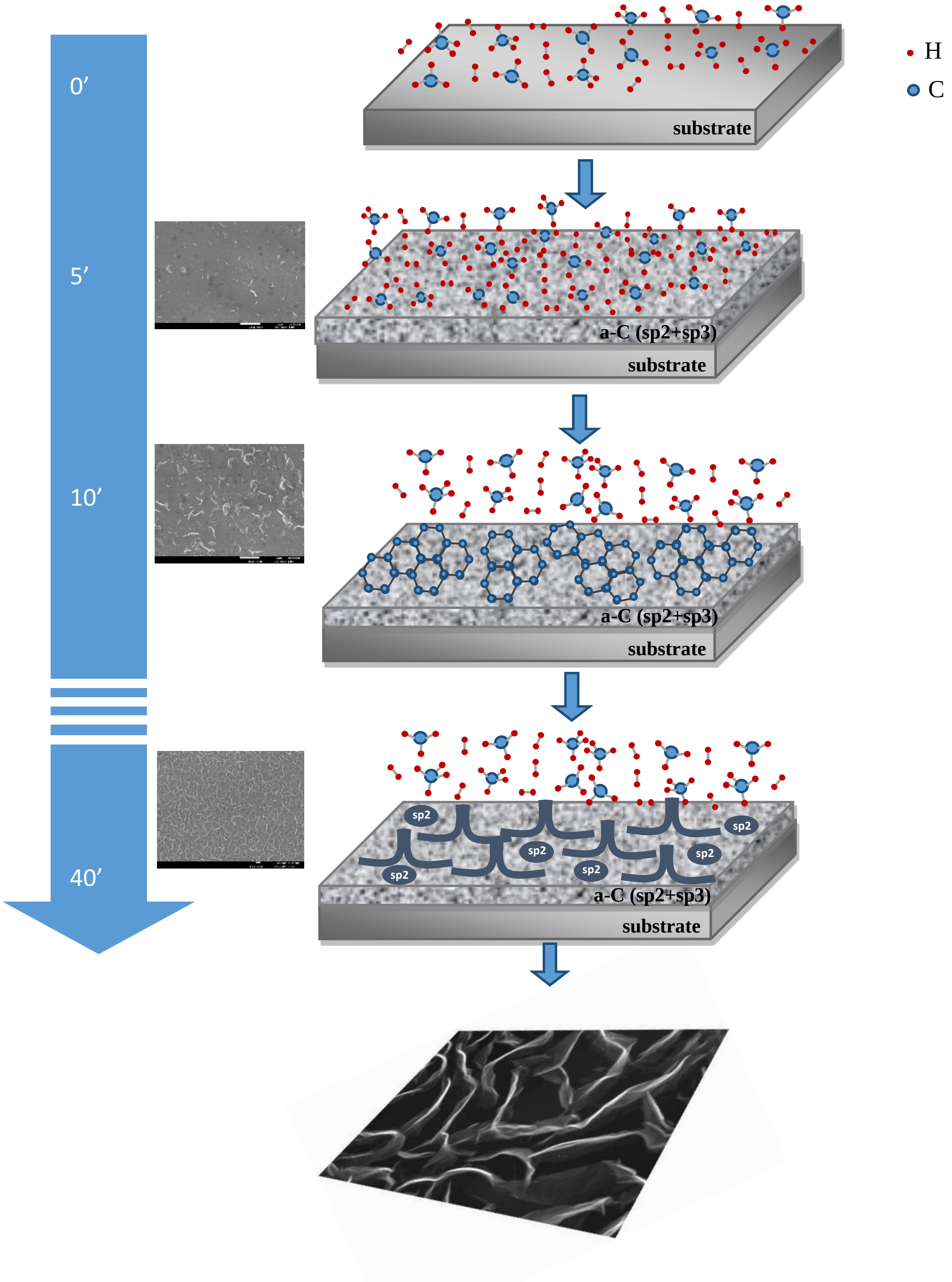

Figure 4.11 Schematic illustration of the seeded growth process of ICP-CVD-grown MLGNWs

oriented vertically, the growth continues in the upward direction, normal to the substrate, due to the open edges of the newly formed nanowalls, as confirmed by the TEM micrograph of the inset image of Fig. 4.12d. The subsequent growth of the nanostructures give place to the formation of vertical MLGNWs, randomly oriented and homogeneously distributed on the substrate (Fig.4.12c).

Another very interesting behavior observed in an ulterior growth step of the carbon nanostructures is an extra nucleation process giving place on the MLMLGNWs. After the vertical alignment, the graphene nanowalls grow in the upward direction for a few minutes, and then the secondary nanowalls formation process begins. The nucleation points of the secondary nanowalls are located on both sides of the nanowalls from which secondary growth occurs (Fig.4.13a). The presence of secondary MLGNWs was confirmed and detailed explained by Krivchenko at al. [Krivchenko, 2013]. They used a configuration of the DC-plasma, which explains the whole process from the point of view of the electric field. In our case, the effect of the electric field is very small or absent. Thus, the appearance of secondary MLGNWs (SMLGNWs) at a certain deposition minute may depend on the geometric structure of the initial nanowalls. It means that, nanowalls growing up after vertical alignment and arriving at certain dimension form nanobags between nanowalls. The carbon radicals of the gas phase penetrate inside and, due to their short residence time, carbon species precipitate on the sides of nanowalls forming nucleation centers from which start the SMLGNWs growth. Secondary nucleation is relatively poor if we consider the low density of defects of MLGNWs and the high mobility of adatoms on the surface of MLGNWs. In addition the hydrogen radicals remain in the nanobags due to their low activity and

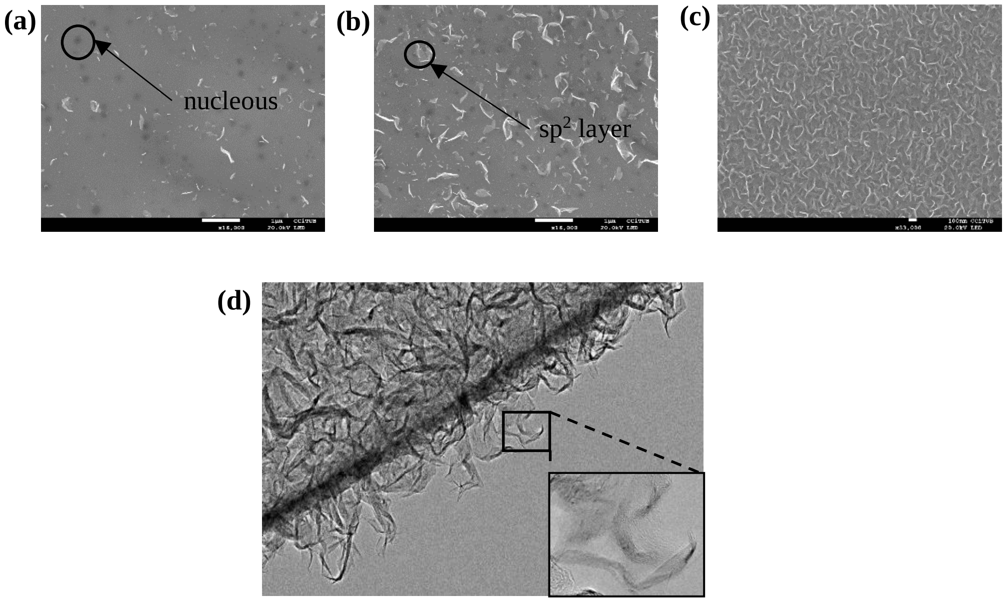

Figure 4.12 SEM images of MLGNWs growth at the first stages of growth: (a) 5 min (17K0701); (b) 10 min (17J0901); (c) final MLGNWs structure (40 min,17J2601); and (d) TEM image of MLGNWs/c-Si (inset image HRTEM) (17G1207)

do not participate in the reactions. Unlike carbon nanotubes, where there is hardly any secondary nucleation on the lateral surfaces, the 2D nature of graphene nano-walls with wider spaces (nanobags) between them makes it easier for carbon species to access on the sides of the nanowalls. That is, it seems that geometry facilitates the formation of nucleation centers that lead to the formation of SMLGNWs. SMLGNWs lead to an increase in the density of the entire grown material, which implies a significant increase in the specific surface. Moreover, the particular conditions of growth of the SMLGNWs facilitate the formation of graphene twining, which is evident in the cross section of the SEM and TEM images (Fig. 4.13b and c). The formation of graphene twins can be the result of an interruption or change in the crystalline lattice, due to its possible deformation by carbon vacancies or an extra carbon atom insertion in the hexagonal carbon rings during the growing process. The TEM analysis suggests that the MLGNWs consists of multilayer graphene. (Fig.4.13c).

Raman analysis provided us information about defects (D-band), in-plane vibration of sp^2 carbon atoms (G-band), as well as the stacking orders (2D-band) and number of layers (Fig.4.14 and Table 4.1). The measurements were carried out at the first stage of growth and after vertical alignment, every 10 minutes of growth. The region between 1200 cm^{-1} and 3200 cm^{-1} includes all main peaks characterizing graphite-like materials [Malard LM, 2009]. Based on spectral

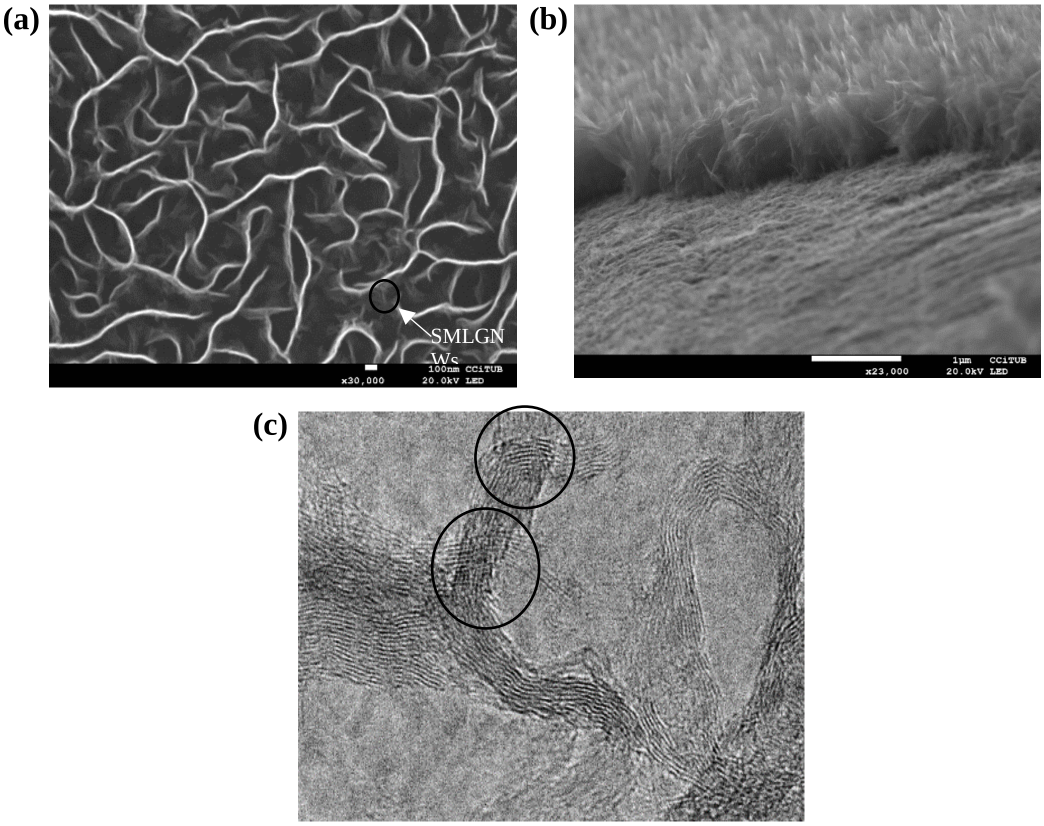

Figure 4.13 SEM image of (a) secondary graphene nanowalls (SMLGNWs); (b) cross-section view of MLGNWs; and (c) TEM image of MLGNWs with crystal twinning (17J2401)

deconvolution, intensity ratios between the main peaks of the samples grown at different deposition times were calculated and summarized in Table 4.1. The observed large D band intensity is due to the presence of disorder, which arises from large amount of edge states, sp^3 bonded C-H species, nanographitic base layer and ion induced defects from the plasma during growth [Ghosh S, 2014]. The analysis of the intensity ratios of D and G peaks (I_D/I_G) at the first stage of growth reveals that, primary nanowall nucleation and growth leads to the formation of defects, which becomes normalized after vertical alignment and repeated during the secondary nucleation and growth of nanowalls after certain minutes of deposition. In addition, Table 4.1 evidence of the multilayer nature of MLGNWs. The ratio of D and D' is independent of the number of defects, but they can point to different types of defects. The $I_D/I_{D'}$ value (~1.3) corresponds to on-site defects, which are described as sp^3- defective graphene and values close to 2.3 correspond to boundary-like defects [Venezuela P, 2011]. On the other hand, the values of the I_G/I_{2D} ratio and FWHM of the 2D peaks for all samples were about 1.7 and 64 cm^{-1} (Table 4.1), respectively, which confirms the multilayer nature of MLGNWs. These values, starting from vertical alignment (after 5 min) to the end of the experiment (40 min), are almost maintained stable. On this way, the MLGNWs from the initial vertical alignment (5 min) to the end of the experiment (40 min) increase in length and height, but the thickness of the walls remains practically stable.

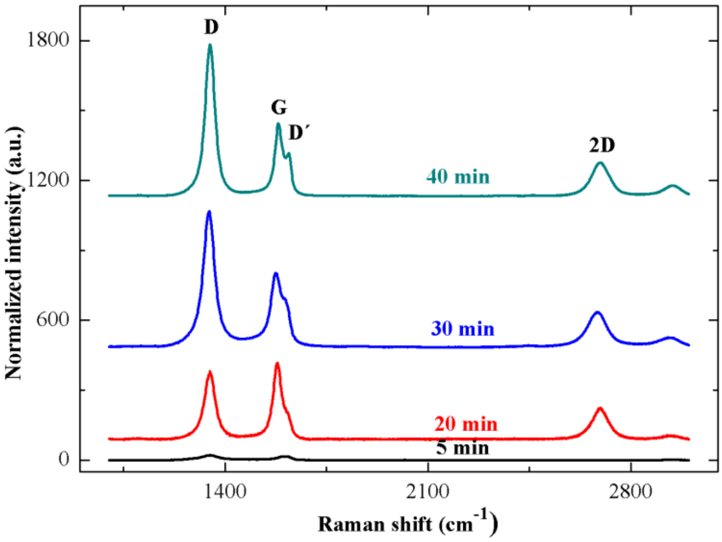

Figure 4.14 Raman spectra of MLGNWs at different deposition time (17K0701, 17G1301, 17G1201, 17J2601)

Table 4.1 Summary of the Raman spectral parameters of the MLGNWs/c-Si at different deposition time

Deposition time (min)	I_D/I_G	$I_D/I_{D'}$	I_G/I_{2D}	**FWHM$_{2D}$ (cm^{-1})**
5	1.4	-	-	-
20	0.9	2.3	1.9	62.4
30	1.2	1.4	1.4	68.1
40	1.7	2.2	1.8	64.2

4.3.3 Conclusion

In this chapter, we have shown that the growth of MLGNWs is a complex process that consists of different stages. The plasma of carbon hydride during ICP-CVD process produces different kind of radicals and active species, which interact with substrate and lead to the nucleation and the consequent growth. In addition, nucleation can occur not only in the first stage of growth but also later, in the vertical alignment of nanowalls and on the vertical structure itself. This stage of secondary nucleation ensures the formation of secondary nanowalls. These SMLGNWs contribute to the increase of the density of the deposited material and to the considerable increase of the specific surface. Also, we have shown the formation of graphene twins crystals in the secondary nucleation stage from the TEM images and the cross-sections observed by SEM. High resolution micrographs confirm once again the crystalline structure of the nanowalls. We believe that the growth model proposed in this thesis can shed light on the understanding of the underlying mechanisms acting in this type of plasma process, which can allow the production of new carbon nanostructures more suitable for future applications.

Part III
Results

Chapter 5

Functional study of tubular reactor for production of multilayer graphene nanowalls

5.1 Functional study of the tubular reactor

5.1.1 Introduction

Carbon nanostructures constitute a numerous set of varied morphologies associated with the also numerous possibilities provided by chemical vapour deposition activated by plasma at low pressure. For more than three decades, during which numerous experiments have been proposed for the synthesis of carbon nanostructures, descriptions of new carbon structures and morphologies have appeared. So, we have micro and nanostructured diamond, amorphous carbon (a-C) and hydrogenated amorphous carbon (a-C:H), diamond like carbon (DLC), carbon nanoparticles, carbon nanotubes (CNT) and carbon nanowires, single and multi-wall carbon nanotubes, graphene and graphene nanostructures, single layer graphene (SLG), few layer graphene (FLG), among others [Sullivan JP, 2000; Robertson J,2002; Paillet M, 2018].

As we have discussed in chapter 1, this extended family of allotropes of carbon has unique and interesting properties such as extreme hardness, ultra-low friction, anti-wear, chemical protection, biocompatibility, low surface energy, very high specific surface, emission by field effect, luminescence, extreme electronic properties (as an example, high and low gap energy, extreme electronic mobility and very high current density) [Falcao EHL, 2007]. Carbon nanostructures also find applications in such fields as, energy, protective materials for metal tools and polymers, chemistry and electrochemistry for catalysts, electrodes for batteries and supercapacitors, high power electric and electronic devices and sensors. Another promising application of the carbon structures is in the area of light emitting and other optoelectronic devices, for doped carbon-based amorphous films, e.g., a-C:H and a-C:N:H films, which can show an outstanding performance such as good light emitting sources [Robertson J, 1986].

More recently, new carbon morphologies, so called carbon nanowalls (CNW), which are associated with technological variations related to the activation of the CVD by high density plasmas, open expectations to new possible applications of carbon nanostructures. In particular, the inductively coupled plasma (ICP) is an easy way for production of remote and high density plasmas ($n_e > 10^{17}$ m^{-3}) [Mackenzie KD, 1999], which enhance the production of carbon species in the gas phase during the deposition process. The description of the reactor used for this doctoral thesis has been described above at §3.2.

5.1.2 Experimental part

Fabrication of vertically oriented carbon nanowalls

One of the main goals of this thesis, after the design and construction of the tubular ICP-CVD reactor, is to find the optimal zone for synthesis of MLGNWs. Carbon structures were synthesized in an inductively coupled plasma chemical vapour deposition (ICP-CVD) (frequency 13.56 MHz, power 440 W) system consisting of: a long quartz tube (100 cm) having an RF resonator (20 cm), for production of remote plasma, and a tubular oven (40 cm) working at up to 1100ºC, 20 cm away around the quartz tube. For exploring the deposited material at the whole length of the tube, we have used a stainless steel (AISI304) ribbon (100 cm long and 4 cm width) (Fig. 5.1). For morphological, chemical and optical analyses, samples were taken from the GNW/SS304 ribbon by cutting with dimensions 5 × 4 cm^2. For each zone different morphologies were obtained, due to the distance from resonator and temperature.

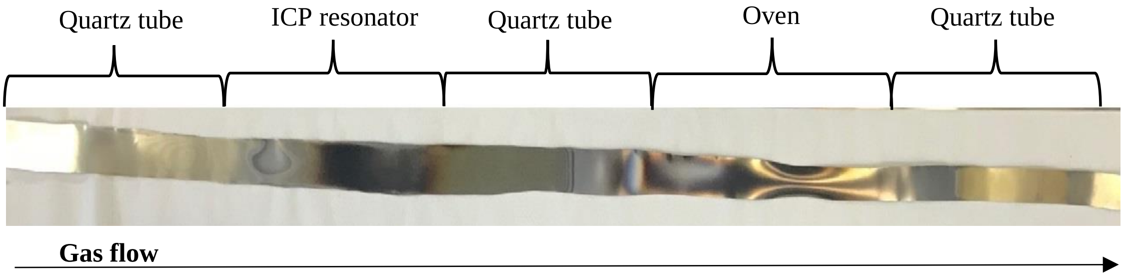

Figure 5.1 Real image of SS304 ribbon with different deposition materials, corresponding on different zone of the reactor (17L2101)

ICP-CVD tubular reactor is composed of four main parts: ICP resonator, oven and 2 border parts of the quartz tube (gas inlet and substrate entrance). Temperature gradient inside the tube is not symmetrical. The temperature variation was measured by a thermocouple-arm. The measured temperature in different parts of the reactor is represented in the Table 5.1. This temperature corresponds to the temperature of the end of the thermocouple, which depends mainly on IR radiation arriving to the thermocouple. The temperature measured by the thermocouple is quite independent of the gas flow because the gas pressure during the process is low (50 Pa). The numbering of the samples was carried out from the zero point, which is on the gas input point, as shown in Fig. 5.1. The constant temperature zone, where the temperature gradient is negligible, is in the middle part of the oven (60-75 cm). Therefore, material grown in this position of the oven has been used for the studies carried out in this thesis.

Table 5.1 Growth temperature, depending on the position of the sample

Distance (cm)	Temperature (°C)	Distance (cm)	Temperature (°C)
5	50	55	748
10	100	60	765
15	150	65	769
20	210	70	765
25	290	75	750
30	350	80	680
35	400	85	587
40	490	90	445
45	570	95	200
50	690	100	50

The temperature profile is different in both ends of the quartz tube, due to the effect of radiative shielding of the resonator positioned near the entrance of the gas (Fig. 5.2).

Prior to synthesis, the substrate was cleaned with acetone, rinsed with deionised-water and dried with nitrogen. The sample was placed inside the quartz tube reactor, which was evacuated to a pressure lower than 1 Pa and heated to 750°C (central part of the 40 cm oven section). A flow rate of 10 sccm of pure methane (99.995%) was introduced as a precursor gas inside the quartz tube. The pumping system was connected through a variable manual conductance valve at the outlet of the quartz tube. Pressure was measured by a capacitance meter and was kept in the range 50-60 Pa. Under these conditions, the plasma was ignited at an RF power of 440 W during 40 min. The ribbon sample was then cooled down to the room temperature for 30 min inside the quartz tube at low pressure conditions.

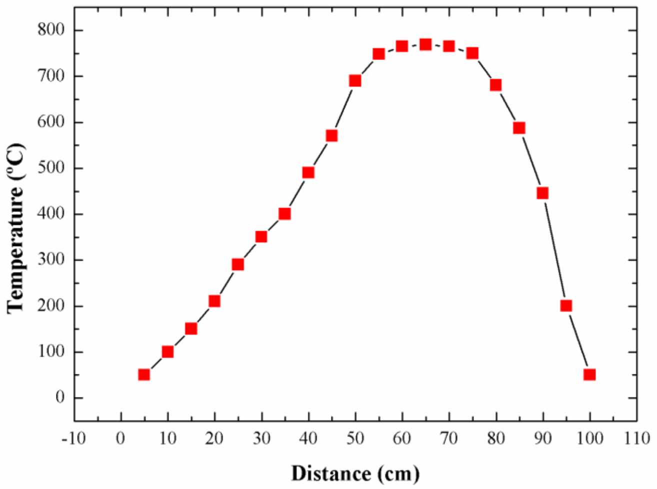

Figure 5.2 Temperature profile of the MLGNWs tubular reactor

Characterization techniques

The chemical reactions inside the tube under plasma deposition were controlled by OES composed of a BLACK-Comet UV-VIS spectrometer and a quartz optical fiber, which is connected to the computer via UV-VIS spectrometer. The spectral range was 300 nm to 800 nm. The OES was connected to the reactor, as shown in Fig. 3.19.

The microstructure and morphology of the grown film were investigated using field emission scanning electron microscopy (SEM), JEOL JSM-7001F, operated at 20 kV, and transmission electron microscopy (TEM), JEOL 1010, operated at 200 kV. The carbon structures were transferred to the TEM grid by simply scratching off from the substrates.

The chemical characteristics of as grown structures were studied by Raman spectroscopy using a microscope HR800 (LabRam) with a 532 nm solid state laser. Also, the chemical characteristics were verified by X-ray photoelectron spectroscopy (XPS) using a PHI ESCA-5500. In addition, the carbon nanostructures grown at different positions and temperatures were studied by using a Thermo SCIENTIFIC NICOLET iZ10 Fourier transform infrared (FTIR) spectrometer with a spectral resolution of 4 cm^{-1}.

The hydrogen and carbon contents in our samples were determined by elemental analysis (EA) using a Thermo EA 1108 CHNS-O Carlo Erba Instruments.

Room-temperature PL spectra were recorded with a chopped Kimmon IK Series He-Cd laser (325 nm and 40 mW). Fluorescence was dispersed through a SpectraPro 2750 (focal length 750 mm) f/9.8 monochromator, detected with a Hamamatsu H8259-02 photomultiplier, and amplified through a Stanford Research Systems SR830 DSP lock-in amplifier. A 360 nm filter was used for filtering the stray light. All spectra were corrected for the response function of the instrumentation.

5.1.3 Results and discussion

Optical Emission spectroscopy

Chemical reactions inside the ICP-CVD reactor were controlled by OES. The measured spectra can be divided in 3 parts: OES spectra in the ICP resonator zone, oven part and cold part (gas inlet and gas outlet) (Fig. 5.3). Radical density is higher in the ICP resonator zone, due to the chemical dissociation of the precursor gas. In methane plasma, the predominant generated species are CH_x molecules and H atoms, which are positioned along the entire length of the quartz tube.

C_2 dimmers, which are found in the middle part of the ICP resonator zone, but they do not appear in a large number of other zones of the quartz tube.

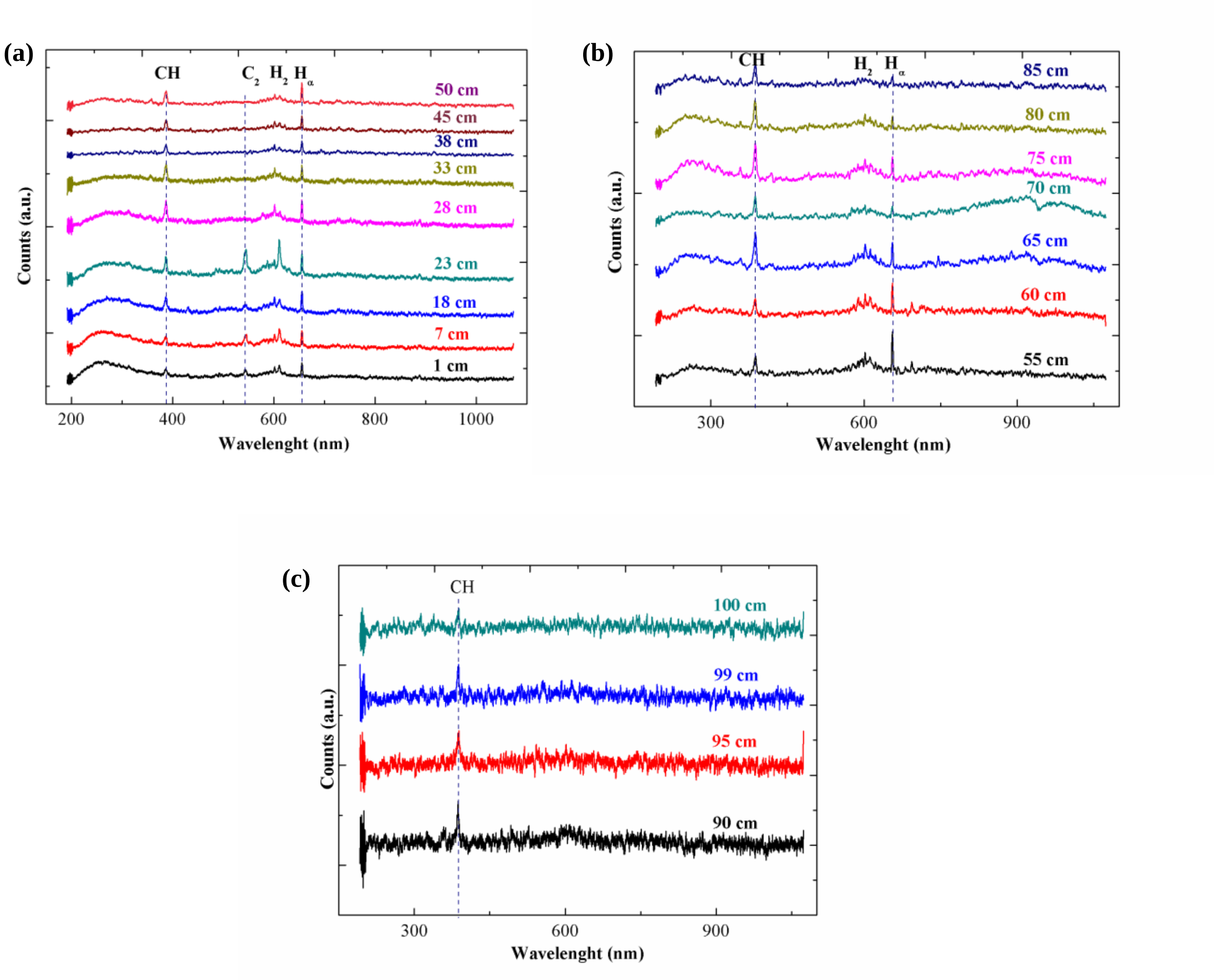

Figure 5.3 Optical emission spectra from the CH_4 methane plasma taken at different reactor zones: a) 1-7cm entrance to resonator, 18-28 cm inside resonator and 33-50 cm resonator exit; b) oven sprectra; c) low temperature zone exiting oven

This could be due to the main part of C_2 dimmers immediately interact with the substrate in the hot zone and are not found in the gas phase (emitting light). CH_4 precursor gas easily converts to CH_x ($x = 1$-3) radicals to produce C_2 through radical recombination and subsequent dissociation according to the following reactions [Bo Z, 2013a; Denysenko IB, 2004]:

$$\mathrm{CH_4 + e^* \rightarrow CH_3 + H + e}$$

$$\mathrm{CH_4 + e^* \rightarrow CH_2 + H_2 + e}$$

$$\mathrm{2CH_4 \xrightarrow{-H_2} C_2H_6 \xrightarrow{-H_2} C_2H_4 \xrightarrow{-H_2} C_2H_2}$$

$$\mathrm{CH_3 + e^* \rightarrow CH + H_2 + e}$$

$$\mathrm{CH_3 + e^* \rightarrow CH_2 + H + e}$$

$$\mathrm{CH_2 + e^* \rightarrow CH + H + e}$$

Higher C_2 radical density facilitates formation of amorphous carbon (a-C) and in case of a high temperature it provides the MLGNWs growth. The low temperature inside the plasma zone provides mainly a-C growth, without MLGNWs synthesis. Inside the oven part, we have a quite stable behaviour for CH radicals, while H_α signal slowly decreases along oven (Fig.5.4). In pure methane plasma, the number of carbon atoms is much smaller than the total number of etchant atoms (H), there are four hydrogen atoms for every carbon atom [Zhu MY, 2007; Kondo S, 2009], hence, the etching monatomic hydrogen density is higher than in other carbon hydride plasmas. When atomic hydrogen reacts with the film surface, it can lead to three elementary reactions [Anthony TR, 1990]:

1) Hydrogen removing from an sp^3 CH_x group to form H_2.
2) Hydrogenation of unsaturated sp and sp^2 hybridized carbon atoms to a sp^3 configuration.
3) Hydrogen induced chemical etching, which is one of the most important reactions for this growth mechanism. The sp^2 clusters or graphitic planes are not etched by atomic hydrogen, due to their high stability, as compared with the sp and sp^3 groups at the edges.

Fig. 5.4 shows the evolution of the CH and atomic hydrogen radicals along of the quartz tube. The relatively high radical density before the resonator zone depends on the backstream effect of CH from the resonator. The resonator zone is the source of generation of radicals and this is the reason of the high radical density as compared with the rest parts of the tube. After ICP resonator, radical density is abruptly dropped and in the middle zone of the furnace is maintained relatively stable.

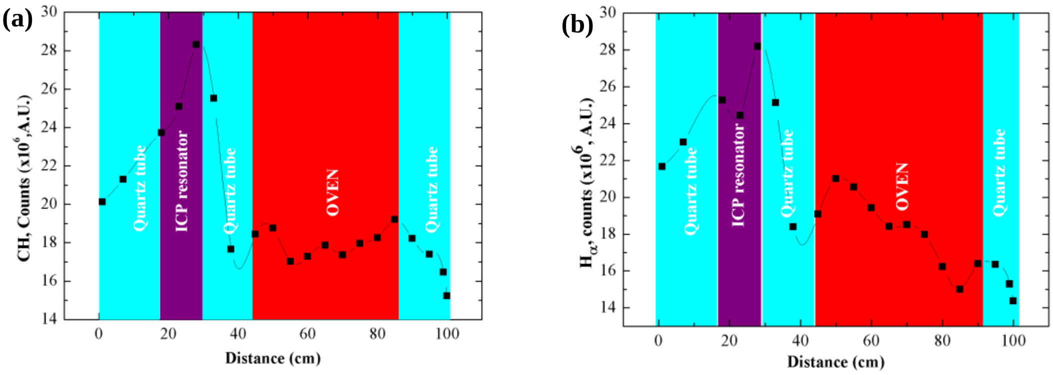

Figure 5.4 (a) CH and (b) H_α radicals dependence on distance from the gas inlet

The decrease of CH density on both ends of tubular oven results from the deposition of hydrogenated carbon species directly on the cold walls of the quartz tube and forming polymer films quite hydrogenated and transparent [Shi B, 2005]. According to Hiramatsu et al., CH radical results from the dissociation reactions of methane and from the hydrogen etching of previously deposited a-C. The mechanism of etching of hydrogen consists of a breaking of the C-C bonds in the gas phase to form CH_X, in our case this gives place to the MLGNWs synthesis through a mechanism of surface migration at high temperature conditions (Fig. 5.5) [Hiramatsu M, 2013]. In the hot part of the tube we have a relatively stable CH behaviour as compared with atomic hydrogen radicals (Fig. 5.4 a and b). The atomic hydrogen decreases from the resonator to the gas outlet, because the formation of molecular hydrogen and the sudden decrease after the resonator can be explained by the deposition of a polymeric film (yellow colour), as we show in Fig. 5.1 in the cold portion of quartz tube between the resonator and the oven.

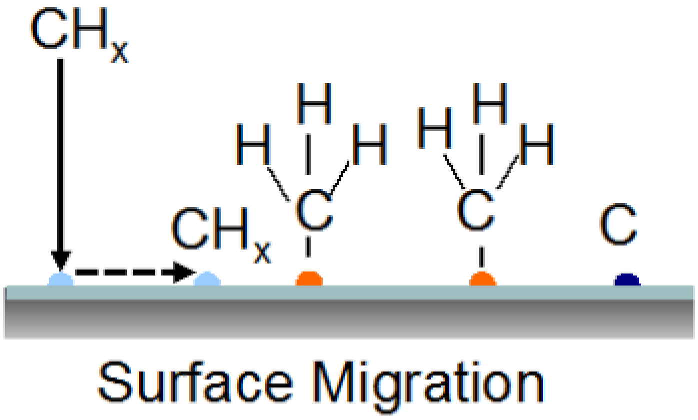

Figure 5.5 Mechanism of Surface migration at high temperature condition [Hiramatsu M, 2013]

Field emission scanning electron microscopy (FE-SEM)

Figure 5.6 shows FE-SEM surface images of the grown carbon microstructure deposited on the SS 304 ribbon at distinct positions and temperatures in the quartz tube. Sample (a) was placed near the entrance of the precursor gas (5 cm), upstream of the resonator, at a temperature 50ºC.

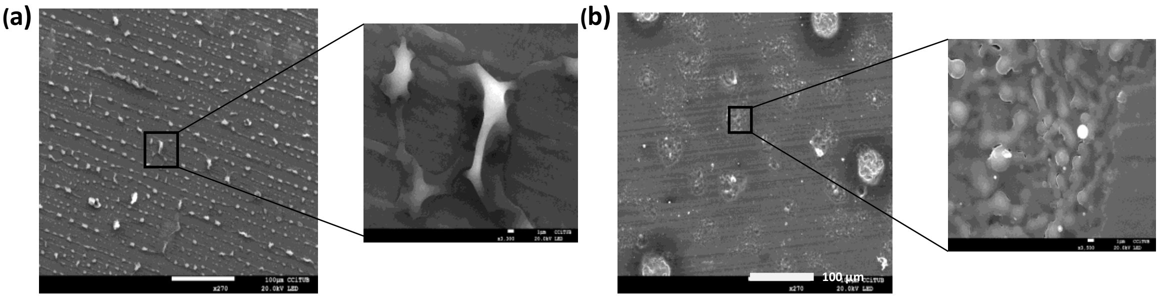

Figure 5.6 FE-SEM images of the carbon microstructures grown at the ends of the quartz tube, outside the oven, at the following growth temperatures and positions from the gas inlet **(a)** 50^{0}C; **(b)** 600^{0}C

Sample (b) was positioned after the oven (85 cm, 600ºC) in a region with a decreasing temperature gradient, downstream of the oven.

Before the carbon deposition, the oven was kept constant at 750^{0}C and, sample (b) at 700ºC during the deposition time (Fig. 5.7) (Table 5.1). The carbon structures deposited on the SS304 ribbon were exposed to very different growth conditions along the quartz tube. The different conditions are affected mainly by the temperature and the plasma characteristics, such as the kind of species and concentration, because they depend on the lifetime of each specie and its residence time, gas parameters (gas temperature, pressure and flow) and the sample position along the quartz tube [Gordiets BF, 2005]. Although the total pressure and gas flow remained constant, the partial pressures of the different gaseous species generated in the plasma (mainly -CH_x, H and H_2, as detected by optical emission spectroscopy) evolved in time and position along the quartz tube. The diversity of growth conditions promotes synthesis of several carbon structures as it can be observed on the FE-SEM micrographs of Figure 5.6 and 5.7, corresponding to carbon structures obtained at both tube ends (50 and 85 cm) and middle (50 and 65 cm) positions of the furnace, respectively. Micrographs of Figure 5.7 show nanometric size in contrast with the micrometric structures in Figure 5.6. In this way, the hot zone of the quartz tube, in the middle of the furnace, is the position of growth of vertically oriented carbon nanostructures.

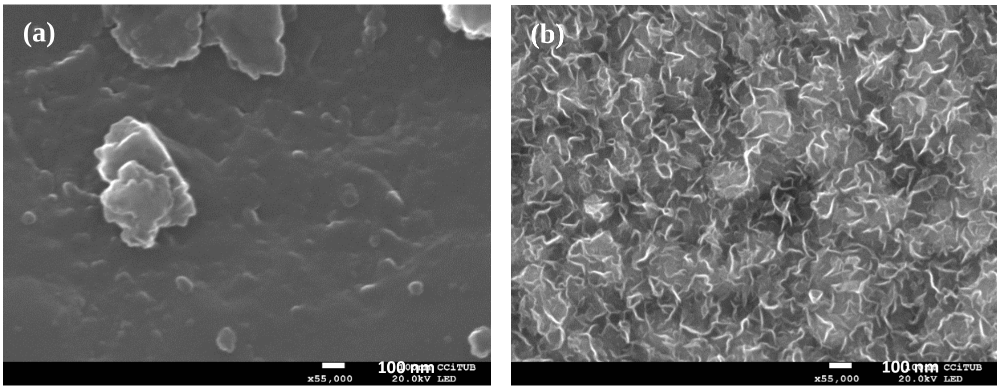

Figure 5.7 FE-SEM images of the carbon nanostructures grown at the extreme oven entrance and middle oven, at the following growth temperatures and positions: **(a)** 700^{0}C; **(b)** 750^{0}C

Raman spectroscopy

Raman spectroscopy was used to evaluate the quality of the carbon structures grown by ICP-CVD. Fig. 5.8 shows the Raman shift of the samples grown at different positions and at different temperatures. For the relatively low temperatures, the growth material provides a strong photoluminescence response on the Raman shift spectra (Fig. 5.8a and d). Therefore, these samples were analysed by PL spectroscopy and the results will be discussed later.

A general list and plot of the Raman peaks of crystalline vertical carbon nanostructures, adjusted by a Lorentzian-Gaussian function (Fig.5.9), is shown in Table 5.2 corresponding to samples of Fig. 5.8b. The presence of the small peak (D+G) at 2940 cm^{-1} is related to sp^2 CH stretching vibrations [Ni Z, 2008].

Fig. 5.8b shows the Raman shift of the samples grown inside the oven at the relatively high temperature zone. For these structures, Raman shift consists of three main peaks D, G and 2D cantered at 1346 cm^{-1}, 1587 cm^{-1} and 2700 cm^{-1} respectively (Table 5.2). Also, close to the G peak, a shoulder appears at 1616 cm^{-1} (D´ peak), which is associated with finite size of graphite crystals and graphene edges [Hiramatsu M, 2004]. The existence of the 2D peak (2700 cm^{-1}) (Fig. 5.8b) confirms the presence of nanostructured graphene on samples. The presence of the small peak (D+G) at 2940 cm^{-1} is related to sp^2 CH stretching vibrations [Ni Z, 2008]. The strong and sharp D and D´ peaks suggest a crystallinity increase of the carbon nanostructure and a high number of graphene edges and defects, which are prevalent features of multilayer graphene

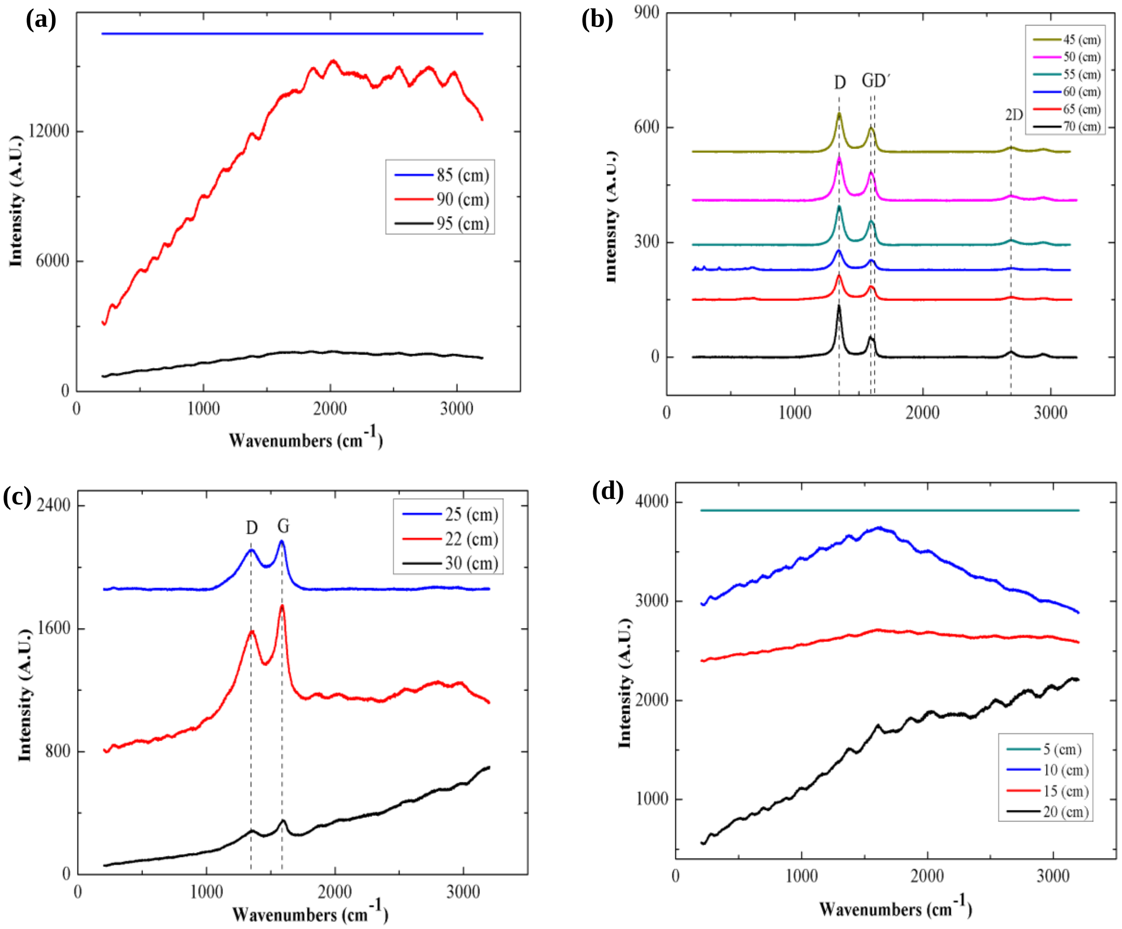

Figure 5.8 Raman spectra of MLGNWs/SS304 at a different part of the quartz tube (a) sample entrance; (b) oven; (c) ICP resonator and; (d) gas inlet. In order to compare signals between the different spectra, the background has been kept

nanowalls. The magnitude and nature of disorder produced inside the oven, changes with the sample position. These differences can be associated with the temperature and plasma density. Figure 5.10 evidences that, inside the oven we have two zones, near and far from ICP resonator. The I_D/I_G ratio, associated with disordered sites, is 2.1 near the resonator and it increases up to 2.8 in the opposite side of the oven. The number of defects near the ICP is lower, because the carbon nanostructures are ¨purified¨ by H etching from methane plasma. As we have seen previously, the density of hydrogen atoms (Fig. 5.4), within the furnace, decreases as we move away from the ICP resonator, and for this reason the effect of hydrogen purification is reduced. The reduction of grain size is related to the decrement of the etchant species, because of the diminution of the H atoms. Calculation of grain size (L_a) of graphene can be represented according to the following equation:

$$L_a\,(nm) = C(\lambda) * (I_D/I_G)^{-1} \qquad (5.1)$$

where $C(\lambda)$ is a constant calculated as a (2.4×10^{-10}) λ^4, where λ is a excitation laser wavelength [Porter DA,1992].

The Raman technique provides the nature of defects formed in the different parts of the quartz tube. According to the resonant Raman scattering theory, the intensity of defect bands (I_D, $I_{D'}$) does not only depend on the amount of defects but also on the type of defects associated with it. According to the classification of the nature of defects reported by Eckman et al., $I_D/I_{D'}$ =13 indicates the presence of sp^3 related defects, and similarly, $I_D/I_{D'}$ =10.5 corresponds to hopping defects, $I_D/I_{D'}$ =7 for vacancy-like defects, 3.5 for boundary-like defects and 1.3 represents the on-site defects in graphene [Venezuela P, 2011; Eckmann A, 2012].

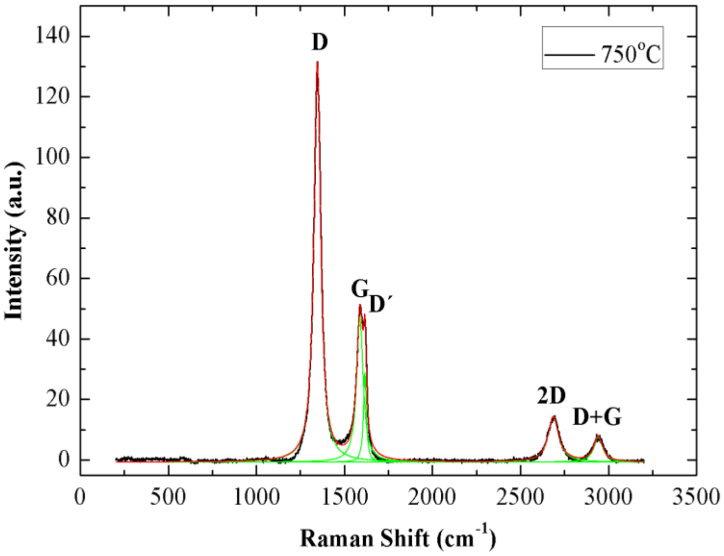

Figure 5.9 Deconvoluted Raman spectrum of vertical carbon nanostructures growth at 750^{0}C

The measured $I_D/I_{D'}$ ratio at different positions ranges from 16.2 to 4.7. Inside the oven we have a wide variety of defects: sp^3 related defects, hopping defects, vacancy like defects and boundary-like defects. Then, these defects are associated to the different plasma conditions and temperature in each position. A general list and plot of the Raman peaks of crystalline vertical carbon nanostructures, adjusted by a Lorentzian-Gaussian function (Fig.5.9), is shown in Table 5.2 corresponding to samples of Fig. 5.8b.

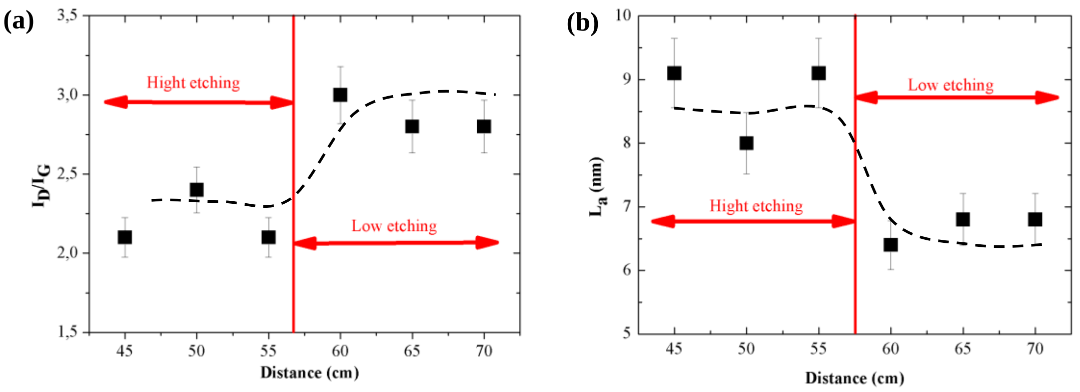

Figure 5.10 (a) I_D/I_G and (b) crystallite size respecting to the distance from ICP resonator . The data were plotted as means with standard deviation error bars

Fig.5.8c shows the Raman shift of the samples growth inside the ICP coil antenna, where a large number of active species compared with the rest of the tubular reactor, according to the high intensity of the azimuthal electric field induced by the RF signal, producing high level of ionization and dissociation. However, a crystalline carbon nanostructure is not observed due to the moderate temperature on the quartz walls. For this zone, the Raman shift shows typical amorphous carbon behaviour.

Transmission electron microscopy (TEM)

TEM analysis was performed to evidence the difference in the morphology of the carbon structures. Fig. 5.11 shows TEM images of carbon structures grown in different positions. The nanostructured carbon sample is made up of multiple layers of graphene sheets stacked together,

Table 5.2 Summary of the Raman spectral parameters of the MLGNWs/SS304 in different tube zones. Peak positions, relative intensities of D, G, D´ and 2D bands, I_D/ I_G and $I_D/I_{D'}$ rations, crystallite size. Each band was analyzed by fitting with a Lorentzian line.

Distance (cm)	**ω_D (cm^{-1})**	**$\omega_{D'}$ (cm^{-1})**	**ω_G (cm^{-1})**	**ω_{2D} (cm^{-1})**	**I_D (a.u.)**	**I_G (a.u.)**	**I_{2D} (a.u.)**	**$I_{D'}$ (a.u.)**	**I_D/ I_G**	**$I_D/I_{D'}$**	**L_a (nm)**
45	1344.7	1618.2	1595.3	2689.6	110.4	52.3	8.8	7.6	2.1	14.5	9.1
50	1344.7	1619.6	1591.7	2687.9	188.9	77.9	22.6	19.3	2.4	9.8	8.3
55	1344.4	1618.5	1595.7	2690.3	119.7	58	8.7	7.4	2.1	16.2	9.1
60	1344.4	1610.7	1588.5	2690.5	103.5	34.3	7.2	22.3	3.2	4.7	6.4
65	1344.3	1620.8	1592.7	2685.2	63.4	22.5	5.3	6.6	2.8	9.6	6.8
70	1347.2	1619.1	1596.4	2691.8	50.9	18	1.9	6.5	2.8	7.8	6.8

as shown in Fig.5.11d. High resolution TEM image in Fig. 5.11d shows slightly curved graphene nanosheets composing a vertical nanostructure. This bending could be attributed to the internal stress induced by the boundary defects, as confirmed by the high value of the $I_D/I_{D'}$ ratio, although we have not observed a significant shift of peak G with this type of stress.

These random oriented vertical carbon nanostructures (Fig. 5.7b) have a high crystallinity along with a huge number of defects, such as evidenced by Raman spectroscopy (Fig. 5.8b) and TEM images (Fig. 5.11d). TEM images for the rest of the samples (Fig. 5.11a, b and c) show the amorphous nature of the synthesized material, as confirmed by selected area electron diffraction.

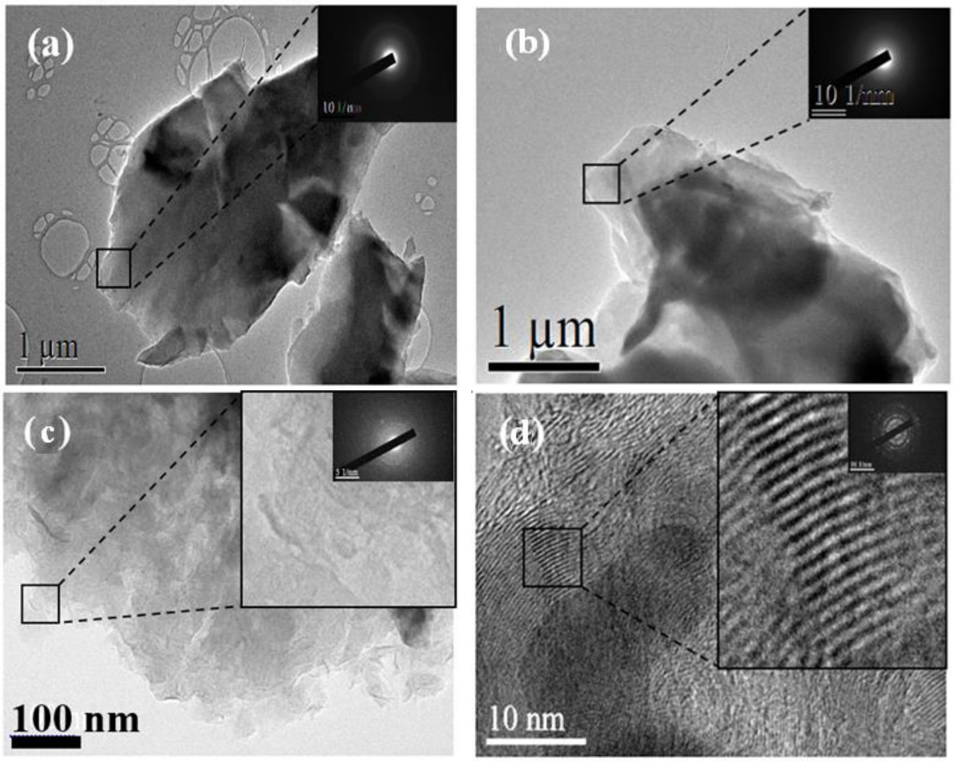

Figure 5.11 TEM images of carbon microstructures and nanostructures grown on a SS304 ribbon at different temperatures (a) 50^0 C; (b) 600^0 C; (c) 700^0 and (d) 750^0 C. The insets show the SAED patterns of carbon structures in each case.

X-ray photoelectron spectroscopy analysis (XPS)

The chemical state of carbon structures has been examined by XPS (Fig. 5.12). The C1s XPS spectra of the samples grown in different positions are shown in Fig. 5.13 Curve fitting of the C1s spectra was performed using a Gaussian-Lorentzian peak shape. XPS spectral peaks were decomposed into multiple components, whose areas are detailed in Table 5.4. The carbon bonds and corresponding bind energies are sp^2 C=C (284.3 eV) and sp^3 C–C (285 eV). The results of XPS analysis of the vertical nanostructures (750ºC) evidence a mixture of sp^2 and sp^3 bonds

(Fig. 5.13c). This mixture was not detected in samples located in the rest of the tube at lower temperatures, in which the sp^3 carbon peak mainly appears. It seems that, the growth of vertically standing carbon nanostructures appears associated to the presence of sp^2 and sp^3 bonds. The presence of sp^2 at the middle part of the oven could explain the formation of the graphene nanowalls. In addition, XPS analysis evidences the presence of carbides only on samples outside the oven. These compounds are related to the reaction of carbon precursors with metals contained

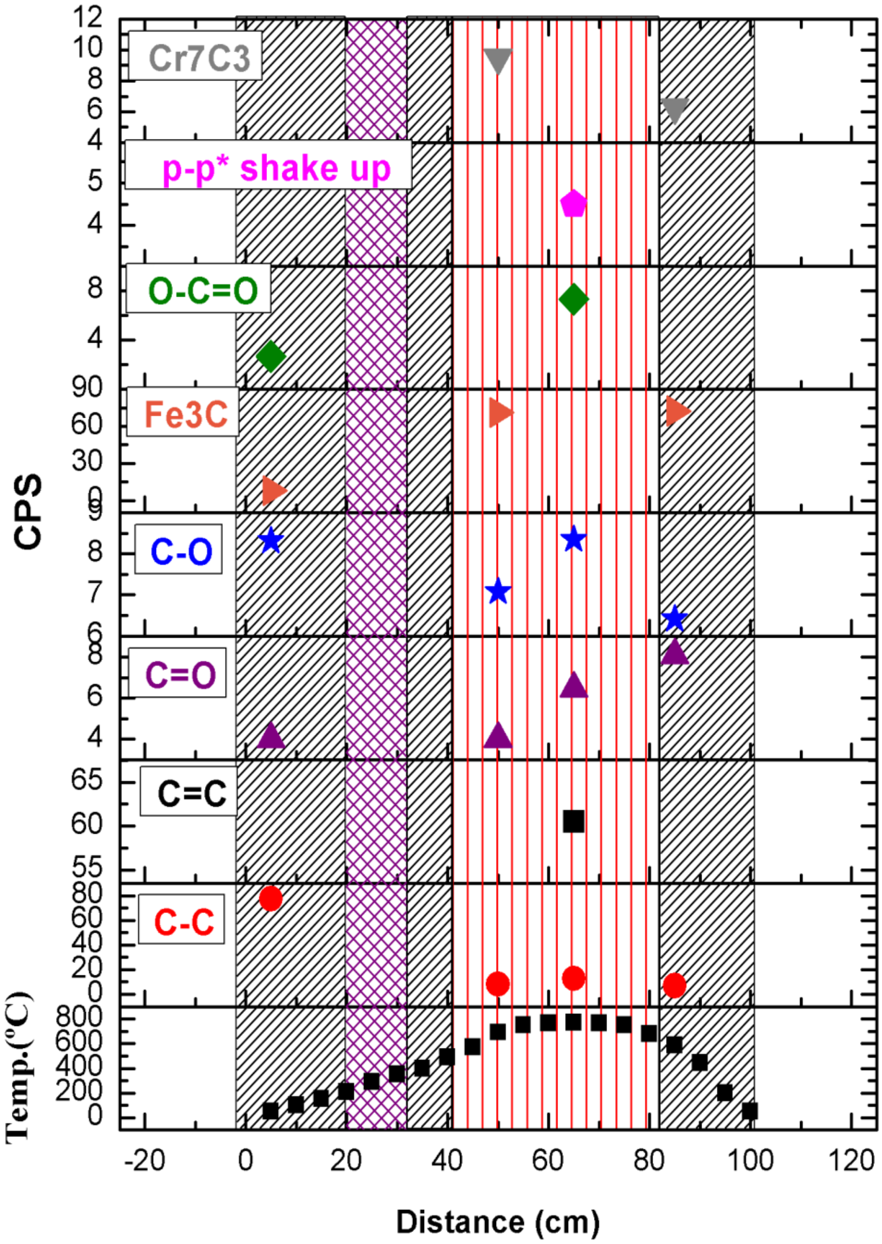

Figure 5.12 Intensity of different Carbon bonds depending on distance from gas entrance

in SS304 (Fe (~70%), Cr (18%)). The absence of carbides from the samples inside the tubular oven may be related to the growth of carbon structures that would hide the first layers of carbides close to the substrate.

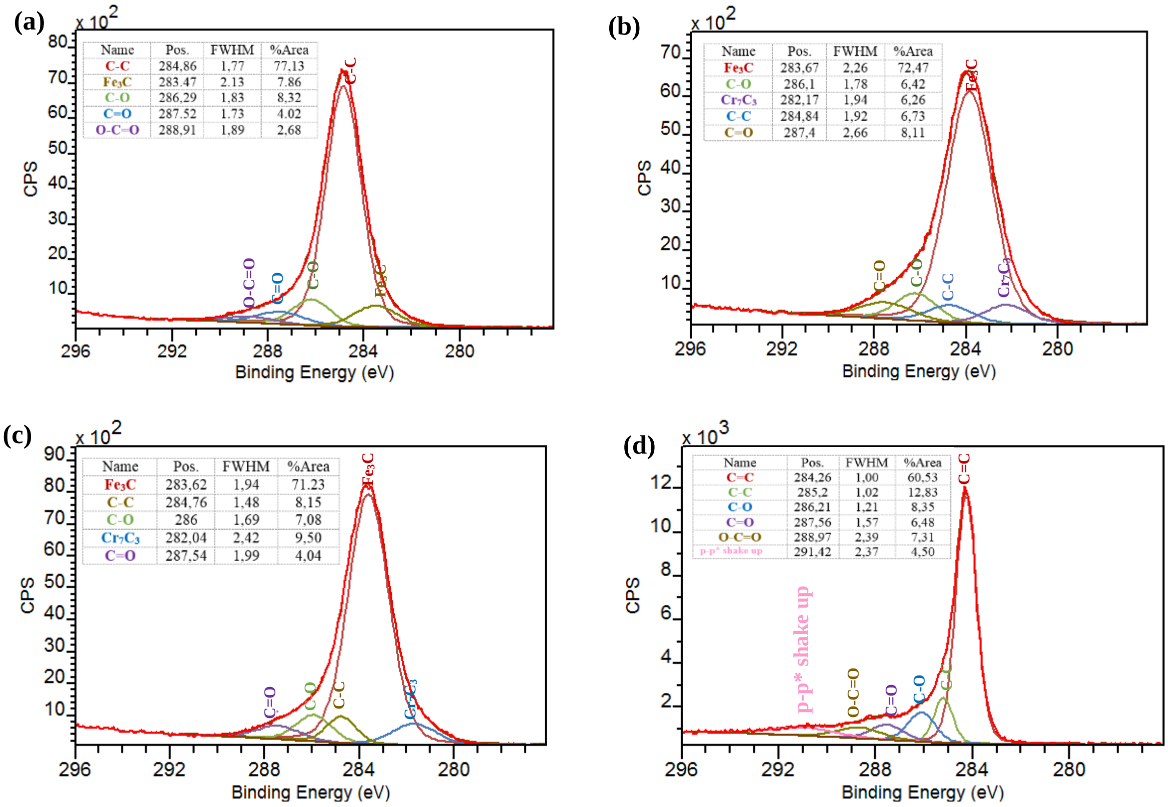

(a)

Name	Pos.	FWHM	%Area
C-C	284,86	1,77	77,13
Fe_3C	283.47	2.13	7.86
C-O	286,29	1,83	8,32
C=O	287.52	1.73	4.02
O-C=O	288,91	1,89	2,68

(b)

Name	Pos.	FWHM	%Area
Fe_3C	283,67	2,26	72,47
C-O	286,1	1,78	6,42
Cr_7C_3	282,17	1,94	6,26
C-C	284,84	1,92	6,73
C=O	287,4	2,66	8,11

(c)

Name	Pos.	FWHM	%Area
Fe_3C	283,62	1,94	71.23
C-C	284,76	1,48	8,15
C-O	286	1,69	7,08
Cr_7C_3	282,04	2,42	9,50
C=O	287,54	1,99	4,04

(d)

Name	Pos.	FWHM	%Area
C=C	284,26	1,00	60,53
C-C	285,2	1,02	12,83
C-O	286,21	1,21	8,35
C=O	287,56	1,57	6,48
O-C=O	288,97	2,39	7,31
p-p* shake up	291,42	2,37	4,50

Figure 5.13 XPS spectra of carbon nanostructure (GNWs) and carbon microstructure grown at different temperatures (positions) (a) 50^0 C; (b) 600^0 C; (c) 700ºC; (d) 750ºC

Table 5.3 Percentage area of the different bonds obtained from the XPS C1s spectra of carbon micro and nanostructures grown at different temperatures

T (ºC)	C=C (eV)	C-C (eV)	Cr_7C_3 (eV)	C=O (eV)	O-C=O (eV)	C-O (eV)	Fe_3C (eV)	π-π* shake up (eV)
50	-	287.76	-	287.52	288.91	286.29	283.47	-
600	-	284.84	282.17	287.4	-	286.1	283.67	-
700	-	284.76	282.04	287.54	-	286	283.62	-
750	284.26	285.2	-	287.56	288.97	286.21	-	291.42

Peaks corresponding to the binding energies of C-O (286.1 eV) are also observed at less intensity and C=O (287.5 eV) is an evidence of an adventitious contamination with oxygen of some of the samples [Delgado JC, 2008; Jackson ST, 1995], after extraction from the quartz tube, due to the reaction with ambient oxygen and moisture at a room temperature (Table 5.3). The peak corresponding to O-C=O (289 eV) binding energy appears on samples with high porosity (50ºC) or high specific surface (750ºC).

Fourier transform infrared spectroscopy analysis (FTIR)

Infrared spectral data analysis of the carboxyl functional group of carbon structures grown by ICP-CVD is presented in Fig. 5.14. The carbon nanostructured sample grown at 750ºC shows a high absorption in all the studied spectral range. This high absorption did not allow to detect the specific vibrations corresponding to different carbon bonds, such as the ones presented below. The rest of samples show a broad peak centred at 3442 cm^{-1} ascribed to the O-H stretching vibration of the adsorbed water from ambient moisture [Balachandran M, 2012]. The presence of the C=O bond detected by XPS is confirmed by FTIR in the stretch oscillation at ~1700 cm^{-1}. The peaks at 2923 and 2846 cm^{-1} correspond to the CH_2 asymmetric stretching vibration and the CH_3 symmetric stretching vibration, respectively [Balachandran M, 2012]. The other broad-band in the range 1000–1300 cm^{-1} usually corresponds to a complex absorption band of the IR spectrum, and it can be assigned to C–C and C-H plane deformation of aromatic groups, according to Santamaria et al. [Santamaria A, 2010].

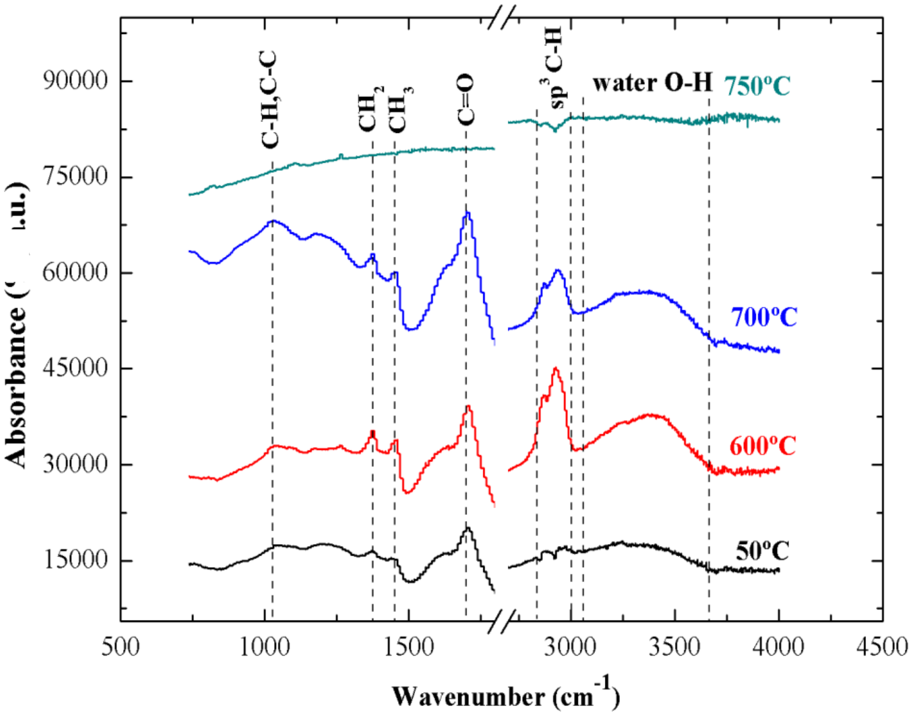

Figure 5.14 FTIR spectra of carbon nanostructure and microstructure grown at different temperature (position)

HCNS elemental analysis

In order to evaluate the hydrogen and carbon contents we used elemental analysis. Hydrogen content resulted to be up to 19 times higher for materials grown at relatively low temperatures (50ºC to 700ºC) in comparison with the sample of the high-temperature zone (750ºC) (Table 5.4).

Table 5.4 Carbon and hydrogen contents of the carbon structures grown at low and high temperature ranges, measured by Elemental Analysis

Temperature range	C (%)	H (%)
Low (50-700ºC)	69.5	7.8
High (750ºC)	93.6	0.4

Photoluminescence

Photoluminescent carbon dots including graphene dots have received considerable interests due to their excellent photoluminescent properties and promising applications [Hola K, 2014; Zhu Z, 2016]. Nevertheless, the physical mechanisms of photoluminescence (PL) emission from carbon based amorphous films measured at different temperatures are not clearly understood. Although it is commonly accepted that the PL emission from amorphous carbon films originates from the radiative recombination of electrons and holes in the band tail states of sp^2 carbon clusters [Robertson J, 1996], there is no consensus on the dominant mechanisms of photoluminescence at different temperatures. Recently, it has been found that carbon nanotip structures with a modest hydrogen and nitrogen incorporation can also generate PL [Wang BB, 2011]. In addition, photoluminescence of oxygen, sulphur, and nitrogen containing nanoporous carbons was detected in the visible range and can open the new route for their applications as sensors and drug delivery carries [Bandosz TJ, 2014].

Figure 5.15 shows the PL spectra of carbon structures grown at different conditions during a single experiment. The PL plot shows high PL spectra for samples growth at relatively low temperatures with negligible shift one relatively another other, besides the MLGNWs samples grow in the high temperature zone, where the PL emission is very weak. Thus, we investigated PL properties just for 4 samples located at different parts of the reactor (Fig. 5.16). A broad emission band in the visible range from 450 to 750 nm is observed. The PL emission spectra of our samples are composed of green (560-520 nm) and red (700-635 nm) bands. According to Henley et al. [Henley SJ, 2004], the PL intensity of samples containing H (from the possible atmospheric contamination with water) is at least 4 times higher than the H-free samples. In all

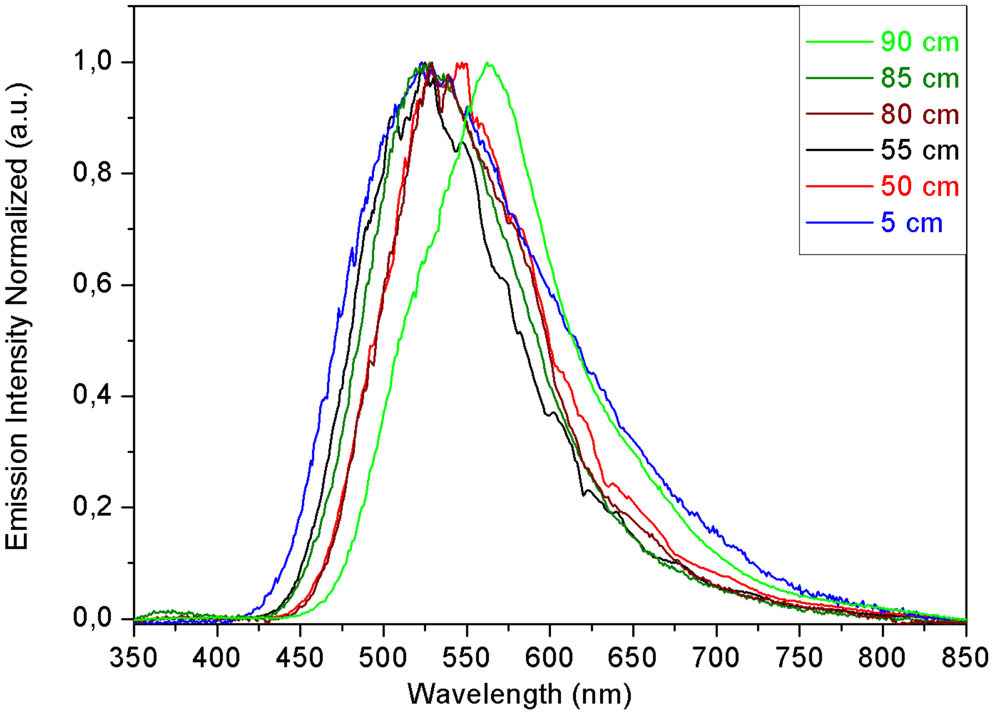

Figure 5.15 PL spectra of carbon structures grown at different temperatures and located at distinct positions within the tubular reactor

our carbon structures grown at relatively low temperatures, the PL efficiency increased several orders of magnitude. These results seem to indicate the possible main role of hydrogen in the emission of PL from structured carbon. However, the samples were contaminated when exposed to the atmosphere, and a water (O-H) absorption band in the FTIR spectra, centred at 3442 cm^{-1}, appears for all the samples showing a high PL emission (Fig. 5.16). A probable reaction because of water contamination could be the replacement of C-H with C-OH, with the release of H_2. This reaction would reduce the C-H content of samples and, consequently, the PL efficiency. Also, we have considered the possible reaction of O_2 and water (air contamination) with the dangling bonds of carbon nanostructures of the sample grown at 750ºC. The results shown at Fig. 6c point to the formation of very few C-OH bonds (probably from surface dangling bonds) for the high temperature sample, and no C-H bonds presence from FTIR (Fig. 5.14), which is associated to as very low PL emission (Fig. 5.16) of this sample. Despite the presence of oxygen detected in the samples due to exposure to the atmosphere, it seems that this is not the origin of the observed PL, as discussed below. All these results seem to confirm that the hydrogen's role contained in the

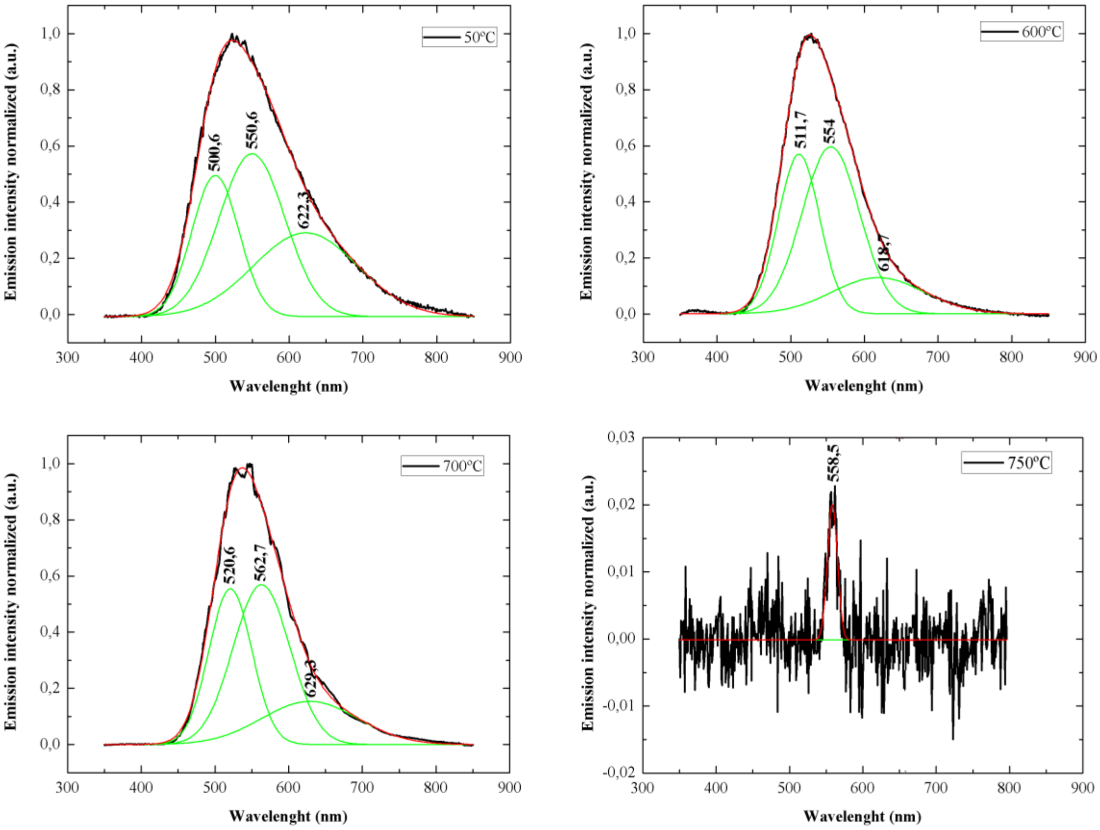

Figure 5.16 PL spectra of carbon structures grown at different temperatures and located at distinct positions within the tubular reactor. The spectrum corresponding to the emission of PL of the sample grown at 750ºC has not been normalized due to its very low emission and considerable noise. This sample, which barely has hydrogen, has more than one order of magnitude less emission as compared with the other PL spectra, which correspond to samples with hydrogen

carbon structures is rather associated with hydrogen coming from CH_4 plasma and more unlikely from the absorbed water after exposure to air [Fanchini G, 2003].

The presence of oxygen in the sample is associated with the reaction with H_2O that displaces the H from C-H and with the reaction of O_2 with dangling carbon-bonds. Photoluminescence (PL) in amorphous carbon, seems to occur due to the radiative recombination of electrons and holes in the band-tail states created by sp^2 rich clusters [Henley SJ, 2004; Tuinstra F, 1970]. The PL spectra for these zones show that photons are emitted in the visible range with the peaks centred at ~ 500 nm (2.5 eV), ~ 520 nm (2.4 eV, green), ~ 560 (2.2 eV, green), ~ 620 nm (2.0 eV) and ~ 630 nm (1.97 eV, red).

In accordance with the results obtained by Iwano et al. [Iwano Y, 2008], the energy higher than 2 eV can generate the transition between the π^* and π bands, or the transition between the σ^* band and the valence band formed by defects, while the transition between the π^* band and the valence band formed by defects occurs for energies lower than or equal to 2eV. For relatively high temperature zone (700ºC) the PL spectra indicate that, the energy difference of π^* and π states is ~2–2.4 eV, although the optical gap is lower than 1 eV for carbon materials [Schwan J, 1997]. Although the PL spectra are very poor from nanostructured carbon nanowalls, they present a single peak at 558.5 nm associated with the transition between the σ^* band and the valence band, formed by the defects [Fanchini G, 2003] as detected by Raman. This result is confirmed because in vertical carbon structures, defects such as dangling bonds of graphene nanowalls play a role of quenching PL [Wang BB, 2012; Casiraghi C, 2005]. In addition, single PL spectra for carbon nanowalls show very narrow shape and low FWHM at 558 nm, as compared with other structures, which are associated with high crystallinity of vertical carbon (Tab. 5.5). Moreover, the narrow band gap of thick MLGNWs reduces the PL efficiency [Wang BB, 2012a].

Table 5.5 Full width of half maximum of PL spectra centered at ~ 560 nm

T(ºC)	FWHM$_{\Delta E}$ (meV)	Structure
50	367	Microstructured carbon
600	315	Microstructured carbon
700	302	Nanostructured carbon
750	54	Carbon nanowalls

The detailed analysis of the carbon structures grown at different conditions during the same experiment, suggests that these varied PL emission bands can be related to the H content coming from CH_4 plasma. The results of this work show the diversity of carbon structures obtained, with very varied PL properties that critically depend not only on the temperature but also on other conditions such as the composition of the gas and density of species in each position. To obtain particular structures it will be necessary an accurate control of the technological parameters of the plasma. The ICP-CVD provides diverse structures having a high PL efficiency. In addition, the carbon structures grown at relatively low temperatures with high PL efficiency can promote development of a simplified technology for producing optoelectronic devices. On the other hand, non-doped nanostructured carbon nanowalls, having poor PL emission, open a new way for easily doping during the gas phase (N_2, NH_3, H_2O, H_2) to enhance PL emission that, can be useful for diverse optoelectronic applications.

5.1.4 Conclusion of functional study of tubular reactor along the entire length

Non-doped sp^2/sp^3 carbon based structures produced by ICP-CVD show a bright visible photoluminescence. The technology to grow them has singular characteristics like, high plasma density (n_e ~10^{11} - 10^{12} m^{-3}) and low energetic $–CH_x$ species (< 10 eV). Furthermore, the technological conditions ($–CH_x$ supersaturation and relatively low temperature, from RT to 700ºC) allow production of a significant variety of morphologies and structures, some of them having PL properties. The study of the PL properties associated to the morphologies obtained in one single experiment by using ICP-CVD has provided diverse results showing that, the origin of PL is associated to the micro and nanostructures containing H. The PL measurements provided a bright and very broad emission band in the visible range from 450 to 750 nm, at room temperature, for samples grown at temperatures between 50ºC and 700ºC. FTIR spectroscopy and XPS analysis of these samples evidenced the presence of oxygen (probably from a post-oxidation of the carbon structures) C-O=C and C=O and a high hydrogen content under the form of -CH, $-CH_n$ and carbon bonds C-C, C=C. In contrast, the carbon nanostructures grown at the highest temperature (750ºC), show different characteristics: (1) presence of nanowalls with boundary like defects (from Raman spectrum), (2) high crystallinity (from TEM images and SAED), (3) very low hydrogen and oxygen contents, as confirmed by FTIR spectroscopy and (4) poor photoluminescence. The detailed analysis of the carbon structures grown at different conditions during the same experiment, suggests that these varied PL emission bands can be related to the H content coming from CH_4 plasma. The results of the tube study show the diversity of carbon structures obtained, with very varied PL properties that critically depend not only on the temperature but also on other conditions such as the composition of the gas and density of species in each position of the quartz tube reactor. In order to obtain particular structures, we accurately had to control the technological parameters of the plasma. In addition, the carbon structures grown at relatively low temperatures with high PL efficiency can promote development of a simplified technology for producing optoelectronic devices. On the other hand, the non-doped nanostructured carbon nanowalls having poor PL emission, open a new way for easily doping during the gas phase (N_2, NH_3, H_2O, H_2) to enhance PL emission that, can be useful for diverse optoelectronic applications.

5.2 The transversal position study of MLGNWs

FE-SEM

As we saw above, the MLGNWs deposition process takes place in the hot zone of a quartz tube. The diameter of the tube is 4cm, which is the maximum length of the sample that can be loaded. A sample with a width of 4 cm, touching the walls of the quartz tube, changes the morphology (height and density) in two extremes, as shown in Fig. 5.17. The SEM images were taken from different parts of the same substrate, which was placed directly on the quartz tube, without substrate holder. It is obvious that, the growth rate would vary from one side to the other due to the distance from the tube. This variation can depend on thermophoretic forces near the quartz tube. The sense of the force is opposite to the temperature gradient [Fotiadis DI, 1990]. Thermophoresis is a phenomenon, which causes small particles to be driven away from a hot surface and towards a cold one. In our case a quartz tube serves as a hot surface.

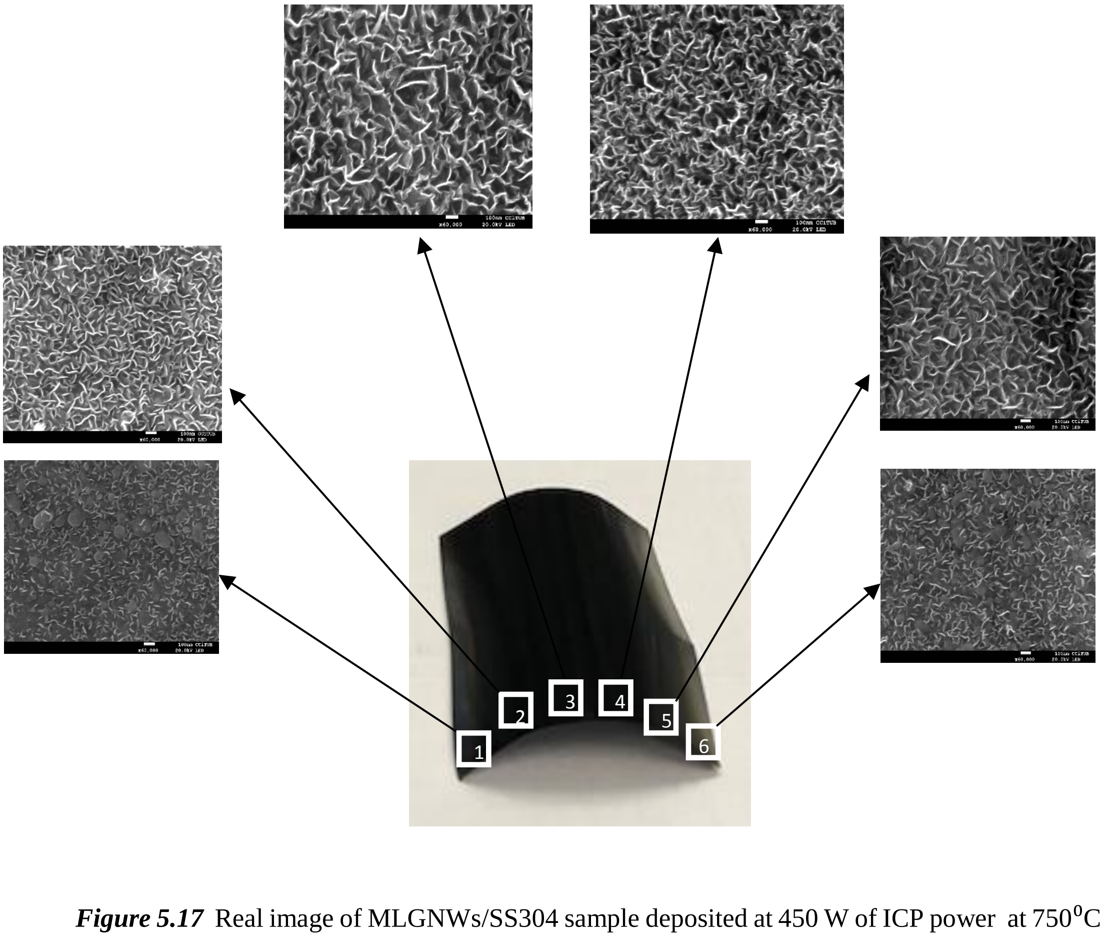

Figure 5.17 Real image of MLGNWs/SS304 sample deposited at 450 W of ICP power at 750^0C of tubular ICPCVD and corresponding magnified SEM images of a sample showing variation of growth rate and morphology with distance from the tube (17L1901)

Two external parts of the substrate, having touched the quartz tube reduce the deposition rate due to the thermophoretic forces between the quartz tube and the sample, and the morphology in these parts varies accordingly. Fig. 5.17 shows a relative decrease in the growth rate of the film with decreasing distance from the tube wall. The homogeneous MLGNWs films were obtained in the middle part of the substrate. The corresponding morphologies of the sample are shown in the magnified images of Fig. 5.17. MLGNWs are formed with high deposition rate in the middle part of the substrate, as distinct from the border parts of the sample.

Raman scattering

For structural characterization, we performed an analysis of Raman scattering of different parts of the substrate (Fig. 5.18). We have analysed the abundance and nature of defects formed during the evolutionary growth of MLGNWs depending on the quartz tube wall distance. The I_D/I_G ratio, which is related to the crystal imperfection of a graphene sheet, varies from 2 to 2.3. This value indicates a higher number of defects if compared to thermal CVD, which is typical for plasma grown nanostructures [Venezuela P, 2011], probably due to hydrogen etching. According to the resonant Raman scattering theory, the intensity of defect bands (I_D, $I_{D'}$) depends on the amount of defects. The ratio of $I_D/I_{D'}$ provides information about the type of defects present in the material and makes the possibility to classify them [Venezuela P, 2011; Eckmann A, 2012]. The $I_D/I_{D'}$ ratio is found between 4.6 and 5.4, which may indicate the presence of boundary-like defects in

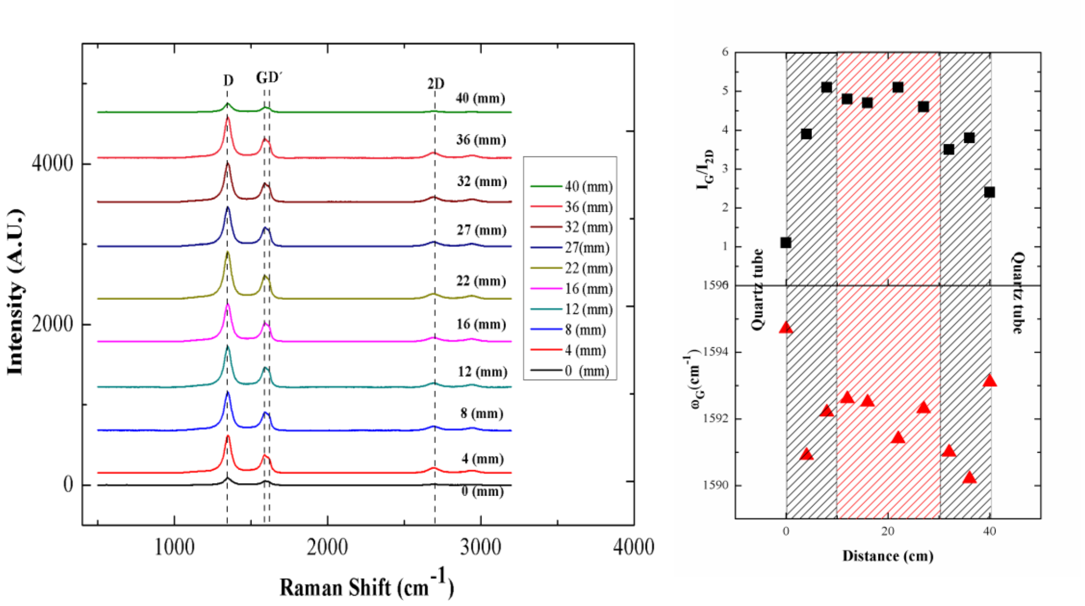

(b)

(a)

Figure 5.18 (a) Raman shift of MLGNWs / SS304 at different distances from the tube; (b) D, G and I_G/I_{2D} position vs tube distance

MLGNWs. Table 5.6 suggests that type of defects of samples located at different distances from the walls of the quartz tube is the same. The significant D-band indicates the high amount of defects in the material and its intensity is directly proportional to the level of defects in the sample. In accordance with the results listed in Table 5.6 high defective nanostructure is in the middle part of the substrate, compared with both ends (Fig. 5.18b), which could depend on high density (edges) in the middle part of the substrate. However, the number of graphene layers varies greatly depending on the position on the same sample. These values of the FWHM of 2D and I_G/I_{2D} evidenced this variation (Tab.5.6b, Fig. 5.18b), which could depend on the low deposition rate at the extremes of the sample. Moreover, the observed position and predictable behaviour of G band and I_G/I_{2D} ratio help to determine the layer thickness as it is highly sensitive to the number of layers present in the sample (Fig. 5.18b). The I_G/I_{2D} ratio change from 5.1 (multilayer graphene) to 1.1 (few-layer graphene) by passing from the middle to the extreme part of the substrate.

Table 5.6 Summary of the Raman spectral parameters of the MLGNWs/SS304 at different tube distances.

(a)

Distance (cm)	ω_D (cm^{-1})	**FWHM**$_D$ (cm^{-1})	ω_G (cm^{-1})	**FWHM**$_G$ (cm^{-1})	$\omega_{D'}$ (cm^{-1})	**FWHM**$_{D'}$ (cm^{-1})	ω_{2D} (cm^{-1})	**FWHM**$_{2D}$ (cm^{-1})
0	1350.1	52.2	1594.7	49	1622.1	24.2	2696.3	69.8
4	1348.8	46.9	1590.9	49.2	1620.3	22	2691.7	69
8	1347.8	48.3	1592.2	48.4	1619.6	22.3	2688.9	73.6
12	1348	50	1592.6	46.2	1619.9	22.4	2690	77.2
16	1348.2	47.5	1592.5	47.2	1619.6	20.3	2690.7	81.7
22	1347.7	50.5	1591.4	48.1	1619.2	22.7	2688.6	70.1
27	1348.4	48.7	1592.3	44.8	1620.2	22.3	2689.1	75.2
32	1348.4	48.4	1591	43.7	1620.2	21.5	2691.2	77.2
36	1348.8	47.3	1590.2	47.5	1619.8	22.5	2690.8	74.6
40	1350.4	50.4	1593.1	48.3	1619.9	24.2	2693.1	79.4

(b)

Distance (cm)	I_D (a.u.)	I_G (a.u.)	$I_{D'}$ (a.u.)	I_{2D} (a.u.)	$I_D/I_{D'}$	I_D/I_G	I_G/I_{2D}
0	77	38	15	33.8	5.1	2	1.1
4	388	189.2	75.7	48.2	5.1	2	3.9
8	391.7	192	76.4	37.4	5.1	2	5.1
12	425.9	194.8	81.1	40.6	5.2	2.2	4.8
16	374	183.3	69.6	39.1	5.4	2	4.7
22	503	236.6	92.8	45.2	5.4	2.1	5.1
27	407	184.2	81.5	40.6	4.9	2.2	4.6
32	411.4	179.5	86.9	50.4	4.7	2.3	3.5
36	422.5	206.7	87.7	54.9	4.8	2	3.8
40	87.7	50	18.8	20.5	4.6	1.7	2.4

Contact angle

The wetting of nanomaterials is a characteristic playing a critical role in material processing. The contact angle measurements of MLGNWs, grown at different distance from the tube wall, were carried out for checking wettability properties in different parts of the same substrate. We observed that, the contact angle notably changes from one side to the other (Fig.5.19). The static contact angle of water droplets was measured by placing a droplet of deionized water (1μl) on the surface of the MLGNWs/SS304 sample as shown in Fig.5.19. We observed a general high hydrophobicity for the MLGNWs grown by ICP-CVD. The contact angle of our MLGNWs (central part of the sample) (θ~126^0) is higher than the contact angle of planar graphene obtained by Shih C. et al. ($30^0<\theta<90^0$) [Shih C, 2012]. The graphene consists of a two-dimensional honeycomb lattice and the attraction of the non-polar lattice to the water molecules is weaker than the binding energy among water molecules [Corbella Roca, 2005]. Wettability could be influenced by chemical composition, geometric structure, or both [Jacob MV, 2015]. In our case,

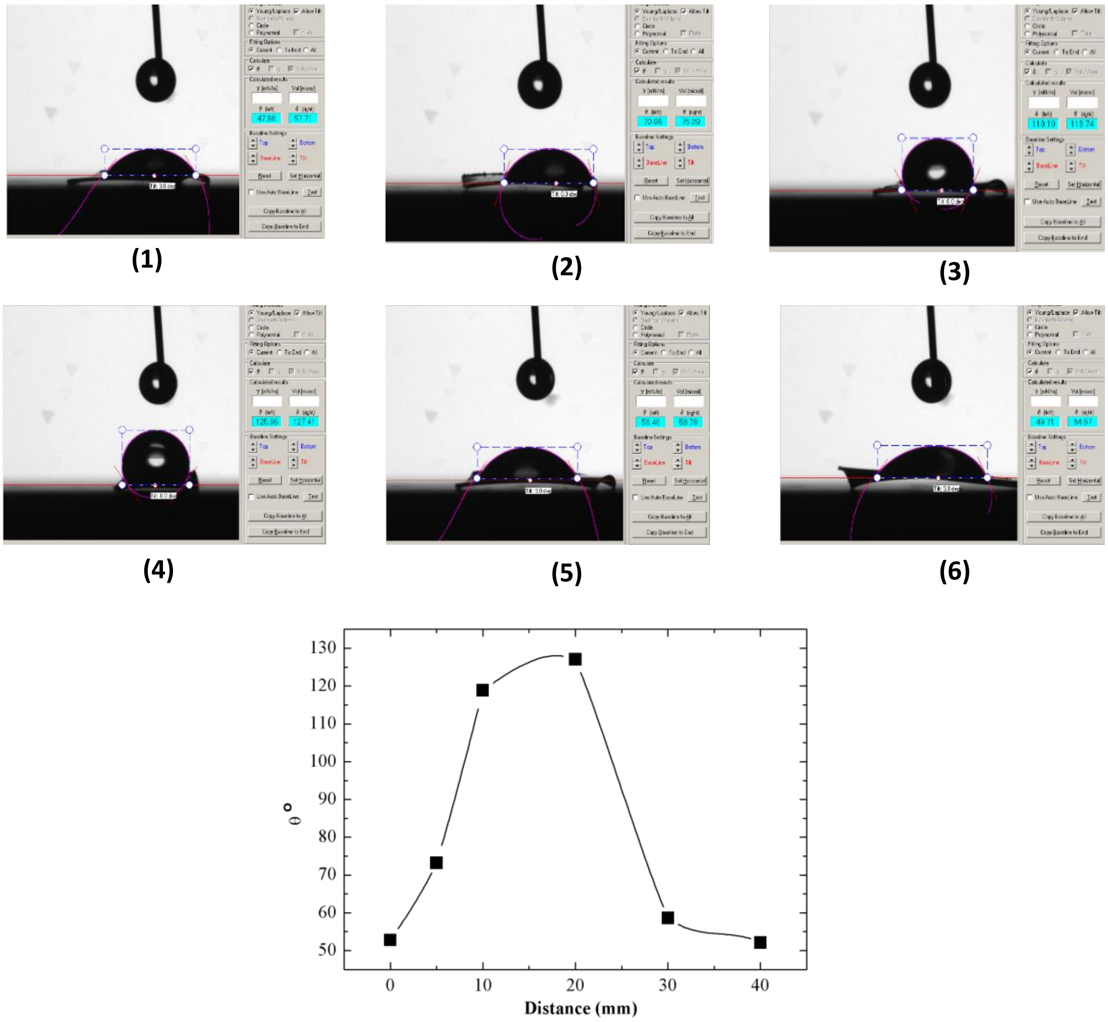
(1)

(2)

(3)

(4)

(5)

(6)

Figure 5.19 Captured images of the water droplet on the surfaces of MLGNWs/SS304 sample for different parts of the same substrate (17L1901) samples with vertical nanowalls show poor wettability, which seems to depend mainly on the geometric structure of MLGNWs and hence the effect of the vertical orientation of multilayer graphene. Wettability properties, as morphological properties, vary from one side to the other (Fig. 5.19), which seems point to a dependence with the density and the dimensions of the nanowalls. Contact angle measurements show a high hydrophobicity in the middle part and a moderate hydrophilicity in the two ends of the sample. This contrast can be due to the influence of the metallic nature of the substrate in the extreme parts of the sample, where the amount of the deposited carbon is poor. The roughness effect in conjunction with the surface chemistry of the MLGNWs is highly hydrophobic. Fig. 5.19 shows the results of the contact angle measurements for different parts of the same sample.

Figure 5.20 MLGNWs/SS304 rolled sample (18A0801)

Overall, depending on the distance from the tube, the internal walls notably change the wettability. We observed that, increasing density of MLGNWs wettability decreased. Using surface rolling method (Fig. 5.20), which is possible for flexible substrates, such as Cu foil, Papyex® graphite and SS304, we can decrease the thermophoretic effect between hot quartz tube and the two extremes of the sample and obtain homogeneity film of MLGNWs with contact angle

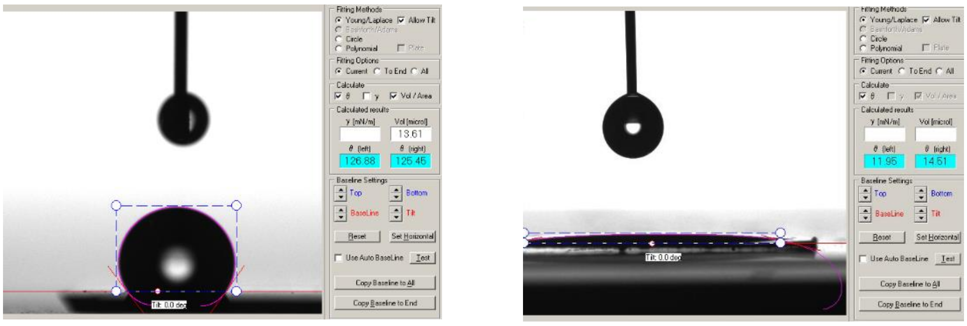

Fitting Methods: ● Young/Laplace ☑ Allow Tilt
Fitting Options: ● Current
Calculate: ☑ θ ☐ γ ☑ Vol / Area
Calculated results: γ [mN/m]: ; Vol [microl]: 13.61; θ (left): 126.88; θ (right): 125.45
☐ Use Auto BaseLine

Fitting Methods: ● Young/Laplace ☑ Allow Tilt
Fitting Options: ● Current
Calculate: ☑ θ ☐ γ ☑ Vol / Area
Calculated results: γ [mN/m]: ; Vol [microl]: ; θ (left): 11.95; θ (right): 14.61
☐ Use Auto BaseLine

(a) **(b)**

Figure 5.21 Captured images of the water droplet on the surfaces of MLGNWs/SS304 (a)without post treatment (17K2201); (b) with 15sec O_2 plasma post treatment(17K2202)

120^{0} ±5^{0} . Depending on the applications area hydrophobicity can be useful properties (bio applications).

The contact angle of water droplets on MLGNWs markedly decreases from 126.1 to 26.4° with the oxygen plasma post-treatment. This indicates the superhydrophobic and superhydrophilic transition of MLGNWs surfaces. After 20 s of oxygen plasma, morphological changes were practically not detected. MLGMNW for electronic applications and for performing electrochemical analysis requires hydrophilicity, which can be achieved with short oxygen plasma post-treatment (Fig. 5.21).

From the structural and morphological characteristics of MLGNW grown on SS304, we have seen that it is impossible to ensure uniformity across the entire width of the substrate by loading relatively wide samples (40mm). Accordingly, for further analysis, we used samples with a width of 30 mm.

Chapter 6

Effects of different parameters on MLGNWs growth

Effects of various parameters on MLGNWs growth

Plasma deposition is a complex process with a large number of parameters, which play a crucial role in MLGNWs growth. Radical behaviour (evolution) and chemical reactions between active species and substrate depend on temperature, substrate material, deposition time, gas flow, plasma power and substrate position. In this chapter, we will discuss one by one the parameters that may influence MLGNWs growth.

6.1 Substrate material influence on MLGNWs growth

6.1.1 Introduction

MLGNWs can be grown on any type of substrates without catalyst as long as the substrate can sustain the growth temperature, which is typically between 600-800°C [Wu YH, 2004; Wang JJ, 2004]. Among the several deposition techniques for synthesizing MLGNWs films, ICP-CVD is one of the most promising techniques because of its potential for low temperature synthesis. Plasma growth of graphene provides a rich chemical environment, including a mixture of radicals, molecules and ions from a simple hydrogen-hydrocarbon feedstock thus allowing for lower deposition temperatures and faster growth [Hiramatsu M, 2013; Li M, 2016]. As we saw in chapter 3, the MLGNWs initial growth contains at least two nucleation stages. The first nucleation provides a buffer layer formation, which is one of the main prerequisites for getting a good quality MLGNWs with significant growth rate. This first buffer layer usually contains a high number of defects like amorphous carbon, which depend on the substrate material. After the formation of the first buffer layer, secondary nucleation and vertical alignment of graphene nano-sheets occurs, which is similar for all types of substrates. A slight change in some of the processing parameters (gas composition, precursor gas flow, temperature, pressure and plasma power) can alter the first nucleation process, but has no effect on the second nucleation.

6.1.2 Experimental part

For this study, MLGNWs were grown on various substrates using a plasma remote ICP-CVD tubular reactor. As a substrate material we used c-Si, SS304, Papyex® (graphite paper) and Cu foil. To clean substrates we first used sonication in an isopropyl alcohol solution and rinsed with de-ionized water, followed by drying with nitrogen gas. After cleaning, these substrates were placed into the centre of quartz tube using a thermocouple-arm and molybdenum holder. The furnace was heated to 750°C under a base pressure of 50 Pa and 10 sccm of precursor methane gas, which was introduced into the chamber before connecting the RF power (I_{RF}) of 440 W. The MLGNWs growth was kept for 40 minutes.

A scanning electron microscope operating at 20 kV was used for imaging and studying the morphology of the vertical graphene. Transmission electron microscopy characterization and selected area electron diffraction (SAED) patterns of MLGNWs were conducted using a HRTEM JEOL 2100 microscope (200 kV). The samples were also investigated on Raman microscope (excitation wavelength of 532 nm) an exposure time of 10 s per single spectrum was used with 10 accumulated acquisitions per each point. Crystallographic orientation, lattice mismatch and order parameter, for various samples were determined by using grazing-incidence X-ray diffraction (GIXD).

6.1.3 Results and discussion

FE-SEM

Figure 6.1 shows SEM images of the initial growth stages of MLGNWs, with duration 5 min, on different substrates under the same conditions. SEM images during the first minutes of deposition evidence that nucleation time is different for different substrates. In order to check the influence of the substrate roughness on the nucleation stage and future growth, we measured it by SensoScan 2300 confocal microscope (Table 6.1). Moreover, the most imperfect and rougher surface was observed in Papyex® graphite. Imperfections and defects in a surface decrease the energy barrier for nucleation, which reduces the critical size of the nuclei (Fig. 6.2) and increases the nucleation density. For c-Si, with very few surface defects, the nucleation is low and its density is small compared with the other substrates. Moreover, the catalytic nature of the substrate can play a crucial role in the growth. This is the case, for example, of SS304 substrate, where multiple nucleation appears (Figure 6.2c). In agreement with the growth mechanism of MLGNWs, for low nucleation density leads to the formation of a continuous a-C (sp^2+sp^3 of low density) buffer layer.

Table 6.1. Average roughness of MLGNWs grown on different substrate materials, MLGNWs average height, L_{wall}, and nucleus density, D_{nucl}

Substrate	**Average roughness (nm)**	**L_{wall} (nm)**	**D_{nucl} ($\times 10^{14}$ m^{-2})**
c-Si	2,2±0,11	315±15	0.335±0,0187
Cu	9,4±0,47	520±26	1.61±0,39
SS 304	3,4±0,17	650±32	4.200±0,302
Papyex® Gr	43,5±2,17	473±23	0.875±0.135 (measured in a crystalline domain)

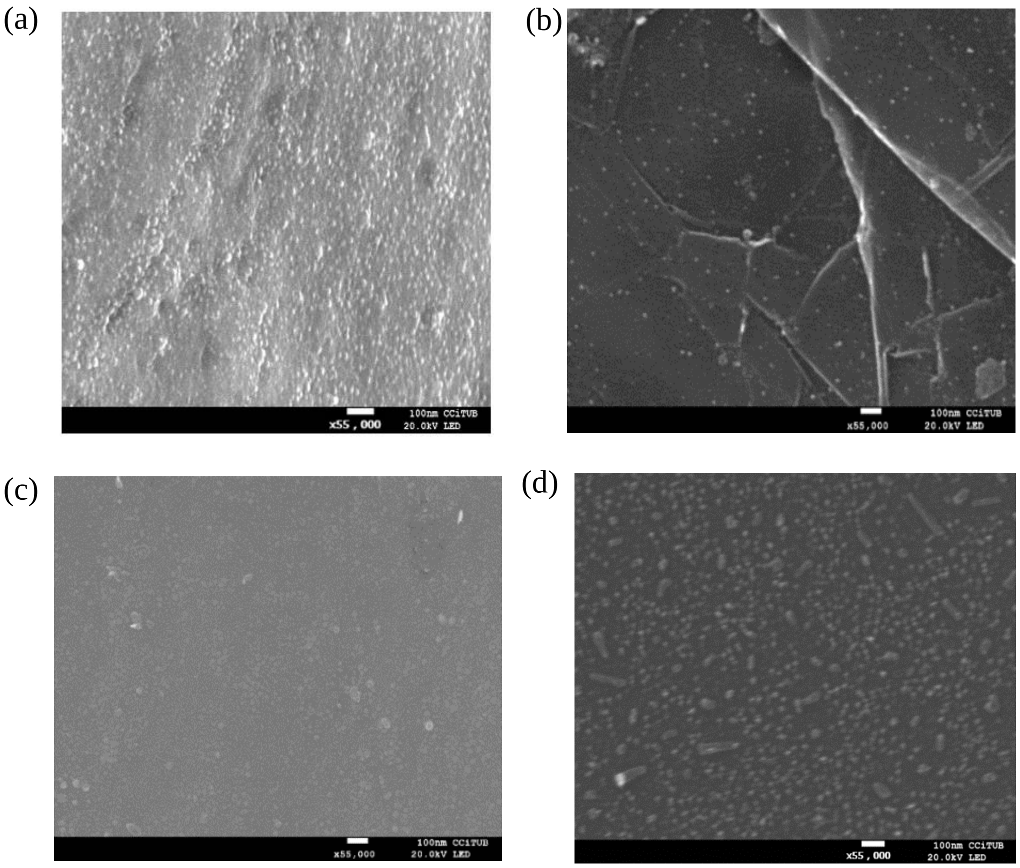

Figure 6.1 SEM images of the nucleation stages of MLGNWs grown on different substrates: (a) SS 304; (b) Papyex® graphite; (c) Cu foil and (d) c-Si **(**18B2202**)**

Samples (SS304) with a high density nucleus contribute to a rapid formation of a buffer layer and, accordingly, a high growth rate. In case of the sparse nucleus (c-Si and Papyex®) this process occurs more slowly. By repeating the same experiment, but prolonging deposition time to 40 min we obtained MLGNWs over c-Si, Cu foil, Papyex® graphite and SS 304. Fig. 6.3 shows that the entire surfaces of different wafers are fully covered by a continuous MLGNWs mat with a similar surface morphology. These nanosheets on different substrates exhibit relatively homogeneous density. However, the average deposition rate is different (Fig. 6.4) depending on substrate. The obtained results correlate with the results of nucleation stage. We see that the average deposition rate increases with the nucleus density (Figure 6.5). Thus, the higher MLGNWs have been grown on SS 304 substrate and the shorter on c-Si substrate. The MLGNWs growth does not seem to require a catalytic substrate, but the presence of catalyst accelerates the growth process (case of iron in SS304) or diminishes the time of the nucleation process.

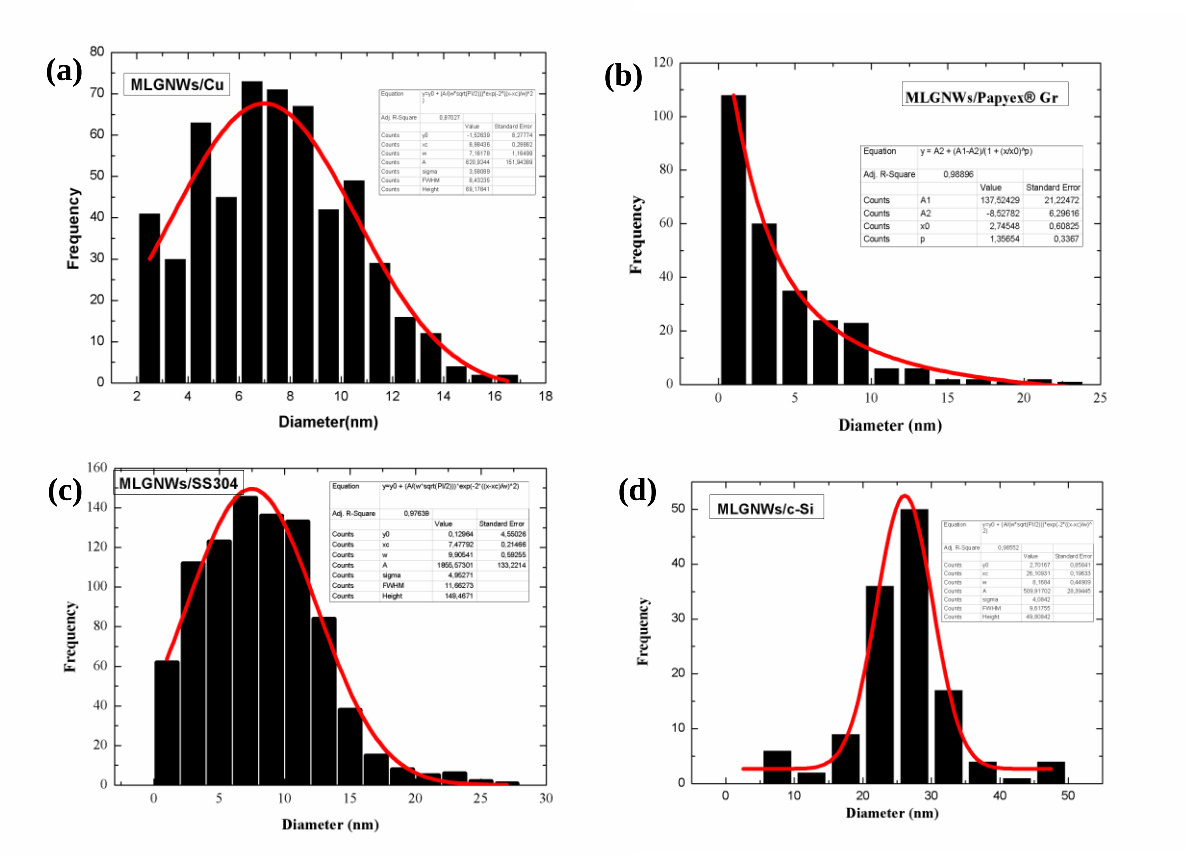

Figure 6.2 Histogram of the nucleus on different substrates a) Cu foil; b) Papyex® graphite; (c) SS 304 foil and (d) c-Si

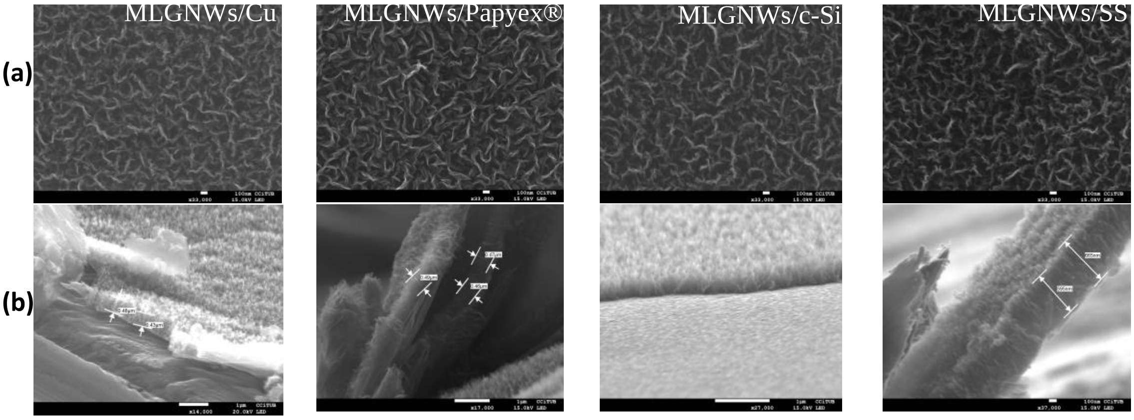

Figure 6.3 (a) MLGNWs on various substrates of Cu foil, Papyex® Gr, c-Si and SS 304; (b) cross- section SEM image of MLGNWs growth on different substrates (17C0302)

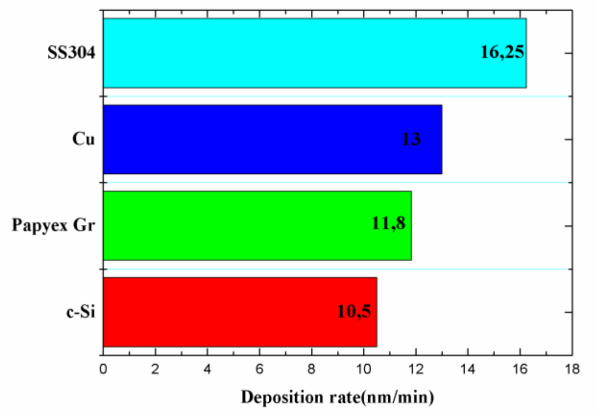

Figure 6.4 Deposition rate for different substrates

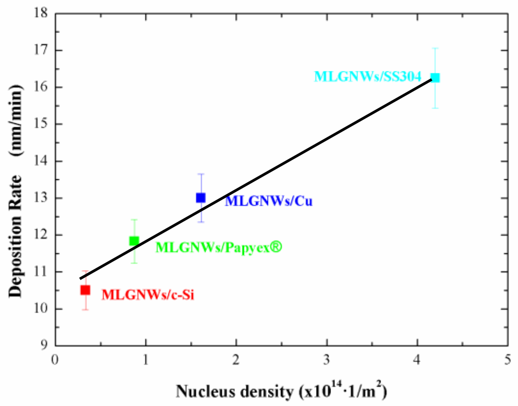

Figure 6.5 Plot of the deposition rate versus the nucleus density of MWGNWs on diverse substrates

Raman scattering

Figure 6.6 shows the Raman spectra of MLGNWs deposited on different substrates. In general, typical Raman spectra for MLGNWs contain three peaks: the G peak at 1590 cm^{-1}, indicating formation of graphitized structure, the D peak at 1350 cm^{-1} corresponding to the disorder-induced phonon mode (defects) and it can be caused by excitation of graphene sheet edges and their

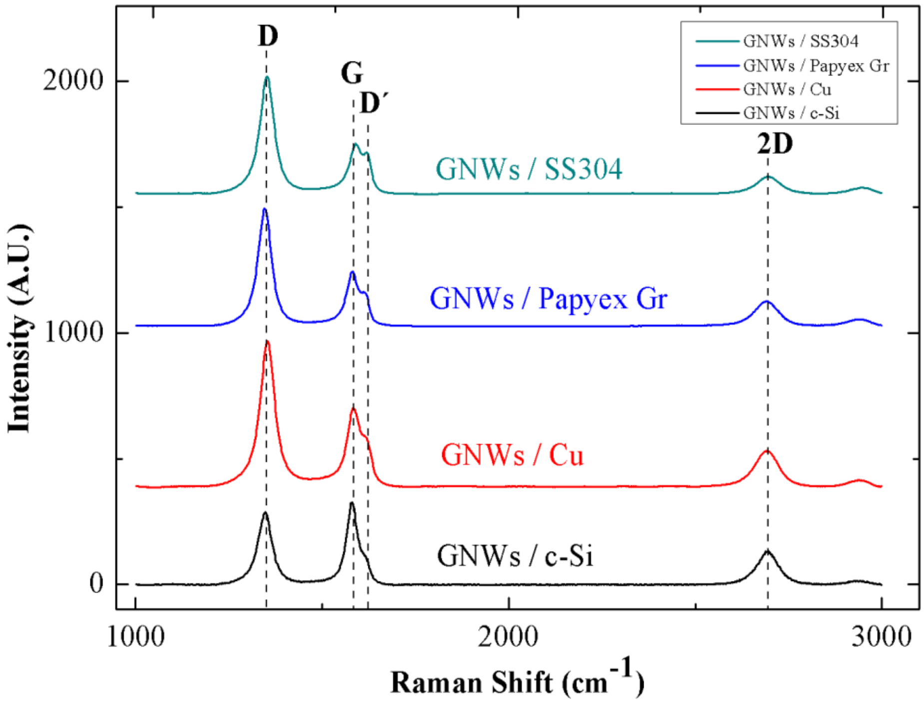

Figure 6.6 Evolution Raman spectra of MLGNWs at different growth substrate under the same conditions

random orientation, and by the presence of amorphous carbon [Zhang XF, 2015], and the 2D peak at 2690 cm^{-1}, which confirm the presence of a graphene structure. In the MLGNWs, the intensity of the D peak of the Raman shift is twice higher than the G peak, which corresponds to the huge number of defects generated under high density plasma deposition. The G peak shows sp^2 vibrations in the graphitic plane and confirms the presence of graphene sheets, accompanied by a shoulder peak at around 1620 cm^{-1}, which is associated with finite-size graphite crystals and graphene edges [Porter DA, 1992; Lv R, 2012]. The shape of the D peak of MLGNWs, as compared with CNTs and graphite, is very sharp probably due to the huge number of defects (distortion, vacancies, and strain in graphitic networks), random orientations of the sheets, high edge density, nanocrystalline structure (presence of D´), surface oxidation (confirmed by XPS analyses), which are typical features in CNWs (so called “multi-layered” GNWs in the present work) [Mori T, 2008; Hiramatsu, 2006].

From our multiple SEM images (for example, Figure 6.3), the MLGNWs alignment has been evidenced. On the other hand, the high intensity and relatively narrow line D obtained from our Raman study seems to be a consequence of the vertical alignment of the MLGNW respect to the substrate with the defects perpendicular to the plane of the graphene nanowalls [Yoshimura A, 2005; Ni ZH, 2006]. Therefore, when defect density is relatively large as in the case of the present study, it is more appropriate to take the peak intensity ratio rather than peak area ratio. The ratio between the intensity of the D and G peaks is the estimated parameter for measuring defects/disorder in the MLGNWs and accordingly the average size (height) of graphene nanowalls. Figure 6.7a shows the dependence of disorder ratio versus nanowalls height. The high intensity ratio of I_D/I_G corresponds to a higher height of the nanowalls, because the higher D peaks reveal more defects and edges, as a result of rapid nucleation and growth [Ferrari AC, 2007]. Comparison of MLGNWs grown on different substrates evidences that the highest nanowalls were grown on SS304 substrate.

Table 6.2 Peak frequencies, bandwidths (FWHM), and relative intensities of D, G and D´ bands in the Raman spectra of carbon nanowalls on top of different materials. Each band was analyzed by fitting with a Lorentzian line.

Substrate material	ω_D (cm^{-1})	I_D (a.u.)	W_D (cm^{-1})	ω_G (cm^{-1})	W_G (cm^{-1})	I_G (a.u.)	$\omega_{D'}$ (cm^{-1})	$W_{D'}$ (cm^{-1})	$I_{D'}$ (a.u.)	I_D/I_G	ω_{2D} (cm^{-1})	W_{2D} (cm^{-1})	I_{2D} (a.u.)
Cu	**1343,2**	**515,3**	**44,2**	**1574,5**	**39**	**270.4**	**1610.2**	**26,9**	**125,3**	**1.9**	**2681**	**67,3**	**121,6**
SS304	**1348,9**	**432.3**	**45**	**1587,3**	**40**	**172,5**	**1618,7**	**22**	**105,7**	**2.5**	**2691,5**	**69,6**	**61,24**
c-Si	**1347**	**255.4**	**41,5**	**1580,4**	**32,7**	**298,8**	**1615,1**	**24,5**	**67,7**	**0.85**	**2693,6**	**63,7**	**116,9**
Papyex	**1346,2**	**430,3**	**42.1**	**1580,7**	**36.6**	**191,5**	**1615,2**	**22,3**	**76,6**	**2.2**	**2688,6**	**68,8**	**86,7**

The number of graphene layers of the MLGNWs also was studied in the base of results obtained by Gupta et al. [Gupta A, 2006]. In accordance with these results, the G band intensity decreases with the increasing of the number of the layers of graphene. Table 6.2 indicates that, a large amount of graphene layers corresponds to MLGNWs/SS304, and a low amount corresponds to MLGNWs/c-Si.

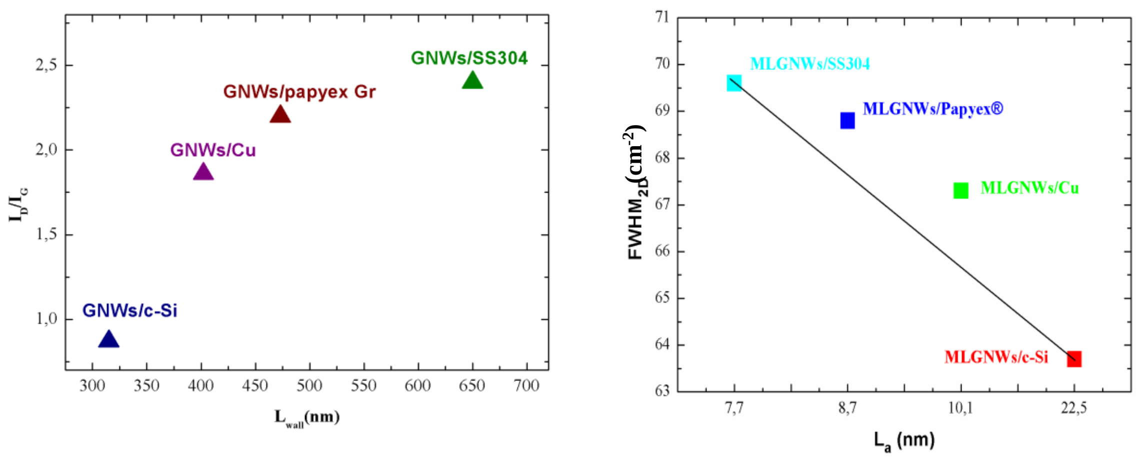

Figure 6.7 (a)MLGNWs wall size vs I_D/I_G ratio for different materials (b) $FWHM_{2D}$ versus of grain size for different materials

Another indicator of the number of graphene layers, is the ratio of 2D and G peaks and FWHM of 2D peak. Figure 6.7b shows the $FWHM_{2D}$ versus the grain size for different substrates. Grain size was calculated by the equation (5.1). The $FWHM_{2D}$ of 63.7-69.6 cm^{-1} (Table 6.2) evidenced to multilayer nature of MLGNWs [Cançado LG, 2002; Cançado LG, 2008; Malard LM, 2009]. Figure 6.8 evidence that the number of graphene layers decreases with increasing grain size. Accordingly, to these results, MLGNWs growth on SS 304 has many graphene layers, compared with nanowalls obtained on c-Si in the conditions of this study. This result is compatible with the result obtained for the nucleation stage. So, in the base of our results, we can conclude that defects lead to a high deposition rate. So, the high number of disorder corresponds to a high deposition rate and a large number of graphene layers.

TEM

The crystalline structure of as MLGNWs grown on c-Si and SS304 are slightly different and are shown in Fig. 6.8. The TEM images demonstrate the sheet-like network structures of MLGNWs. The corresponding SAED pattern in the inset exhibits concentric rings and small nanocrystals for MLGNWs/SS304 and MLGNWs/c-Si. Fig. 6.8a shows the sheet structure of MLGNWs grown on c-Si. The inset image corresponds to SAED pattern focusing on single crystal (Fig.6.8a). Fig. 6.8b shows the TEM image of MLGNWs grown on SS304. Inset image corresponds to a SAED pattern, including a larger region that confirms the presence of crystalline structures embedded in a randomly oriented polycrystalline matrix of MLGNWs/SS304 (Fig. 6.8b). The

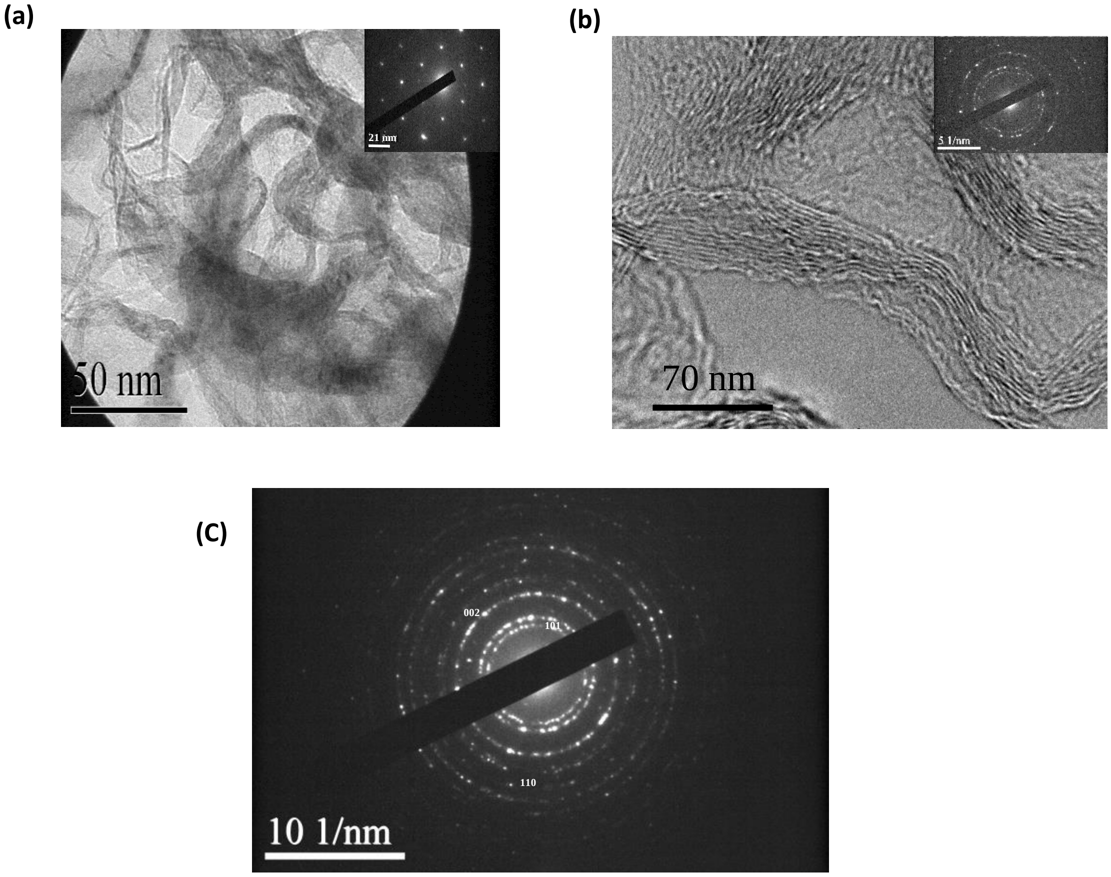

Figure 6.8 TEM micrographs and selected area electron diffraction (SAED) patterns of MLGNWs growth on (a) c-Si substrate; (b) SS304 substrate and (c) SAED pattern with indexed lattice planes of MLGNWs/SS304 (17C0302)

HRTEM image shows that these sheets consist of several layers of graphene with lattice spacing of approximately 0.366 nm, corresponding to the lattice spacing of graphite (0 0 2) [Zhu MY, 2011]. The concentric rings for the MLGNWs/SS304 sample could be indexed to lattice planes (0 0 2), (1 0 1), (1 1 0) of graphite (Fig.6.8c).

X-ray diffraction

Moreover, the crystalline structure of MLGNWs grown on different substrates was analysed by Grazing-incidence X-ray diffraction (GIXD) (Fig. 6.9). The MLGNWs grown on Papyex® graphite shows two diffraction peaks at $2\theta = 26.5^0$ and 54.6^0, which are indicative of (002) and (004) reflections of graphite, respectively [Moon IK, 2010]. The sharp peak at 26.5^o is attributed to a high crystallinity and indicates that MLGNWs are composed of well-ordered graphene with an interlayer space of ~0.34 nm (Fig. 6.9a) [French BL, 2005]. These results are particularly similar to those of natural graphite, which is the material used as a substrate. It can lead to confusion as if these results were originated by the carbon structures.

The XRD measurement for MLGNWs/c-Si was successful and the characteristic diffraction peaks at 11.7^0, 26.5^0, 42.2^0, 53.9^0 and 77.2^0 corresponding to the (002), (100), (004) and (110) reflections of graphite, respectively (JCPDS card no. 75-1621). The resulting graphene nanosheets have a structure between the crystalline and amorphous carbon (Fig. 6.9b). The carbon peak at 2θ ~ 42.2°, corresponding to a combination of turbostratic graphite and crystalline graphite [French BL, 2005; Dimovski S, 2004]. The XRD measurements for MLGNWs/SS304 and MLGNWs/Cu only provide information on the substrate materials due to the rough surface nature of these foils that hides the information on the growing film (Fig. 6.9c).

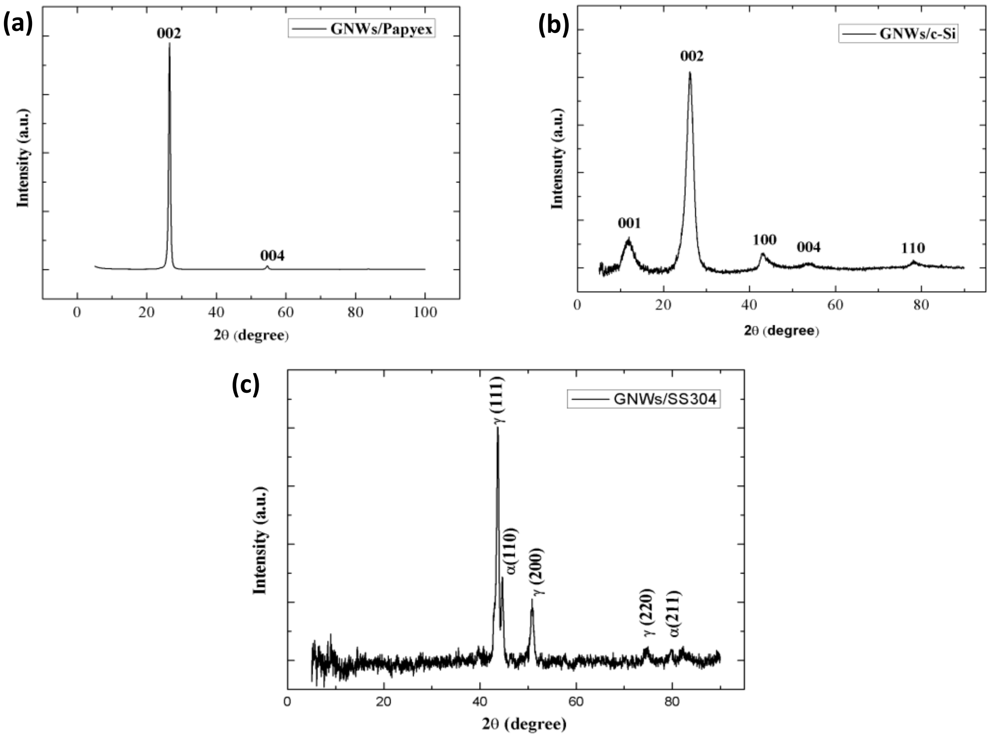

Figure 6.9 Asymmetric grazing angle XRD scans of MLGNWs grown on different substrates (a) MLGNWs/Papyex® graphite;(b)MLGNWs/c-Si and (c) MLGNWs/SS304 (18A1601)

6.1.4 Conclusion

Raman scattering, SEM, TEM and XRD have provided contrasted information on the structure and morphology of MLGNWs on different materials. We have evidenced the influence of the surface material on the first stage of nucleation. The SS304 sample show the highest nucleation density associated to the grain size of the alloy (Fe, Ni, Cr). The other analysed material are compounds of only one phase (c-Si, Cu, graphite) and their nucleation density is smaller. After nucleation we have demonstrated that the MLGNWs deposition was practically independent of the materials of substrates. Therefore, it is possible to fully cover entire surfaces of different wafers with continuous MLGNWs film. These properties make MLGNWs an attractive material for various applications. For example, MLGNWs grown on Cu foil becomes an excellent electrode for supercapacitors [Hiralal P, 2014;Amade,2019], meanwhile, MLGNWs on dielectric (SiO_2) substrate could be used to fabricate gas or bio-sensors [Terse-Thakoor T, 2017], also MLGNWs on semiconductor substrates could be used rather for potential application of solar cells [Liu J, 2015].

6.2 Processing time study of graphene nanowalls

Results of systematic study of time dependence growth of MLGNWs on c-Si and SS304 will be discussed in this section. The SEM, Raman and TEM analyses revealed a structural transformation, from amorphous carbon to vertical oriented multilayer graphene, with the increase of growth time. Transmission electron microscopy shows that these structures have highly graphitized edge planes which terminate in a multilayer of the graphene sheet. The Raman parameters were interpreted by amorphization trajectory theory, which explains the structural transformation during the growth process. In addition, for the growth process of ICP-CVD, plasma is an essential parameter, so we highlight the studies carried out by OES, to detect the active species within the plasma and the evolution with the increase of the growth time.

Experimental details

Synthesis of MLGNWs was carried out in ICP-CVD system, equipped with a 13.56 MHz radio frequency source. The substrates were cleaned via ultrasonication in isopropanol/DI water. The cleaned substrates were then loaded into the reactor without a holder using a thermocouple arm and placed directly over the quartz tube. Chamber pumped down via a rotary pump to ~$2x10^{-3}$ Torr. Once the desired base pressure was obtained, the substrate temperature was reached up to 750^0C as monitored by thermocouple connected to the sensor. Methane (CH_4) was injected when temperature and pressure was stabilized and growth process was started when plasma was introduced and MLGNWs growth was carried out for different durations of time. The overall morphology and structure of the MLGNWs at various growth times (a 5 to 80 min), was characterized by scanning electron microscopy (SEM) and Raman Spectroscopy. Also in this section, chemical gas analysis during plasma deposition via OES will be discussed.

6.2.1 Growth on c-Si substrate

FE-SEM study

The overall morphology and structure of the MLGNWs were characterized by field emission scanning electron microscopy (FE-SEM). Fig. 6.10 shows the SEM images of the MLGNWs/c-Si at various growth times from 5 to 80 min. Vertical nanostructures begin to form after 5 min. The first minutes of deposition corresponds to the stage of nucleation, which provides amorphous carbon buffer layer deposition without vertical graphene growth. After 5 minutes, vertical graphene nanostructures start to appear with randomly interwoven sharp edges and with open spaces between them. Fig. 6.10 evidences that deposition time plays a crucial role in MLGNWs

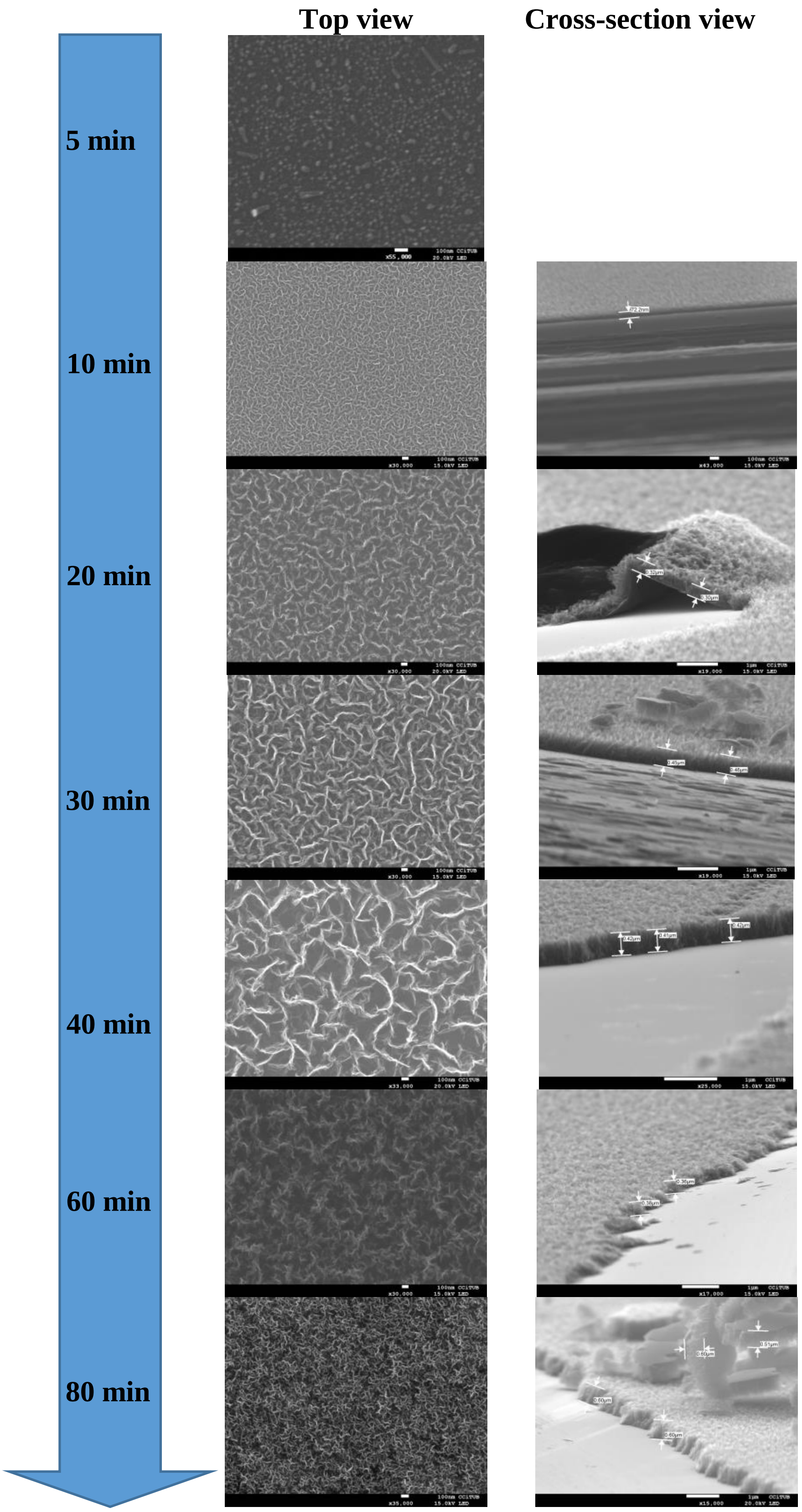

Figure 6.10 (a) Scanning electron microscopy (SEM) images of MLGNWs/c-Si at various growth times (16K2801,16K2802,16L0101,16L1901,17A2401,17A3001,17A3101); (b) Cross-section SEM image of vertical alignment of the MLGNWs to the underlying Si substrate tilted 85°

deposition process. FE-SEM images show that with increasing growth time, the degree of interlinking increases along with the overall increase of the wall height. At the early growth stage, amorphous carbon buffer layer is formed, which was shown by Raman analysis. The formation time of the buffer layer depends on the type of plasma. Inductively coupled plasma leads to rapid nucleation and growth, due to the high plasma density and a larger plasma volume (10^{19} m^{-3}) [Sato G, 2006; Lieberman MA, 2005; Bo Z, 2013]. The growth rate using ICP-CVD of MLGNWs is rather higher than that using radical injection PECVD and electron beam excited PECVD [Hiramatsu M, 2004; Kondo S, 2008; Mori T, 2008]. In our experiment after 5 min nucleation was formed a continuous film, which serves as a buffer layer for the future growth of vertical nanowalls. The cross-section SEM image evidenced the presence of the buffer layer (Fig.6.10, 20 min growth, cross-section view).

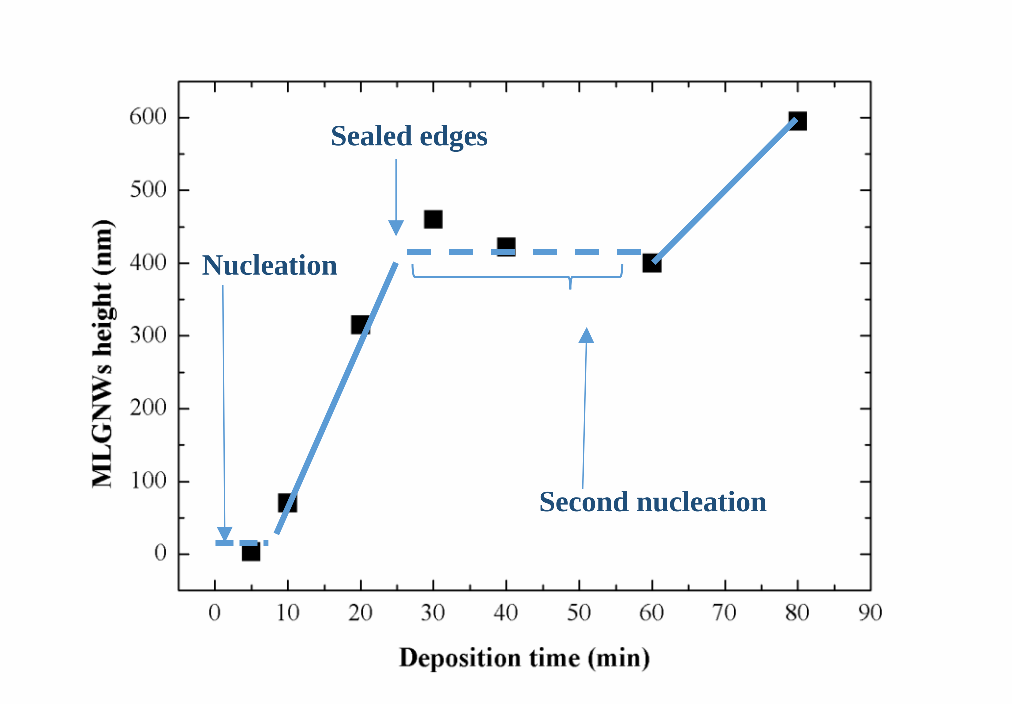

Figure 6.11 Nanowalls average height vs deposition time for MLGNWs/c-Si samples

After the synthesis of the buffer layer, the formation of 2D graphene (sp^2) islands begins, which ensure the future growth of vertical graphene. Figure 6.11 shows the height of MLGNWs as a function of deposition time. The time range, from 30 min to 60 min, corresponds to the secondary nanowalls formation as described in the chapter 4. The sealing process might be associated to the decrement of the number of graphene layers on the edges observed by TEM (Fig. 6.12). After 60 min, the height and density of nanowalls increases due to the formation of secondary MLGNWs, which continue growing as usual (Fig.6.11).

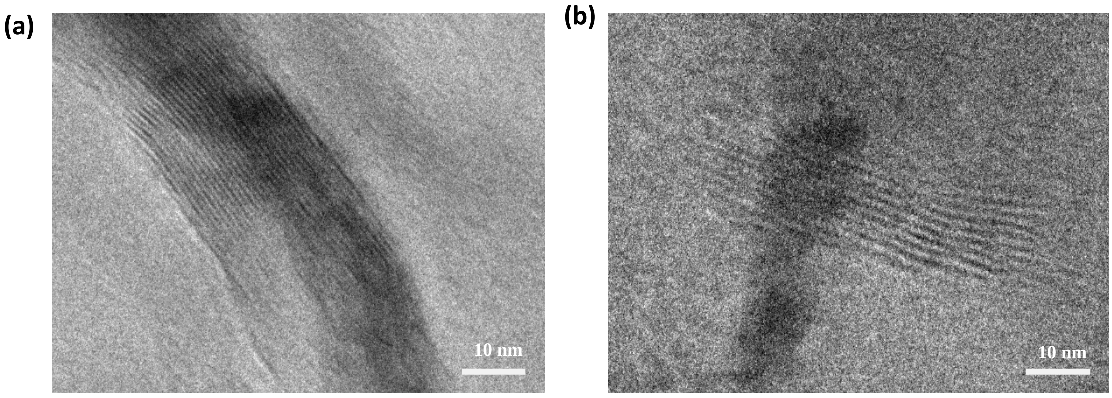

Figure 6.12 TEM images of MLGNWs at different growing time (a) 10min (16K2802) (b) 40min (17A2401)

Raman scattering

Raman spectroscopy analysis using Horiba Raman Microscope with operating 532 nm solid-state visible lasers was performed to study the structure of MLGNWs at different deposition time (Fig.6.13). The Raman spectra of carbon based material exhibit several typical peaks, denoted as D, G, D´ and 2D peak. Raman spectra for MLGNWs/c-Si at different deposition time have a G peak around 1590 cm^{-1} and a D band peak at around 1350 cm^{-1} (Table 6.3a). The D band of all the samples corresponds to the high number of open edges of small-sized graphene sheets and the defects inside the graphene domains [Jensen K, 1991]. Raman spectra evidenced a variation of

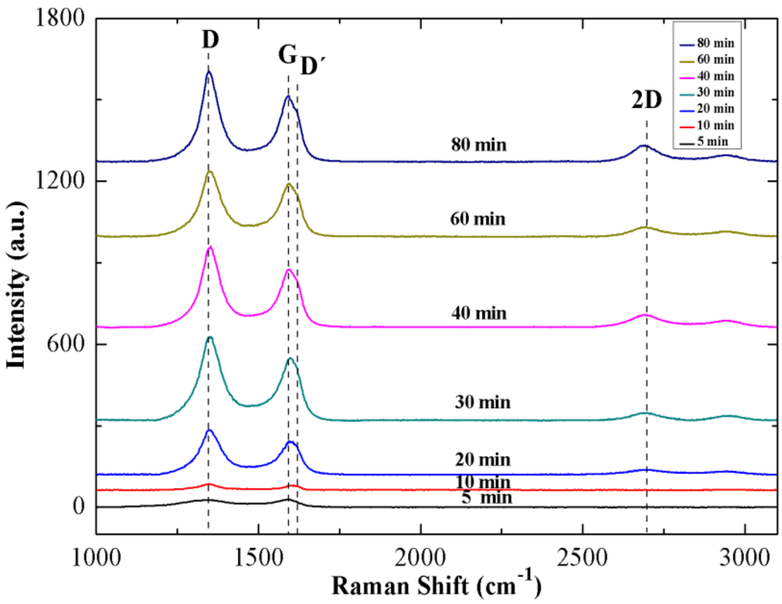

Figure 6.13 Raman spectra for MLGNWs/c-Si in different growth time

the D peak intensity with the plasma exposure time following the same process described in the Fig.6.11 (Fig.6.14). The second order of D peak is a 2D, which confirms the presence of graphene and helps to determine the number of graphene layers. In this study 2D appear starting 20 min.

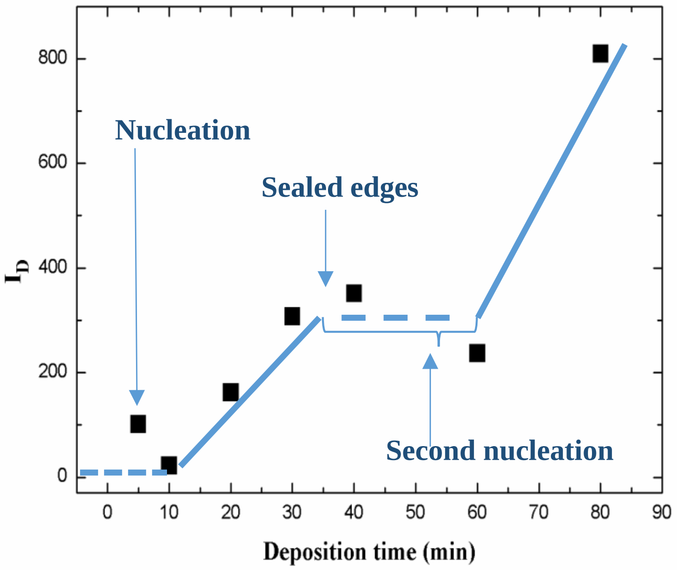

Figure 6.14 Nanowalls average height vs deposition time for MLGNWs/c-Si samples

In the initial step of nucleation (0-10 min) we have an amorphous carbon buffer layer, which is determined by the Raman spectra. Raman spectra of amorphous carbon phase is composed of two peaks, D and G. The D peak is associated to sp^2 hybridized carbon structure [Robertson, 1986]. The physical properties of amorphous carbon films strongly depend on the ratio of these two types of C–C bonds. The ratio of sp^3/sp^2 carbon phases depends on deposition conditions and can be changed in a broad range from pure diamond to pure graphite. Using amorphization trajectory theory (Fig. 6.15a), we have determined that our material is located in the stage 1 of the plot from graphite to nanocrystalline graphite (nc-G) [Ferrari AC, 2000] (position of the G band is around 1600 cm^{-1} and I_D/I_G ~1 (Table 6.3)). Also, this changes confirmed by the G peak position shift from 1592 to 1600 cm^{-1} and I_D/I_G ratio increases [Ferrari AC, 2000], which also corresponds to the transformation from graphite to nanocrystalline graphite phase (Fig. 6.15b). D´ peak, which is associated with symmetry breaking, due to the finite size of sp^2-hybridized crystallites, suggests relatively low order of graphitization with a large amount of inter-crystalline defects [Zhang N, 2018]. The c-Si substrate is monocrystalline and have not inter-crystalline defects, thus in Raman spectra of MLGNWs/c-Si is not observed the D' band for a shorter deposition time, because the growth starts after a long nucleation stage. However, for longer growing process, starting 40 min is observed small D' band, which is associated with a disordered of the deposited material, than from the substrate.

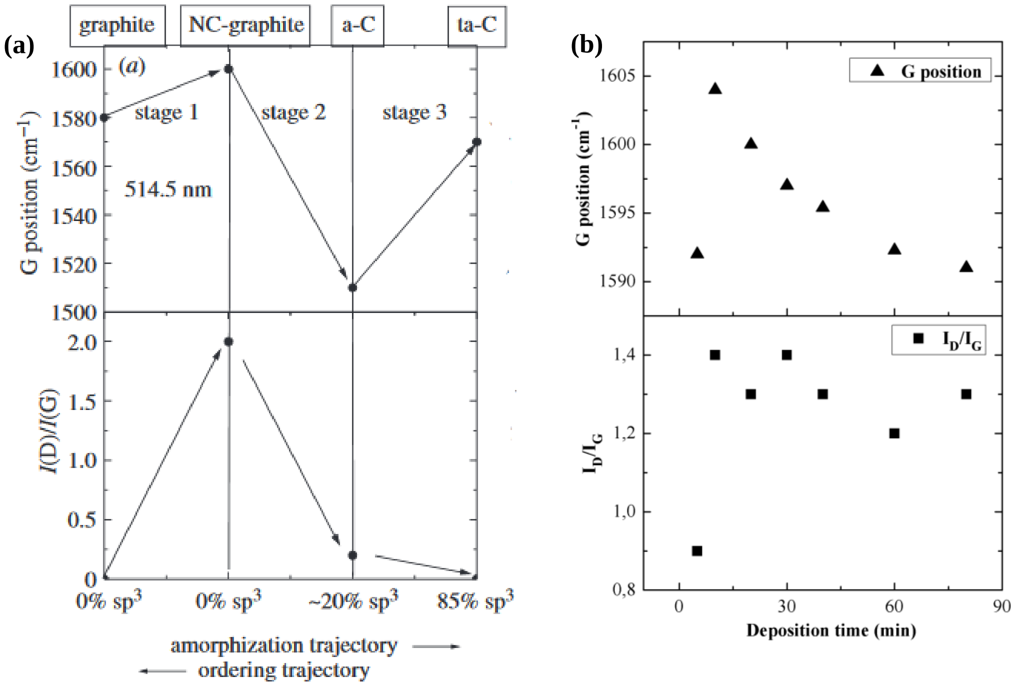

Figure 6.15 (a)Three-stage model of the variation of the Raman G position and the D-to-G intensity ratio, I_D/I_G, with increasing disorder [Ferrari AC,2000];(b) experimental results of Raman analyses (samples of Fig.6.11)

Table 6.3b shows the wall height, the I_D/I_G ratio, which is related to the crystal imperfection of the graphene sheets, the nano-graphite crystallite sizes (L_a), calculated from the Tuinstra-Koenig relation (equation 5.1), and the I_{2D}/I_G ratio related to the number of graphene layers.

The size of the crystallites (L_a) depends on defects (disorders), which means that a large number of defects reduces the size of the crystallite. Table 6.3b lists the nano-graphite crystallite sizes for different deposition time on c-Si. The results presented in Table 6.3b reveal that the initial growth stage is associated with the formation of crystals of relatively large size, probably due to the flat morphology of c-Si and its small number of defects. Then, with an increase in plasma exposure time, the process of hydrogen etching leads to a large number of defects and, accordingly, to a decrease in the size of crystallites. The hydrogen etching process also influences the number of graphene layers (Table 6.3b) through the $FWHM_{2D}$, 2D position and I_{2D}/I_G [Hodkiewicz J, 2010].

Table 6.3 (a) Summary of the structural and Raman spectral parameters of the MLGNWs/c-Si films; (b) intensity rations I_{2D}/I_G, I_D/I_G, FWHM of 2D and crystallite size at different deposition times

(a)

Time (min)	**L_{wall} (nm)**	**ω_D (cm^{-1})**	**ω_G (cm^{-1})**	**ω_{2D} (cm^{-1})**	**I_D (a.u.)**	**I_G (a.u.)**	**I_{2D} (a.u.)**
5	3	1345	1592	-	101.4	94.9	-
10	70	1350	1604	-	22.3	16.25	-
20	315	1348	1600	2698	162.1	121.7	17.6
30	460	1351	1597	2695.5	307.4	225.8	24.8
40	422	1351.6	1595.4	2688.8	351.4	270.1	103.4
60	400	1348.4	1592.3	2688.8	236.8	193	32.3
80	595	1348.4	1591	2688.8	810	719	535.6

(b)

Time (min)	**I_{2D}/I_G**	**I_D/I_G**	**FWHM 2D (cm^{-1})**	**L_a (nm)**
5	-	0.9	-	21.3
10	-	1.4	-	13.7
20	0.1	1.3	95.9	14.7
30	0.1	1.4	92.4	13.7
40	0.4	1.3	91.4	14.7
60	0.2	1.2	94.4	16
80	0.7	1.3	83.4	14.7

The observed 2D band position downshifts along with the $FWHM_{2D}$ decrease and I_{2D}/I_G ratio increase are a consequence of the decrease of the number of graphene layers by the deposition time. As the deposition time increases, the I_D/I_G value, associated with the presence of nano-crystalline graphite, increases suddenly after the first 5 minutes (after the nucleation stage). The large number of graphite nano-crystals (high I_D/I_G) at the first stage of deposition comes associated with the formation of MLGNWs as shown in Fig. 6.10 since 10-30 min.

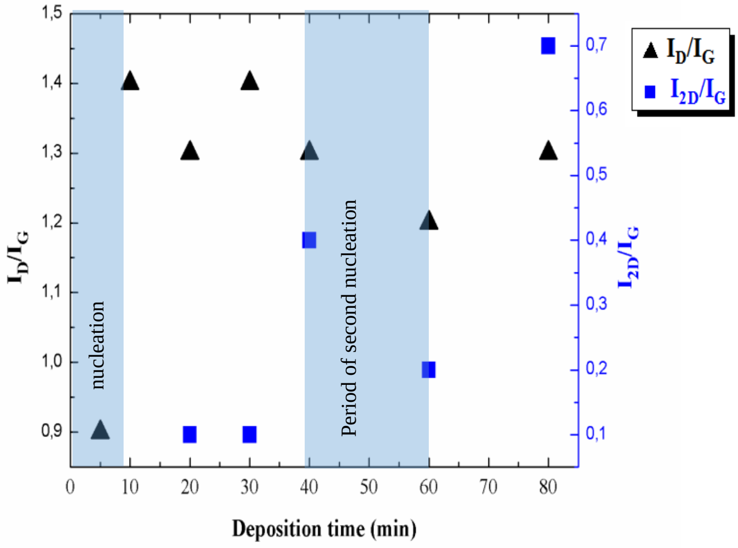

Figure 6.16 Intensity rations I_D/I_G and I_{2D}/I_G of MLGNWs/c-Si deposited at various growth time

The high intensity plasmas during seem to be the origin of the formation of nano-crystals, but this interpretation will be discussed below in the §6.2.3 in the part of OES study. Finally, the carbon structure grown on c-Si substrate after 80min appears as nano-crystalline graphite structure with a low number of layers (MLGNWs).

6.2.2 Growth on SS304 substrate

FE-SEM

Fig. 6.17 shows the SEM images of the MLGNWs grown on SS 304 at various growth times. These results indicate that the average growth rate for MLGNW / SS304 is higher than MLGNWs grown on a c-Si substrate, due to the high nucleation density, as discussed above (Fig.6.2 and 6.3). The growth of MLGNWs on SS304 has the similar behaviour as on c-Si with one difference in growth rate and nucleation density (Fig. 6.18). For MLGNWs/SS304 also observed the secondary MLGNWs formation after the second nucleation from 40-60min. We observed in the Fig. 6.19 clear differences between the thickness of the nanowalls grown after the first and second nucleation. The maximum height of nanowalls which we have observed was on SS304 (~1400 nm).

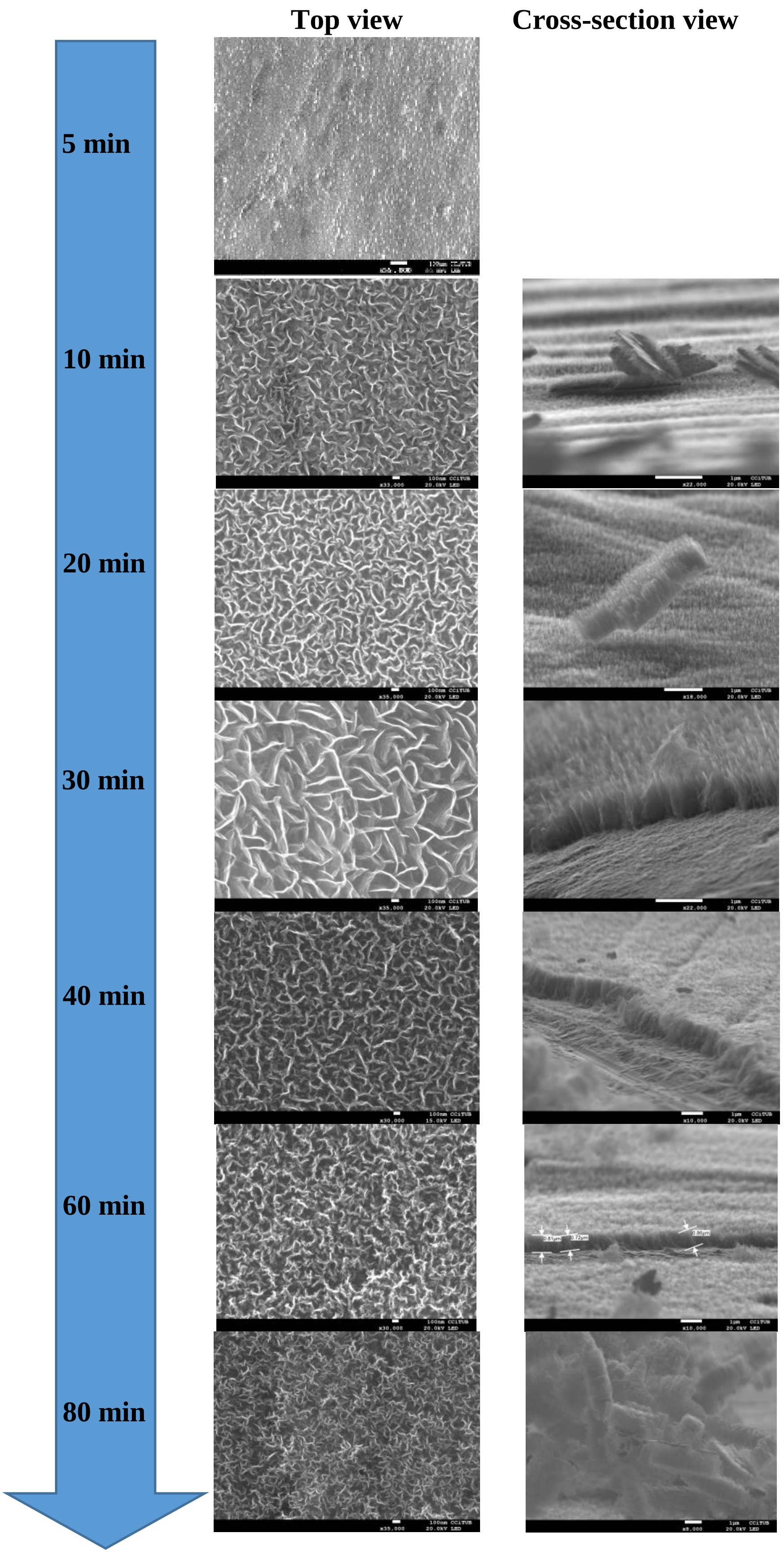

Figure 6.17 (a) Scanning electron microscopy (SEM) images of MLGNWs/SS304 at various growth times (18B2202, 18B1401, 18B1401, 18B2601, 18B0903, 18B0801, 18B0802). Cross-section SEM images of vertical alignment of the MLGNWs to the underlying SS304 substrate tilted 85°

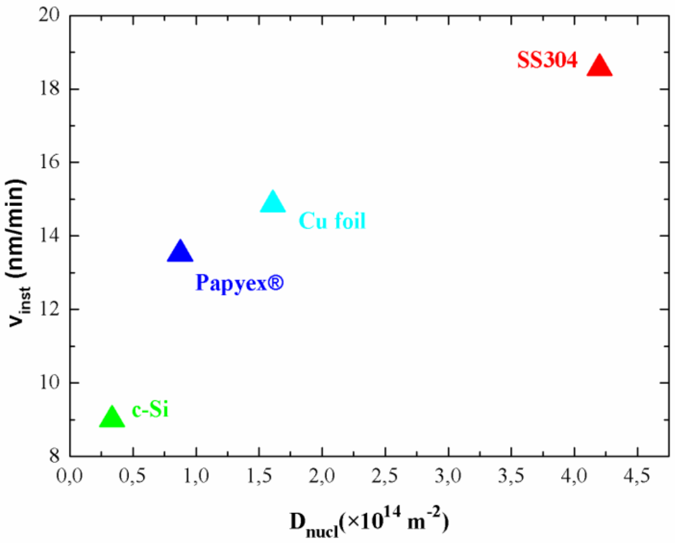

Figure 6.18 Nucleation density vs instant growth rate for different materials

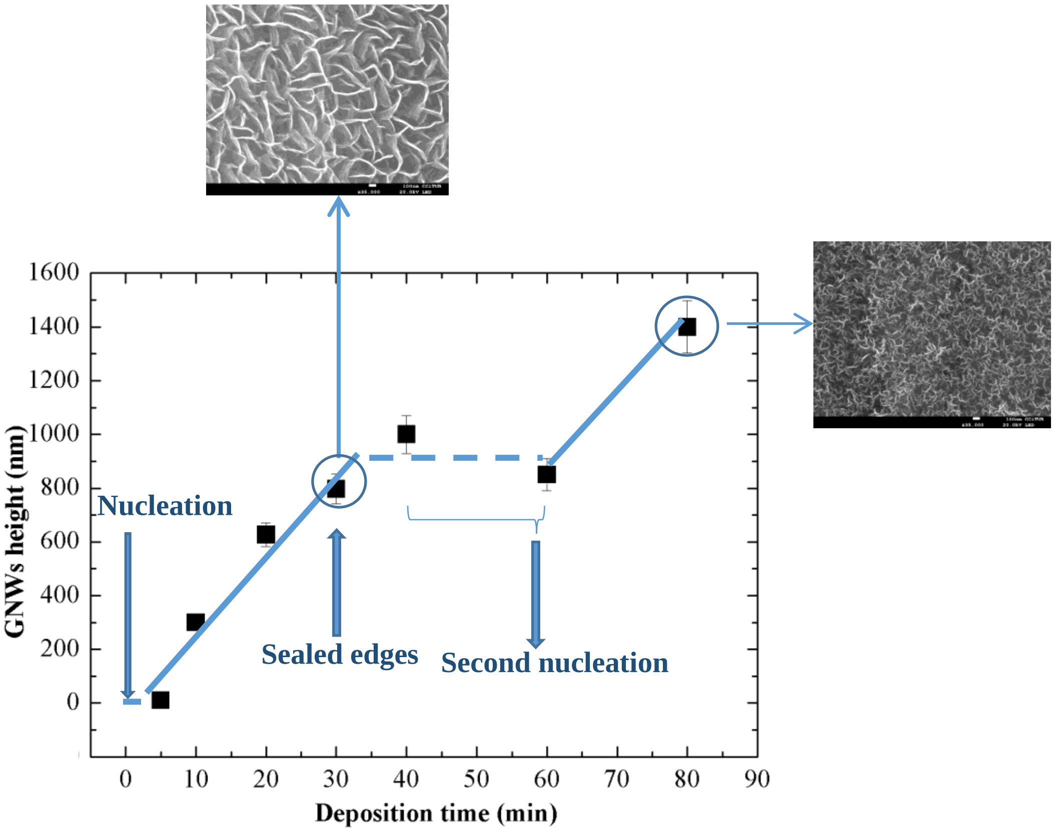

Figure 6.19 (a)MLGNWs/SS304 at 40 min growth time (18B0903); (b)MLGNWs/SS304 at 80 min growth time (18B0802); (c) MLGNWs average height vs deposition time for MLGNWs/SS304 samples

Raman scattering

The observed Raman scattering parameters at the different deposition time provide direct experimental data of phase transformation from nucleation to MLGNWs formation. The transformation from graphite to nanocrystalline graphite phase in case of SS304 substrate was carried out very quickly. In this way, from Raman spectra we can see that, after 5 min deposition we observed typical four peaks of MLGNWs spectra (D, G, D´ and 2D peaks) (Fig.6.20). For MLGNWs grown on c-Si, 2D and D´ peaks were observed after 20 min of deposition (Fig.6.13). For MLGNWs growing at different time scale, the D- and G-peaks have considerable higher intensities than the 2D-peak, which is typical of disordered carbon films [Schwan J, 1996].

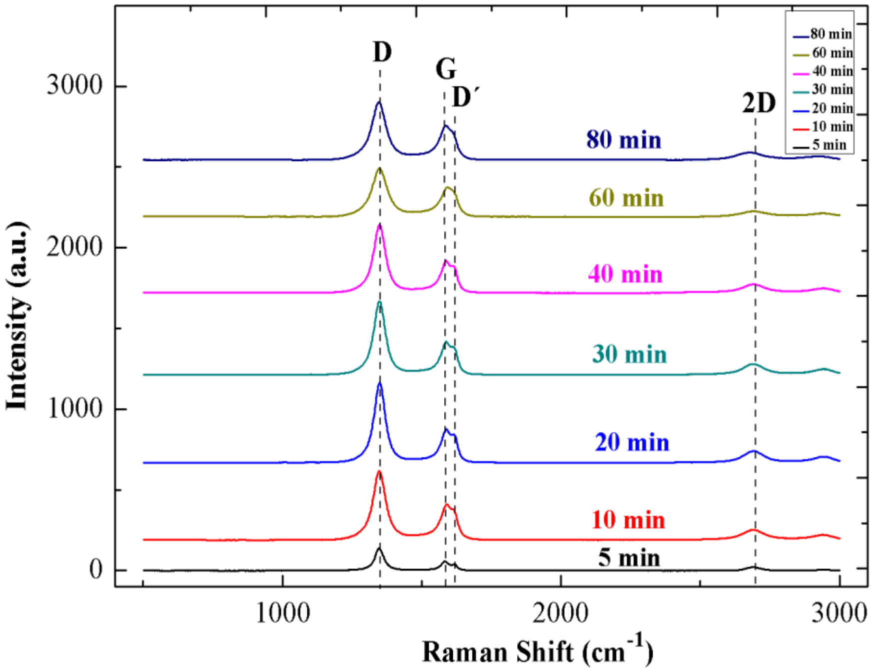

Figure 6.20 Raman spectra for MLGNWs/SS304 at different growth times

Peak positions and width values from Raman spectra was performed by fitting with a Lorentzian function (Fig. 6.21). It provides a natural convergence and does not induce any shifts in the band. The corresponding spectral parameters of the growing films at different times are shown in Table 6.4. The I_D/I_G ratio changes in carbon based nanomaterials can depend on the following two factors: firstly, defects in the crystalline structure and secondly, due to the edge defects (such as edge shape and curvature) [Soin N, 2011]. For MLGNWs grown on SS304 substrate we observed the decrement of the I_D/I_G ratio over deposition time, as compared with MLGNWs/c-Si where I_D/I_G ratio increases. Defects observed at the first minutes of deposition for

MLGNWs/SS304 sample come from the substrate rather than grown material. Number of disorder using SS304 substrate decreases with a simultaneous increase of nanowalls density (deposition time). In contrast, for c-Si substrate the defects come from the grown material (MLGNWs), and this is the reason of the increase of the I_D/I_G ratio with deposition time (Table 6.3 and 6.4).

Table 6.4 (a)Summary of the structural and Raman spectral parameters of the MLGNWs/SS304 films; (b) Intensity rations I_{2D}/I_G , I_D/I_G , FWHM of 2D and crystallite size at different deposition time

(a)

Time (min)	L_{wall} (nm)	ω_D (cm^{-1})	W_D (cm^{-1})	ω_G (cm^{-1})	W_G (cm^{-1})	$\omega_{D'}$ (cm^{-1})	$W_{D'}$ (cm^{-1})	ω_{2D} (cm^{-1})
5	10	1345.3	37.3	1583.5	33.8	1617.2	20.4	2690
10	300	1349.6	44	1585	43.4	1617.6	18.7	2688.7
20	626	1349.6	45.5	1588.2	42.1	1616	19.6	2690.6
30	797	1348.1	47.7	1589.5	44.3	1618.9	20.9	2690.1
40	1000	1347.8	50.9	1590.4	44.5	1618.2	21.6	2690.2
60	850	1347	60.6	1594.8	52.7	1617.8	15.4	2688.8
80	1400	1344.7	59.6	1587.8	54.5	1615.5	15.7	2674.1

(b)

Time (min)	I_{2D}/I_G	I_D/I_G	L_a (nm)	W_{2D} (cm^{-1})
5	0.33	2.5	7.7	59
10	0.14	1.9	10.1	77.6
20	0.3	2.4	8	79
30	0.27	2.2	8.7	80.6
40	0.22	2.1	9.1	81.5

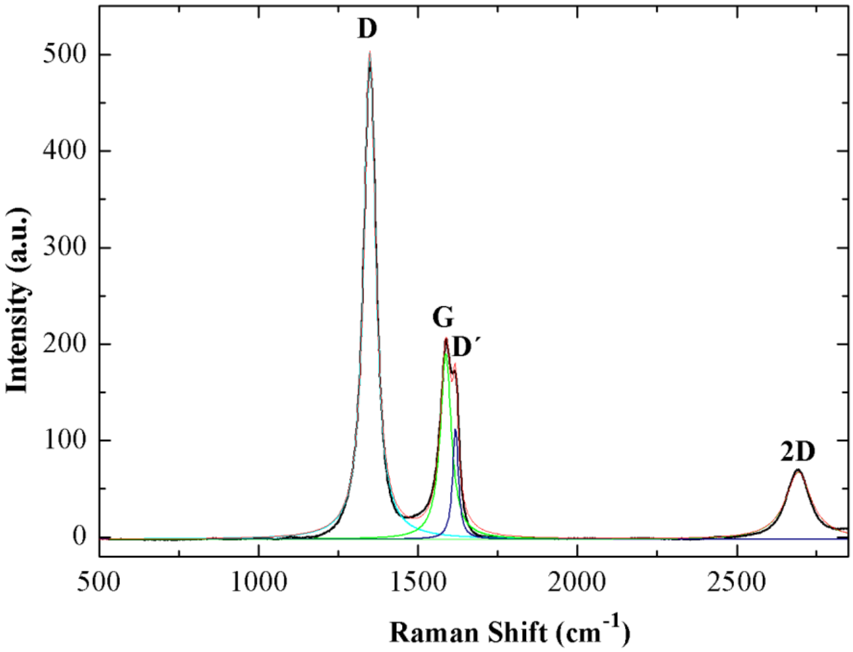

Figure 6.21 Deconvolution of the Raman spectrum of MLGNWs/SS304 grown by ICPCVD (20min, 750^{0}C, 440W). The black line is the experimentally observed Raman spectrum; the red line is the fitted spectrum from the four components contributing to the experimental data.

An increase of compressive stress in the nanostructure is evidenced by a shift of the G band to a larger wavenumber. Fig. 6.23 shows the plot of G peak position and I_D/I_G ratio as a function of growth time [Gupta A, 2006]. In the graph, we observed three stages of G-peak changes: first is 5-10 min, corresponding to the nucleation and the first nanowalls formation, second is 20-40 min, corresponding to the primary nanowalls growth and third 40-60 min secondary nanowalls formation and 60-80 nanowalls growth after second nucleation. For each deposition stage, we observed a compressive stress except for the last stage after 60min where the graphene structure relaxes. We should note that the number of layers of the MLGNWs is quite lower after the second nucleation and the defects evidenced by the I_D/I_G ratio are also lower. This facilitates the relaxation of the graphene structure observed after 60 min of growth (Fig.6.22).

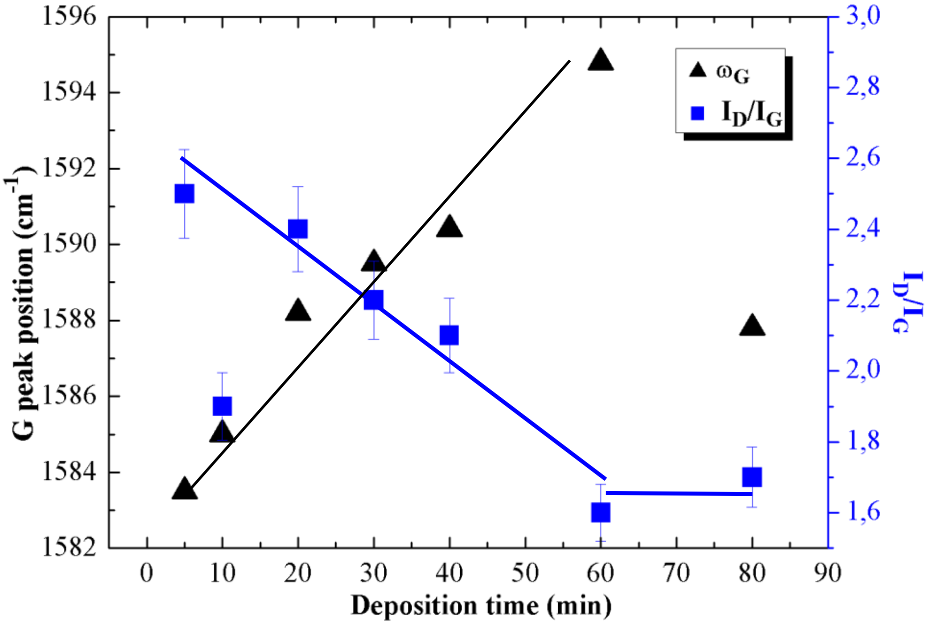

Figure 6.22 Variation of the I_D/I_G ratio and the G peak position when the growth time increases.

TEM and HRTEM

The detailed structure of graphene nanowalls grown at different time range was studied by HRTEM. Fig. 6.23 shows the HRTEM images of MLGNWs/SS304 grown by ICP-CVD method (growth temperature 650^{0}C, plasma power 440W, methane gas flow 10 sccm) at a deposition times of 10, 20 and 40 min. The deposited material was transferred to the copper grid by scratching MLGNWs from the substrate. Fig. 6.23 shows the number of vertical graphene layers, which are 10–30 graphene layers at 10 min of growth and ≤ 10 graphene layers at 40 min of growth. The number of graphene layers decreased with deposition time, probably due to the etching during the growth. These results are compatible with the results of the evolution of the I_{2D}/I_G ratio from Raman analysis (Table 6.4b).

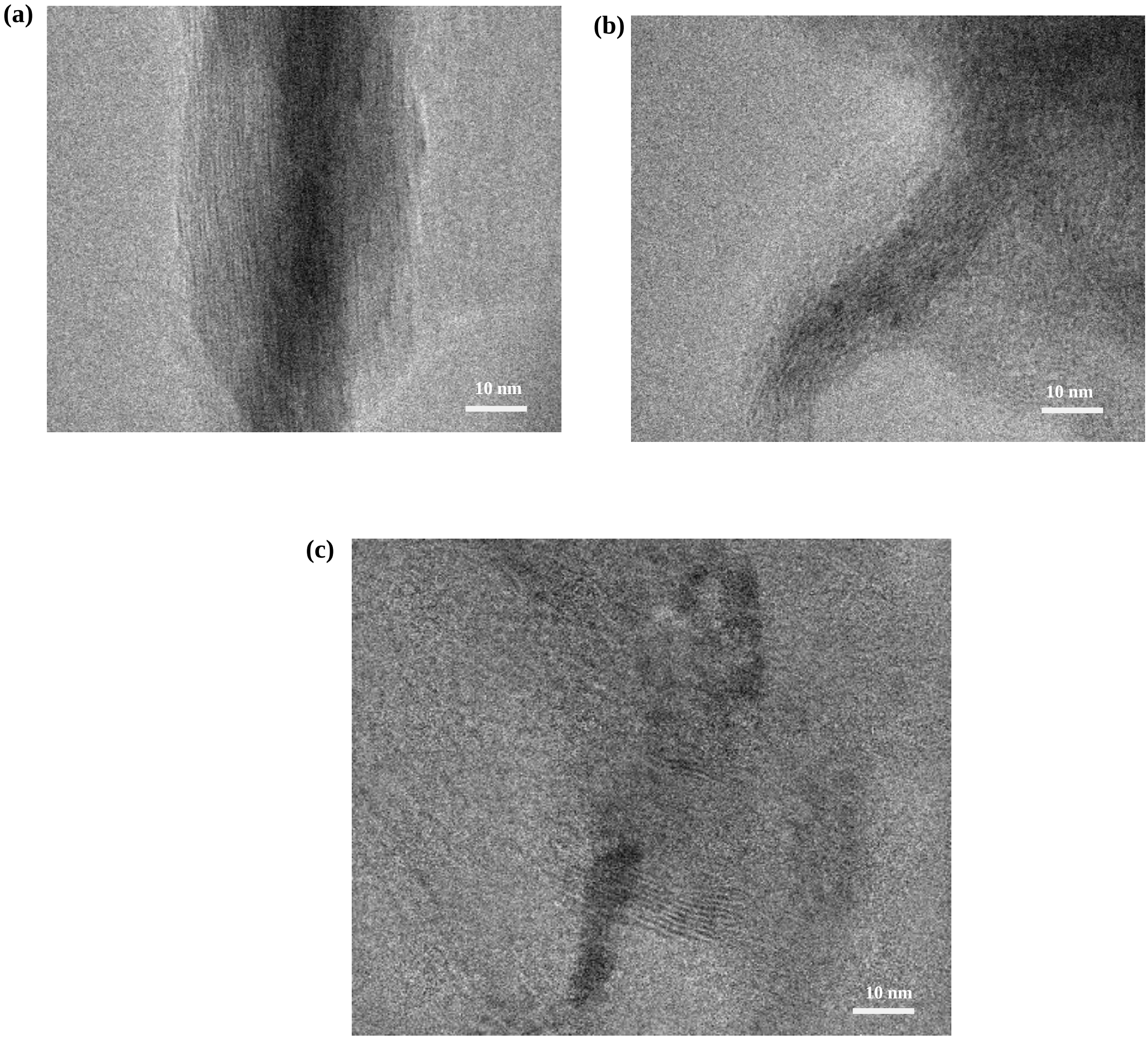

Figure 6.23 High-resolution TEM image of MLGNWs grown at (a) 10 min; (b) 20 min and (c) 40 min (18B2703, 18B2602, 18B2702)

The TEM images and SAED pattern show bi-dimensional nanostructures, of few layers, like wrinkled nanosheets with a random orientation giving place to diffused concentric rings (Fig.6.24b). The HRTEM image shows that these sheets were composed of 13±2 layers of graphene with a distance of 0.366±0.030 nm, corresponding to the lattice spacing of graphite (002) [Kolmogorov AN, 2005]. Also, HRTEM image shows open graphitic edges (shown with a black arrow in Figure 6.24a). Figure 6.24b evidenced the bent nanowalls which can be the consequence of defects generating the compressive stress as we have observed above.

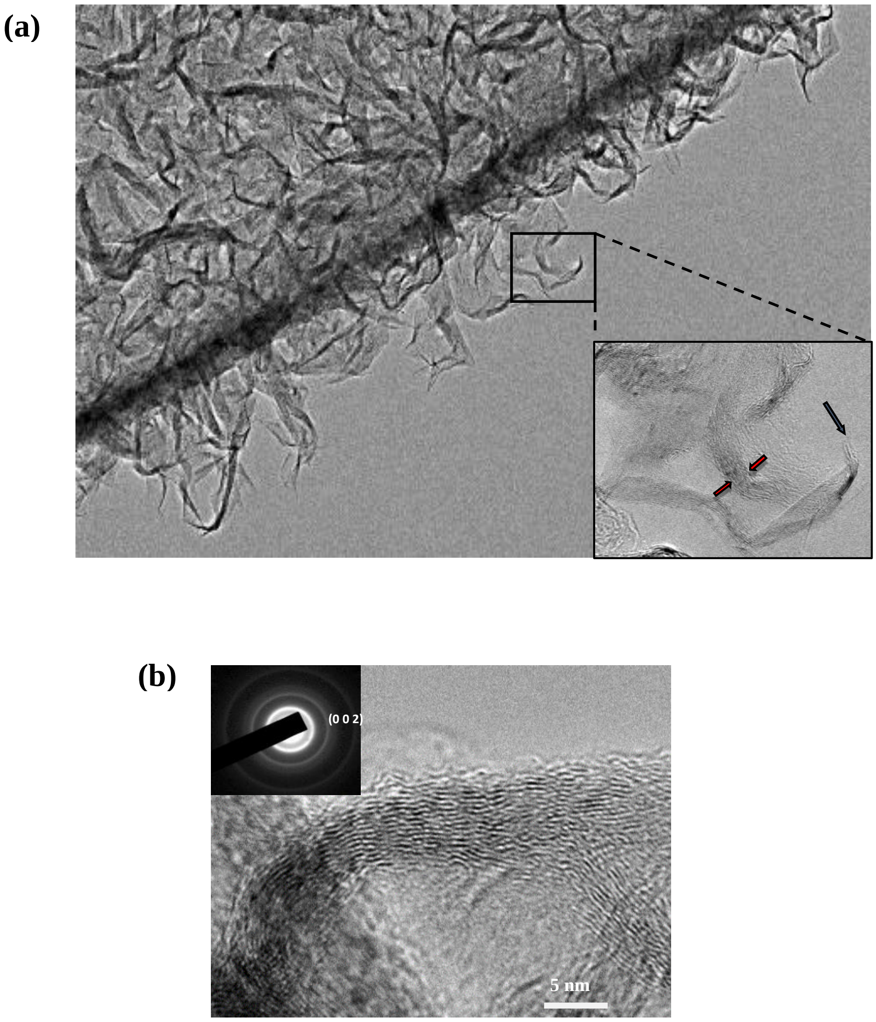

Figure 6.24 (a) High-resolution TEM image of MLGNWs (inset figure: high resolution TEM image of a MLGNWs fragments); (b) high-resolution TEM image of MLGNWs (inset image: SAED pattern (17L0102)

6.2.3 Evolution of the nanowalls structure with processing time on other substrates

As discussed above, the growth time has a different effect on the MLGNWs growth process on the c-Si semiconductor and the metal SS304 substrates. In order to investigate the deposition time influence on MLGNWs grown on Cu foil (for production of graphene one of the most useful catalysts) and on polycrystalline Papyex® graphite paper, we conducted one single for each deposition time experiment using two different substrates Cu, Papyex® and compared with results of MLGNWs grown on SS304. For this study, we have used 2cm x 2cm substrates, washed in isopropanol and then raised with deionized water and dried, with nitrogen pistol. The three samples were introduced simultaneously into ICP-CVD reactor using molybdenum support. The furnace was heated to 650°C. The plasma was generated by a copper helical antenna, applying RF power (I_{RF}) of 440W. The growth process was carried out under 10 sccm methane gas flow. This experiment was repeated for deposition times of 5, 10, 20 and 40 min. SEM images show that, the entire surfaces of different substrates are fully covered with continuous MLGNWs with a similar surface morphology under the same conditions and relatively homogeneous density after 10min of growth (Fig.6.25).

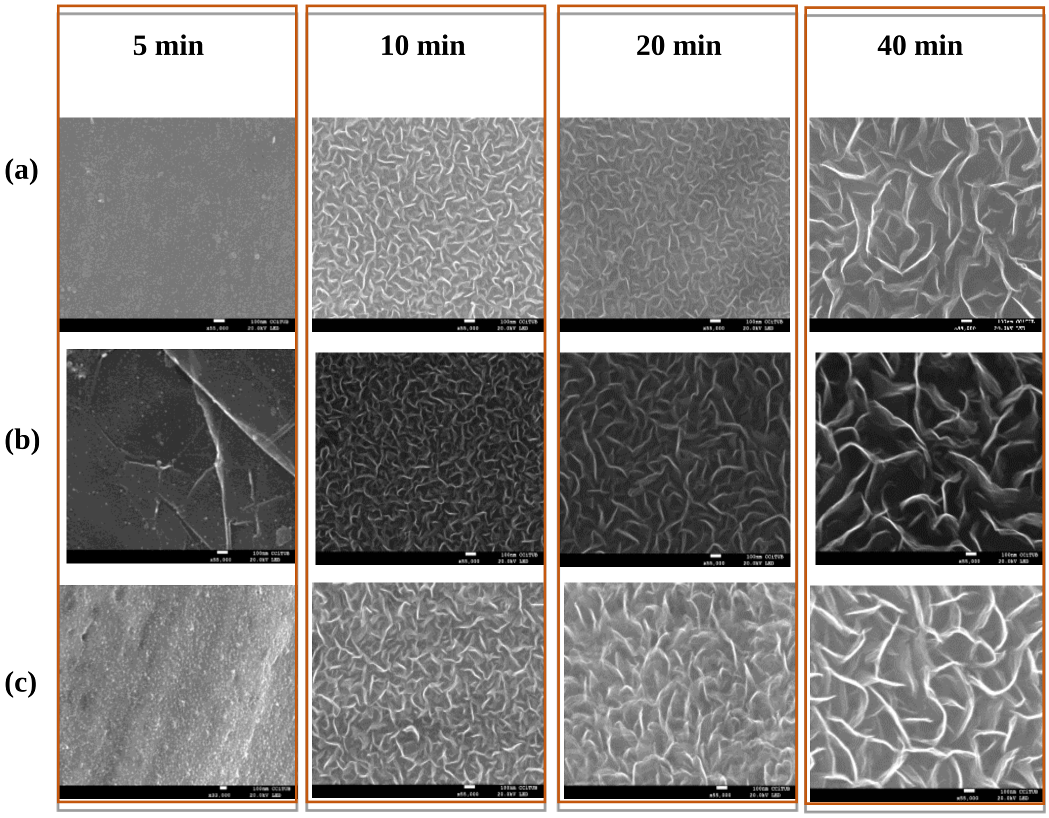

Figure 6.25 SEM images of MLGNWs growth in different substrates at different growth time: (a) Cu foil; (b) Papyex graphite; (c) SS304 (18B2202, 18B1501, 18B1402, 18B1901)

Fig. 6.26 shows the OES spectra for the evolution of the CH_4 precursor gas radicals from 5 to 40 min of deposition. In thermal CVD, only ~0.0002% of incoming methane dissociates forming active species in the gas phase at a temperature of 900°C. However, due to plasma activity, more than 80% of the methane dissociates to give rise to other species such as H, H_2, CH and C_2H_2 [Crudena BA, 2005]. We observed that recombination lines of the atomic (656nm, H_α) and molecular (550-650nm, H_2) hydrogen dominate in the emission spectrum. This high H content

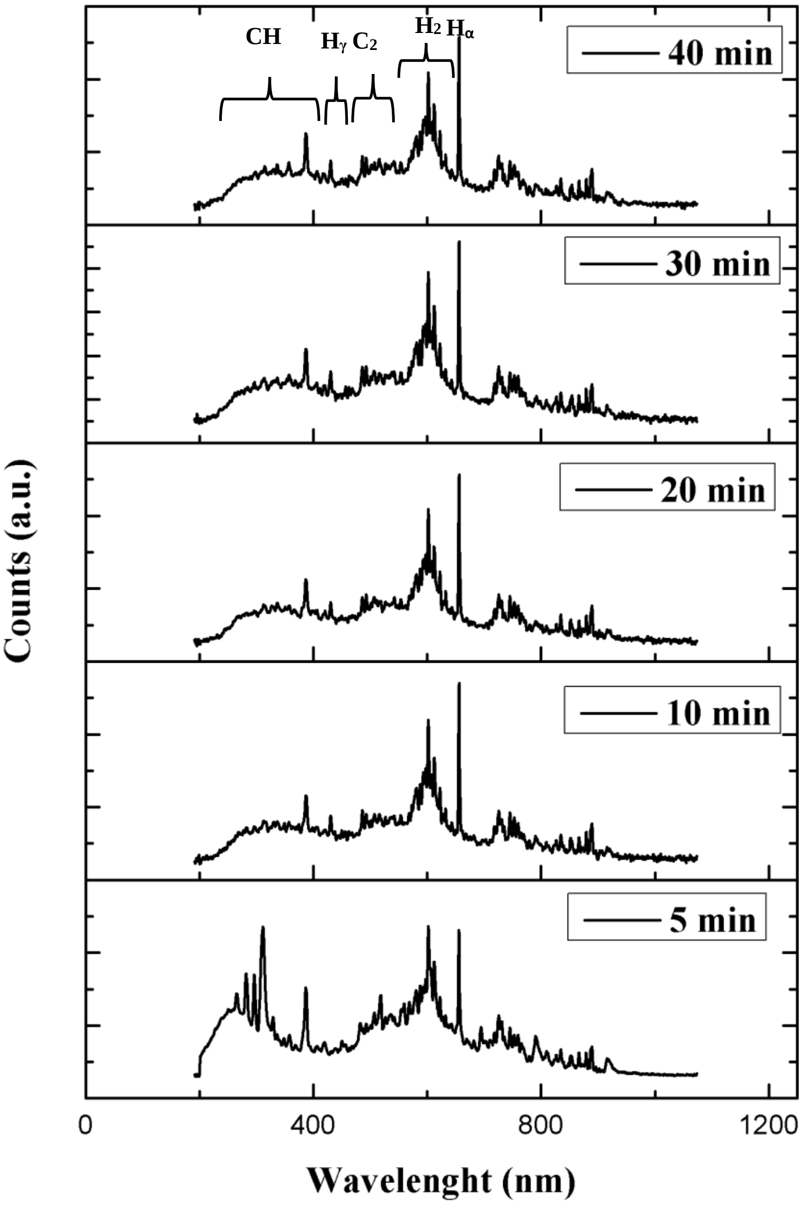

Figure 6.26 Optical emission spectra from the CH_4 methane plasma taken at different deposition times

depends on the CH_4 gas precursor (1:4). H atoms are formed as a result of CH_4 dissociation in a high plasma density and provide effective removal of amorphous carbon (etching), which contributes to the ulterior growth of MLGNWs, where pure hydrocarbon radicals can simultaneously serve as a carbon source or as a by-product after hydrogen etching. Emission lines of CH radicals at 387nm and 430nm, C_2 Swan band system in the range 465–590 nm and Balmer

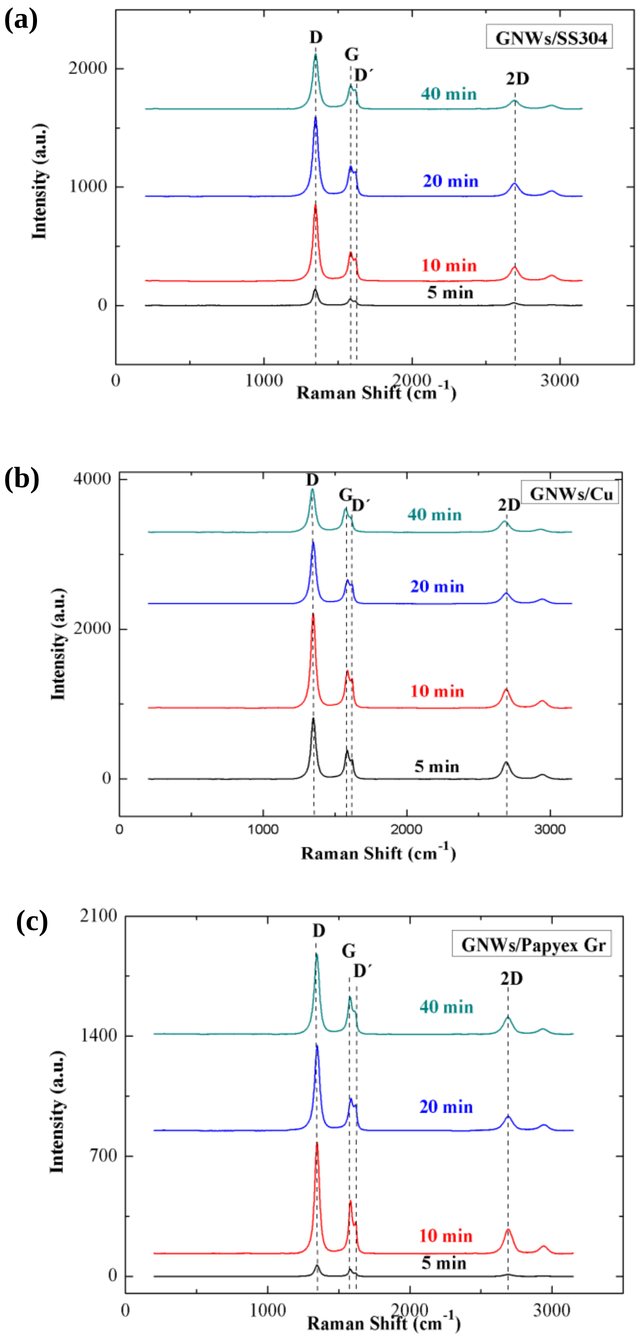

Figure 6.27 Raman spectra of MLGNWs growing in different time, at 650°C, under 10sccm methane flow, plasma power 440W on top of (a) SS304; (b) Cu foil; (c) Papyex® graphite substrates

lines at 410 nm, 434 nm, 486 nm, and 656 nm were also analysed. During plasma deposition CH_4 precursor was able to easily convert to CH_X (x=1-3) radicals, to produce carbon dimers (C_2) through radical recombination and subsequent dissociation [Yoon SF, 2000; Hofmann S, 2004]. The C_2 Swan band system has a large influence on the nucleation process [Mantzaris NV, 1996]. OES spectra within 5 minutes of deposition show a Swan band system with high intensity, which decreases after 10 minutes due to the nucleation in the first stage of growth. The radical density of C_2 ranging from 10^{17}–10^{19} m^{-3}, in ICP system, is favourable for the initial growth of vertical nanostructures [Shiomi T, 2001]. Furthermore, the hydrogen plasma has proven to be effective in promoting the crystallinity of the carbon materials by the following factors: (1) atomic hydrogen can preferentially etch amorphous phase and (2) atomic hydrogen can induce crystallization [Zhu MY, 2007; Vizireanu S, 2010]. Cheng et al. reported that, hydrogen radical etched away loosely bonded carbons and promoted the graphitization in diamond like carbon (DLC) films [Cheng CL, 2005]. In our case the hydrogen radical would etch away disordered components (carbon atoms) such as amorphous carbon rather than ordered, because the bond strength of disordered carbons is weaker than that of ordered ones. Therefore, hydrogen radical would etch away disordered phase selectively and by this way decrease of the disordered carbon formation, which would affect positively to the growth of MLGNWs. Decrement of disorders will also be checked by Raman scattering.

Table 6.5 Summary of the Raman spectral parameters of the MLGNWs on top of different substrates

Material	Time (min)	I_{2D}/I_G	I_D/I_G	FWHM 2D (cm^{-1})	ω_{2D} (cm^{-1})
SS	5	0.4	2.4	59.6	2689.9
	10	0.6	2.1	66.3	2691.8
	20	0.7	1.7	73.4	2691.8
	40	0.8	1.3	75.2	2691.6
Cu	5	0.6	2.1	63.9	2693.6
	10	0.6	1.5	66.1	2692.4
	20	0.8	1.4	72.9	2692.6
	40	0.9	1.2	75.7	2689.5
Papyex Graphite	5	0.2	1.5	67.3	2691.8
	10	0.7	1.6	69.9	2692.8
	20	0.8	1.4	73.7	2691.8
	40	0.9	1.3	74.7	2689.3

The MLGNWs films on Cu foil, SS304 and Papyex® graphite substrates were directly measured by Raman spectroscopy with a laser excitation energy of 532nm (Fig. 6.28). The results of the Raman scattering analysis are shown in Table 6.5. The intensity ratio of the 2D and G bands and FWHM of 2D, indicate number of graphene layers [Ferrari AC, 2007]. Representation of the I_{2D}/I_G, I_D/I_G and $FWHM_{2D}$ peak, versus the growth time for different substrates are presented in Figure 6.28 a, b and c, respectively. Raman spectra for 20 min and 40 min of deposition time for three samples show similar 2D positions and values of $FWHM_{2D}$, I_D/I_G and I_{2D}/I_G, which reflects the similar nature and quality of MLGNWs on different substrates. However, for initial stage of deposition we have different I_{2D}/I_G , I_D/I_G and $FWHM_{2D}$ values (Fig.6.28 a, b), which is related to different nucleation densities such it was discussed above. Moreover, results shown in Fig. 6.28 a, b, c confirm the hydrogen plasma influence on the number of layers and the number of defects, which decrease with plasma exposure time.

Fig. 6.28d shows the evolution of H_α and CH radicals as a function of deposition time from OES measurements, which show that after 5 minutes of growth, the number of hydrogen radicals decreases weakly compared to CH radicals, which present a sustained increase. The high concentration of CH_X radicals in the first minutes corresponds to the first growth stage (nucleation and buffer layer formation), which facilitates the ulterior growth of MLGNWs. These results are directly related to those obtained from Raman scattering (Fig. 6.28a, b, c).

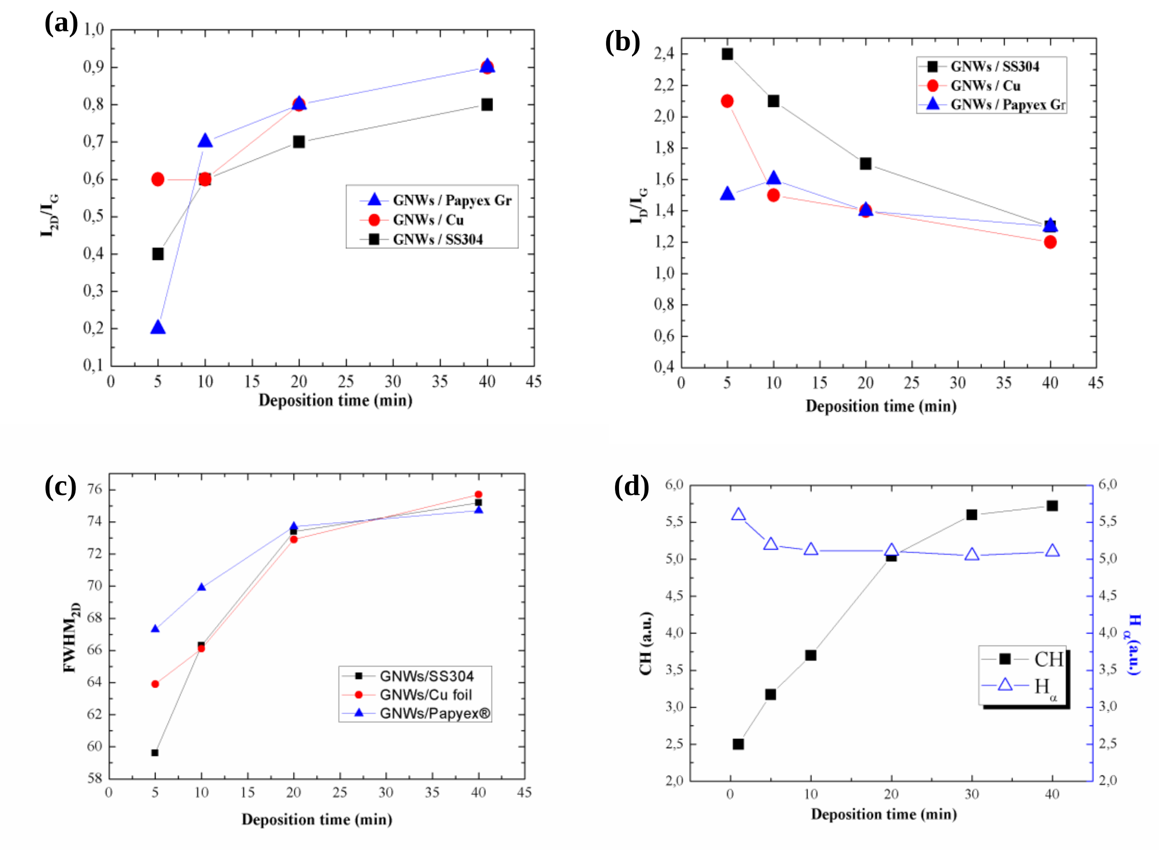

Figure 6.28 (a) Intensity rations I_{2D}/I_G as a function of deposition time; (b) I_D/I_G ration as a function of deposition time; (c) time dependence of H_a and CH radicals

After 10 min of MLGNWs growth, the three samples provide a similar behaviour (Fig.6.28 a, b, c) and confirm that, after the first stage of growth, when the buffer layer is formed, the substrates becomes hidden and their influence on growth minimises. Moreover, the number of defects decreases with increasing intensity of CH radicals probably due to the etching process (Fig.6.28b). In addition, the number of graphene layers (Fig.6.28 a, c) in the MLGNWs structure decreases due to an increase in the CH radicals density in gas phase (Fig.6.28 d), which is a result of hydrocarbon etching [Shiji K, 2005] or due to the long exposition time of the methane precursor gas to the plasma.

ICP-CVD process provides a high MLGNWs growth rate on SS304 substrate with the height of graphene nanowalls from 300 nm to 1000 nm since 10min to 40 min of deposition. Once again, these results confirm that the etching process for this type of deposition is a constructive rather than a destructive process. In a plasma deposition process, the reactive carbon radicals from plasma-enhanced dissociation still contribute to the formation of successive layer at a relatively higher rate if compared to a CVD process [Li XS, 2009].

6.3 Growth temperature study of MLGNWs

6.3.1 Introduction

Temperature is one of the significant growth factors for graphene nanowalls. The temperature in PECVD process can be provided by an external source or by the plasma itself or by combining both. It is reported that a temperature above 500ºC is in demand for obtaining carbon nanostructure [Malesevic A, 2007; Vizireanu S, 2010]. Much lower temperature growth is possible using microwave plasma CVD or helicon plasma enhanced CVD, which permit to grow MLGNWs in 400-700ºC temperature range. The optimum growth temperature was established with the aid of transmission electron microscopy, scanning electron microscopy, and Raman spectroscopy. As compared with thermal CVD, PECVD approach enables graphene deposition at low temperature with better control in the deposition uniformity, due to the presence of energetic and reactive species generated in the plasma region [Sun J, 2015; Bo Z, 2013]. Lowering the substrate temperature is interesting for applications to a broader range of materials and represents a challenge for new production technologies. Low-temperature synthesis can be helpful for substrate materials, which are not compatible with high temperature, for example, in a growth on a polymeric or in a low melting point (glass) substrate. The advantage of using plasma comes from the fact that they are able to fragment molecules into reactive radicals at room temperature. So, in this thesis, we have used the ICP-CVD system, which provides the decomposition of the gas precursor at low temperatures [Hopwood J, 1993]. Moreover, the temperature during the process affects the growth rate, density and morphology of the nanowalls.

In this section we present the main results on the effects of temperature on the properties of MLGNWs.

6.3.2 Experimental part

The growth of MLGNWs was carried out in an inductively coupled plasma-enhanced chemical vapour deposition (ICP-CVD, 13.56 MHz) reactor. Stainless steel SS304, c-Si, Cu foil and Papyex® graphite were used as substrates. These substrates were ultrasonically cleaned for 10 min in the acetone bath, rinsed with deionized (D.I.) water and dried with N_2 pistol. At a low vacuum level in the chamber, 10 sccm of CH_4 was injected into the chamber. CH_4 was used as a precursor gas without dilution and was fed into the reactor for the deposition of MLGNWs. The plasma was generated at a chamber pressure of 50 Pa using 440 W of RF power. The chamber pressure and RF power were kept constant during the growth process. The temperature was measured in situ (attached to the sample holder) and externally using two thermocouples. The oven temperature is controlled by the external K-type thermocouple by means a PID temperature controller. A series of samples of MLGNWs were synthesized at different growth temperatures from 550ºC to 800ºC, in 50ºC increments.

The analyses of morphological and electronic structures of MLGNWs were performed using field emission scanning electron microscopy (FE-SEM) and Raman spectroscopy. In addition, we conducted plasma diagnostics at different growth temperatures using OES.

6.3.3 Results and discussion

FE-SEM

Figure 6.29 shows diverse MLGNWs morphologies grown at different temperatures on different substrates. Diverse growth temperatures lead to different deposition rates on the same substrate material. Lower temperature tends to slow down the deposition rate, which in its turn reduces the possibility of vertical growth. As the temperature increases, a higher nucleation density results and the island growth of graphene happens rather than layer by layer growth [Seah C-M, 2014]. The graphene islands originate the vertical growth of graphene nanostructures, as described in chapter 4.

Vertical nanostructures are not observed on any studied substrate at a growth temperature of 550ºC (Fig.6.29). The absence of MLGNWs at this temperature probably depends on the lower surface mobility of radicals (CH and H) or/and an insufficient radicals density as will be discussed below in OES study, preventing the nucleation of sp^2 structures. SEM images for low-temperature deposition show an irregular continuous structure without any vertical nanowalls. This continuous irregular structure most likely has a-C (sp^2/sp^3) nature, which will be verified by Raman scattering.

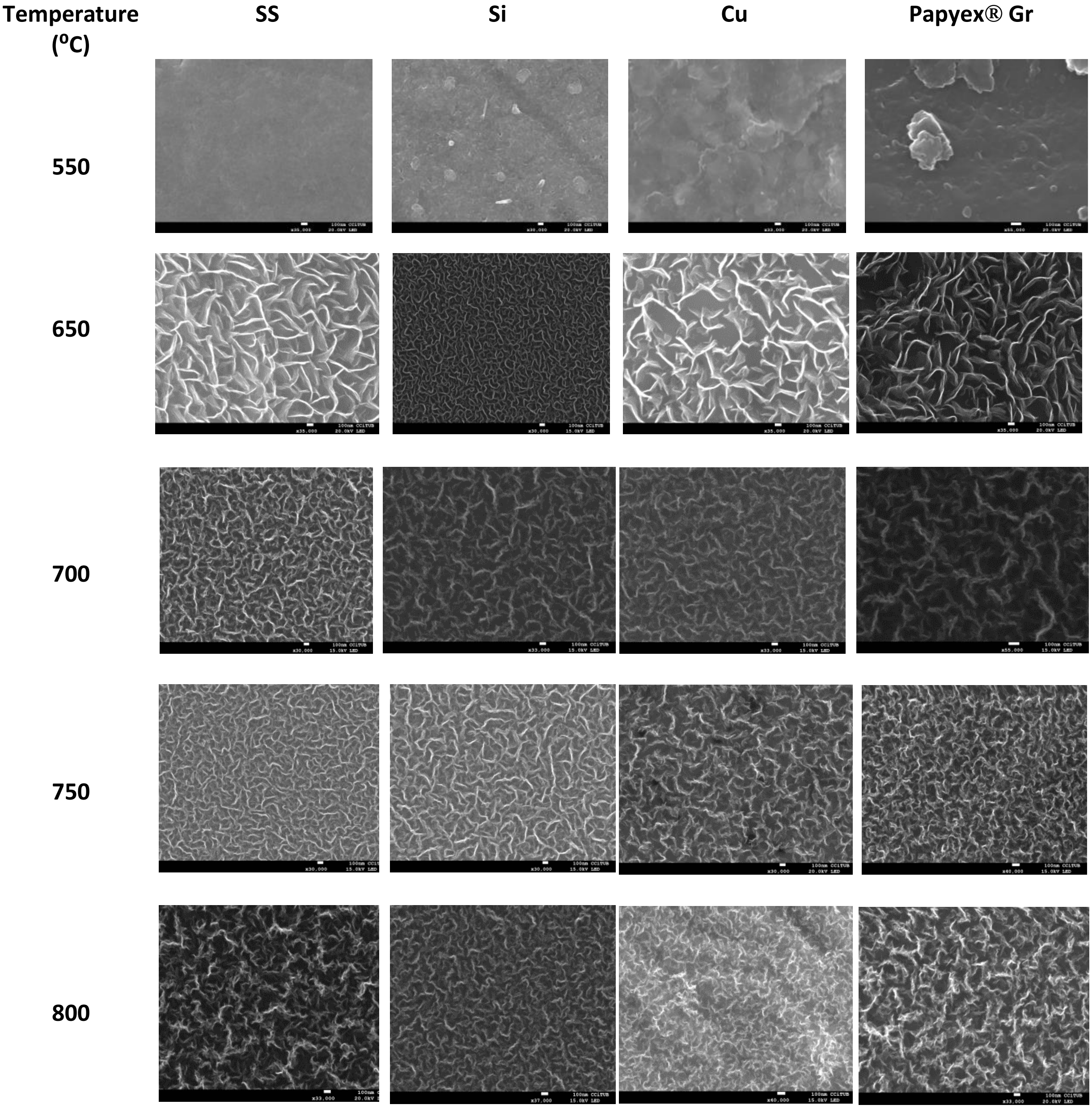

Figure 6.29 SEM images of the graphene nanowalls grown on different substrate at different temperatures under CH_4 precursor gas, 40min , 440W plasma power (18A2901, 18A2903, 18B0902, 18A3101, 18A2902)

For a growth temperature of 650ºC, we obtained MLGNW with straight edges, low density and large inter-wall distance. An increase in temperature up to 800⁰C resulted in a high density and a high degree of corrugation due to secondary MLGNWs formation. High temperature contributes to high growth rate and high density. When comparing the morphologies and the evolution of growth in the various substrates, the difference is negligible. Fig. 6.30 shows the SEM crosssectional images of the MLGNWs at different growth temperatures and with different materials. The cross section view images evidence that, the height of MLGNWs increases with temperature. The graphene sheets grown at low temperature have leaf shape morphologies, and at high temperatures, graphene scales grow on the primary nanowalls in all the samples. Fig 6.31 shows the height variation in accordance with the temperature of growth. This graph shows a sustained increase in the height of the MLGNWs with increasing temperature. MLGNWs grown on SS304 substrate have a high growth rate, as compared to the other substrates.

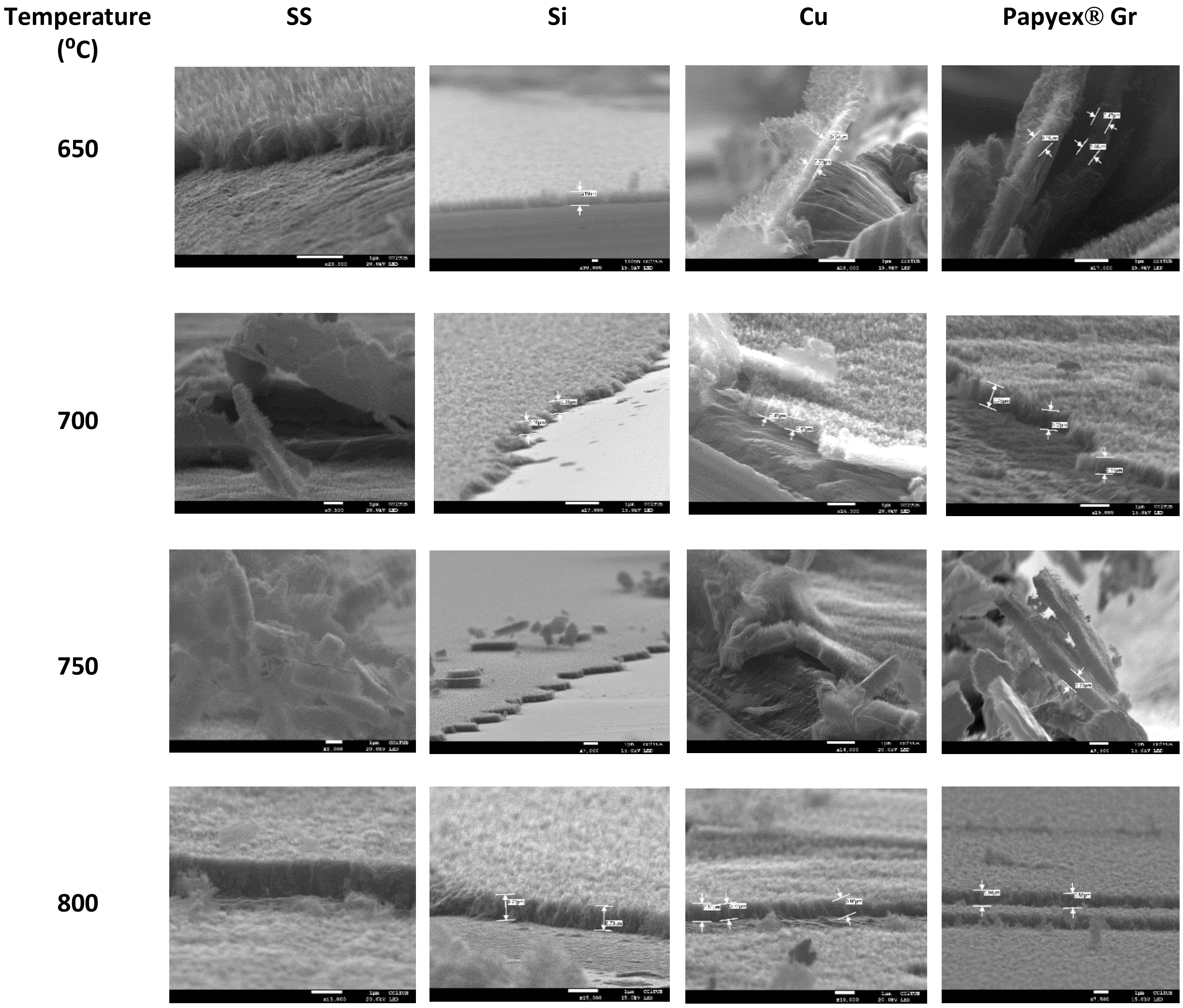

Figure 6.30 Cross-section SEM images of the graphene nanowalls grown on different substrate at different temperatures under CH_4 precursor gas, 40 min, 440W plasma power.

To study the growth kinetics of ICP-CVD MLGNWs grown on different substrates, we calculate the activation energy E_a for vertical graphene growth using the Arrhenius equation:

$$\alpha = ae^{-E_a/kT} \qquad (6.1)$$

where, α represents the rate constant, E_a is the activation energy, k is the Boltzmann's constant $(8{,}6173324\cdot10^{-5}\ \text{eV}\cdot\text{K}^{-1})$, T is the temperature expressed in Kelvin and a is known as the frequency factor. From the Arrhenius plot shown in Figure 6.32, we obtain E_a for MLGNWs grown on c-Si (0.679eV), SS304 (0.328eV), Cu foil (0.423eV) and Papyex® (0.324eV). Remarkably, activation energy was found significantly lower because the catalytic nature of Cu foil and SS304 substrates and the particular composition of Papyex® based on pure graphite. As

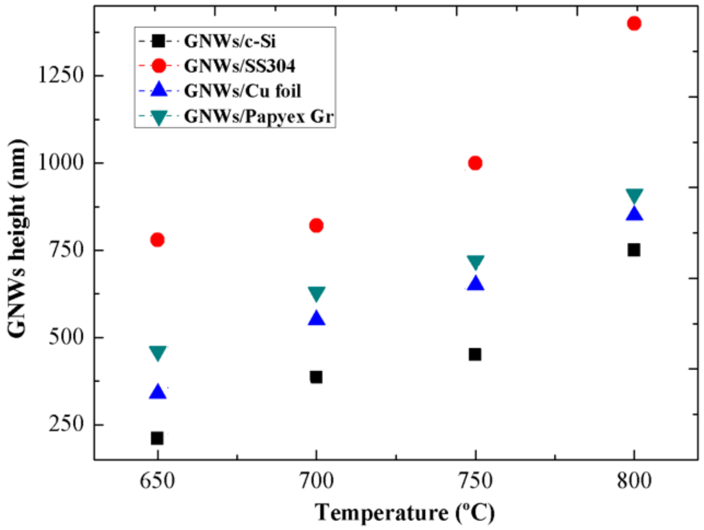

Figure 6.31 Heights of the MLGNWs according to the growth temperature

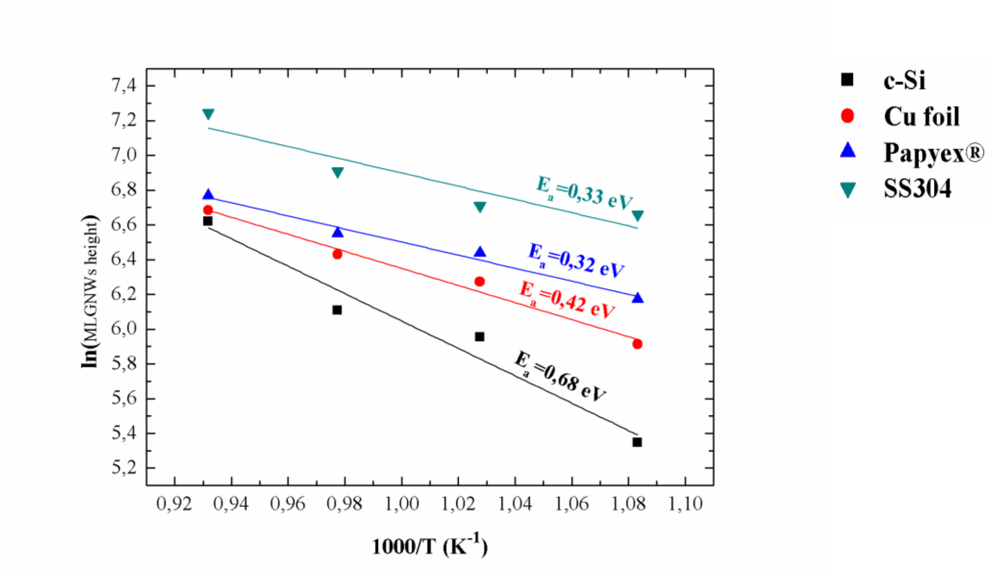

Figure 6.32 Arrhenius plot of the natural logarithm of MLGNWs height as a function of 1000/T. The activation energy for the growth of graphene nanowalls is computed from the slope of the linear fitting.

we observed above (§6.1) MLWGNWs grown on SS304, Cu foil and Papyex® have a high nucleation density and a small grain size, as compared with c-Si which is provides slightly different growth conditions and growth rate.

Fig. 6.33 evidences an increase in grain size and nucleation density with activation energy. Papyex® substrate has an unwanted low nucleation density, whose value does not correspond to the behaviour of the other samples. At this point, we should note that unlike other substrates, the growth on Papyex® corresponds to a homogeneous nucleation. The nucleation density reaches the order of 4×10^{14} on a meter square and drops to 0.3 x10^{14} as the activation energy rises from 0.328 to 0.679 eV. On the other hand, the average grain size increases from 7.7 to 22.5 nm at 0.324 eV and 0.679 eV, respectively. Kim et al. has suggested a wide range of activation energies (1–3 eV) for graphene nucleation and growth on Cu by CVD [Kim H, 2012]. However, our results for vertical graphene grown on Cu substrate (E_a=0.422eV) evidence that plasma deposition reduces significantly the activation energy and provides the possibility of deposition at lower temperatures.

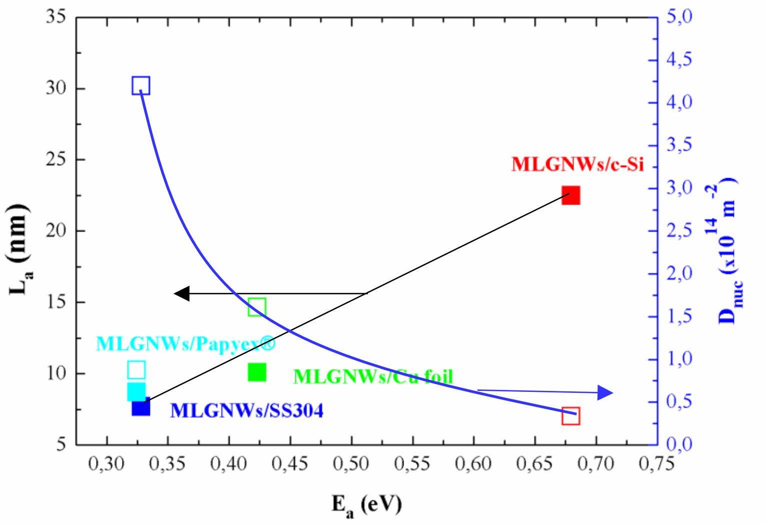

Figure 6.33 MLGNWs nucleation density and grain size as a function of activation energy

Raman scattering

Fig. 6.34 shows the Raman spectra of the MLGNWs grown on c-Si and SS304 substrates at a temperature range 550-800ºC. 2D band is absent from the sample grown at 550 °C and this spectrum points to a-C structure. Raman spectrum of amorphous carbon phase is composed of D peak located in the range of 1320 to 1360 cm^{-1} and a G peak located from 1500 to 1600 cm^{-1}. The physical properties of amorphous carbon strongly depend on the ratio of sp^3/sp^2 carbon phases. It depends on deposition conditions and can be changed in a broad range as it becomes reflected in their Raman spectra [Ferrari AC,2004a; Schwan J,1996]. The rest of the samples shows a high D peak, which corresponds to the disordered graphene growth. Figure 6.34 evidences that the possibility of MLGNWs growth appears at temperatures as low as 650ºC.

Table 6.6 Raman peaks corresponding to MLGNWs grown on various substrates at different temperatures by ICP-CVD

Materials	**Temperature (^{0}C)**	**L_{Wall} (nm)**	**I_{2D}/I_G**	**I_D/I_G**	**$I_D/I_{D'}$**	**ω_D (cm^{-1})**	**ω_G (cm^{-1})**	**ω_{2D} (cm^{-1})**	**W_{2D} (cm^{-1})**	**L_a (nm)**
SS	**550**	-	-	1.6	3.6	1349	1595.4	-	-	12
	650	780	0.2	2.7	4	1347.9	1588	2689.8	80.4	9.1
	700	820	0.47	2	4.3	1349.7	1587.7	2692.4	71.7	11.3
	750	1000	0.4	2	4.3	1348.8	1587.5	2691.4	69.5	10.1
	800	1400	0.4	2.7	4.4	1348.6	1587.3	2691.4	66	7.1
Si	**550**	-	-	1.5	3.3	1345	1604.7	-	-	13
	650	210	0.5	1.8	4.2	1351	1586.9	2693.9	65.1	16
	700	385	0.6	1.2	3.4	1350	1582.3	2695.8	65.3	16
	750	450	0.8	1.3	4	1351	1583.2	2695.1	58.1	17.4
	800	750	0.3	1.3	3.7	1346	1581	2684	79.2	17.4

Raman spectra of MLGNWs grown on c-Si and SS304 show that the D band and G band were found in all the samples explored in this study. Thus, the increase of disorder and defective states of the synthesized MLGNWs identified over the entire temperature range seems to be originated from plasma deposition, because it is known that carbon nanowalls grown by plasma contain a lot of structural defects and conditionally may be described as an agglomeration of nanometric size graphene-like domains [Kobayashi K, 2007]. Thus, appearance of D mode at temperatures higher than 650ºC may be associated with the presence of both carbon nanowalls and domain edges. Taking into account I_D/I_G ratios shown in Table 6.6, the estimated domain linear size can be calculated from the equation of Cançado et al.(Eq.5.1). For our samples the domain size varies from 7 nm to 12 nm for MLGNWs/SS304 and 13-17nm for MLGNWs/c-Si at a temperature range 550ºC-800ºC. Fig.36d shows the plot of L_a in front of growth temperature for MLGNWs/c-Si and MLGNWs/SS304. Results point to significative decrease of L_a due to the secondary nucleation on SS304.

The intensity ratio of the D band and G band, the G band position and the intensity ration of the 2D band and G band (I_{2D}/I_G) are important characteristics of deposited material (Figure 6.36). In view of Figure 6.36, the behaviour of the sample grown at the lowest temperature of 550ºC is different from the rest of temperatures. As we discussed earlier, it could be because this sample has an amorphous carbon nature, different from the others. The I_D/I_G ratio for MLGNWs grown on c-Si and SS304 at 550ºC has a similar behaviour and suggests that the growth of MLGNW at low temperature forms a similar disordered structure regardless of the substrate material. However, the temperature jump affects differently on these two substrates.

Fig.6.35a shows the I_D/I_G ratio as a function of deposition temperature for MLGNWs grown on SS304 and c-Si. The balance among the disordered and crystalline character is generally quantified by the I_D/I_G ratio [Ni ZH, 2006; Kurita S, 2005]. The observed large D band intensity is due to the presence of disorder which arises from the large amount of edge states, sp^3 bonded C-H species and ion induced defects from the plasma during growth. In the case of MLGNWs/c-Si, the number of edges/defects initially decreases and stabilizes at high temperatures.

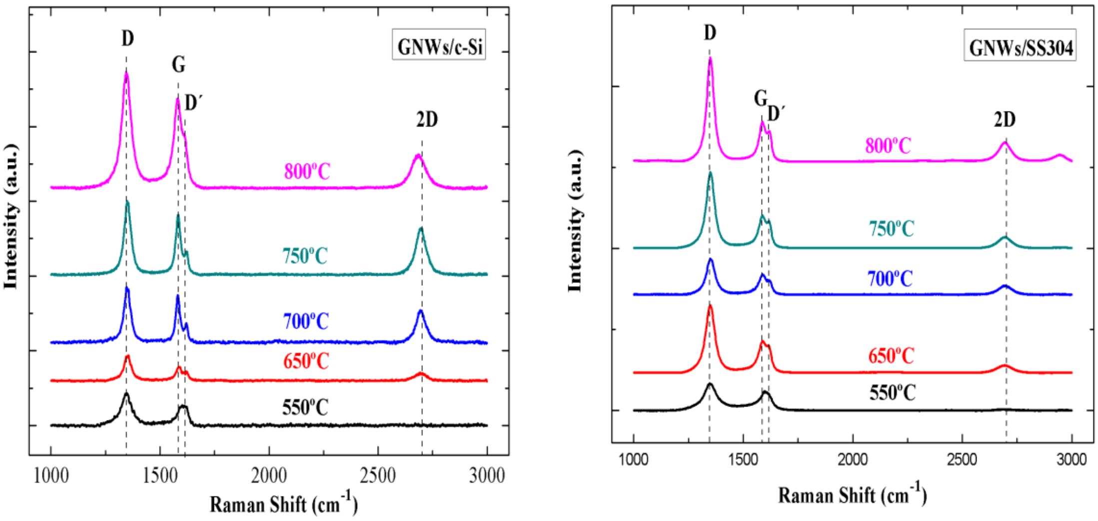

Figure 6.34 Raman spectra of the graphene nanowalls grown on different substrate at different temperatures under CH_4 precursor gas, 40 min, 440 W plasma power

In contrast, in the case of MLGNWs/SS304 initially decreases like MLGNWs/c-Si, but at 800ºC after happening the second nucleation (Fig.6.29 at 800ºC for SS304) the number of edges increases, which provides I_D/I_G ratio increases. The number of disorder defects for SS304 increased with the temperature and provided high growth rate. In contrast, MLGNWs grown on c-Si has less defects and low growth rate. These results once again evidence that the disorder plays an important role in the growth rate of MLGNWs.

In addition, for graphene nanowalls samples it was shown that the $I_D/I_{D'}$ ratio does not depend on the concentration of defects, but it is sensitive to the type of defects [Eckmann AA, 2012]. For our MLGNWs, the value of $I_D/I_{D'}$ ratio varies between 3.3 and 4.4 (Table 6.6), which indicates a presence of boundary-like defects in a carbon nanowalls structure. The defect types did not change with the temperature and with the substrate material. In addition, an increase in growth temperature leads to a decrease in the position of G peak from 1595cm^{-1} (1605cm^{-1} for MLGNWs/c-Si) to 1587 cm^{-1} (1581cm^{-1} for MLGNWs/c-Si) for the MLGNWs grown on SS304 substrate indicating the improvement in crystallinity [Casiraghi C, 2009].

Moreover, an increase of stress is accompanied by the movement of G peak to a higher wavenumber. Fig. 6.35b evidences that, at low-temperature deposition, the G peak appears at high frequency for two different samples, which is associated with stress. After ~550ºC, the G peak position decreased sharply with increasing temperature and remained stable for SS304 and decreased for the c-Si sample.

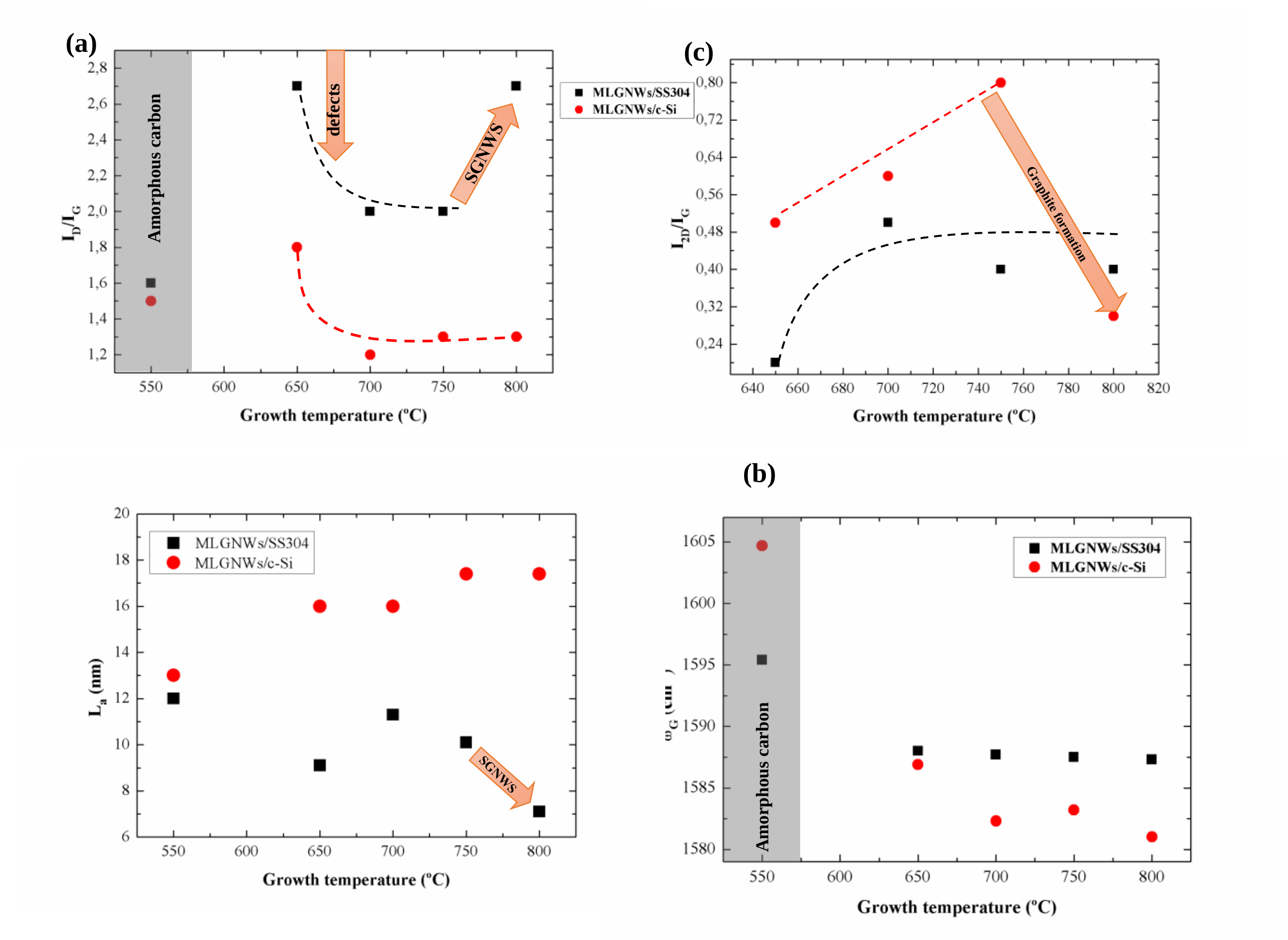

Figure 6.35 (a) G-band shift; (b**)** I_{2D}/I_G and (c) I_D/I_G ratios of the MLGNWs according to the growth temperatures

The second-order Raman peak (2D) does not depend on the presence of the defects, however, its position, FWHM and shape are sensitive to the layer stacking character, namely, turbostratic stacking or ABAB (like in graphite) [Krivchenko V, 2013]. For carbon nanowalls the 2D peak is symmetrical and relatively broad, thus indicating the apparently turbostratic structure. Importantly, ratio of 2D and G bands indicate the number of graphene layers [Ferrari A, 2007, *2009*]. The grown vertical nanostructures with the value of I_{2D}/I_G ratio ~0.6 and the width of the 2D band ~80 cm^{-1} correspond to multilayer graphene. MLGNWs grown on c-Si substrate in the temperature range 650ºC-750ºC, the number of graphene layers decreases as temperature increases. However, MLGNWs/c-Si grown at 800°C, the number of layers suddenly increases, probably because, at this temperature, a graphite deposition process was carried out on all the walls of the quartz reactor. MLGNWs/SS304 grown in the temperature range 650ºC-800ºC presents an initial increase of the I_{2D}/I_G ratio (decrease of number of layers) and keeps at a low value at higher temperatures. The number of the layers for MLGNWs/c-Si at the 650ºC-750ºC temperature range is lower than MLGNWs/SS304.

OES analysis

In addition, the influence of the growth temperature on the chemical reaction in the plasma has been studied. As we have verified above, below 550ºC, the growth of MLGNWs was not detected in any of the tested substrates. It means that after the first stage of nucleation, the substrate does not play a key role in the formation of MLGNWs. Therefore, the cause of the formation of MLGNWs should be sought in the conditions and chemical reactions within the plasma.

Plasma diagnosis was carried out using optical emission spectroscopy (OES). Fig. 6.36 shows an OES spectrum for the CH_4 plasma in the ICP-CVD system with a plasma power of 440 W and a pressure of 50 Pa at different growth temperatures. For plasma diagnosis, the deposition time was 10 min, which is corresponding to the first stage of growth. For different growth temperatures, plasma produced the same OES bands with diverse intensities. Fig. 6.36 shows OES with a variety of species produced by plasma. After a series of studies of plasma diagnostics, it was found that of all chemical species formed by plasma there are two more prominent, which play an important role in the process of deposition of MLGNWs: CH_x carbon radicals, which mostly contribute to the deposition of amorphous carbon, and atomic hydrogen, which activates the surface dangling bonds and etches away the amorphous carbon phase [Vizireanu S, 2010]. Fig. 6.37 shows CH and H_α emission intensities as a function of growth time at different growth temperatures. The most intense emission comes from the CH transition for four diverse growth temperatures. Except C_2 species (responsible for the nucleation stage), also CH play crucial role in the alignment and future vertical growth of graphene nanowalls [Shiji K, 2005; Obraztsov AN, 2003].

OES is a powerful technique for valuable real-time study of species intensities without disturbing the plasma. However, the studied spectra contain information about the gas phase without information about the formation of species on the solid state (substrate). Therefore, at high temperatures (higher than 750ºC) the carbon precursor species decrease due to their condensation on all the walls of the hot region of the reactor. This has been evidenced by the black deposition on the internal walls of the quartz tube.

Atomic hydrogen is the second most intense emission, which leads to the elimination of amorphous carbon. The intensities of atomic hydrogen and CH transition are lower for 550ºC growth temperature as compared with relatively high temperatures. It should be noted that for low temperature the structure of graphene nanowalls was not observed. At 550 °C, insufficient radicals do not lead to the vertical graphene growth. Starting from 650ºC the number of CH radicals increases in a factor 2, which leads to the growth of MLGNWs. For relatively high growth temperatures (from 650ºC to 750ºC), the etching (atomic hydrogen) and growing (CH_x) processes were balanced and it provided the vertical growth of graphene.

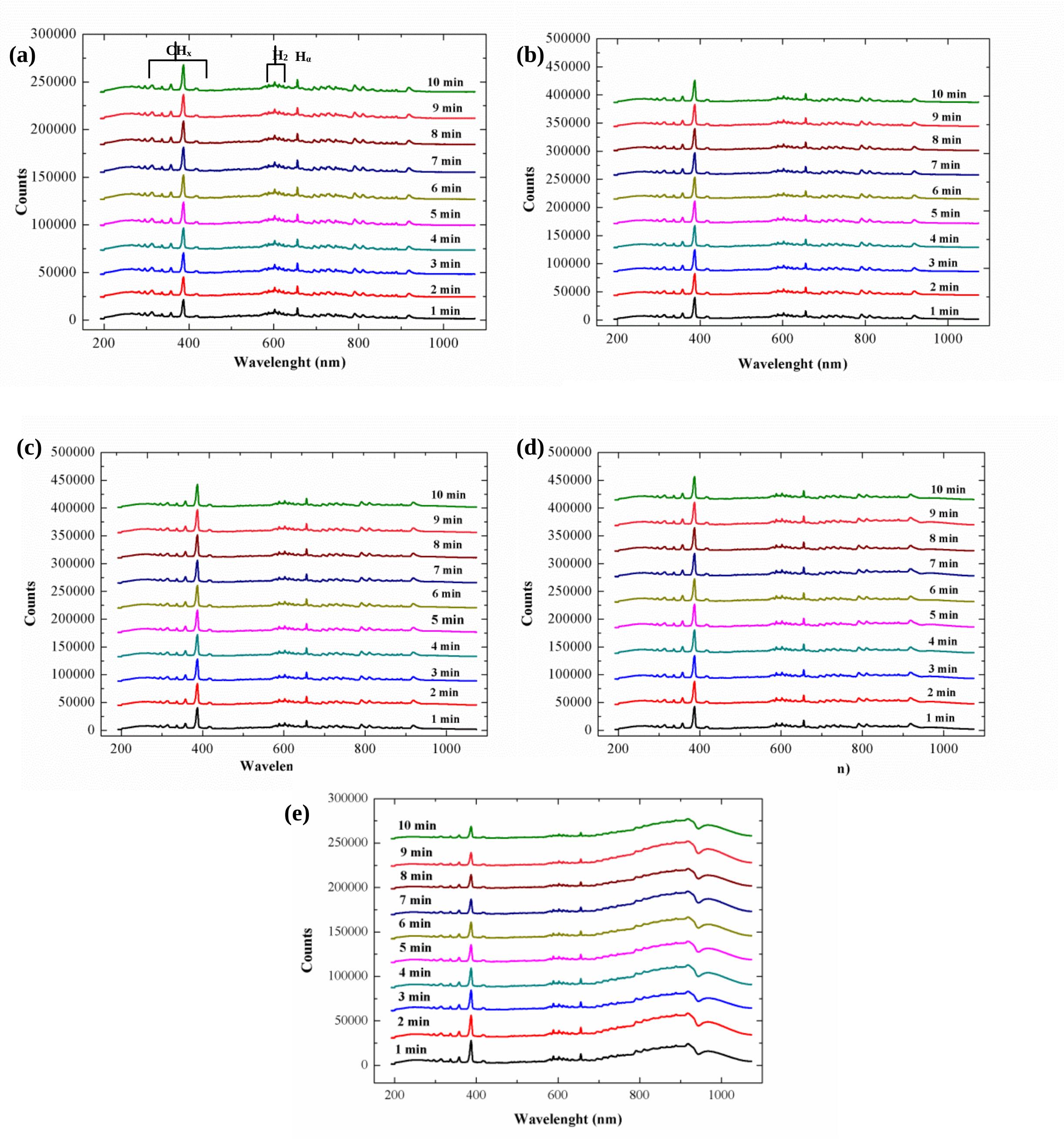

Figure 6.36 Optical emission spectra for ICP-CVD with CH_4 as precursor gas, power of 440 W, pressure of 50 Pa at different growth temperatures (a) 550ºC; (b) 650ºC; (c) 700ºC; (d) 750ºC and (e) 800ºC

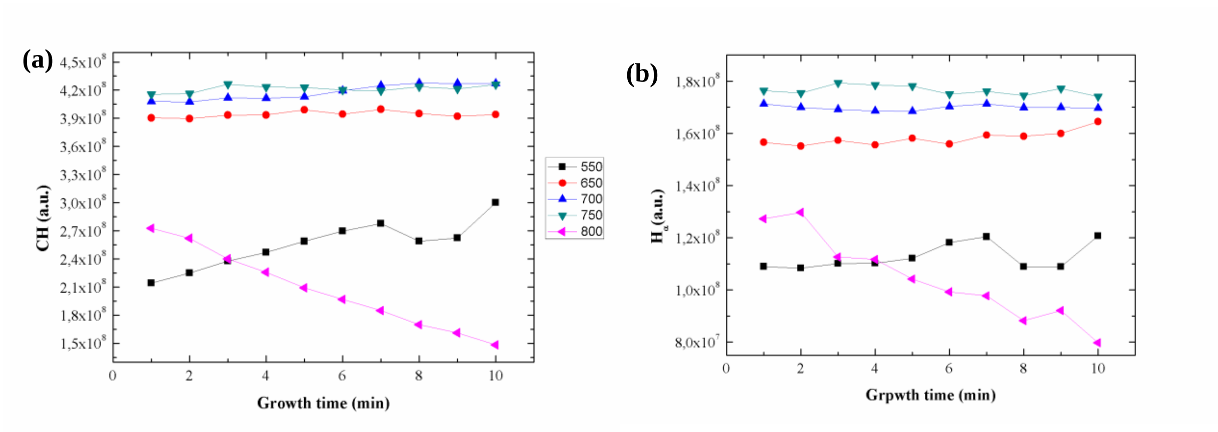

Figure 6.37 (a) CH and (b) H_α radicals as a function of growth time for temperature range 550ºC-750ºC

6.3.4 Conclusion

So, from this temperature study, we have concluded that, the successful MLGNWs grown process starting at 650^{0}C. In addition, we observed that activation energy is at least 2 times lower for graphene grown by PECVD than by CVD. The lower value of activation energy (0.42 eV) allows deposition at low-temperature. The morphology of the MLGNWs grown on different substrates shows a higher nanowalls density and height with increasing growth temperature.

The Raman scattering shows the different behaviour of MLGNWs grown on SS304 and c-Si substrates. In the case of MLGNWs/SS304 the number of defects, for the temperature range of 650ºC-800ºC, is higher than for MLGNWs/c-Si. Moreover, MLGNWs grown on c-Si substrate have a small number of graphene layers in the temperature range of 650-750ºC and above 750ºC, the number of layers increases due to the graphitic structure formation. For MLGNWs/SS304, the graphite structure (more than 15 graphene layers) is observed over the entire temperature range and for that reason the difference is not noticed at 800ºC.

MLGNWs synthesis on different substrates at different temperatures depends on the number of the radicals in the gas phase, ions and other active species formed during the plasma deposition. For temperature range 650ºC-750ºC the hydrocarbon and atomic hydrogen radicals do not show sudden changes. These decreased intensities result in differences in the dissociation mechanism of hydrocarbon precursor, such as for temperatures 550ºC and 800ºC.

Chapter 7

MLGNWs/CNTs hybrid structure Morphology and electrochemical characterizations

7.1 Introduction

Carbon nanostructures are a numerous set of very varied morphologies associated with the numerous possibilities offered by plasma deposition, which is a common way of synthesis of materials with nanoscale characteristics [Ostrikov K, 2007]. Graphene nanowalls, as discussed in many articles, have a high interest in a huge number of applications. For example, vertical orientation improves the mechanical stability of graphene, which is from the device perspective on electronic, optoelectronic, and electrochemical applications can enable new designs and potentially improve the device performance [Seo DH, 2011; Bo Z, 2013]. On the other hand, self-organized graphene nanostructures, comprised of planar graphene multilayers, have a high surface-to-volume ratio, high aspect ratio and abundant open channels between the sheets, which make them useful materials for sensors and electrochemical devices that require maximized accessible surface area [Yang J, 2015; Chen Q, 2017]. In addition, in our experience, MLGNWs do not require catalytic substrates for growing. They can be grown on substrate of different nature (metals and semiconductors, ceramics and oxides). Thus, MLGNWs are considered to be one of the most promising carbon materials used for nanoscale electronic devices. However, they have some limitation, which requires additional research. One of the main drawback is the difficulty in the selective control of growth of graphene nanowalls on different places, because, unlike the carbon nanotube growth, carbon nanowalls can be grown on a variety of substrates without the use of catalyst. This is an advantage and a disadvantage at the same time.

In order to solve this problem, different growth rate and morphology on different substrates have been studied as a control method of selective area or position-controlled growth. In this chapter, we will discuss the selective growth of MLGNWs by using carbon nanotubes (CNTs) sample as a substrate material. In addition, also was observed MLGNWs growth on capillarity-driven assembly of CNTs. The outstanding properties of the cellular pattern of CNTs may lead to applications for these structures as shock-absorbing reinforcements, in nano-filtration devices and in elastic membranes. Moreover, MLGNWs growth on the cellular pattern, CNTs may enable the high efficiency of these applications, due to the huge number of open edges and the large possibility to functionalization.

7.2 Experimental part

In order to carry out a selective area growth of MLGNWs, we have used a hybrid structure of MLGNWs/CNTs. For the MLGNWs synthesis, a substrate of c-Si (p-type boron doped) was used, on which vertically aligned CNTs were previously grown with water assisted CVD. For that, before CNTs growth, a 10 nm diffusion barrier layer of alumina was deposited by reactive sputtering from an Al target. Then, prior to the sputtering deposition, the reactor was purged down to a pressure of 4×10^{-4} Pa and the aluminium target was cleaned during 10 min at a flow rate of 20 sccm of argon to remove the thin oxide layer. Afterwards, the Al target was sputtered with a mixture of Ar/O_2 (17 and 3 sccm, respectively) during 100 s at a pressure of 1Pa and 120W of plasma DC-pulsed power to render a 10 nm layer of alumina. Next, samples were introduced in a CVD/PECVD homemade reactor [Amade R, 2011] (Fig.7.1). Once the base pressure inside the reactor was $4x10^{-4}$ Pa, 128 sccm of Ar were introduced and a 2 nm thick layer of Fe catalyst was sputtered on the Al_2O_3 /c-Si substrate under a pressure of 2 Pa and plasma power 60W. Then, without breaking the vacuum to avoid oxidation of the catalyst, the sample was placed under a heating element inside the reactor in order to anneal the catalyst layer and grow the CNTs (Fig.7.2). The heating element consists of a graphite resistance (2Ω) placed above the substrate and connected to a DC power supply. The temperature on the top surface of the sample was monitored using an external optical pyrometer, and controlled by a feedback loop with the DC power supply using a proportional-integral-derivative (PID) controller. The whole process was controlled by LabVIEW software. Annealing of the catalyst thin film was done at temperatures up to 600ºC with a ramp time of 750s in a reducing atmosphere of hydrogen (100 sccm) at a pressure of 2 mbar. After a hold time of 120 s the pressure inside the reactor was lowered down to 1 mbar and C_2H_2 was introduced into the chamber (100 sccm). Then, the temperature was rapidly increased during the next 10 s up to 700ºC. The water flask outlet was opened ~15 s after the introduction of C_2H_2. The calculated water flow was 0.04 sccm, controlled by opening ~0.5 mm the circular scale of a metering valve [Hussain, 2014]

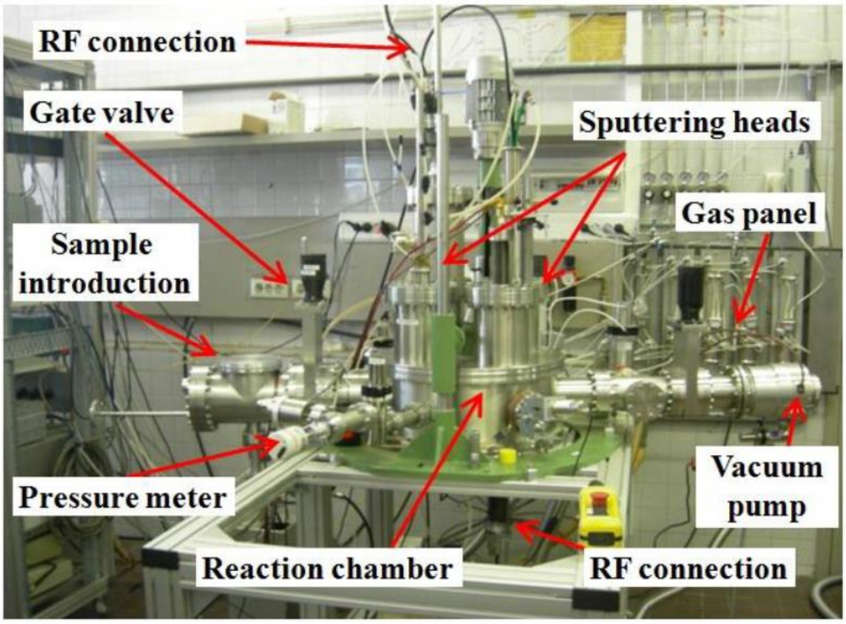

Figure 7.1 Plasma enhanced chemical vapour deposition (PECVD) reactor for CNTs growth.

A honeycomb like lattice of CNTs was formed by wetting nanotubes with water and drying with N_2 at room temperature [Chakrapani N, 2004]. After obtaining CNTs, the sample was transferred to an ICP-CVD reactor, where MLGNWs synthesis takes place. MLGNWs growth was carried out under methane gas flow at 750^{0}C, during 40 min with an RF power of 440W.

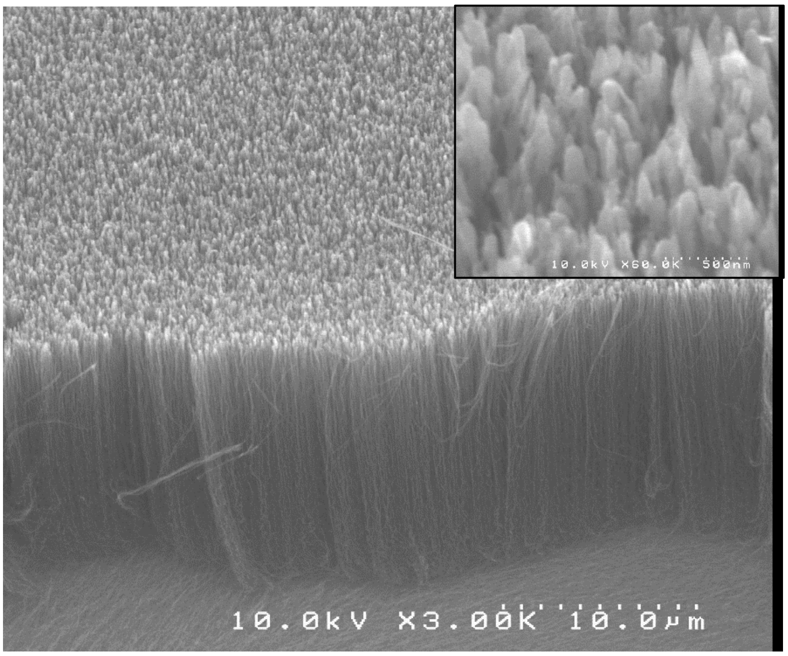

Figure 7.2 FE-SEM images of CNTs

7.3 Results and discussion

The vertically oriented 3-D hybrid structure MLGNWs/CNTs/c-Si have been characterized by scanning electron microscopy, transmission electron microscopy, selected area electron diffraction pattern (SAED), Raman spectroscopy and nitrogen gas adsorption-Brunauer-Emmet-Teller (BET). This approach is capable of producing selective growth MLGNWs with large quantities and with high purity. Moreover, a high-purity hybrid 3D structures have an enormous potential for applications in electronic devices, biological sensors, gas uptake and storage, fuel cells, lithium ion batteries and supercapacitors.

SEM analysis

Figure 7.3 shows a top-view and cross-section view of the FE-SEM micrograph images of CNTs (~14 μm long) structures decorated by MLGNWs. The MLGNWs/CNTs/c-Si forest shows a uniformly flat surface with high density. CNTs are only covered on the top part due to their high density (Fig.7.3b, c). Fig.7.3c shows in more detail the nanowalls structure at the CNTs edges. The penetration of nanowalls inside nanotubes is very superficial, as shown in Fig.7.3c. The full coverture of CNTs with the high edge density of MLGNWs enables to increase the surface area of a three-dimensional framework of the CNTs. For obtaining one by one covering of CNTs with MLGNWs is necessary density control growth of CNTs. However, this is one of the tasks that need to be improved.

In this work we have used water patterned CNTs for obtaining 3D structure with low density,

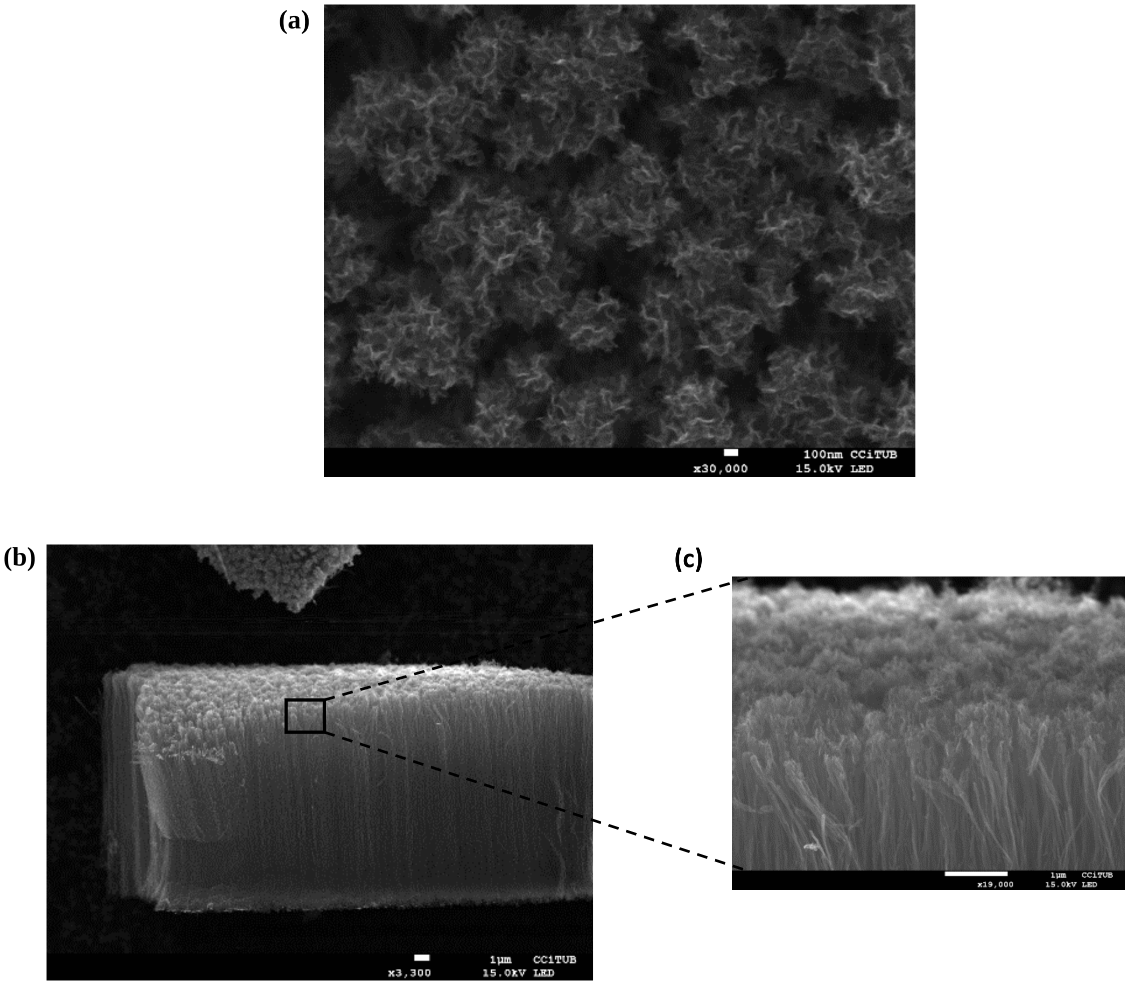

Figure 7.3 FE-SEM image of MLGNWs/CNTs/c-Si substrate (a) top view; (b) cross-section view; (c) highly magnified image of MLGNWs on vertically aligned CNT structure

which will lead to a growth of nanowalls on the open honeycomb CNTs structure (Fig.7.4). The honeycomb like microstructures were formed after dipping CNTs/c-Si substrate inside deionized water and dried with nitrogen (Fig.7.4). Fig.7.4b shows the two parts of the CNTs/c-Si sample as is and immersed in water. These self-assembling honeycomb structures were formed by attractive forces of aggregation due to capillarity [Lim X, 2010; Chakrapani N, 2004; De Volder M, 2010; De Volder M, 2013].

A honeycomb cell comprises two main parts, vertically standing CNT microwalls and a collapsed CNT sheet on the bottom area. As shown in the Fig.7.4a honeycomb microstructures are polygonal, composed of mainly hexagons, from triangles to octagons. After honeycomb microstructure formation, MLGNWs growth was repeated under the same conditions. The temperature in the growth process of the MLGNW has no effect on the CNT honeycomb morphology, but the CNTs layer that initially covered the lower area in the centre of the

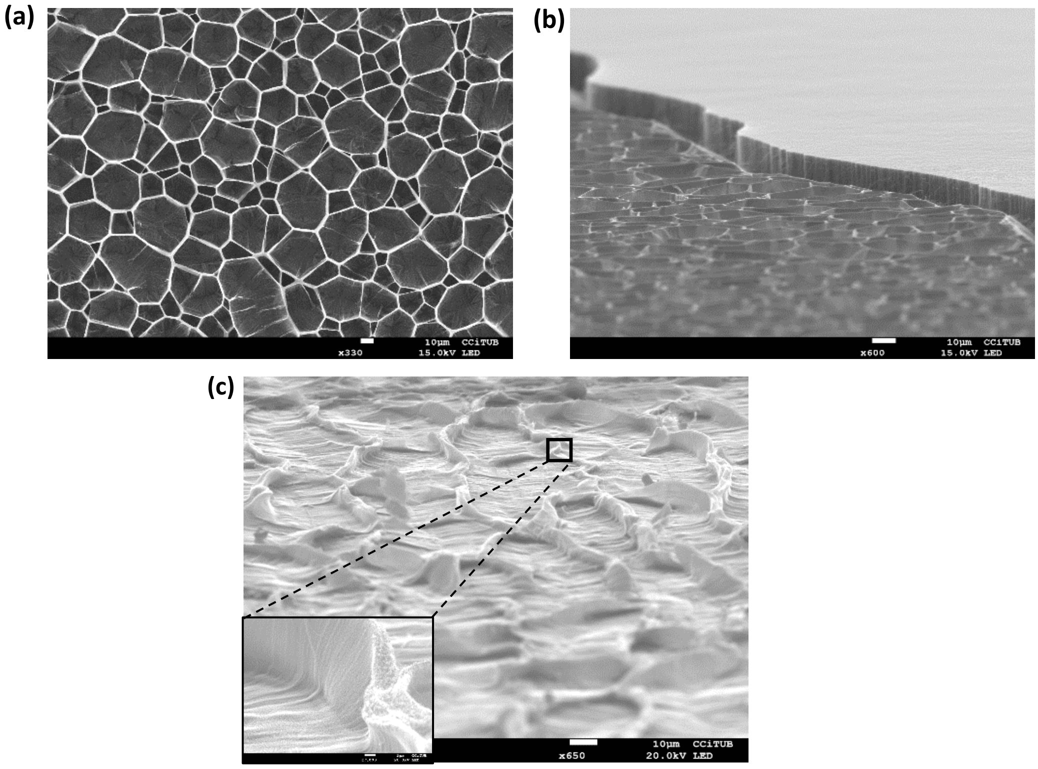

Figure 7.4 FE-SEM micrographs of CNT honeycomb structures CNTs/c-Si; (b) cross-section view of CNTs microstructures with and without water assistance; (c) cross-section view of honeycomb microstructure and walls size in the under-left inset image

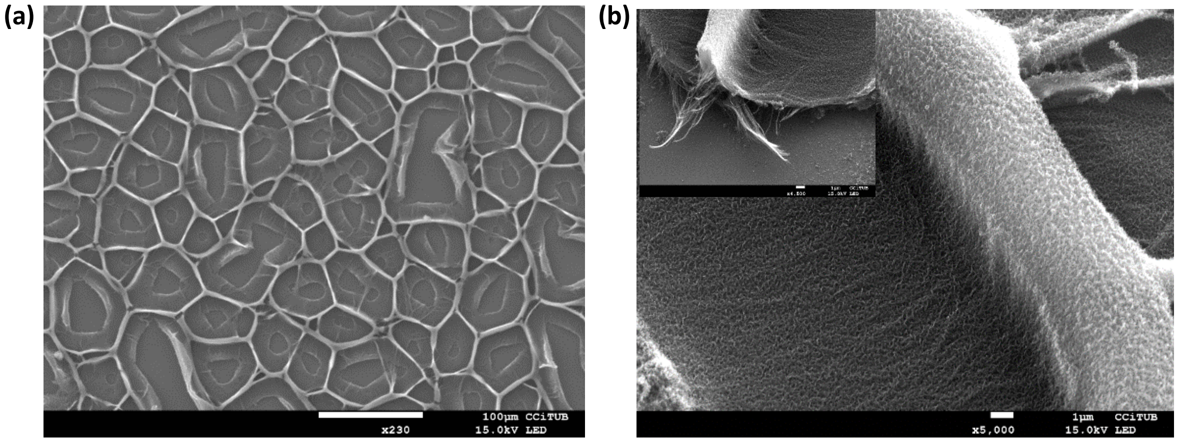

Figure 7.5 (a) FE-SEM micrographs of the top view of MLGNWs/CNTs/c-Si honeycomb like microstructures; (b) high resolution SEM image of MLGNWs/CNTs/c-Si honeycomb microstructure (cross-section view of GNWs/CNTs/c-Si honeycomb microstructure in the upper-left inset image)

microstructures appeared peeled, leaving the silicon substrate uncoated (Figure 7.5a). This could be associated with the high-temperature synthesis and rapid cooling, which provides stress in the microstructures and patterns with average wall height of 8 μm (Fig. 7.5b, inset).

TEM analysis

Further, the morphology of 3D hybrid structures was also analysed by TEM, high resolution TEM and selected-area electron diffraction (SAED) (Fig. 7.6). Fig. 7.6a and Fig.7.6b evidence stacking honeycomb CNTs structures totally covered with graphene nanowalls, which are composed of periodic graphene layers. Furthermore, Fig.7.6a shows a denser region (black) corresponding to the set of CNTs tips, where are located the Fe catalyst particles. Figure 7.6c (inset image) shows the SAED pattern of MLGNWs. SAED pattern shows the typical multilayer graphene rings with a slight orientation.

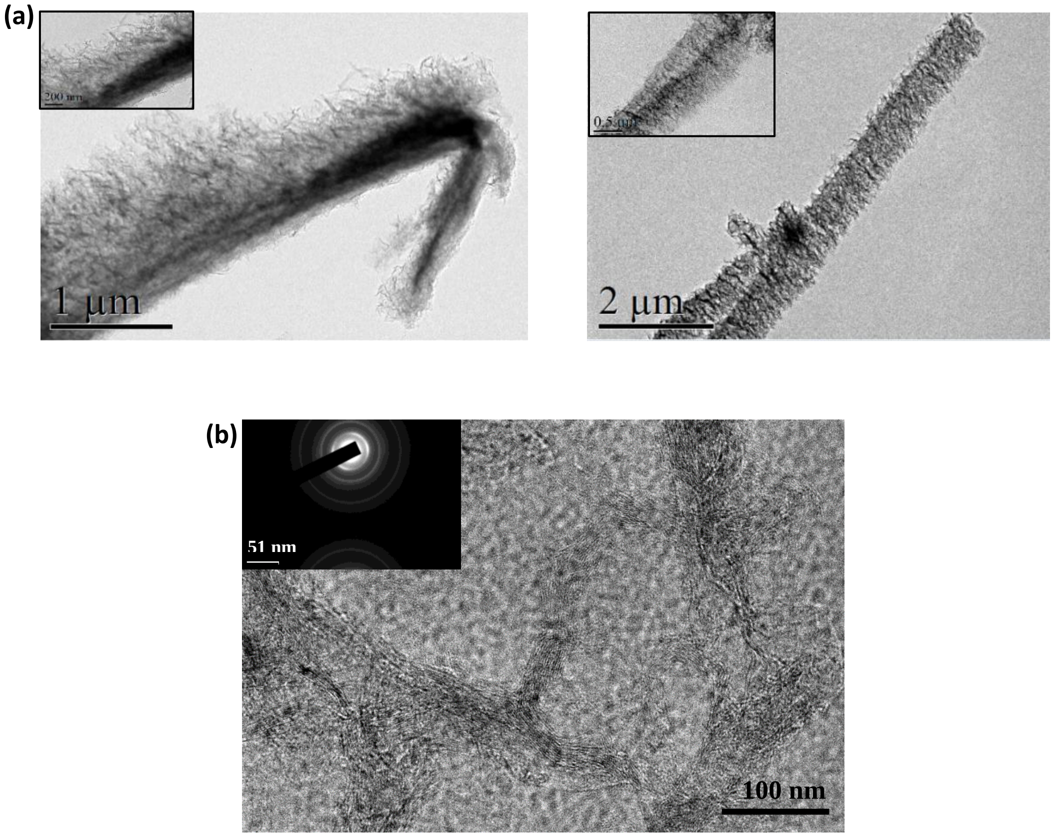

Figure 7.6 HRTEM images of MLGNWs/CNTs/c-Si honeycomb structure; (b) TEM image of GNWs/CNTs/c-Si (inset image SAED diffraction pattern)

Raman analysis

Raman spectroscopy provided information on structural properties of carbon nanotubes, graphene nanowalls, MLGNWs/CNTs/c-Si 3D hybrid structure and patterned MLGNWs/CNTs/c-Si 3D hybrid structure. A comparison between the Raman spectra of these materials is presented in Fig. 7.7. Each spectrum shows three characteristic carbon bands, i.e., the disorder induced D-band around 1350 cm^{-1}, the G-band around 1580 cm^{-1} that is related to in-plane sp^2 vibrations, and the disorder induced D´-band around 1610 cm^{-1}. The enhancement of the Raman scattering signal in the 1584 cm$^{−1}$ (G band) and the appearance of the relatively sharp 2D peak at 2668 cm$^{−1}$ provide the graphene nature (several layers) of vertical nanowalls [Khan U, 2010; Huang Y, 2012]. Raman peaks of CNTs have a wide shape, which is typical of CNTs. After the MLGNWs growth on the CNTs, the ratios of the Raman peaks changed. In case of MLGNWs grown on micropatterned CNTs/c-Si and MLGNWs/CNTs/c-Si, the peak ratios of Raman spectra remain unchanged, which points to a similar nature of both hybrid nanostructures.

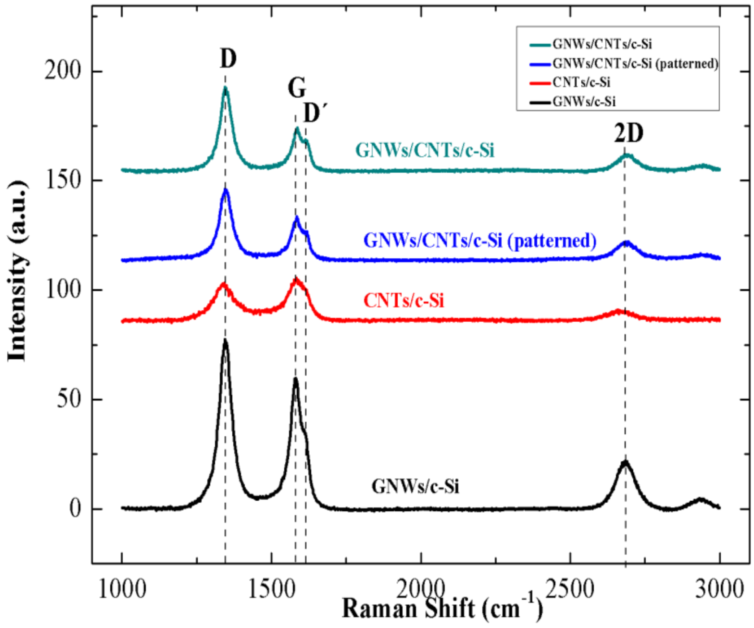

Figure 7.7 Raman spectra of MLGNWs/c-Si, CNTs/c-Si, MLGNWs on CNTs/c-Si and MLGNWs on micropatterned CNTs/c-Si

For a qualitative analysis of graphite-like structures, the intensity ratio of the D-band to the G-band was measured (I_D/I_G). MLGNWs usually have a high number of defects and are known for their relatively large I_D/I_G >1 value [Kurita S, 2005; Ni ZH, 2006], while pure CNTs and highly ordered graphite can have $I_D/I_G < 1$ values [Kastner J, 1994; Dresselhaus MS, 2002; Dresselhaus MS, 2005]. The Raman spectra in Fig.7.7 display a relatively large I_D/I_G of 2.1 for the combined MLGNWs/CNTs/c-Si in contrast to the value of 0.8 for the CNTs/c-Si system. I_D/I_G

is 1.62 for the honeycomb MLGNWs/CNTs/c-Si sample, and for MLGNWs/c-Si is 1.33. These results indicate that I_D/I_G value for CNTs changes very crucially after functionalization with MLGNWs (0.8→2.1), due to the twisted graphitic planes of the MLGNWs sp^2 structures.

BET analysis

In addition, we measured the specific surface area of carbon nanotubes, graphene nanowalls, MLGNWs/CNTs/c-Si 3D hybrid structures and patterned MLGNWs/CNTs/c-Si 3D hybrid structures by nitrogen gas adsorption—BET (Brunauer-Emmet-Teller) technique. The measured values of specific surface area (SAA) are listed in Table 7.1.

The structure of CNTs is bamboo like. These structures were processed by water assisted plasma for synthesizing hydrophilic CNTs for the future water post-treatment. CNTs obtained by water assisted plasma have open bamboo like structure. The SAA of bamboo like (S_{open}) CNTs is composed of the external surface (S_{closed}) plus the internal surface of the first segment of the bamboo structure (Fig.7.8)

$$S_{open} = S_{closed}(1 + \frac{a}{l}) \qquad (7.1)$$

where l length of CNTs and a length of one segment.

Table 7.1 Specific surface area for as-prepared MLGNWs and other carbon materials

Carbon material	**References**	**$A_{BET}(m^2g^{-1})$**
Water assisted open bamboo like MWCNTs	Our material	872.7 ±21.6
MLGNWs/MWCNTs/c-Si 3D hybrid structure	Our material	1412 ±25
Graphene (theoretical)	[Rao CNR, 2009]	2630
Graphene aerogel	[Sui ZY, 2014]	830-1230
Carbon nanotubes (2WCNTs) (theoretical)	[Peigney A, 2014]	680-850
Open carbon nanotubes (SWCNTs)	[Hiraoka T, 2010]	2240
Carbon nanofibers (CNFs)	[Liu Z, 2014]	800

The specific surface of closed CNTs was calculated by different authors. Peigney et al. were calculated the value of the specific surface of closed CNTs respect of the nanotube diameter and number of walls (Fig.7.9) [Peigney A, 2001]. However, our CNTs have a much more specific surface, due to the open edges, according to the equation 7.1.

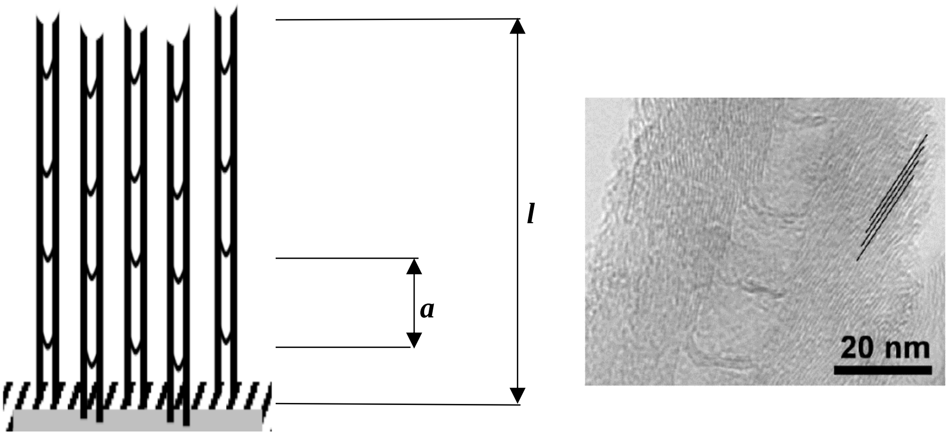

Figure 7.8 Bamboo like CNTs [Garcia J,2008]

In accordance to the Equation 7.1 and Fig.7.9 we can calculate the specific surface of an open MWCNTs structure (Tab.7.2). Our MWCNTs with SSA 872.7 m^2/g accordingly with this theoretical calculation correspond to 3-4 bamboo segments. In addition, we also can obtain a theoretical SAA value for our nanowalls, supposed that these nanowalls are composed of more than 2 layers, it means that the maximum SSA for our vertical nanostructures is 1050 m^2/g.

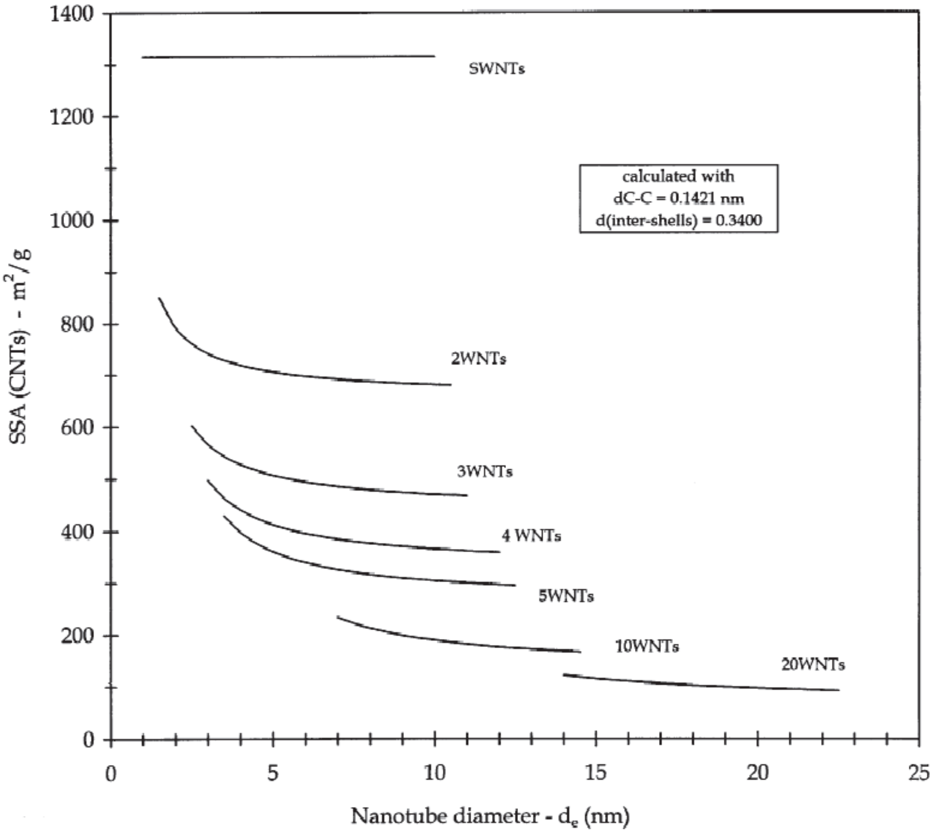

Figure 7.9 Specific surface area of carbon nanotubes versus their diameter and number of nanowalls [Peigney A, 2001]

We also tried to measure the specific surface of nanowalls by BET, but we obtained the SSA high value with a large error. However, the incorporation of nanowalls to form a hybrid structure with MWCNTs significantly increases its specific surface area. This hybrid structure could be useful material for a high number of applications, such as biological sensors, fuel cells, lithium ion batteries and supercapacitors.

Table 7.2 Theoretical value of specific surface area for MLGNWs and CNTs

Structure		S_{closed} (m^2/g)	S_{open} (m^2/g)	S_{closed} (m^2/g)	S_{open} (m^2/g)	S_{closed} (m^2/g)	S_{open} (m^2/g)	S_{closed} (m^2/g)	S_{open} (m^2/g)
Bamboo like CNTs		1315	2630	700	1050	500	666.6	400	500
	a/l	1/2	1/2	1/3	1/3	1/4	1/4	1/5	1/5
MLGNWs		-	-	-	1050	-	666.6	-	500

Electrochemical performance

The average specific capacitance of the samples was determined from the cyclic voltammograms using the following equation:

$$C_S = \frac{(q_a+|q_c|)}{(2m\Delta V)} \qquad (7.2)$$

where C_s is the average specific capacitance in F·g^{-1}, q_a and q_c are the anodic and cathodic charges, respectively in C, m is the mass of the active material in g and ΔV the applied voltage window in V.

Fig.7.10a shows the cyclic voltammograms at a scan rate of 50 mV·s^{-1} of MLGNWs/MWCNTs/c-Si, MLGNWs/CNTs/c-Si honeycomb structure, MWCNTs/c-Si honeycomb structure and MWCNTs/c-Si. Cyclic voltammograms of the samples exhibit a square shape that indicates the capacitive nature of the MLGNWs and CNTs nanocomposites. Untreated MWCNTs present relatively high current density compared with patterned and functionalized structures with MLGNWs. After the deposition of MLGNWs decreases the current density of MWCNTs/c-Si by a factor lower than 10 (Fig.7.10b). This phenomena can be related to the hydrophobicity of the hybrid structure. The specific capacitance of hybrid structure can be improved by using oxygen plasma, which removes the amorphous carbon without etching the structure. The areal density of MLGNWs/CNTs and CNTs was measured with a microbalance and found to be about 87 µg/cm^2 and 47 µg/cm^2, respectively.

Furthermore, contact angle measurements indicate that most of the samples containing MLGNWs present super-hydrophobic behaviour before oxygen plasma treatment, which is especially interesting for biosensors for gas detectors and electrochemical biosensors for earlier cancer detection [Ma L, 2016; Malara N, 2016] and electrochemistry experiments, in which a low wettability can limit the efficiency of MLGNWs/MWCNTs.

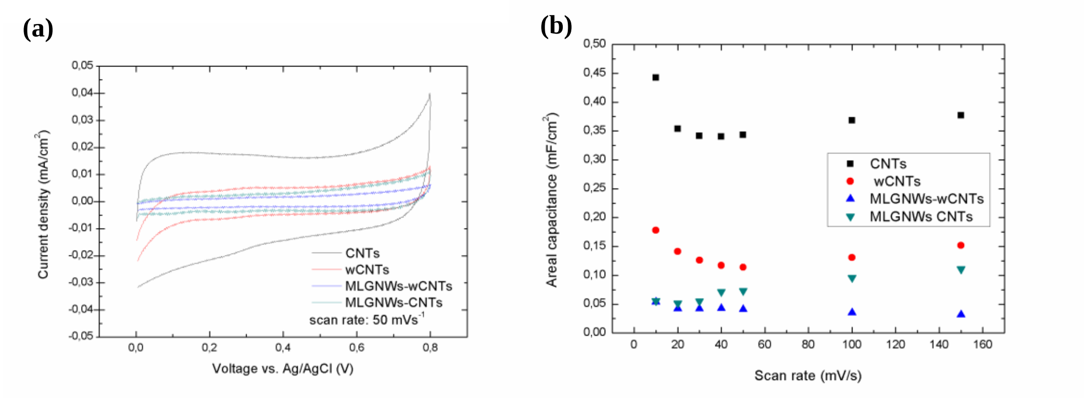

Figure 7.10 (a) Cyclic voltammograms of MLGNWs/c-Si, CNTs/c-Si, MLGNWs on CNTs/c-Si and MLGNWs on micropatterned CNTs/c-Si; (b) Specific capacitance MLGNWs/c-Si, CNTs/c-Si, MLGNWs on CNTs/c-Si and MLGNWs on micropatterned CNTs/c-Si versus the scan rate

Table 7.3 Specific capacitances of untreated and patterned MWCNTs

Sample	**Scan rate (mV·s^{-1})**	***C_S* (F/g)**	***Areal C_S* (mF/cm^2)**
MLGNWs/CNTs/c-Si	10	0,64±0,032	0,055± 0,003
MLGNWs/CNTs/c-Si honeycomb	10	0,62±0,031	0,054±0,027
CNTs/c-Si honeycomb	10	3,8±0,19	0,18±0,009
CNTs/c-Si	10	9,5± 0,475	0,44±0,022

7.4 Conclusion

In this chapter, we demonstrate that the position-controlled MLGNWs selective growth is possible by using micropatterned MWCNTs. Water treatment of MWCNTs is easy (simple) way for patterned it, based on capillarity forces. These results can broad the field of the applications using graphene nanowalls and MWCNTs. Honeycomb structure permits to cover the external surface the packed CNTs in the over the entire length by active edges of MLGNWs. In contrast the hybrid MLGNWs/CNTs without water treatment the active edges of MLGNWs are deposited on the top part of all carbon nanotubes increasing their specific surface, which can boost the chemical activity of CNTs for biomedical applications.

Chapter 8

Supercapacitive performance of manganese dioxide/graphene nanowalls electrodes deposited on stainless steel current collectors and annealing temperature effect

8.1 Introduction

Carbon-based nanostructured electrodes are suitable for different electrochemical applications due to their large surface area, thermal and chemical stability, mechanical strength and high conductivity. Carbon nanotubes (CNTs), graphene and multilayer graphene nanowalls (MLGNWs) are promising materials to improve performance of different electrochemical devices such as sensors, batteries, electrochemical capacitors and fuel cells [Bo Z, 2015; Wen L, 2016; Baptista FR, 2015; Dai L, 2015; Yang J, 2015; Li B, 2015].

Carbon-based nanostructured electrodes such as MLGNWs are especially promising for supercapacitor devices. These electrochemical devices present higher power density values than batteries as well as higher energy density values than electrolytic capacitors. Supercapacitors are used and are under development to improve performance of electric vehicles, memory backups, and absorption of high peak power transients.

There are two main charging mechanisms in a supercapacitor: electrostatic due to the formation of an electric double layer at the interface between the solid electrode and the ions in the electrolyte (double-layer capacitance), and through redox reactions near the surface region of transition metal oxides or conductive polymers involving electrolyte ions (pseudocapacitance). In general, carbon electrodes have a higher contribution of double layer capacitance (DLC) than of pseudocapacitance (PC) [Conway BE, 1999]. Due to their rich redox behaviour, thermal and chemical stability, the transition metal oxides provide a higher energy density than conventional carbon materials and better electrochemical stability than polymer materials [Wang G, 2012].

Among supercapacitive transition metal oxides, manganese dioxide is one of the most investigated due to its environmental friendliness, cost and low toxicity [Wang G, 2012]. The proposed mechanism for pseudocapacitance in manganese oxides is described by the following equation [Raymundo-Piñero E, 2005]:

$$MnO_{\alpha}(OC)_{\beta} + \delta C^{+} + \delta e^{-} \leftrightarrow MnO_{\alpha-\delta}(OC)_{\beta+\delta} \tag{8.1}$$

Where C^+ are protons or alkali metal cations (Li^+, Na^+, K^+) in the electrolyte. In the case of adsorption/desorption of protons, $MnO_{\alpha}(OH)_{\beta}$ and $MnO_{\alpha-\delta}(OH)_{\beta+\delta}$ indicate interfacial manganese hydroxides at high and low oxidation states, respectively. A major drawback of manganese dioxide is its low conductivity that reduces the charging/discharging rate of the electrode. Thus, a thin layer of the oxide is deposited to minimize the series resistance. In addition, a thermal treatment may help to improve the contact between the transition metal oxide and the carbon-based nanostructured electrode improving the charge transfer process [Zheng JP, 1995]. Optimization of this thermal treatment allows maximum charge/discharge rates without sacrificing electrochemical performance.

Different methods can be used to deposit and prepare MnO_2, such as hydrothermal [Tang N, 2009], sol gel methods [Raymundo-Piñero E, 2005; Pang SC, 2000] and electrodeposition [Raymundo-Piñero E, 2005; Pang SC, 2000; Amade R, 2011]. In previous works, we have demonstrated the excellent electrochemical performance of galvanostatically electrodeposited MnO_2 on vertically aligned carbon nanotubes (VACNTs) [Amade R, 2011; Hussain S, 2013] as well as laser-coated MnO_2-VACNTs [Pérez del Pino A, 2017]. In addition, there is a need to reduce overall costs of electrochemical devices by, *e.g.*, the use of cost-effective current collectors such as stainless-steel foil. This substrate has the advantages of being flexible, relatively chemically stable and with low resistance.

In this chapter, we will discuss of the electrodeposition of a thin layer of MnO_2 on the MLGNWs/SS304 nanostructure, synthesized by ICP-CVD method. Afterwards, we have performed a thermal annealing process to improve the electrochemical properties of the electrodes and analysed their performance. A mild thermal treatment at 70°C resulted in ultrafast charge/discharge rates without giving up performance and stability.

8.2 Materials and methods

Growth of MLGNWs and MnO_2/MLGNWs

Graphene nanowalls were synthesized on a SS substrate (100 µm thick and about 2 cm^2 of geometrical area) using an inductively coupled plasma chemical vapour deposition (ICP-CVD) (13.56 MHz, power 440 W) system, as discussed above. The sample was placed inside the quartz tube reactor, which was evacuated down to a pressure below 1 Pa and heated up to 750°C. Then, pure methane (99.995%) was introduced as a precursor gas at one end of the quartz tube (10 sccm) and the pressure maintained in the range of 50-60 Pa. Under these conditions, the plasma was ignited at an RF power of 440 W during 40 min. Finally, the sample was allowed to cool down to room temperature for 30 min. The areal density of the MLGNWs was measured with a microbalance and found to be about 58 µg cm^{-2}.

The electrochemical deposition was carried out using a galvanostatic method described elsewhere [Amade R, 2011]. Briefly, GNWs were used as anode and a graphite electrode as the cathode in a 0.2 M Na_2SO_4 aqueous solution with about 4 cm separation between the electrodes. About 0.5 cm^3 of a 0.2 M $MnSO_4{\cdot}H_2O$ solution was added drop wise to the electrolyte through a hole in the cathode applying 1 mA cm^{-2} during 2 minutes [Fan Z, 2008]. After this process, the loading mass of MnO_2 was about 16 µg.

The MnO_2/MLGNWs samples were annealed at different temperatures to study their electrochemical performance: 70°C, 200°C and 600°C. The annealing process was carried out during 20 minutes under argon atmosphere to avoid oxidation of the SS substrate. MnO_2/MLGNWs without annealing (room temperature) and bare MLGNWs samples were also characterized for comparison.

Samples characterization

The microstructure and morphologies of the grown samples were investigated using field emission scanning electron microscopy (SEM) (JEOL JSM-7001F, operated at 20 kV) and transmission electron microscopy (TEM) (JEOL 1010, operated at 200 kV). The carbon structures were transferred to the TEM grid by simply scratching off from the substrates.

The physical and chemical characteristics of as grown structures were studied by Raman spectroscopy using a microscope HR800 (LabRam) with a 532 nm solid state laser (5 mW laser power).

The electrochemical properties of the samples were analysed by means of cyclic voltammetry (CV), electrochemical impedance spectroscopy (EIS), and galvanostatic charge/discharge (GCD) cycling in a 1 M Na_2SO_4 aqueous solution using a potentiostat/galvanostat (AutoLab, PGSTAT30, USA). All experiments were carried out at room temperature in a typical three-electrode cell. A Ag/AgCl electrode (3 M KCl internal solution) and a Pt-ring electrode were used as the reference and counter electrode, respectively. The working electrode was a sample of GNWs or MnO_2/MLGNWs nanocomposite. The geometrical area of the working electrode was set to a constant value of 0.57 cm^2.

The CV analysis was performed using a voltage window of 0.0-0.7 V vs. Ag/AgCl at scan rates between 10 and 150 $mV\cdot s^{-1}$. An alternating voltage of 10 mV amplitude was applied to the samples between 1 Hz and 100 kHz for the EIS analysis. Finally, several thousands of charge/discharge cycles were applied to the samples between 0.7 V and 0.0 V vs. Ag/AgCl at different current densities.

8.3 Results

Morphological and structural characterization

Figure 8.1a shows a top view image of bare MLGNWs grown on SS. The nanowalls are homogeneously distributed, and present an open structure with voids between the nanowalls. Their length is of several hundreds of nm and a few nanometer thick (about 10 graphene layers, see Figures 8.1e and 8.1f).

After deposition of MnO_2 a layer of the oxide is observed coating the nanowalls. For samples without thermal treatment and annealed at 200°C or below (Figures 8.1b and 8.1c, respectively), the open structure of the nanowalls is still recognized. However, a completely different morphology is presented by the sample annealed at 600°C (Figure 8.1d) with a homogeneous layer of the oxide covering the nanowalls without visible voids and with a more compact structure.

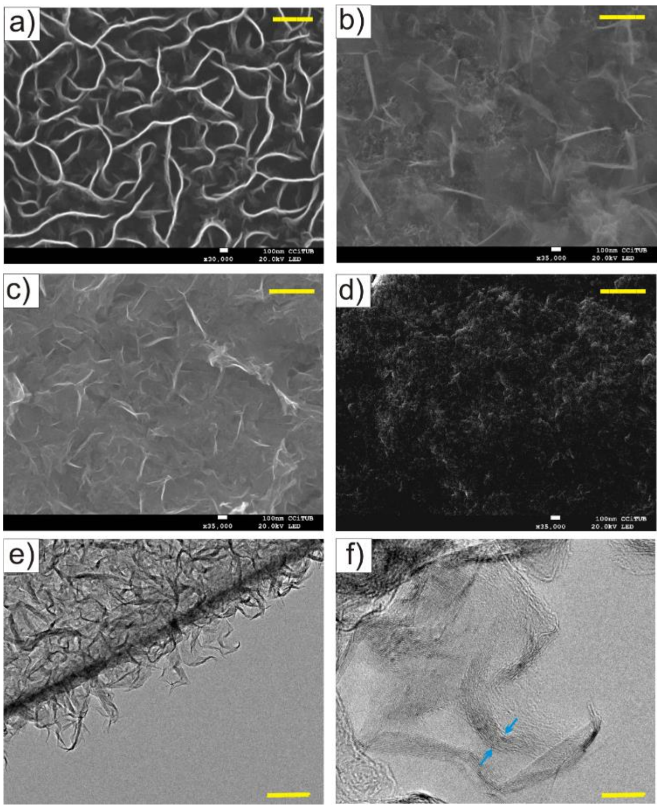

Figure 8.1 a)SEM images of MLGNWs grown on SS; b) MnO_2/MLGNWs without thermal treatment; c) MnO_2/MLGNWs with annealing at 200°C; d)600°C and e)f) TEM images of as grown MLGNWs. Arrows indicate the thickness of the nanowalls. Scale bars correspond to 500 nm in (a-d). 100 nm in (e) and 10 nm in (f)

Raman spectra of bare MLGNWs show typical D and G bands at 1346 cm^{-1} and 1587 cm^{-1} (Figure 8.2). The large number of defects (high D-peak) is associated with the plasma deposition technique. A shoulder appears next to the G band at 1616 cm^{-1} (D´ band) related to the finite size of graphite crystals and graphene edges [Hiramatsu M, 2004]. Furthermore, the presence of a peak at 2700 cm^{-1} (2D) and $I_{2D}/I_G = 0.8$ confirms the presence of a few-layered graphene in accordance with TEM images (Figures 8.1e and 8.1f). An additional peak appears at 2940 cm^{-1} related to sp^2 CH stretching vibrations [Ni Z, 2008]. MnO_2/MLGNWs samples without and with annealing at different temperatures show similar Raman spectra, which indicate little or no alteration of the graphene nanowalls structure after MnO_2 deposition and thermal treatment (Figure 8.2). Main D and G bands are clearly recognized for all the samples without big differences between them. However, unlike for the bare MLGNWs sample, the D´ shoulder is not appreciable for these samples. Also, 2D and D+G bands appear much weaker than for bare MLGNWs sample due to the presence of MnO_2 coating on the surface and edges of the nanowalls. No specific bands of MnO_2 are recorded, probably due to its low loading, low crystallinity and/or small crystal size [Pérez del Pino A, 2017].

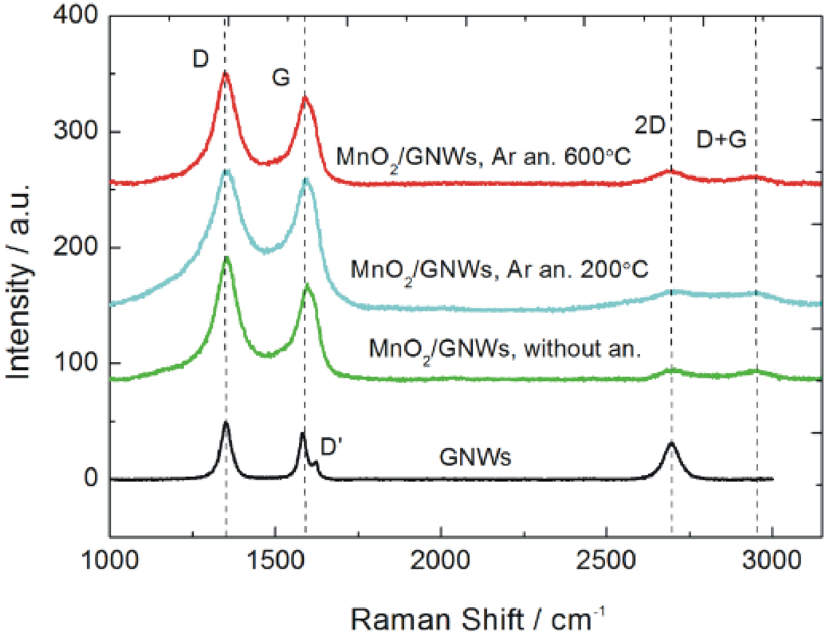

Figure 8.2 Raman spectra of MLGNWs grown on SS and MnO_2/MLGNWs samples without annealing and Argon annealing at 200 and 600°C

8.3.2 Electrochemical performance

The average specific capacitance of the samples was obtained from the cyclic voltammograms applying equation 2.

$$C_s = \frac{q_a + |q_c|}{2m\Delta V} \tag{8.1}$$

Where C_s is the average specific capacitance in $F\cdot g^{-1}$, q_a and q_c are the anodic and cathodic charges, respectively in C. m is the mass of the active material in g and ΔV the applied voltage window in V.

Alternatively, the specific capacitance was also obtained from galvanostatic discharge curves according to the following equation:

$$C_s = \frac{I}{(\Delta V/\Delta t)m} \tag{8.2}$$

Where C_s and m have the same meaning and units as previously (Eq.8.2). ΔV is the voltage difference during the discharge in V and Δt the discharge time in s. I is the current applied during discharge in A.

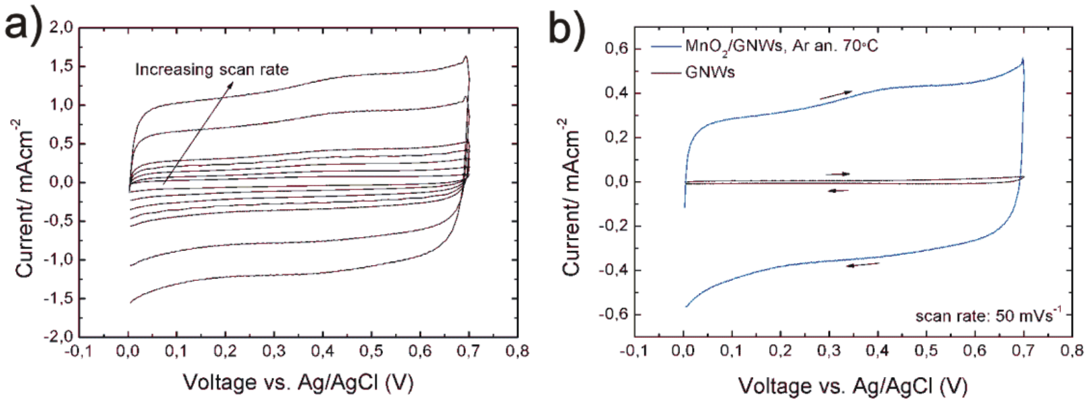

Figure 8.3 a) Cyclic voltammograms of MnO_2/MLGNWs sample annealed at 70°C using scan rates from 10 to 150 mV·s^{-1}; b) Bare MLGNWs and MnO_2/ MLGNWs sample annealed at 70°C using a scan rate of 50 mV·s^{-1} and a voltage window between 0.0-0.7 V vs Ag/AgCl. Arrows indicate direction of scan.

Cyclic voltammograms of the samples exhibit a rectangular shape that indicates the capacitive nature of the GNWs and the MnO_2/MLGNWs nanocomposites (Figure 8.3a and 8.3b). Deposition of MnO_2 increases the current density of MnO_2/MLGNWs by a factor of greater than 20 compared to bare MLGNWs samples due to the pseudocapacitive effect of the transition metal oxide (Figure 8.3b).

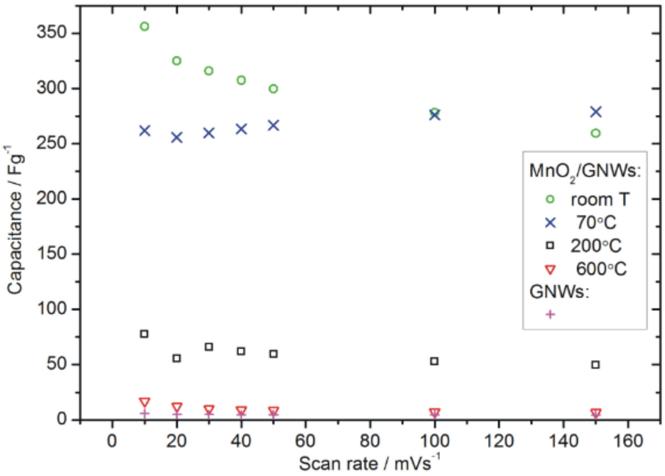

Figure 8.4 a) Specific capacitance of bare MLGNWs and MnO_2/MLGNWs samples without (room T) and with annealing at different temperatures versus the scan rate.

At a scan rate of 10 mV·s^{-1} MnO_2/MLGNWs sample without annealing provides the highest specific capacitance (SC) of 356 F·g^{-1} (Figure 8.4). However, at high scan rates (150 mV·s^{-1}), the highest SC is presented by MnO_2/GNWs sample annealed at 70°C (278 F·g^{-1}). In addition, this sample also shows the highest cycling stability at high current densities (14 A·g^{-1}) during more than fourteen thousand cycles (Figure 8.5).

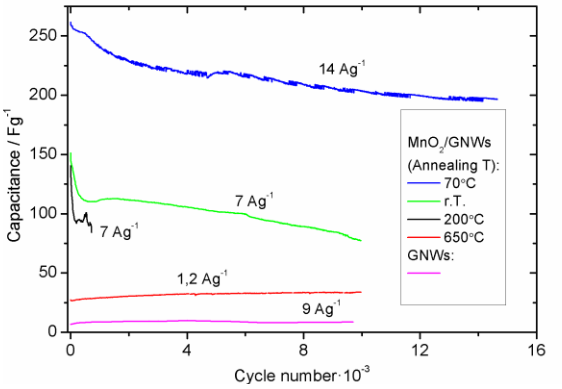

Figure 8.5 Cycling stability of bare MLGNWs and MnO$_2$/MLGNWs samples without annealing (room T) and annealed at different temperatures.

Impedance spectroscopy

Further information about the electrochemical processes taking place at the interfaces and the bulk of the electrode materials can be obtained by means of electrochemical impedance spectroscopy.

The Nyquist plot of the samples is in accordance with their morphology and show the typical behaviour for capacitive porous electrodes (Figure 8.6). A modified Randles circuit can be used to fit the experimental data [Masarapu C, 2009] (Figure 8.6), which describe charge storage and transfer properties of the different interfaces and the bulk of the electrode/electrolyte system. The equivalent circuit consist of capacitances (C) and resistances (R) in series and/or parallel configuration. The internal resistance of the cell is given by R_S, which corresponds to the

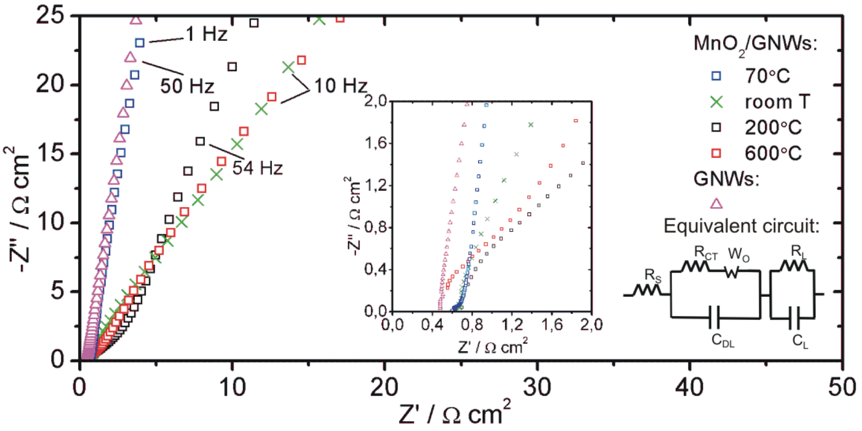

Figure 8.6 Nyquist plot of the samples: bare MLGNWs and MnO$_2$/MLGNWs nanocomposite without annealing (room T) and annealed at 70, 200 and 600°C. Inset shows the real axis intersection and the modified Randles equivalent circuit used to fit the data.

intersection point to the real axis at high frequencies in the Nyquist spectra (inset in Figure 8.6). The charge transfer resistance between electrode and electrolyte is represented by R_{CT}. The double layer capacitance connected in parallel is given by C_{DL}. In the mid-frequency region of the spectrum a Warburg element (W_O) describes diffusion processes of the ions through the porous structure of the electrodes, which is expressed as $A/(j\omega)^n$, where A is the Warburg coefficient, n is an exponent and ω is the angular frequency. At low frequencies the spectra show an almost straight line parallel to the imaginary axis, which is related to a perfect polarized capacitive behaviour described by mass capacitance (C_L), connected in parallel to a leakage resistance (R_L) [Pandit B, 2017].

The whole spectra (1 Hz to 100 kHz) were fitted using ZVIEW software and the equivalent circuit parameters obtained are shown in Table 8.1. As expected, the series resistance values are similar to all the samples, which are related to the electrolyte resistance, cables and contact resistances of the cell [Conway BE, 1999].

Table 8.1 Equivalent circuit parameters obtained from fitting the EIS data of MLGNWs and MnO_2/MLGNWs nanocomposites.

Electrode Material/ Annealing *T* (°C)	R_S (Ω·cm²)	R_{CT} (Ω·cm²)	$W_0 = A/(j\omega)^n$		C_{DL} ($F \cdot g^{-1}$)	R_L (Ω·cm²)	C_L ($F \cdot g^{-1}$)
			A ($\Omega \cdot s^{-n}$)	*n*			
MLGNWs/ -	0.5	1.7	423	0.65	3.3	$4.9 \cdot 10^3$	4.3
MnO_2/MLGNWs / -	0.7	0.9	490	0.54	6.7	637	206
MnO_2/MLGNWs / 70	0.6	0.1	8.52	0.65	25	195	231
MnO_2/MLGNWs / 200	0.7	1.5	101	0.60	0.63	124	14
MnO_2/MLGNWs / 600	0.5	0.6	923	0.61	0.84	4.3	187

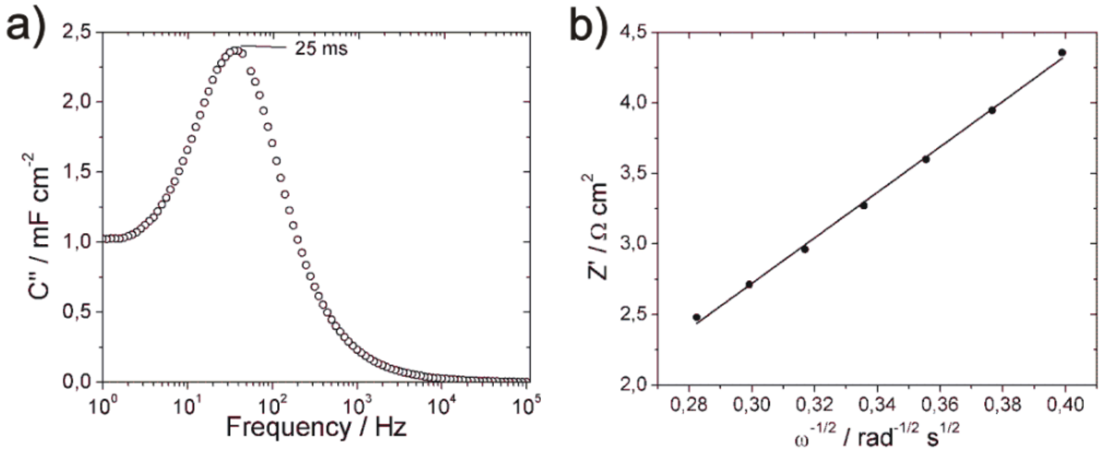

Figure 8.7 a) *Z'* vs. $\omega^{1/2}$ plot to evaluate the diffusion coefficient. b) *C''* vs. frequency plot to determine the relaxation time constant of MnO_2/MLGNWs heated at 70°C.

The proton diffusion coefficient (*D*) is obtained from the slope of the *Z'* vs. $\omega^{1/2}$ plot (Figure 8.7a) through the following equation [Wang X, 2011; Ouksel L, 2016]:

$$D=\frac{R^2T^2M^2}{2A^2n^4F^4\sigma^2} \tag{8.3}$$

Where *R* is the gas constant in $J\cdot mol^{-}1\cdot K^{-1}$, *T* is the temperature in K, *M* is the molar volume (taken as 17.30 $cm^3\cdot mol^{-1}$ for MnO_2), *A* is the geometric area of the electrode in cm^2, *n* is the number of electrons involved in the reaction, *F* is the Faraday constant in $C\cdot mol^{-1}$ and σ is the slope of Figure 8.7a in $\Omega\cdot s^{-1/2}$. The maximum proton diffusion coefficient is obtained for the sample annealed at 70°C with a value of $1.3\cdot 10^{-13}$ $cm^2\cdot s^{-1}$.

The relaxation time constant (τ_0) can be obtained from the *C''* vs. frequency plot (figure 8.7b) using equation 8.5 [Pandit B, 2017; Li T, 2016].

$$C'' = \frac{Z'}{2\pi f|Z|^2} \tag{8.4}$$

where *C''* is the imaginary part of the capacitance in $F\cdot cm^2$, *Z'* is the real part of the impedance in $\Omega\cdot cm^2$, *f* is the frequency in Hz and $|Z|$ is the modulus of the impedance in $\Omega\cdot cm^2$. The position of the maximum in Figure 8.7a provides the characteristic frequency, which is the inverse of τ_0. The fastest relaxation time was 25 ms, obtained for the sample annealed at 70°C.

8.4 Discussion

The heat-treated samples are expected to show lower open porosity and lower surface area, especially those heated at high temperatures above 200°C. In addition, it has been suggested that a high scan rate limits proton and Na^+ ion diffusion and makes some pores and voids inaccessible [Wei J, 2007], which implies a decrease in SC with scan rate. It is also known that a heat treatment below 220°C removes water and trace amounts of oxygen [Devaraj S, 2007], and around 500°C a transition occurs from α-MnO_2 to crystalline Mn_2O_3 by loss of oxygen (chemical transformation) [Devaraj S, 2007; Chang JK, 2004; Lin CK, 2007], which explains the low SC of the samples treated above 200°C. However, the sample annealed at 70°C shows a particular behaviour, increasing its SC with the scan rate. This phenomenon has already been reported previously and has been assigned to an excellent contact between the porous collector (MLGNWs in this case) and the oxide that allows efficient access of both electrons and ions to afford a faster redox reaction at high scan rates [Lang X, 2011]. This redox process takes place at the surface of MnO_2 where only a thin layer of MnO_2 is involved and is electrochemically active [Toupin M, 2004].

Clearly, high annealing temperatures drastically reduce the capacitance due to the removal of bound water and lower open porosity of the electrode [Wei J, 2007]. A mild treatment at 70°C improves the SC and provides a better cycling stability even at high current densities (Figure 8.5). The Coulombic efficiency of this sample remained at 100%, even after 14k cycles at 14 Ag^{-1}, and the capacitance retention was 73%.

The cycling stability of manganese oxides is mainly controlled by their microstructure (physical property), while their specific capacitance is governed primarily by their chemically hydrous state [Chang JK, 2009]. Thus, when the annealing temperature is too high (above 200°C) the hydrous state is reduced and, without annealing, or at low temperatures the microstructure is not as stable as after a heat treatment. Optimum conditions are found at 70°C annealing temperature.

The charge transfer resistance presents its lowest value after annealing the MnO_2/MLGNWs at 70°C. It is assumed that this mild temperature allows better contact of the oxide with the GNWs and avoids fast water evaporation that can result in big voids, cracks and bad adhesion between oxide and MLGNWs. This is probably the case for the sample annealed at 200°C. At higher temperatures the R_{CT} decreases again due to the increased diffusivity of the metal-oxide ions during annealing that result in better contact between MLGNWs and MnO_2. Both double layer capacitance and mass capacitance have its maximum after annealing at 70°C, which correlates with the cyclic voltammetry results. The leakage resistance diminishes with increasing annealing temperature. The origin of this resistance is usually related to some faradaic process [Conway BE, 1999], and may be related to chemical reactions or phase changes of the manganese oxide. At annealing temperatures below 500°C there is a loss of water and slight loss of oxygen [Tsang C, 1998], while a phase change from α-MnO_2 to Mn_2O_3 takes place above 500°C [Chang JK, 2009]. Lower resistance implies higher leaking currents and poor performance. Hence, low annealing temperatures should be used. The Warburg coefficient presents its lowest value for the sample annealed at 70°C. The exponent n is usually 0.5 for porous carbon electrodes. The high value of 0.65 obtained for the 70°C annealed sample signifies that ion diffusion takes place only at the surface of the electrode and does not behave as a typical porous electrode [Masarapu C, 2009]. This result is in accordance with the proton diffusion coefficient (D) obtained from the slope of the Z' vs. $\omega^{1/2}$ plot (Figure 8.7a).

In agreement with previously reported values [Qu D, 2003], the obtained proton diffusion coefficients in manganese dioxide range from $3.3 \cdot 10^{-16}$ to $2.4 \cdot 10^{-15}$ $cm^2 \cdot s^{-1}$ for all the samples except for the one annealed at 70°C, which presents a value of $1.3 \cdot 10^{-13}$ $cm^2 \cdot s^{-1}$. The fast diffusion of protons in this sample is in accordance with the low Warburg coefficient and high n value obtained (Table 8.1).

The relaxation time is related to the power delivery and, ideally, should be as small as possible. The shortest relaxation time is obtained after annealing at 70°C (Figure 8.7a), which facilitates fast rate performance during charge-discharge cycles.

8.5 Conclusion

In summary, graphene nanowalls have been successfully grown on conductive and flexible stainless steel substrate by ICP-CVD method. Galvanostatic electrodeposition of MnO_2 increases the SC of the samples up to 356 $F\cdot g^{-1}$ at 10 $mV\cdot s^{-1}$ for the sample without thermal treatment. However, after a mild annealing at 70°C the MnO_2/MLGNWs nanocomposite exhibits optimum electrochemical performance, *i.e.*, small charge transfer resistance, high cycling stability, excellent coulombic efficiency and SC even at high charge/discharge rates, which is related to optimum contact between MLGNWs and MnO_2 and fast surface redox reactions. In accordance with these results, a maximum in the proton diffusion coefficient and short relaxation time is found at 70°C annealing temperature, which suggests fast surface diffusion processes. Samples annealed above the 200°C show low SC and stability due to the reduced open porosity, bound water removal from manganese oxide and faradaic reactions or phase changes.

Part IV
Conclusions

Conclusions

The main conclusions extracted from all experiments and results are:

- According to the goal of the present thesis to develop new graphene based structures useful for energy storage applications, we have designed and built a tubular reactor based on inductively coupled remote plasma chemical vapor deposition using RF from methane precursor, with the following characteristics: (1) low temperature of graphene growth (<750ºC) (2) high growth rate (3) high reproducibility (4) catalyst-free process (5) growth on diverse nature substrates (6) low cost.
- The MLGNWs growth mechanism was described in detail. We have shown that, the growth of MLGNWs is a complex process that consists of different stages. The plasma of carbon hydride during ICP-CVD process produces different kind of radicals and active species, which interact with the substrate and lead to the nucleation and the consequent growth.
- Nucleation can occur in the first stage of growth to form vertical wall structures. A secondary nucleation takes place on the previous vertically aligned nanowalls. This stage of secondary nucleation ensures the formation of secondary nanowalls. These SMLGNWs contribute to the increase of the active surface of the deposited material.
- A growth model has been proposed to understand the underlying mechanisms acting in this type of plasma process, which can allow the production of new carbon nanostructures for future applications in energy storage, catalysis and chemical and bio sensors.
- The samples show diverse structures and properties depending on the axial position inside the quartz tube, due to the different temperatures and environmental conditions. In this experiment we have obtained structures with different scale (micro- and nano-), depending on the growing temperature and the position inside the reactor.
- The study by SEM and TEM provided information of structure and morphology of the MLGNWs samples. Samples morphology shows vertically aligned nanometric walls having typical dimensions: hundreds of nanometers of height, tens of nanometers of width and few hundreds of nanometers in length depending on the growth conditions and substrate nature. High resolution micrographs show multilayer crystalline structure of several, typically in the range of 5-20 layers. SAED patterns evidenced the graphene nature of these multilayer structures.
- Raman scattering provided structural information on the number and type of defects, sp^2/sp^3 content, number of graphene layers, edges and structural stress.

- XPS, FTIR and elemental analysis provided information on the composition and chemical structure of the samples. Samples grown at temperatures below 700ºC showed typical carbon bonds C-C and C=C of graphene and the presence of oxygen (probably from a post-oxidation of the carbon structures) into the carbon structure, in the form of C-O=C and C=O. Also, samples showed a high hydrogen content under the form of -CH, $-CH_n$.
- Carbon nanostructures, grown at the highest temperature (750ºC), exhibited different characteristics: (1) presence of nanowalls with boundary like defects, (2) high crystallinity and (3) very low hydrogen and oxygen contents.
- The study of the PL properties was carried out on different morphologies obtained at very different conditions (temperature and radical density) in one single experiment on a tape shaped substrate of SS304, 100cm long and 4cm wide. The origin of PL is associated to the micro and nano non-doped sp^2/sp^3 carbon structures containing H. The PL measurements provided a bright and very broad emission band in the visible range from 450 to 750 nm, at room temperature, for samples grown at temperatures between 50ºC and 700ºC.
- The non-doped nanostructured carbon nanowalls (750ºC) having poor PL emission, open a new way for easily doping during the gas phase (N_2, NH_3, H_2O, H_2) to enhance PL emission that, can be useful for diverse optoelectronic applications.
- The transversal position study of MLGNWs was performed in order to observe the variation of their morphology at different quartz tube radial distances. The thermophoretic forces play a significant role in the substrate borders close to the walls of the quartz tube. Thus, MLGNWs density is smaller near the quartz tube. The homogeneous deposition was observed in the midway portion of the SS304 substrate (< 4cm wide).
- The contact angle measurements indicate that most of the samples present super-hydrophobicity ($\theta > 120º$), which can be changed to super- hydrophilicity after a short oxygen plasma treatment. This kind of oxygen functionalization can be useful for electrochemical measurements and for the future applications.
- MLGNWs were successfully grown on different types of substrates (Si wafer, copper, Papyex® graphite and SS304). Raman scattering, SEM, TEM and XRD provided contrasted information on the structure and morphology of MLGNWs on different substrates. We have evidenced the influence of the surface material on the first stage of nucleation. The SS304 sample showed the faster and the highest nucleation density associated to the grain size of the alloy (Fe, Ni, Cr). The other analyzed materials were compounded of only one phase (c-Si, Cu, graphite) and their nucleation density was smaller.

- It is possible to fully cover entire surfaces of different samples with a continuous MLGNWs film. These properties make MLGNWs an attractive material for various applications. For example, MLGNWs grown on Cu foil has a great potential as electrode for supercapacitors, meanwhile, MLGNWs on dielectric (SiO_2) substrate could be used to fabricate gas or bio-sensors, also MLGNWs on semiconductor substrates could be used rather for potential application of solar cells.
- The time evolution of the MLGNWs on different substrates is characterized by a secondary nucleation after 40 min of growth. The secondary MLGNWs limits the growth rate of the nanostructures associated to the formation of new edges on the secondary structures.
- The transformation from graphite to nanocrystalline graphite phase in case of MLGNWs/SS304 substrate was occurring very quickly compared with MLGNWs/c-Si.
- ICP-CVD process provides a high MLGNWs growth rate on SS304 substrates with the height of graphene nanowalls from 300 nm to 1000 nm since 10min to 40 min of deposition.
- The evolution of the CH_4 precursor gas radicals from 5 to 40 min of deposition was evidenced by OES. The C_2 dimers were detected during the deposition process. These are the main radicals for nucleation stage and they disappear after 1-2 min of growth.
- The density of CH and H radicals varies with deposition time, which points to the reaction between plasma species and substrate.
- Temperature plays an important role for a successful growth of MLGNWs. After a series of experiments conducted at the 550ºC-800ºC temperature range, the successful MLGNWs growth lower temperature was established 650^0C.
- The activation energy is at least 2 times lower for graphene grown by PECVD than by CVD. The lower value of activation energy (0.42eV) allows deposition at low-temperature.
- The morphology of the MLGNWs grown on different substrates shows a higher nanowalls density and height with increasing growth temperature. For the objectives of this thesis, the low density of MLGNWs obtained at low temperature range facilitates the functionalization of these nanostructures, needed for energy and sensor applications. In addition, the high number of surface defects in the case of MLGNWs/SS304, for the low temperature range facilitates the electron transfer in the electrochemical processes.
- We have demonstrated that the position-controlled MLGNWs selective growth is possible by using micropatterned MWCNTs. Water treatment of MWCNTs is an easy way for patterned it in the form of honeycomb structures, due to the capillarity forces.

These results can improve the efficiency of chemical activity of CNTs for biomedical applications, using new hybrid structures formed by graphene nanowalls and CNTs.

- Graphene nanowalls have been successfully grown on conductive and flexible stainless steel substrate by ICP-CVD method. Galvanostatic electrodeposition of MnO_2 increases the SC of the samples up to 356 $F\cdot g^{-1}$ at 10 $mV\cdot s^{-1}$ for the sample without thermal treatment. However, after a mild annealing at 70°C the MnO_2/MLGNWs nanocomposite exhibits optimum electrochemical performance, *i.e.*, small charge transfer resistance, high cycling stability, excellent coulombic efficiency and SC even at high charge/discharge rates, which is related to optimum contact between MLGNWs and MnO_2 and fast surface redox reactions. In accordance with these results, a maximum in the proton diffusion coefficient and short relaxation time is found at 70°C annealing temperature, which suggests fast surface diffusion processes. Samples annealed above 200°C show low SC and stability due to the reduced open porosity, bound water removal from manganese oxide and faradaic reactions or phase changes.

Despite the fact that a number of important conclusions were made during this thesis, several of the phenomena reported here need further study. Below we will suggest a few ideas for improving some points of our research for the looking at future work:

- Designing software (virtual instruments) for automatic control of growth parameters.
- Improving adhesion for MLGNWs on SS304 by removing a thin oxide film by oxygen etching.
- Profound study of electrochemical performance for the future applications of MLGNWs.
- MLGNWs growth by various hydrocarbon precursors and comparison of morphology and electrochemical performances.

References

- Ajayan PM, Ebbesen TW, *Nanometre-size tubes of carbon*, Rep. Prog. Phys. 60(1997)1025-1062
- Akhavan O, Ghaderi E and Rahighi R, *Toward Single-DNA Electrochemical Biosensing by Graphene Nanowalls*, ACS Nano 6(2012)2904–2916
- Al-Temimy A, Riedl C, and Starke U, *Low temperature growth of epitaxial graphene on SiC induced by carbon evaporation*, Appl. Phys. Lett. 95(2009)231907
- Alaoui MI, *Applications of Luminescence to Fingerprints and Trace Explosives Detection*, Unexploded Ordnance Detection and Mitigation, NATO Science for Peace and Security, Ser. B: Phys. Biophys. Springer Berlin(2009)189–196
- Alymov G, Vyurkov V, Ryzhii V and Svintsov D, *Abrupt current switching in graphene bilayer tunnel transistors enabled by van Hove singularities*, Scientific Reports 6(2016)24654
- Amade R, Jover R, Caglar B, Mutlu T, Bertran E, *Optimization of MnO_2/vertically aligned carbon nanotube composite for supercapacitor application*, Journal of Power Sources 196(2011)5779-5783
- Amade R , Muyshegyan-Avetisyan A, González JM, Pérez del Pino A, György E, Pascual E, Andújar JL, Bertran E, *Super-Capacitive Performance of Manganese Dioxide/Graphene Nano-Walls Electrodes Deposited on Stainless Steel Current Collectors*, Materials 12(2019)483
- Anthony TR, *Metastable synthesis of diamond*, Vacuum 41(1990)1356-1359
- Ashfold MNR, May PW and Rego CA, Everitt NM, *Thin Film Diamond by Chemical Vapour Deposition Methods* , Chemical Society Reviews 23(1994)21-30
- Avouris P, Freitag M and Perebeinos V, *Carbon-nanotube photonics and optoelectronics*, Nature Photonics 2(2008)341-350
- Babayan SE, Joeng JY, Tu VJ, Park J, Selwyn GS and Hicks RF, *Deposition of silicon dioxide filmswith an atmospheric-pressure plasma jet*, Plasma Sources Sci.Technol. 7(1998)286-288
- Bae S, Kim H, Lee Y, Xu X, Park J-S, Zheng Y, Balakrishnan J, Lei T, Kim HR, Song YL, Kim Y-J, Kim KS, Ozyilmaz B, Ahn J-H, Hong BH, Iijima S, *Roll-to-roll production of 30-inch graphene films for transparent electrodes*, Nature Nanotechnology 5(2010)574 – 578
- Balachandran M., *Synthesis and characterization of carbon nanospheres from hydrocarbon soot*, J. Electrochem. Sci. 7(2012)9537-9549
- Balandin AA, Ghosh S, Bao W, Calizo I, Teweldebrhan D, Miao F, Lau CN, *Superior thermal conductivity of single layer grapheme*, Nano Lett. 8(2008)902–907
- Balandin AA, *Thermal properties of graphene and nanostructured carbon materials*. Nat. Mater. 10(2011)569–581
- Bandosz TJ, Rodriguez-Castellon E, Montenegro JM, Seredych M, *Photoluminescence of nanoporous carbons: Opening a new application route for old materials*, Carbon 77(2014)651-659
- Baptista FR, Belhout SA, Giordani S, Quinn SJ, *Recent developments in carbon nanomaterial sensors*, Chemical Society Reviews 44(2015)4433-4453

- Bar-Tow D, Peled E, Burstein L, *A Study of Highly Oriented Pyrolytic Graphite as a Model for the Graphite Anode in Li-Ion Batteries*, J. Electrochem. Soc 146(1999)824
- Baringhaus J, Ruan M, Dler F, Tejeda A, Sicot M, Taleb-Ibrahimi A, Li AP, Jiang Z, Conrad EH, Berger C, *Exceptional ballistic transport in epitaxial graphene nanoribbons*, Nature 506(2014)349–354
- Bashir M, Rees JM, Bashir S and Zimmerman WB, *Characterization of atmospheric pressure microplasma produced from argon and a mixture of argon–ethylenediamine*, Phys. Lett. 378(2014)2395-2405
- Belin T, Epron F, *Characterization methods of carbon nanotubes: a review*, Materials Science and Engineering B 119(2005)105–118
- Berger C, Song Z, Li T, Li X, Ogbazghi AY, Feng R and De Heer WA, *Ultrathin epitaxial graphite: 2D electron gas properties and a route toward graphene-based nanoelectronics*, The Journal of Physical Chemistry B 108(2004)19912-19916
- Bhaviripudi S, Jia X, Dresselhaus MS, Kong J, *Role of kinetic factors in chemical vapor deposition synthesis of uniform large area graphene using copper catalyst*. Nano Letters 10(2010)4128–4133
- Birkholz M, *Thin Film Analysis by X-Ray Scattering*, J.Appl.Cryst 39(2006)925–926
- Blake P, Novoselov KS, Castro Neto AH, Jiang D, Yang R, Booth TJ, Geim AK and Hill EW, *Making graphene visible*, Appl. Phys. Lett. 91(2007)063124
- Bo O, Mohan VJ, Rawat RS, *Free standing 3D graphene nano-mesh synthesis by RF plasma CVD using non-synthetic precursor*, Materials Research Bulletin 71(2015)61–66
- Bo Z, Zhu WG, Ma W, Wen ZH, Shuai XR, Chen JH, Yan J, Wang Z, Cen K, Feng X,*Vertically oriented graphene bridging active-layer/current-collector interface for ultrahigh rate supercapacitors*, Advanced Materials 25(2013)5799–5806
- Bo Z, Mao S, Han ZJ, Cen K, Chen J, Ostrikov K, *Emerging energy and environmental applications of vertically-oriented graphenes*, Chemical Society Reviews 44(2015)2108-2121
- Bo Z, Yang Y, Chen J, Yu K, Yan J and Cen K, *Plasma-enhanced chemical vapor deposition synthesis of vertically oriented graphene nanosheets*, Nanoscale 5(2013a)5180
- Bokobza L, Bruneel J-L and Couzi M, *Raman Spectra of Carbon-Based Materials (from Graphite to Carbon Black) and of Some Silicone Composites*, C 1(2015)77-94
- Bonaccorso F, Sun Z, Hasan T and Ferrari AC, *Graphene photonics and optoelectronics*, Nature Photonics 4(2010)611-622
- Brame J and Griggs C, *Surface Area Analysis Using the Brunauer-Emmett-Teller (BET) Method*, ERDC/EL SR-16-3(2016)
- Brault JW. *New Approach to high-precision Fourier transform spectrometer design*, Applied Optics 35(1996)2891–2896
- Brunauer S, Emmett PH and Teller E. *Adsorption of gases in multimolecular layers*, Journal of the American Chemical Society 60(1938)309-19
- Bubenzer A,Dischler B, Brandt G and Koidl P, *Rf-plasma deposited amorphous hydrogenated hard carbon thin films: Preparation, properties, and applications*, J. Appl. Phys 54(1983)4590

- Cançado LG, Pimenta MA, Saito R, Jorio A, Ladeira LO, Grüneis A, Souza-Filho AG, Dresselhaus G, Dresselhaus MS, *Stokes and anti-Stokes double resonance Raman scattering in two-dimensional graphite*, Phys. Rev. B 66(2002)035415
- Cançado LG,Takai K, Enoki T, Endo M, Kim YA, Mizusaki H, Speziali NL, Jorio A, Pimenta A *Measuring the degree of stacking order in graphite by Raman spectroscopy*, Carbon 46(2008)272-275
- Carey P, Sc B, *Plasma enhanced chemical vapor deposition of thin carbon films*, Submitted for the award of Master of Engineering, School of Electronic Engineenng, Dublin City Umversity(1989)
- Casiraghi C, Ferrari AC and Robertson J, *Raman spectroscopy of hydrogenated amorphous carbons*, Physical Review B 72(2005)085401
- Castro-Neto AH, Guinea F, Peres NMR, Novoselov KS, Geim K, *The electronic properties of graphene*, Rev. Mod. Phys. 81(2009)109-162
- Céspedes JG, *Nanotubos de carbono: síntesis, caracterización y aplicaciones,* PhD thesis, Universitat de Barcelona (2008)
- Chabert P and Braithwaite N, *Physics of Radio-Frequency Plasmas*, Cambridge University Press(2011), ISBN 978-0-521-76300-4
- Chakrapani N, Wei B, Carrillo A, Ajayan PM, Kane RS, *Capillarity-driven assembly of two-dimensional cellular carbon nanotube foams,* Proc. Natl. Acad. Sci. 101(2004**)**4009–4012
- Chang JK, Huang CH, Lee MT, Tsai WT, Deng MJ, Sun IW, *Physicochemical factors that affect the pseudocapacitance and cyclic stability of Mn oxide electrodes*, Electrochimica Acta 54(2009)3278-3284
- Chang JK, Chen YL, Tsai WT, *Effect of heat treatment on material characteristics and pseudo-capacitive properties of manganese oxide prepared by anodic deposition*, J. Power Sources 135(2004)344-353
- Chatei H, Belmahi M, Assouar MB, Le Brizoual L, Bourson P, Bougdira J, *Growth and characterisation of carbon nanostructures obtained by MPACVD system using* CH_4/CO_2 *gas mixture,* Diamond and Related Materials 15(2006)1041-1046
- Chen T, Dai L, Carbon *nanomaterials for high-performance supercapacitors,* Materials Today 16(2013)272-280
- Chen S, Wu Q, Mishra C ,Kang J ,Zhang H , Cho K ,Cai W, Balandin AA , Ruoff RS , *Thermal conductivity of isotopically modified graphene,* Nat. Mater. 11(2012)203
- Chen JH, Ishigami M, Jang C, Hines DR, Fuhrer MS and Williams ED, *Printed Graphene Circuits,* Advanced Materials 19(2007)3623–3627
- Chen Q, Sun T, Song X, Ran Q, Yu C, Yang J, Feng H, Yu L, Wei D, *Flexible electrochemical biosensors based on graphene nanowalls for the real-time measurement of lactate*, Nanotechnology 28(2017)315501
- Choudhary V and Gupta A, *Polymer/Carbon Nanotube Nanocomposites*, *Carbon Nanotubes-Polymer Nanocomposites*, Dr. Siva Yellampalli(Ed.), InTech(2011), ISBN 978-953-307-498-6

- Choudhary V, Dhawan SK and Saini P, *Polymer based nanocomposites for electromagnetic interference (EMI) shielding*, Jaroszewski M and Ziaja J(Ed.), EM Shielding – Theory and Development of New Materials, India (2012), ISBN 978-81-308-0499-6
- Chuang ATH, Boskovic BO and Robertson J, *Freestanding carbon nanowalls by microwave plasma-enhanced chemical vapor deposition,* Diamond Relat. Mater. 15(2006)1103–1106
- Chung DDL, *Review Graphite*, Journal of materials science 37(2002)1475 – 1489
- Cheng CL, Chen CF, Shaio WC, and Tsai DS, Chen KH, *The CH stretching features on diamonds of different origins*, Diamond and Related Materials 14(2005)1455-1462
- Conway BE, *Electrochemical Supercapacitors: Scienti, Fundamentals and Technological Applications*, Springer Science + Business Media, Ottawa(1999), ISBN 9781475730586
- Corbella CR, *Thin film structures of diamond-likecarbon prepared by pulsed plasma techniques*, PhD thesis, Universidad de Barcelona(2005)
- Crudena BA, Meyyappan M, *Characterization of a radio frequency carbon nanotube growth plasma by ultraviolet absorption and optical emission spectroscopy*, J. Appl. Phys. 97(2005)084311
- Cuxart MG, Šics I, Goñi AR, Pach E, Sauthier G, Paradinas M, Foerster M, Aballe L, Moreno Fernandez H, Carlino V, Pellegrin E, *Inductively coupled remote plasma-enhanced chemical vapor deposition (rPE-CVD) as a versatile route for the deposition of graphene micro- and nanostructures,* Carbon 117(2017)331-342
- Dahlberg T, *The first order Raman spectrum of isotope labelled nitrogen-doped reduced graphene oxide,* PhD thesis, Umeå University(2016)
- Dai L, Xue Y, Qu L, Choi H-J, Baek J-B, *Metal-free catalysts for oxygen reduction reaction,* Chemical Reviews 115(2015)4823-4892
- Das A, Chakraborty B, Sood AK, *Raman spectroscopy of graphene on different substrates and influence of defects,* Bull. Mater. Sci. 31(2008)579–584
- Dash GN, Pattanaik SR and Behera S, *Graphene for Electron Devices: The Panorama of a Decade,* Journal of the electron devices society 2(2014)2168-6734
- De Volder M, Tawfick, SH, Park SJ, Copic D, Zhao Z, Lu W, Hart AJ, *Diverse 3D microarchitectures made by capillary forming of carbon nanotubes*, Adv. Mater. 22(2010)4384-4389
- De Volder M, Hart AJ, *Engineering Hierarchical Nanostructures by Elastocapillary Self-Assembly*, Angew. Chem. Int. Ed. 52(2013)2412–2425
- Delgado JC, Herrera JMR, Jia X, Cullen DA, Muramatsu H, Kim YA, et al. *Bulk production of a new form of sp2 carbon: crystalline graphene nanoribbons*, Nano Lett. 8(2008)2773-2778
- Denysenko IB, Xu S, Long JD, Rutkevych PP, Azarenkov NA and Ostrikov K, *Inductively coupled Ar/*CH_4*/*H_2 *plasmas for low-temperature deposition of ordered carbon nanostructures,* J. Appl. Phys. 95(2004)2713
- Devaraj S, Munichandraiah N, *Electrochemical supercapacitor studies of nanostructured a-MnO2 synthesized by microemulsion method and the effect of annealing*, J. Electrochem. Soc. 154(2007)A80-A88

- Dikonimos T, Giorgi L,Giorgi L, Lisi N, Salernitano E and Rossi R, *DC plasma enhanced growth of oriented carbon nanowalls films by HFCVD*, Diamond Relat. Mater. 16(2007)1240–1243
- Dimovski S, Nikitin A, Ye H and Gogotsi Y, *Synthesis of graphite by chlorination of iron carbide at moderate temperatures*, J. Mater. Chem. 14 (2004)238–243
- Dresselhaus MS, Dresselhaus G, Avouris Ph, *Carbon nanotubes*, Topics Appl. Phys., Berlin 80(2001), ISBN 9783540399476
- Dresselhaus MS, Dresselhaus G and Eklund PC, *Science of Fullerenes and Carbon Nanotubes*, Academic Press 118(1996) 8987-8987, ISBN 0-12-221820-5
- Dresselhaus MS, Dresselhaus G, Jorio A, Souza Filho AG, Saito R. *Raman spectroscopy on isolated single wall carbon nanotubes*, Carbon 40(2002)2043–61
- Dresselhaus MS, Dresselhaus G, Saito R, Jorio A. *Raman spectroscopy of carbon nanotubes.* Phys Reports 409(2005)47–99
- Dresselhaus MS, *Perspectives on Carbon Nanotubes and Graphene Raman Spectroscopy*, Nano Lett. 10(2010)751–758
- Droes SR, Kodas TT and Hampden-Smith MJ , *Plasma-enhanced chemical vapor deposition (PECVD)*, Carbide, Nitride and Boride Materials Synthesis and Processing (1997)579-603, ISBN 978-94-010-6521-4
- Eckmann AA, Felten A, Mishchenko A, Britnell L, Krupke R, Novoselov KS, Casiraghi C, *Probing the nature of defects in graphene by raman spectroscopy*, Nano Lett.12(2012) 3925-3930
- Enoki T, Kobayashi Y and Fukui K, *Electronic structures of graphene edges and nanographene*, Int. Rev. Phys. Chem.26(2007)609
- Enoki T, *Role of edges in the electronic and magnetic structures of nanographene*, Physica Scripta T146(2012)014008
- El-Kady MF, Shao Y and Kaner RB, *Graphene for batteries, supercapacitors and beyond*, Nature Reviews Materials 1(2016)16033
- Eliasson B. and Kogelschatz U, *Nonequilibrium Volume Plasma Chemical-Processing.* Ieee Transactions on Plasma Science 19(1991)1063-1077
- Falcao EHL and Wudl F, *Carbon allotropes: beyond graphite and diamond, Review*, J. Chem. Technol. Biotechnol 82(2007)524–531
- Fan Z, Chen J, Zhang B, Sun F, Liu B, Kuang Y, *Electrochemically induced deposition method to prepare γ-MnO_2/multi-walled carbon nanotube composites as electrode material in supercapacitors*, Materials Research Bulletin 43(2008)2085-2091
- Fanchini G, Ray SC, Tagliaferro A, *Photoluminescence investigation of carbon nitride-based films deposited by reactive sputtering*, Diamond and Related Materials 12(2003)1084
- Ferrari AC, Robertson J, Raman *spectroscopy of amorphous, nanostructured, diamond-like carbon, and nanodiamond*, Philos. Trans. R. Soc. Lond. Ser. A362(2004)2477
- Ferrari AC, J. Robertson (Eds.), *Raman spectroscopy in carbons: From nanotubes to diamond.* Philos. Trans. R. Soc. Ser. A 362(2004a)2267–2565

- Ferrari AC and Robertson J, *Interpretation of Raman spectra of disordered and amorphous carbon*, Phys. Rev. B 61(2000)14095
- Ferrari AC, Meyer JC, Scardaci V, Casiraghi C, Lazzeri M, Mauri F, Piscanec S, Jiang D, Novoselov KS, Roth S, and Geim AK; *Raman Spectrum of Graphene and Graphene Layers*, The American Physical Society 97(2006)187401
- Ferrari AC. *Raman spectroscopy of graphene and graphite: disorder, electron-phonon coupling, doping and nonadiabatic effects*, Solid State Commun 143(2007)47–57
- Ferrari AC et al. *Science and technology roadmap for graphene, related two-dimensional crystals, and hybrid systems*, Nanoscale 7(2015)4598
- Ferrari AC and Basko DM, *Raman spectroscopy as a versatile tool for studying the properties of graphene*, Nature Nanotechnology 8(2013)235-46
- First PN, De Heer WA, Seyller T, Berger C, Stroscio JA, and Moon JS, *Epitaxial graphenes on silicon carbide,* MRS Bulletin 35(2010)1–35
- Fotiadis DI, Jensen KF, *Thermophoresis of solid particles in horizontal chemical vapor deposition reactors*, Journal of Crystal Growth 102(1990)743-761
- French BL, Wang JJ, Zhu MY and Holloway BC, *Structural characterization of carbon nanosheets via x-ray scatterin,* J. Appl. Phys. 97(2005)114317
- French BL, Wang JJ, Zhu MY, Holloway BC, *Evolution of structure and morphology during plasma-enhanced chemical vapor deposition of carbon nanosheets,* Thin Solid Films 494(2006) 105-109
- Geim A, Novoselov K**,** *Graphene – the perfect atomic lattice*, The Royal Swedish Academy of Sciences (2010), https://www.nobelprize.org/uploads/2018/06/popular-physicsprize2010.pdf
- Goncalves RGF, Lacerda RG, Ferlauto AS, Ladeira LO, Krambrock K, Pinheiro MVB, Leal AS, Viana GA, and Marques FC, *New material for low-dose brachytherapy seeds: Xe-doped amorphous carbon films with post-growth neutron activated 125,* Appl. Radiat. Isot. 69(2011)118
- Goldston RJ and Rutherford PH, *Introduction to plasma physics*, IOP Publishing Ltd. (1995), ISBN 0-7503-0325-5
- González J, Hernández MA, Guinea F, *La electrónica del grafeno*, Investigación y Ciencia (2010)42-49
- Ghosh S, Ganesan K, Polaki SR, Ravindran T, Krishna NG, Kamruddin M, et al. *Evolution and defect analysis of vertical graphene nanosheets,* J Raman Spectrosc 45(2014)642-9
- Griffiths PR, James A. De Haseth, Fourier Transform Infrared Spectrometry (2nd ed.), Wiley Interscience, Hoboken(2007), ISBN 9780470106297
- Grill A, *Diamond-like carbon: state of the art*, Diamond Relat. Mater.8(1999)428
- Guo Z, Dong R, Chakraborty PS, Lourenco N, Palmer J, Hu Y, Ruan M, Hankinson J, Kunc J, Cressler JD, et al. *Record Maximum Oscillation Frequency in C-Face Epitaxial Graphene Transistors,* Nano Lett. 13(2013)942–947
- Gupta A, Chen G, Joshi P, Tadigadapa S, Eklund PC, *Raman Scattering from High-Frequency Phonons in Supported n-Graphene Layer Films,* Nano Lett. 6(2006) 2667

- Hackley J, Ali D, DiPasquale J, Demaree JD and Richardson CJK, *Graphene growth by molecular beam epitaxy on the carbon-face of SiC*, Appl. Phys. Lett. 95(2009)133114
- Hafner B, *Scanning Electron Microscopy Primer, Characterization Facility*, Characterization Facility University of Minnesota—Twin Cities (2007), http://www.charfac.umn.edu/sem_primer.pdf
- Hasan T, Sun Z and Ferrari AC, *Nanotube–polymer composites for ultrafast photonics,* Advance Materials 21(2009)3874-3899
- Hass J, De Heer WA and Conrad EH, *The growth and morphology of epitaxial multilayer graphen,* Journal of Physics: Condensed Matter 20(2008)323202
- Heitz T , Drevillon B, Godet C, Bouree JE, *C–H bonding of polymer-like hydrogenated amorphous carbon films investigated by in-situ infrared ellipsometry*, Carbon 37(1999)771–775
- Henley SJ, Carey JD and Silva SRP, *Room temperature photoluminescence from nanostructured amorphous carbon,* Appl. Phys. Lett. 85(2004)6236
- Hershey W, The Book of Diamonds, J. Chem. Educ. 17(1940)22–28, ISBN 978-1-4179-7715-4
- Hicks J, Tejeda A, Taleb-Ibrahimi A, Nevius MS, Wang F, Shepperd K, Palmer J, Li X, Cai W, An J, Kim S, Nah J, Yang D, et al. *Large-Area Synthesis of High-Quality and Uniform Graphene Films on Copper Foils,* Science 324(2009)1312-4
- Hicks J, Tejeda A, Taleb-Ibrahimi A, Nevius MS, Wang F, Shepperd K, Palmer J, Bertran F, Le Fevre P, Kunc J, Heer WA, Berger C, Conrad EH, *A wide-bandgap metal-semiconductor-metal nanostructure made entirely from graphene*, Nat Phys 9(2013)49-54
- Hiralal P, Rius G, Andrew P, Yoshimura M and Gehan A, Amaratunga J, *Tailoring Carbon Nanostructure for High Frequency Supercapacitor Operation*, Journal of Nanomaterials (2014)619238
- Hiramatsu M, Shiji K, Amano H and Hori M, *Fabrication of vertically aligned carbon nanowalls using capacitively coupled plasma-enhanced chemical vapor deposition assisted by hydrogen radical injection***,** Appl. Phys. Lett. 84(2004)4708–4710
- Hiramatsu M, Nihashi Y, Kondo H, Hori M, *Nucleation control of self-organized vertical nano-graphenes using inductively coupled plasma enhanced chemical vapor deposition*, Japanese Journal of Applied Physics 51(2012)01AK05
- Hiramatsu M and Hori M, *Carbon Nanowalls: Synthesis and Emerging Application,* chapter 1, Springer, Vienna(2010), ISBN 978-3-211-99718-5
- Hiramatsu M, Kondo H, Hori M, *Graphene nanowalls*, New progress on graphene research, Chapter 9, Gong JR(Ed.), In Tech(2013)235-260, ISBN 978-953-51-1091-0
- Hiramatsu M and Hori M, *Fabrication of carbon nanowalls using novel plasma processing*, Japanese Journal of Applied Physics Part 1-Regular Papers Brief Communications & Review Papers 45(2006)5522-5527
- Hiraoka T, Izadi-Najafabadi A, Yamada T, Futaba DN, Yasuda S, Tanaike O, Hatori H, Yumura M, Iijima S,Hata K, *Compact and light supercapacitor electrodes from a surface-only solid by opened carbon nanotubes with 2200* m^2g^{-1} *surface area*, Adv Funct Mater 20(2010)422e8
- Hirth JP and Lothe J, *Theory of Dislocations*, Wiley, New York(1982)

- Hodkiewicz J, *Characterizing Graphene with Raman Spectroscopy*, Thermo Fisher Scientific, Madison(2010), https://tools.thermofisher.com/content/sfs/brochures/D19505~.pdf
- Hofmann S, Kleinsorge B, Ducati C, Ferrari AC, Robertson J, *Low-temperature plasma enhanced chemical vapour deposition of carbon nanotubes*, Diamond Relat Mater. 13(2004)1171–1176
- Hola K, Bourlinos AB, Kozak O, Berka K, Siskova KM, Havrdova M et al. *Photoluminescence effects of graphitic core size and surface functional groups in carbon dots: COO-induced red-shift emission*, Carbon 70(2014)279-286
- Holland L, Ojha SM, Deposition *of hard and insulating carbonaceous films on an r.f. target in a butane plasma*, Thin Solid Films 38(1976) L17
- Hone J, Whitney M and Zettl A, *Thermal conductivity of single-walled carbon nanotubes*, Synthetic Metals 103(1999)2498-2499
- Hopwood J, Guarnieri CR, Whitehair SJ, and Cuomo JJ, *Langmuir probe measurements of a radio frequency induction plasma*, J. Vac. Sci. Technol. A 11(1993)152–156
- Huang Y, Liang J, Chen Y, *An Overview of the Applications of Graphene‐Based Materials in Supercapacitors*, WILEY-VCH Verlag GmbH & Co 8(2012)1805-34
- Hussain S, Amade R, and Bertran E, *Study of CNTs structural evolution during water assisted growth and transfer methodology for electrochemical applications*, Mater. Chem. Phys. 148(2014)914–922
- Hussain S, Amade R, Jover E, Bertran E, *Water plasma functionalized CNTs/MnO_2 composites for supercapacitors*, The Scientific World Journal (2013)832581
- Hwang C, Yoo K, Kim SJ, Seo EK,Yu H and Biró LP, *Initial stage of graphene growth on a Cu substrate*, J. Phys. Chem. C 115(2011)22369–22374
- Hwang N, Barron AR, *BET Surface Area Analysis of Nanoparticles*, OpenStax-CNX module m38278(2011)
- Iijima S, *Helical microtubules of graphitic carbon*, Nature 354(1991)56
- Ion R, Vizireanu S, Luculescu C, Cimpean A and Dinescu G, *Vertically, interconnected carbon nanowalls as biocompatible scaffolds for osteoblast cells*, J. Phys. D: Appl. Phys. 49(2016)274004
- Iwano Y, Kittaka T, Tabuchi H, *Study of amorphous carbon nitride films aiming at white light emitting devices*, Jpn. J. Appl. Phys. 47(2008)7842–7844
- Jain HG, H. Karacuban, D. Krix, H. W. Becker, H. Nienhaus and Buck V, *Carbon nanowalls deposited by inductively coupled plasma enhanced chemical vapor deposition using aluminum acetylacetonate as precursor*, Carbon 49(2011)4987–4995
- Jackson ST, Nuzzo RG, *Determining hybridization differences for amorphous carbon from the XPS C1s envelope*, Appl Surf Sci 90(1995)195–203
- Jawhari T, *Handbook of instrumental techniques from CCiTUB, Raman spectroscopy as a powerful analytical tool: probing the structure of matter*, Universidad de Barcelona (2012)
- Jensen K , Kern W, Vossen JL and Kern W, *Thin Film Processes II*, Academic Press, New York(1991), ISBN 9780080524214

- Jhang SH, Craciun MF, Schmidmeier S, Tokumitsu S, Russo S, Yamamoto M, Skourski Y,Wosnitza J, Tarucha S, Eroms J, Strunk C, *Stacking-order dependent transport properties of trilayer graphene,* Phys. Rev. B 84(2011)1401–1408
- Jorio A, Dresselhaus M, Saito R and Dresselhaus G, *Raman Spectroscopy in Graphene Related Systems*, Wiley-VCH, Germany(2011), ISBN 978-3-527-40811-5
- Jung HK and Lee HW, *Effect of Catalytic Layer Thickness on Diameter of Vertically Aligned Individual Carbon Nanotubes,* Journal of Nanomaterials (2014)270989
- Kalita G and Tanemura M, *Fundamentals of Chemical Vapor Deposited Graphene and Emerging Applications,* Kyzas GZ and Mitropoulos ACh(Ed.), InTech(2017)
- Kalita G , Wakita K and Umeno M, *Low temperature growth of graphene film by microwave assisted surface wave plasma CVD for transparent electrode application*, RSC Adv. 2(2012)2815-2820
- Kastner J, Pichler T, Kuzmany H, Curran S, Blau W, Weldon DN et al., *Resonance Raman and infrared spectroscopy of carbon nanotubes,* Chem Phys Lett 221(1994)53–8
- Kelly BT, *Physics of graphite*, Applied Science, London 13(1981) 447, ISBN 0 85334 960 6
- Khan U, O'Neill A, Lotya M, De S, Coleman JN, *High-Concentration Solvent Exfoliation of Graphene*, Wiley-VCH Verlag GmbH & Co 6(2010)864–871
- Kim H, Mattevi C, Calvo MR, Oberg JC, Artiglia L, Agnoli S, Hirjibehedin CF, Chhowalla M, Saiz E, *Activation energy paths for graphene nucleation and growth on Cu*, ACS Nano 6(2012)3614
- Kim P, Shi L, Majumdar A and McEuen PL, *Thermal Transport Measurements of Individual Multiwalled Nanotubes*, Physical Review Letters 87(2001)215502-1-4
- Kim S, Kim J, Lim J, Lee H, Jun Y, and Kim D, *Coaxial Structure of Multiwall Carbon Nanotubes on vertically Aligned Si Nanorods and Its Intrinsicn Characteristics*, supplementary information, The Royal Society of Chemistry 2(2014)6985-6990
- Kimoto T, Itoh A, and Matsunami H. *Step-controlled epitaxial growth of high-quality SiC layers,* Phys. Status Solidi. 202(1997)247–262
- Kneipp K, Wang Y, Kneipp H, Perelman LT, Itzkan I, Dasari RR, Feld MS, Single *Molecule Detection Using Surface-Enhanced Raman Scattering (SERS),* Phys. Rev. Lett. 78(1997)1667-1670
- Kobayashi K, Tanimura M, Nakai H,Yoshimura A, Yoshimura H, Kojima K, Tachibana M, *Nanographite domains in carbon nanowalls,* J. Appl. Phys. 101(2007) 094306
- Kolmogorov AN, Crespi VH. *Registry-dependent interlayer potential for graphitic systems*, Phys. Rev. B 71 (2005)235415
- Kondo S and Hori M., *Highly reliable growth process of carbon nanowalls using radical injection plasma-enhanced chemical vapor deposition,* Journal of Vacuum Science & Technology B 26(2008)1294-1300
- Kondo S, Kawai S, Takeuchi W, Yamakawa K, Den S ,Kano H, Hiramatsu M and Hori M, *Initial growth process of carbon nanowalls synthesized by radical injection plasma-enhanced chemical vapor deposition*, Journal of Applied Physics 106(2009)094302-094302-6

- Koshino M. *Interlayer screening effect in graphene multilayers with ABA and ABC stacking*, Phys. Rev. B 81(2010) 760–762
- Krivchenko V, Evlashin S, Mironovich K, Verbitskiy N, Nefedov A, Wöll C, Kozmenkova AY, Suetin N, Svyakhovskiy S and Vyalikh D, *Carbon nanowalls: the next step for physical manifestation of the black body coating*, Sci. Rep. 3(2013)3328–3334
- Kroto HW, Heath JR, O'Brien SC, Curl RF & Smalley RE, *C60: Buckminsterfullerene*, Nature 318(1985)162–163
- Kumar P, Wani MF, *Synthesis and tribological properties of graphene: A review*, Jurnal Tribologi 13(2017)36-71
- Kurita S, Yoshimura A, Kawamoto H, Uchida T, Kojima K, Tachibana M, Molina-Morales P, Nakai H, *Raman spectra of carbon nanowalls grown by plasma-enhanced chemical vapor deposition*, Journal of Applied Physics 97(2005)104320
- Lancelot E, *Perspectives on Raman Spectroscopy of Graphene*, HORIBA Scientifi, Jobin Yvon Technology(2013),http://www.horiba.com/fileadmin/uploads/Scientific/Documents/Raman/RA50-Perspective_on_Raman_Spectroscopy_of_Graphene.pdf
- Landau LD, Lifshitz EM, *Statistical Physics, Part I*, Lifshitz EM and Pitaevskii LP(Ed.), Pergamon, Oxford(1980)
- Lang X, Hirata A, Fujita T, Chen M, *Nanoporous metal/oxide hybrid electrodes for electrochemical supercapacitors*, Nat. Nanotechnol. 6 (2011)232-236
- Lee C, Wei XD, Kysar JW, Hone J, *Measurement of the elastic properties and intrinsic strength of monolayer graphene*, Science 321(2008)385-388
- Lens M, *Use of fullerenes in cosmetics*, Recent Pat Biotechnol 3(2009)118-23
- Li B, Li S, Liu J, Wang B, Yang S, *Vertically aligned sulfur-graphene nanowalls on substrates for ultrafast lithium-sulfur batteries*, Nano Letters 15(2015)3073-3079
- Li M, Liu D, Wei D, Song X, Wei D, and Thye Shen Wee A, *Controllable Synthesis of Graphene by Plasma-Enhanced Chemical Vapor Deposition and Its Related Applications*, Adv. Sci. 3(2016)1600003
- Li T, Beidaghi M, Xiao X, Huang L, Hu Z, Sun W, Chen X, Gogotsi Y, Zhou J, *Ethanol reduced molybdenum trioxide for Li-ion capacitors*, Nano Energy 26(2016)100-107
- Li XS, Cai W, An J, Kim S, Nah J, Yang D, Piner R, Velamakanni A, Jung I, Tutuc E, Banerjee SK, Colombo L, Ruoff RS, *Large-area synthesis of high-quality and uniform graphene films on copper foils*, Science 324(2009)1312
- Liao Y et al., *Analysis of optical emission spectroscopy in diamond chemical vapor deposition*, Diamond and Related Materials 9(2000)1716-1721
- Lieberman MA and Lichtenberg AJ, *Principles of Plasma Discharges and Materials Processing*, Second ed., Hoboken, John Wiley & Sons Inc.(2005), ISBN 0-471-72001-1
- Lifshitz Y, *Diamond-like carbon — present status*, Diamond Relat. Mater. 8(1999)1659
- Lin CK, Chuang KH, Lin CY, Tsay CY, Chen CY, *Manganese oxide films prepared by sol-gel process for supercapacitor application*, Surf. Coat. Technol. 2002(2007)1272-1276

- Lin YM, Dimitrakopoulos C, Jenkins KA, Farmer DB, Chiu H-Y, Grill A, Avouris P, *100-GHz Transistors from Wafer-Scale Epitaxial Graphene*, Science 327(2010)662
- Lim X, Foo GHW, Chia GH, Sow CH, *Capillarity-assisted assembly of carbon nanotube microstructures with organized initiations*, ACS Nano 4(2010)1067–1075
- Lisi N, Giorgi R, Re M, Dikonimos T, Giorgi L, Salernitano E, Gagliardi S, Tatti F, *Carbon nanowall growth on carbon paper by hot filament chemical vapour deposition and its microstructure*, Carbon 49(2011)2134-2140
- Liu H, Xu Q, Yan C, Qiao Y, *Corrosion behavior of a positive graphite electrode in vanadium redox flow battery*, Electrochimica Acta 56(2011)8783
- Liu J, Sun W, Wei D, Song X, Jiao T, He S, Zhang W, Du C, *Direct growth of graphene nanowalls on the crystalline silicon for solar cells*, Appl. Phys. Lett. 106(2015)043904
- Liu XSJ, Yu L,Yang J, Fang L, Shi H, Du C, Wei D, Direct *versatile PECVD growth of graphene nanowalls on multiple substrates*, Materials Letters 137(2014)25–28
- Liu Z, Fu D, Liu F, Han G, Liu C, Chang Y, et al. *Mesoporous carbon nanofibers with large cage-like pores activated by tin dioxide and their use in supercapacitor and catalyst support*, Carbon 70(2014)295e307
- Lowe M, Tokuoka S, Trigg T and Gereffi G, *Lithium-ion Batteries for Hybrid and All-Electric Vehicles*, Center on Globalization, Governance & Competitiveness Duke University(2010), https://unstats.un.org/unsd/trade/s_geneva2011/refdocs/RDs/LithiumIon%20Batteries%20(Gereffi%20-%20May%202010).pdf
- Lui CH, Li ZQ, Chen ZY, Klimov PV, Brus LE, Heinz TF, *Imaging Stacking Order in Few-Layer Graphene*, Nano Lett. 11(2011)164–169
- Lv R, Li Q, Botello-Mendez AR, Hayashi T, Wang B, Berkdemir A, Hao Q,Elıas AL, Cruz-Silva R , Gutierrez HR, Kim YA, Muramatsu H, Zhu J, Endo M, Terrones H, Charlier J-C, Pan M, Terrones M: *Nitrogen-doped graphene: Beyond single substitution and enhanced molecular sensing*, Sci. Rep. 2(2012)586
- Ma L,Wang L,Chen R,Chang K,Wang S, Hu X, Sun X, Lu Z, Sun H, Guo Q, Jiang M and Hu J, *A Low Cost Compact Measurement System Constructed Using a Smart Electrochemical Sensor for the Real-Time Discrimination of Fruit Ripening*, Sensors (Basel) 16(2016)
- Macdonald JR, *Impedance Spectroscopy*, Macdonald JR(Ed.), John Wiley & Sons, New York(1987), ISBN 0471831220
- Maeda F and Hibino H, *Graphitic Structure Formation on Various Substrates by Gas-Source Molecular Beam Epitaxy Using Cracked Ethanol*, Appl. Phys. 49(2010)04DH13
- Mackenzie KD, Lee JW, and Johnson D, *Inductively-coupled plasma deposition of low temperature silicon dioxide and silicon nitride films for III-V applications*, 195Th Electrochemical Society Meeting, Seattle WA. Proc. Symp. 30th State-of-the-Art Program on Compound Semiconductors, 99-4, 1-12, Electrochemical Society, Pennington, NJ (1999)
- Malara N, Gentile F, Ferrara L, Villani M, Iannotta S,Zappettini A, Di Fabrizio E, Trunzo V, Mollace V and Coppedé N, *Tailoring super-hydrophobic properties of electrochemical biosensor for early cancer detection*, Soft Materials and Biomaterials 1(2016)3545-3552

- Malard LM, Pimenta MA, Dresselhaus G, Dresselhaus MS, *Raman spectroscopy in graphene*, Physics Reports 473(2009)51–87
- Malesevic A, Vitchev R, Schouteden K, Volodin A, Zhang L, Tendeloo GV, Vanhulsel A, Haesendonck CV, *Synthesis of few-layer graphene via microwave plasma-enhanced chemical vapour deposition*, Nanotechnology 19(2008)305604
- Malesevic A, Vizireanu S, Kemps R, Vanhusel A, Haesendonck C.V, Dinescu G, *Combined growth of carbon nanotubes and carbon nanowalls by plasma-enhanced chemical vapor deposition*, Carbon 45(2007)2932-37120
- Mansour KM, Soileau J and Van Stryland EW, *Nonlinear optical properties of carbon-black suspensions (ink)*, Journal of the Optical Society of America B-Optical Physics 9(1992)1100-1109
- Mantzaris NV, Gogolides E, Boudouvis AG, Rhallabi A, Turban G, *Surface and plasma simulation of deposition processes: CH_4 plasmas for the growth of diamondlike carbon*, J. Appl. Phys. 79 (1996)3718–3729
- Marchon B, Vo PN, Khan MR, Ager JW, S*tructure and mechanical properties of hydrogenated carbon films prepared by magnetron sputtering*, IEEE Trans. Magn. 27(1991)5160
- Masarapu C, Zeng HF, Hung KH, Wei B, *Effect of temperature on the capacitance of carbon nanotube supercapacitors*, ACS Nano 3(2009)2199-2206
- McCulloch DG, McKenzie DR, Goringe CM, *Ab initio simulations of the structure of amorphous carbon*, Phys. Rev. B 61(2000)2349
- McKenzie DR, *Tetrahedral bonding in amorphous carbon*, Rep. Prog. Phys. 59(1996)1611
- Merlen A, Buijnsters JG and Pardanaud C, *A Guide to and Review of the Use of Multiwavelength Raman Spectroscopy for Characterizing Defective Aromatic Carbon Solids: from Graphene to Amorphous Carbons*, Coatings 7(2017)153
- Meyer J, *Carbon sheets an atom thick give rise to graphene dreams*, Science 324(2009)875-7
- Mori T, Hiramatsu M, Yamakawa K, Takeda K, Hori M , *Fabrication of carbon nanowalls using electron beam excited plasma enhanced chemical vapor deposition*, Diamond and Related Materials 17(2008)1513-1517
- Mori T, Hiramatsu M, Yamakawa K, Takeda K, Hori M: *Synthesis and electrical characterization of n-type carbon nanowalls Diamond*, Relat. Mater. 17(2008a)1513
- Moon IK, Lee J, Ruoff RS, Lee H, *Reduced graphene oxide by chemical graphitization*, Nat. Commun. 1(2010)73
- Moulder JF, Stickle WF, Sobol PE, Bomben KD, *Handbook of X-Ray Photoelectron Spectroscopy: A Reference Book of Standard Spectra for Identification and Interpretation of XPS Data*, Chastain J(Ed.), Physical Electronics Division, Minnesota(1995)
- Musheghyan-Avetisyan A,Gonzalez JM and Bertran E, *Direct low temperature growth of vertically oriented graphene nanowalls on multiple substrates by Low Temperature Plasma-Enhanced Chemical Vapor Depositin*, TNT2017,Dresden,Oral presentation(2017)
- Nair RR, Blake P , Grigorenko AN, Novoselov KS, Booth TJ, Stauber T, Peres NMR, Geim AK, *Fine structure constant defines visual transparency of Graphene*, Science 320(2008)1308

- Nelis T and Payling R, *Glow Discharge Optical Emission Spectroscopy: A Practical Guide*, Barnett NV (Ed.), The Royal Society of Chemistry, Cambridg(2003), ISBN 0-85404-521-X
- Neuville S and Matthews A, *A perspective on the optimisation of hard carbon and related coatings for engineering applications*, Thin Solid Films 515(2007)6619
- Ni Z, Wang Y, Yu T, Shen Z, *Raman spectroscopy and imaging of graphene*, Nano Research 1(2008)273–291
- Ni ZH, Fan HM, Fan XF, Wang HM, Zheng Z, Feng YP, Wu YH, Shen ZX, *High temperature Raman spectroscopy studies of carbon nanowalls*, Journal of Raman Spectroscopy 38(2007)1449-1453
- Ni ZH, Wang HM, Kasim J, Fan HM, Yu T, Wu YH, Feng YP and Shen ZX, *Graphene thickness determination using reflection and contrast spectroscopy*, Nano Lett 7(2007a)2758–2763
- Ni ZH, Fan HM, Feng YP, Shen ZX, Yang BJ, Wu YH ,*Raman spectroscopic investigation of carbon nanowalls,*Journal of Chemical Physics 124(2006)204703
- Nie S, Wofford JM, Bartelt NC, Dubon OD, McCarty KF, *Origin of the mosaicity in graphene grown on Cu(111)*, Physical Review B 84(2011)155425
- Nika DL, Balandin AA, *Two-dimensional phonon transport in graphene*. J. Phys 24(2012)233203
- Novoselov KS, Geim AK, Morozov SV, Jiang D, Zhang Y, Dubonos SV, Grigorieva IV and Firsov AA, *Electric Field Effect in Atomically Thin Carbon Films*, Science 306(2004)666-9
- Novoselov KS, Falko VI, Colombo L, Gellert PR, Schwab MG, and Kim K, *A roadmap for graphene*, Nature 490(2012)192–200
- Novoselov KS, Jiang D, Schedin F, Booth TJ, Khotkevich VV, Morozov SV, and Geim AK, *Two-dimensional atomic crystals*, PNAS 102(2005)10451-10453
- Novoselov KS, Geim AK, Morozov SV, Jiang D, Katsnelson MI, Grigorieva IV, Dubonos SV, Firsov AA, *Two-dimensional gas of massless Dirac fermions in graphene*, Nature 438(2005a)197-200
- Obraztsov AN, Volkov AP, Nagovitsyn KS, Nishimura K, Morisawa K, Nakano Y and Hiraki A, *CVD growth and field emission properties of nanostructured carbon films*, J. Phys. D-Appl. Phys. 35(2002)357–362
- Obraztsov AN, Zolotukhin AA, Ustinov AO, Volkov AP, Svirko Y and Jefimovs K, *DC discharge plasma studies for nanostructured carbon CVD*, Diamond Relat. Mater. 12(2003)917-920
- Ojha SM, *Plasma-Enhanced Chemical Vapor Deposition of Thin Films*, Physics of Thin Films 12(1982)237-296
- Ostrikov K and Xu S, *Plasma-Aided Nanofabrication*, Wiley-VCH Verlag GmbH & Co. KGaA, Weinheim(2007), ISBN 9783527611553
- Ostrikov K, *Plasma Nanoscience*, Wiley-VCH Verlag GmbH & Co. KGaA, Weinheim(2008), ISBN 9783527407408
- Ouksel L, Kerkour R, Chelali NE, *Proton diffusion process manganese dioxide for use in rechargeable alkaline zinc manganese dioxide batteries and its electrochemical performance*, Ionics 22(2016)1751-1757

- Paillet M , Parret R , Sauvajol JL , Colomban P, *Graphene and related 2D materials: An overview of the Raman studies,* J. Raman Spectrosc 49(2018)8–12
- Pan Y, Sahoo NG, Li L. *The application of graphene oxide in drug delivery*, Expert Opin Drug Deliv. 9(2012)1365–76
- Pandit B, Dubai DP, Gómez-Romero P, Kale BB, Sankapal BR, *V_2O_5 encapsulated MWCNTs in 2D surface architecture: Complete solid-state bendable highly stabilized energy efficient supercapacitor device,* Sci. Rep. 7(2017)43430:1-12
- Pang SC, Anderson MA, Chapman T, *Novel electrode materials for thin-film ultracapacitors: Comparison of electrochemical properties of sol-gel-derived and electrodeposited manganese dioxide,* Journal of the Electrochemical Society 147(2000)444-450
- Park S, Vosguerichian M and Bao Z, *A review of fabrication and applications of carbon nanotube film-based flexible electronics,* Nanoscale 5(2013)1727
- Parvez K, *Chemical exfoliation of graphene and its application in organic electronics and energy storage devices,* dissertation, Max Planck Institute for Polymer Research, Germany(2014)
- Peigney A, Laurent C, Flahaut E, Bacsa R, Rousset A, *Specific surface area of carbon nanotubes and bundles of carbon nanotubes,* Carbon 39(2001)507-514
- Peng B, Locascio M, Zapol P, Li S, Mielke SL, Schatz GC and Espinosa HD, *Measurements of near-ultimate strength for multiwalled carbon nanotubes and irradiation-induced crosslinking improvements*, Nature Nanotechnology 3(2008)626-631
- Peres NMR, *The transport properties of graphene: an introduction*, Rev.Mod. Phys. 82(2010)2673–2700
- Pérez del Pino A, György E, Alshaikh I, Pantoja-Suárez F, Andújar J-L, Pascual E, Amade R, Bertran-Serra E, *Laser-driven coating of vertically aligned carbon nantoubes with manganese oxide from metal organic precursors for energy storage*, Nanotechnology 28(2017)395405
- Popov C, Kulisch W, Jelinek M, Bock A, and Strand J, *Nanocrystalline diamond/amorphous carbon composite films for applications in tribology, optics and biomedicine*, Thin Solid Films 494(2006)92-97
- Porter DA and Easterling KE, *Phase Transformations in Metals and Alloys,* Second ed., Chapman & Hall, Hong Kong(1992), ISBN 978-0-442-31638-9
- Prasher R, *Thermal Interface Materials: Historical Perspective, Status, and Future Directions*, Proc. of the IEEE 94(2006)1571–1586
- Qu D, *Application of a.c. impedance technique to the study of the proton diffusion process in the porous MnO_2 electrode,* Electrochim. Acta 48(2003)1675-1684
- Raman CV, *The diamond: Its structure and properties,* Proc. Indian Acad. Sci. A 67(1968)231-246
- Raman CV, *The structure and properties of diamond,* Curr. Sci. (Suppl.) 12(1943)33-42
- Rashid H and Ralph SF, *Carbon Nanotube Membranes: Synthesis, Properties, and Future Filtration Applications,* Nanomaterials (Basel) 7(2017)99

- Ravula S, Baker SN, Kamath G and Baker GA, *Ionic liquid-assisted exfoliation and dispersion: stripping graphene and its two-dimensional layered inorganic counterparts of their inhibitions*, Nanoscale **7**(2015)4338-4353
- Raymundo-Piñero E, Khomenko V, Frackowiak E, Béguin F, *Performance of manganese oxide/CNTs composites as electrode materials for electrochemical capacitors*, Journal of the Electrochemical Society 152(2005)A229-A235
- Reina A, Son H, Jiao L, Fan B, Dresselhaus MS, Liu ZF, Kong J, *Transferring and Identification of Single - and Few-Layer Graphene on Arbitrary Substrates*, J. Phys. Chem. C 112(2008)17741-17744
- Reinert F and Hufner S, *Photoemission spectroscopy—from early days to recent applications*, New Journal of Physics **7**(2005)97
- Rizzuto T, *Fundamentals of Raman Spectroscopy*, StellarNet, Inc. Tampa FI USA(2017), https://www.stellarnet.us/fundamentals-of-raman-spectroscopy/
- Robertson J, *Amorphous carbon*, Adv. Phys. 35(1986)317
- Robertson J., *Recombination and photoluminescence mechanism in hydrogenated amorphous carbon*, Phys Rev 53(1996)16302
- Robertson J, *Diamond-like amorphous carbon*, Materials Science and Engineering R Paillet 37(2002)129-281
- Rosso MA, *Origins, Properties, and Applications of Carbon Nanotubes and Fullerenes*, California State University Fresno, Spring(2001)
- Saito R, Hofmann, M, Dresselhaus, G, Jorio A, Dresselhaus MS, *Raman spectroscopy of graphene and carbon nanotubes*, Adv. Phys. 30(2011)413-550
- Sandeep KV, Venkatesh AG, *Advances in Graphene-Based Sensors and Devices*, J Nanomed Nanotechol 4(2013)e127
- Santamaria A., Yang N, Mondragon F and Eddings EG, *Chemical and morphological characterization of soot and soot precursors generated in an inverse diffusion flame with aromatic and aliphatic fuels*, Combustion and flame 157(2010)33
- Sarangdevot K and Sonigara BS, The wondrous *world of carbon nanotubes: Structure, synthesis, properties and applications*, J. Chem. Pharm. Res. 7(2015)916-933
- Sarma D, Adam S, Hwang EH, and Rossi E, *Electronic transport in two-dimensional graphene*, Rev. Mod. Phys. 83(2011)407–470
- Sato G, Morio T, Kato T and Hatakeyama R, *Fast growth of carbon nanowalls from pure methane using helicon plasma enhanced chemical vapor deposition*, Jpn. J. Appl.Phys. 45(2006)5210-5212
- Scherrer P, *Bestimmung der Grosse und der Inneren Struktur von Kolloidteilchen Mittels Rontgenstrahlen*, Nachrichten von der Gesellschaft der Wissenschaften, Mathematisch-Physikalische Klasse 2(1918)98-100
- Patterson A, *The Scherrer Formula for X-Ray Particle Size Determination*, Phys. Rev. 56(10)(1939)978–982
- Schwan J, Ulrich S, Batori V, Ravi S, Silva P, *Raman Spectroscopy on Amorphous Carbon Films*, Journal of Applied Physics 80(1996)440 – 447

- Schwan J, Ulrich S, Theel T, Roth H, Ehrhardt H, Becker P, et al., *Stress-induced formation of high-density amorphous carbon thin films,* J Appl Phys. 82(1997)6024-30
- Seah C-M, Chai S-P, Mohamed AR, *Mechanisms of graphene growth by chemical vapour deposition on transition metals,* Carbon 70(2014)1 –21
- Seo DH, Kumar S, Ostrikov K, *Control of morphology and electrical properties of self-organized graphenes in a plasma*, Carbon 49(2011)4331–4339
- Shahil KMF, Balandin AA, *Thermal Properties of Graphene: Applications in Thermal Interface Materials*, Solid State Communications 152(2012)1331–1340
- Shang NG, Papakonstantinou P, McMullan M, Chu M, Stamboulis A, Potenza A, Dhesi SS and Marchetto H, Catalyst-Free Efficient Growth, *Orientation and Biosensing Properties of Multilayer Graphene Nanoflake Films with Sharp Edge Planes*, Adv. Funct. Mater. 18(2008)3506–3514
- Shi B, Meng WJ, Evans RD, Hershkowitz N, *Deposition of highly hydrogenated carbon films by a modified plasma assisted chemical vapor deposition technique,* Surface & Coatings Technology 200(2005)1543-1548
- Shinde KN, Dhoble SJ, Swart HC, Park K, *Basic Mechanisms of Photoluminescence. In: Phosphate Phosphors for Solid-State Lighting,* Springer Series in Materials Science, Berlin 174(2012), ISBN 978-3-642-34312-4
- Siburian R, Sihotang H, Lumban Raja S, Supeno M, Simanjuntak C, *New Route to Synthesize of Graphene Nano Sheets,* Orient J Chem 34(2018)
- Simon P and Gogotsi Y, *Materials for electrochemical capacitors,* Nat. Mater. 7(2008) 845-854
- Singh R, Kumar D , Tripathi CC, *Graphene: Potential material for nanoelectronics applications*, Indian Journal of Pure & Applied Physics 53(2015)501-513
- Shih CJ, Wang QH,Lin S, Park K-C, Jin Z, Strano MS, and Blankschtein D, *Breakdown in the Wetting Transparency of Graphene,* Phys. Rev. Lett. 109(2012)176101
- Shiomi T, Nagai H, Kato K, Hiramatsu M, Nawata M, *Detection of* C_2 *radicals in low-pressure inductively coupled plasma source for diamond chemical vapor deposition*, Diam. Relat. Mater. 10(2001)388–392
- Shiji K, Hiramatsu M, Enomoto A, Nakamura N, Amano H and Hori M, *Vertical growth of carbon nanowalls using rf plasma-enhanced chemical vapor deposition*, Diamond Relat. Mater. 14(2005)831–834
- Sivudu KS and Mahajan Y, *Challenges and opportunities for the mass production of high quality graphene:an analysis of worldwide patents,* Nanotech Insights 3(2012)6-19
- Smith E, Dent G, *Modern Raman Spectroscopy- A Practical Approach,* John Wiley & Sons Ltd, Chichester(2005), ISBN 0-471-49794-0
- Soin N, Roy SS, O'Kane C, James AD, McLaughlin,T, Lim H, Crispin JD, Hetherington D, *Exploring the fundamental effects of deposition time on the microstructure of graphene nanoflakes by Raman scattering and X-ray diffraction,* CrystEngComm 13(2011)312
- Song Y, Chang S, Gradecak S,Kong J, *Visibly-Transparent Organic Solar Cells on Flexible Substrates with All-Graphene Electrodes,* Advanced Energy Materials 6(2016)1600847

- Srivastava SK, Kumar V and Vankar VD, *Carbon Nanowalls: A Potential 2-Dimensional Material for Field Emission and Energy-Related Applications*, Khan ZH (Ed.), Nanomaterials and Their Applications 84(2018), ISBN 978-981-10-6214-8
- Stillahn JA, Trevino KJ, and Fisher ER, *Plasma Diagnostics for Unraveling Process Chemistry*, Annual Review of Analytical Chemistry 1(2008)261-291
- Sui Z-Y, Meng Q-H, Li J-T, Zhu J-H, Cui Y, Han B-H. *High surface area porous carbons produced by steam activation of graphene aerogels*, J Mater Chem A 2(2014)9891e8
- Sullivan JP, Robertson J, Zhou O, Allen T B, Coll BF(eds.), *Amorphous and Nanostructured Carbon*, CambridgeUniversityPress, Materials Research Society 593(2000)
- Sun J, Chen Y, Cai X,Ma B, Chen Z, Kr. Priydarshi M, Chen K, Gao T, Song X, Ji Q, Guo X, Zou D, Zhang Y and Liu Z, *Direct low temperature synthesis of graphene on arbitrary glasses by plasma-enhanced CVD for versatile, cost-effective electrodes*, Nano Res. (2015)
- Takeuchi W, Ura M, Hiramatsu M, Tokuda Y, Kano H and Hori M, *Electrical conduction control of carbon nanowalls*, Appl. Phys. Lett. 92(2008)213103
- Tanaike O, Kitada N, Yoshimura H, Hatori H, Kojima K and Tachibana M, *Lithium insertion behavior of carbon nanowalls by DC plasma CVD and its heat-treatment effect*, Solid State Ionics 180(2009)381–385
- Tang N, Tian XK, Yang C, Pi ZB, *Facile synthesis of a-MnO_2 nanostructures for supercapacitors*, Materials Research Bulletin 44(2009)2062-2067
- Tarascon JM, Armand M, *Issues and challenges facing rechargeable lithium batteries*, Nature 414(2001)359-67
- Thompson M, *CHNS Elemental Analysers*, The Royal Society of Chemistry (2008), https://www.rsc.org/images/chns-elemental-analysers-technical-brief-29_tcm18-214833.pdf
- Teii K, Shimada S, Nakashima M and Chuang ATH, *Synthesis and electrical characterization of n-type carbon nanowalls*, Journal of Applied Physics 106(2009)084303
- Terasawa T, Saiki K, *Growth of graphene on Cu by plasma enhanced chemical vapor deposition*, Carbon 50(2012)869–874
- Terse-Thakoor T, Badhulika S , Mulchandani A , *Graphene based biosensors for healthcare*, Materials Research Society 32(2017)2905-2929
- Theye ML and Paret V, *Spatial organization of the sp^2-hybridized carbon atoms and electronic density of states of hydrogenated amorphous carbon f*ilms, Carbon 40(2002)1153
- Thostenson ET, Ren Z, Chou T-W, *Advances in the science and technology of carbon nanotubes and their composites: a review*, Composites Science and Technology 61(2001)1899-1912
- Torrisi F, Hasan T, Wu W, Sun Z, Lombardo A, Kulmala T, Hshieh GW, Jung SJ, Bonaccorso F, Paul PJ, Chu DP, Ferrari AC, *Ink-Jet Printed Graphene Electronics*, ACS Nano 6(2012)2992-3006
- Toupin M, Brousse T, Bélanger D, *Charge storage mechanism of MnO_2 electrode used in aqueous electrochemical capacitor*, Chem. Mater. 16(2004)3184-3190
- Tsang C, Kim J, Manthiram A, *Synthesis of manganese oxides by reduction of $KMnO_4$ with KBH4 in aqueous solutions*, J. Solid State Chem. 137(1998)28-32

- Tuinstra F. and Koening J.L., *Raman Spectrum of Graphite*, J.Chem.Phys. 53(1970)1126
- Tutt LW and Kost A, *Optical Limiting Performance of C60 and C70 Solutions,* Nature 356(1992)225-226
- Tutt LW and Boggess TF, *A review of optical limiting mechanisms and devices using organics, fullerenes, semiconductors and other materials*, Progress in Quantum Electronics 17(1993)299-338
- Tzalenchuk A, Lara-Avila S, Kalaboukhov A, Paolillo S, Syväjärvi M. Yakimova R, Kazakova O, Janssen TJBM, Fal'ko V, Kubatkin S, *Towards a quantum resistance standard based on epitaxial graphene,* Nat. Nanotechnol. 5(2010)186–189
- Ulloa E, *Fullerenes and their Applications in Science and Technology,* Introduction to Nanotechnology Spring (2013)4138296
- Venables JA, Spiller GDT, Hanbucken M, *Nucleation and Growth of Thin Films,* Rep. Prog. Phys. 47(1984)399-459
- Venezuela P, Lazzeri M, and Mauri F, *Theory of double-resonant Raman spectra in graphene: Intensity and line shape of defect-induced and two-phonon bands*, Phys. Rev. B 84(2011) 035433
- Veprek S, *Structural Nanocrystalline Materials: Fundamentals and Applications*, Cambridge University Press, Cambridge(2007), ISBN-13 978-0-521-85565-5
- Vickerman JC and Gilmore IS, *Surface Analysis – The Principal Techniques*, 2nd Edition, Wiley-Blackwell (Verlag), Teddington(2009) , ISBN 978-0-470-01764-7
- Vignaud D, Moreau E, *Graphene growth by molecular beam epitaxy,* in Mol. Beam Epitaxy, chapter 23,Henini M (Ed.), Elsevier (2013)547-557
- Vizireanu S, Stoica S-D, Mitu B, Husanu M-A, Galca AC, Nistor LC, Dinescu G., *Radiofrequency plasma beam deposition of various forms of carbon based thin films and their characterization*, Applied Surface Science 255(2009)5378-5381
- Vizireanu S, SD Stoica, C Luculescu, LC Nistor, B Mitu, G Dinescu, *Plasma techniques for nanostructured carbon materials synthesis. A case study: carbon nanowall growth by low pressure expanding RF plasma,* Plasma Sources Science and Technology 19(2010)034016
- Vizireanu S, Nistor L, Haupt M, Katzenmaier V, Oehr C, Dinescu G. *Carbon nanowalls growth by radio frequency plasma-beam-enhanced chemical vapor deposition,* Plasma Processes Polym 5(2008)263–8
- Wang BB, Cheng QJ, Chen YA, Ostrikov K. *Room-temperature photoluminescence from nitrogenated carbon nanotips grown by plasma-enhanced hot filament chemical vapor deposition*, J Appl Phys 110(2011)054323
- Wang BB, Cheng QJ, Wang LH, Zheng K, Ostrikov K, *The effect of temperature on the mechanism of photoluminescence from plasma-nucleated, nitrogenated carbon nanotips,* Carbon 50(2012)3561
- Wang BB, Cheng QJ, Wang LH, Zheng K, Ostrikov K, *Structure and photoluminescence properties of carbon nanotip-vertical graphene nanohybrids* , Carbon 50(2012a)3561
- Wang G, Zhang L, Zhang J, *A review of electrode materials for electrochemical supercapacitors,* Chemical Society Reviews 41(2012)797-828

- Wang H, Gao E, Liu P, Zhou D, Geng D, Xue X, Wang L, Jiang K, Xu Z, Yu G, *Facile growth of vertically-aligned graphene nanosheets via thermal CVD: The experimental and theoretical investigations*, Carbon 121(2017)1-9
- Wang JJ, Zhu MY, Outlaw RA, Zhao X, Manos DM, Holloway B C and Mammana VP, *Improved field emission property of graphene paper by plasma treatment*, Appl. Phys. Lett. 85(2004)1265
- Wang JJ, Zhu MY, Outlaw RA, Zhao X, Manos DM and Holloway BC, *Synthesis of carbon nanosheets by inductively coupled radio-frequency plasma enhanced chemical vapor deposition*, Carbon 42(2004a)2867–2872
- Wang J and Blau WJ, *Inorganic and Hybrid Nanostructures for Optical Limiting*, Journal of Optics A – Pure and Applied Optics 11(2009)024001
- Wang X, Hao H, Liu J, Huang T, Yu A, *A novel method for preparation of macroporous lithium nickel manganese oxygen as cathode material for lithium ion batteries*, Electrochim. Acta 56(2011)4065-4069
- Wang YY, Ni ZH, Yu T, Wang HM, Wu YH, Chen W, Wee ATS, Shen ZX, *Raman studies of monolayer graphene: the substrate effect*, J. Phys. Chem. C 112(2008)10637-10640
- Wasa K, Kitabatake M and Adachi H, *Thin Film Materials Technology - Sputtering of Compound Materials*., William Andrew Publishing(2004), ISBN 9780815519317
- Wei J, Nagarajan N, Zhitomirsky I, *Manganese oxide films for electrochemical supercapacitors*, Journal of Materials Processing and Technology 186(2007)356-361
- Wen L, Li F, Cheng H-M, *Carbon nanotubes and graphene for flexible electrochemical energy storage: from materials to devices*, Advanced Materials 28(2016)4306-4337
- Williams ATR, *An Introduction to Fluorescence Spectroscopy*, Perkin-Elmer, Buckinghamshire(1981),https://www.chem.uci.edu/~dmitryf/manuals/Fundamentals/Fluorescence%20Spectroscopy.pdf
- Williams DB, Carter CB, *Transmission Electron Microscopy*, A Textbook for Materials Science, Springer Science+Business Media LLC(1996), ISBN 978-0-387-76501-3
- Williams D, Carter C. *Transmission Electron Microscopy: A Textbook for Materials Science*, Springer, New York(2009), ISBN 978-0-387-76500-6
- Woehrl N, Olivr Ochedowski O, Gottlieb S, Shibasaki K, Schulz S, *Plasma-enhanced chemical vapor deposition of graphene on copper substrates* , AIP Advances 4(2014)047128
- Wu A, Xiaodong Li, Yang J, Du C, Shen W and Yan J, *Upcycling Waste Lard Oil intoVertical Graphene Sheets by Inductively Coupled Plasma Assisted Chemical Vapor Deposition*, Nanomaterials *7*(2017)318
- Wu YH, Qiao P, Chong T, Shen Z, *Carbon nanowalls grown by microwave plasma enhanced chemical vapor deposition*, Advanced Materials 14(2002)64-67
- Wu YH, Yang B, Zong B, Sun H, Shen Z and Feng Y, *Carbon nanowalls and related materials*. Journal of Materials Chemistry 14(2004)469-477
- Wu YH, Yu T and Shen ZX, *Atomic lattice structure and continuum plate theories for the vibrational characteristics of graphenes*, J. Appl. Phys. 108(2010)071301

- Wu Y, Yang B, Zong B, Sun H, Shen Z, Feng Y, *Carbon nanowalls and related materials*, Journal of Materials Chemistry 14(2004)469-477
- Yadav BC and Kumar R, *Structure, properties and applications of fullerenes*, International Journal of Nanotechnology and Applications 2(2008)15-24
- Yakobson BI, Brabec CJ, Bernholc J, *Nanomechanics of Carbon Tubes: Instabilities beyond Linear Response*, Phys.Rev.Lett. 76(1996)2511
- Yang J, Wei D, Tang L, Song X, Luo W, Chu J, Gao T, Shi H and Du C, *Wearable temperature sensor based on graphene nanowalls*, RSC Adv. 5(2015)25609-25615
- Yang N, Yang D, Zhang G, Chen L, Liu D, Cai M and Fan X, *The Effects of Graphene Stacking on the Performance of Methane Sensor: A First-Principles Study on the Adsorption, Band Gap and Doping of Graphene*, Sensors 18(2018)422
- Yang W, Ni M, Ren X, Tian Y, Li N, Su Y, Zhang X, *Graphene in Supercapacitor Applications*, Current Opinion in Colloid & Interface Science 20(2015)416–428
- Yazdi GZ, Iakimov T and Yakimova R, *Epitaxial Graphene on SiC: A Review of Growth and Characterization*, Crystals 6(2016)53
- Yoon SF, K.H. Tan, Rusli, J. Ahn, Q.F. Huang, *Modeling and analysis of hydrogen–methane plasma in electron cyclotron resonance chemical vapor deposition of diamond-like carbon,* Diamond Relat. Mater. 9(2000)12
- Yoshimura A, Kurita S, Tachibana M, Kojima K, Molina-Morales P and Nakai H, *Fabrication of Carbon Nanowalls by DC Plasma Enhanced Chemical Vapor Deposition and Characterization of Their Structures*, Proceedings. 5th IEEE Conference. on Nanotechnology, Nagoya(2005)
- Yuan Y and Lee TR, *Contact Angle and Wetting Properties*, Springer-Verlag Berlin Heidelberg(2013), ISBN 978-3-642-34243-1
- Yu K, Bo Z, Lu G, Mao S, Cui S, Zhu Y, Chen X, Ruoff RS and Chen J, *Growth of carbon nanowalls at atmospheric pressure for one-step gas sensor fabrication,* Nanoscale Res. Lett. 6(2011)202
- Zhang N, Li J, Liu Z, Yang S, Xu A, Chen D,, Guo Q and Wang G, *Direct synthesis of vertical graphene nanowalls on glass substrate for thermal management*, Mater. Res. Express 5(2018)065606
- Zhang XF, Zhou KS, Deng CM, Liu M, Deng ZQ. Deng CG, Song JB, *Gas-deposition mechanisms of 7YSZ coating based on plasma spray-physical vapor deposition*, Journal of the European Ceramic Society 36(2015)697-703
- Zhang Y, Du J, Tang S, Liu P, Deng S, Chen J and Xu N, *Optimize the field emission character of a vertical few-layer graphene sheet by manipulating the morphology***,** Nanotechnology 23(2012)015202
- Zheng JP, Cygan PJ, Jow TR, *Hydrous ruthenium oxide as an electrode material for electrochemical capacitors*, Journal of the Electrochemical Society 142(1995)2699-2703
- Zhou P, *Choosing the Most Suitable Laser Wavelength For Your Raman Application*, B&W Tek Inc.(2015)1-6, http://bwtek.com/wp-content/uploads/2015/07/raman-laser-selection-application-note.pdf

- Zhu H, Wei J, Wang K and Wu D, *Applications of carbon materials in photovoltaic solar cells,* Sol. Energy Mater. Sol. Cells 93(2009)1461
- Zhu MY, Wang J, Holloway BC, Outlaw RA, Zhao X, Hou K, Shutthanandan V and Manos DM, *Initial growth process of carbon nanowalls synthesized by radical injection plasma-enhanced chemical vapor deposition*, Carbon 45(2007)2229
- Zhu MY, Outlaw RA, Bagge-Hansen M, Chen HJ, Manos DM. *Enhanced field emission of vertically oriented carbon nanosheets synthesized by* C_2H_2/H_2*plasma enhanced CVD,* Carbon 49(2011)2526–31
- Zhu W, Inspektor A, Badzian AR, McKenna T and Messier R, *Effects of Noble-Gases on Diamond Deposition from Methane-Hydrogen Microwave Plasmas,* Journal of Applied Physics 68(1990)1489-1496
- Zhu Z, Wang S, Chang Y, Yu D, Jiang Y, *Direct photodissociation of toluene molecules to photoluminescent carbon dots under pulsed laser irradiation*, Carbon 105(2016)416-423

Publications and communications

Articles

- ¨Supercapacitive performance of graphene nanowalls/manganese dioxide electrodes deposited on stainless steel current collectors and annealing temperature effect¨, Roger Amade, Arevik Muyshegyan-Avetisyan, Joan Martí, Esther Pascual, Jose Luís Andújar, Enric Bertran, Materials 12(2019)483
- ¨ Structure Dependent Photoluminescence from Undoped sp^2 Carbon Micro- and Nanostructures Grown by Inductively Coupled Plasma Chemical Vapour Deposition¨, Arevik Musheghyan-Avetisyan, Frank Güell, Paulina R Martínez-Alanis, Roger Amade, Joan Martí González and Enric Bertran-Serra, submitted in the Journal of Physical Chemistry C (2019)

Congresses

- Congress: **Jornada d'Investigadors Predoctorals Interdisciplinària (JIPI 2016)**

  Autors: Musheghyan-Avetisyan A. and Chaitoglou S.
  Title: “Cooking tommorow's materials”
  Venue: University of Barcelona, Barcelona, Spain, February 2016.
  Group organizer: University of Barcelona
  Type of participation: Flash talk
- Congress: **ICSNN 2016**

  Autors: Bertran E., Chaitoglou S., Musheghyan-Avetisyan A. and Martí-González J., Andújar J.L., Pascual E. and Amade R.
  Title: Morphology of graphene bidimensional crystals grown by chemical vapor deposition and related technologies
  Venue: Hong-Kong (China), 25-30 July, 2016
  Type of participation: Oral presentation
- Congress: **Trends in Nanotechnology International Conference (TNT2016)**

  Autors: Arevik Musheghyan-Avetisyan, J. Marti-Gonzalez and E. Bertran-Serra
  Title: Low temperature PECVD growth of vertically oriented graphene
  Nanowalls for supercapacitor applications
  Venue: Fribourg (Switzerland), September 5-9, 2016
  Group organizer: Phantoms Foundation
  Type of participation: Oral presentation (Invited)

- Congress: **GraphIn2016, Graphene Industry – challenges & opportunities**
  Autors: Musheghyan-Avetisyan A., J. Marti-Gonzalez, Amade R., Andújar J-L , Pascual E. and Bertran-Serra E.
  Title: Low temperature Inductively Coupled Plasma Chemical Vapor Deposition of vertically oriented graphene nanowalls for supercapacitor applications
  Group organizer: Phantoms Foundation
  Venue: Barcelona (Spain), December 13, 2016
  Type of participation: Poster
- Congress: **10th Anniversary IN2UB event**
  Autors: Arevik Musheghyan-Avetisyan, R. Amade, J. Marti-Gonzalez, J-L. Andújar, E. Pascual, F. Pantoja, I. Alshaikh and E. Bertran-Serra
  Venue: University of Barcelona (Spain), 26 January 2017,
  Type of participation: Poster
  Title: Low temperature Inductively Coupled Plasma Chemical Vapor Deposition of vertically oriented graphene nanowalls
- Congress: **European Graphene Forum-EGF2017; Smart Material and Surfaces-SMS EUROPE**
  Autors: Arevik Musheghyan-Avetisyan, R. Amade, J. Marti-Gonzalez, J-L. Andújar, E. Pascual, F. Pantoja, I. Alshaikh and E. Bertran-Serra
  Group organizer: SETCOR conferences & exhibition
  Venue: Paris-France, 26-28 April, 2017
  Type of participation: Oral presentation
  Title: Direct growth of vertically oriented graphene nanowalls on multiple substrates by Low Temperature Plasma-Enhanced Chemical Vapor Deposition
- Congress: **Trends in Nanotechnology International Conference (TNT2017)**
  Autors: Arevik Musheghyan-Avetisyan, R. Amade, J. Marti-Gonzalez, J-L. Andújar, E. Pascual,F. Pantoja, I. Alshaikh and E. Bertran-Serra
  Group organizer: Phantoms Foundation
  Venue: Dresden (Germany) , 5-9 June,2017
  Type of participation: Oral presentation (Invited)
  Title: Direct growth of vertically oriented graphene nanowalls on multiple substrates by Low Temperature Plasma-Enhanced Chemical Vapor Deposition
- Congress: **14th Global Experts Meeting on Nanomaterials and Nanotechnology**
  Autors: Bertran-Serra E., Musheghyan-Avetisyan, A., Pantoja-Suarez F., Alshaikh I., Martí-González J., Chaitoglou S., Amade R., Andújar J.L., Pascual E.

Title: Graphene and fullerene based nanostructures grown by chemical vapor deposition and related technologies
Venue: Madrid (Spain), March 30-31,2017
Type of participation: Invited Conference

- Congress: **Applied Nanotechnology and nanoscience international conference 2018**
  Autors: Arevik Musheghyan-Avetisyan, R. Amade, J. Marti-Gonzalez, J-L. Andújar, E. Pascual,F. Pantoja, I. Alshaikh and E. Bertran-Serra
  Title: Bottom up mechanism that describes the graphene nanowalls synthesis by inductively coupled plasma chemical vapor deposition
  Venue : Berlin (Germany),22-24 Octubre,2018
  Type of participation: Oral presentation
- Congress: **Surface functionalisation of materials for high added value applications 2018**
  Autors: Arevik Musheghyan-Avetisyan, J. Marti-Gonzalez, F. Pantoja, I. Alshaikh, S. Hussain, R. Amade, J-L. Andújar, E. Pascual and E. Bertran-Serra
  Title: Study of the morphology effect of carbon nanostructures on the electrochemical performance of EDLC
  Venue: Barcelona (Spain), 2018
  Type of participation: Poster
- Congress: **Graphene2017**
  Autors: J. Martí-Gonzalez, A. Musheghyan-Avetisyan, R. Amade, J.-Luis Andújar, E. Pascual and E. Bertran-Serra
  Title: Structural study of high specific surface graphene nanowalls growth by inductively coupled plasma chemical vapor deposition
  Venue: Barcelona (Spain), March 28-31, 2017
  Type of participation: Poster
- Congress: **World congress and Expo on Nanotechnology and Materials Science**
  Autors: Enric Bertran-Serra, A. Musheghyan-Avetisyan, F. Pantoja-Suarez, I. Alshaikh, J. Martí-González, S. Chaitoglou, R. Amade, JL Andújar, E. Pascual
  Title: New carbon based nanostructures grown by chemical vapor deposition
  Venue: Barcelona (Spain), April 5-7, 2017
  Type of participation: Oral presentation
- Congress: **TNT2018**
  Autors: J. Marti-Gonzalez, F. Pantoja, A. Musheghyan-Avetisyan, I. Alshaikh, R. Amade, J.L. Andújar, E. Pascual and E. Bertran-Serra
  Title: Synthesis and characterization of graphene nanowalls / carbon nanotubes hybrid nanostructures
  Venue: Lecce (Italy), September 3-7, 2018
  Type of participation: Poster

- Congress: **Advanced Materials 2018**

  Autors: Amade R., Musheghyan-Avetisyan A., Martí-González J, Pantoja-Suárez F., Alshaikh I, Hussain S., Andújar J.L., Pascual E., Bertran E., Pérez del Pino A. and György E.

  Title: Growth and electrochemical characterization of graphene nanowalls and carbon nanotubes

  Venue: Zürich (Switzerland), September 04-06, 2018

  Type of participation: Poster

Attended Seminars

- CCiTUB seminars on "RamanDay: Workshop on Advanced Applied Raman Spectroscopy", Horiba Scientific i MTB, 8 de abril 2014, CCiTUB, Barcelona
- Tecnologías de Medida de Materiales: Caracterización Electromagnética y Medida de Materiales,Keysight Technologies, 8 de Octubre 2015, Facultat de Física, Universitat de Barcelona, Barcelona.
- Advanced TEM imaging tools for materials science, Lluís López, IN^{2}UB, 30 de noviembre 2017, Universitat de Barcelona, Barcelona
- Fundamentos de Medida en Dispositivos de RF/MW, Keysight Technologies, 10 de abril 2017, Facultat de Física, Universitat de Barcelona, Barcelona
- Surface Engineering by a Nanosecond Laser Texturing, Dr. Peter Grigorcic, 8 de febrero 2018, Facultat de Física, Universitat de Barcelona, Barcelona
- Low temperature Inductively Coupled Plasma Chemical Vapor Deposition of vertically oriented graphene nanowalls for supercapacitor Applications, A. Musheghyan-Avetisyan, IN^{2}UB 22 de Febrero 2018, Universitat de Barcelona, Barcelona
- Nanofils de ZnO: síntesi, espectroscòpia òptica i aplicacions, Dr. Frank Güell, 19 de marzo 2018, Universitat de Barcelona, Barcelona
- Growth of carbon nanotubes on stainless steel using nitrided multi-layer as diffusion barrier, Luis Fernando Pantoja, IN^{2}UB, 22 de marzo 2018, Universitat de Barcelona, Barcelona
- Native oxide film reduction on stainless steel for direct growth of carbon nanotubes, Luis Fernando Pantoja, 27 de julio 2018, Facultat de Física, Universitat de Barcelona, Barcelona
- ADHES project meeting, Enric Bertran Serra, Eniko Gyorgy & Ángel Pérez del Pino, Roger, Amade Rovira ,Arevik Musheghyan Avetisyan ,Fernando Pantoja Suárez, Joan Martí González ,Islam Alshaikh , ENPHOCAMAT Group (ICMAB-CSIC + UB), 28 de noviembre 2018, Facultat de Física, Universitat de Barcelona, Barcelona
- Estratègies de divulgació I comunicació cientifica, Guillem Aromí, Jordi Diaz, P. Serena, CCiTUB, 22 de enero 2019, Universitat de Barcelona, Barcelona
- Marker-free monitoring of cells and tissues, Katja Schenke-Layland, IN^{2}UB, March 1st, 2019, Universitat de Barcelona, Barcelona

Appendix

Appendix

A. List of figures and tables

Figures

Tables

B. SAMPLE LIST

Substrate	Sample	Previous pressure (Torr)	Reactor pressure (Torr)	Temperature (ºC)	Time (min)	Plasma power (W)	Gas	Gas flow (sccm)
1	2	3	4	5	6	7	8	9
Graphene growth without plasma								
16A1801	Fe/glass	0,01	0,2	450	40	-	CH_4	20
16A2001	Fe/glass, Cu foil	0,03	0,5	450	60	-	CH_4	40
16A2101	glass	0.03	0,5	450	60	-	CH_4	40
16A2701	Cu, c-Si, glass	0.01	0.7	450	60	-	CH_4	50
16A0801	Cu, Si, glass	0.005	0.3	1000	20	-	CH_4/H_2	5/20
16B1001	Cu foil	0.01	0.5	500	20	-	CH_4/H_2	5/20
16B1801	Quartz	0.005	0.3	900	20	-	CH_4/H_2	5/20
16B1901	Quartz	0.007	0.4	950	20	-	CH_4/H_2	5/20
16B2301	Quartz	0.006	0.4	750	20	-	CH_4/H_2	5/20
16B2501	Quartz	0.004	0.4	1000	20	-	CH_4/H_2	5/20
16B2601	Quartz	0.002	0.36	1015	20	-	CH_4/H_2	5/20
16B2901	Quartz	0.002	0.4	1015	20	-	CH_4/H_2	5/20

Substrate	**Sample**	**Previous pressure (Torr)**	**Reactor pressure (Torr)**	**Temperature (ºC)**	**Time (min)**	**Plasma power (W)**	**Gas**	**Gas flow (sccm)**
16C0101	Quartz	0.001	0.35	1030	20	-	CH_4/H_2	5/20
16C0701	Quartz, Cu foil	0.003	0.3	1030	30	-	CH_4/H_2	5/20
16C0801	Quartz, Cu foil	0.002	0.4	1000	30	-	CH_4/H_2	5/20
16C0901	Quartz, Cu foil	0.002	0.4	1030	30	70	CH_4/H_2	5/20
16C1401	Quartz, Cu foil	0.004	0.47	1015	30	90	CH_4/H_2	5/20
16C1501	Quartz, Cu foil	0.004	0.42	1000	30	90	CH_4/H_2	5/20
16C1601	Quartz, Cu foil	0.005	0.47	950	30	90	CH_4/H_2	5/20
16C3001	Quartz, Cu foil	0.000	0.35	1030	15	90	CH_4/H_2	5/20
16C3101	Quartz, Cu foil	0.001	0.35	1015	10/15	90	CH_4/H_2	10/20
16D0501	Quartz, Cu foil	0.008	0.4	900	30	90	CH_4/H_2	5/20
16D0601	Quartz, Cu foil	0.002	0.43	850	30	90	CH_4/H_2	5/20
16D0801	Quartz, Cu foil	0.003	0.43	800	30	90	CH_4/H_2	5/20
16D1201	Quartz, Cu foil	0.005	0.44	900	45	122	CH_4/H_2	5/20
16D1301	Quartz, Cu foil	0.001	0.42	850	45	180	CH_4/H_2	5/20
16D1801	Quartz, Cu foil	0.005	0.4	800	30	197	CH_4/H_2	5/20

Substrate	Sample	Previous pressure (Torr)	Reactor pressure (Torr)	Temperature (ºC)	Time (min)	Plasma power (W)	Gas	Gas flow (sccm)
16D2501	Quartz, Cu foil	0.005	0.44	800	60	180	CH_4/H_2	5/20
16D2701	Quartz, Cu foil	0.005	0.3	850	45	200	CH_4/H_2	3.5/10
16D2901	Quartz, Cu foil	0.003	0.29	700	45	220	CH_4/H_2	3,6/10
16E0201	Quartz, Cu foil	0.002	0.3	600	45	250	CH_4/H_2	3,6/10
16E1101	Quartz, SiO_2/c-Si, c-Si	0.007	0.47	750	30	300	CH_4/H_2	7.5/15
16E1201	Quartz, SiO_2/c-Si ,c-Si	0.001	0.4	750	30	300	CH_4/H_2	5/20
16E1202	Quartz, SiO_2/c-Si ,c-Si	-	0.4	700	30	300	CH_4/H_2	5/20
16E1801	Quartz, SiO_2/c-Si, c-Si	0.006	0.4	650	30	350	CH_4/H_2	5/20
16E2401	Quartz, SiO_2/c-Si ,c-Si	0.008	0.4	750	30	350	CH_4/H_2	5/20
16F0301	Quartz, $SiO_{2,}$/c-Si, c-Si	0.001	0.4	750	45	300	CH_4/H_2	5/20
16F0701	Quartz, $SiO_{2,}$/c-Si, c-Si	0.000	0.4	750	45	350	CH_4/H_2	5/20
16F0801	Quartz,$SiO_{2,}$/c-Si, c-Si	0.005	0.43	750	45	350	CH_4/H_2	5/20
16F1001	Quartz, $SiO_{2,}$/c-Si, c-Si	0.007	0.4	750	20	370	CH_4/H_2	5/20
16F1301	Quartz, $SiO_{2,}$/c-Si, c-Si	0.002	0.4	750	40	400	CH_4/H_2	5/20
16F1701	$SiO_{2,}$/c-Si, c-Si	0.002	0.5	700	30	400	CH_4/H_2	5/30
16F2101	Quartz, $SiO_{2,}$/c-Si, c-Si	0.007	0.4	900	30	350	CH_4/H_2	5/20

Substrate	**Sample**	**Previous pressure (Torr)**	**Reactor pressure (Torr)**	**Temperature (ºC)**	**Time (min)**	**Plasma power (W)**	**Gas**	**Gas flow (sccm)**
MLGNWs plasma growth								
16F2701	Ni/c-Si, Ni/ SiO_2/c-Si	0.001	0.42	750	20	350	CH_4/H_2	7/20
16G0401	c-Si, SiO_2/c-Si	0.003	0.4	700	20	400	CH_4/H_2	7/20
16G0501	c-Si, Ni/ SiO_2/c-Si	0.008	0.4	650	10	450	CH_4/H_2	7/20
16G0602	c-Si, SiO_2/c-Si, Ni/c-Si Ni/ SiO_2/c-Si	0.004	0.4	750	10	450	CH_4/H_2	7/20
16G0801	c-Si, SiO_2/c-Si, Ni/c-Si Ni/ SiO_2/c-Si	0.004	0.8	750	30	450	CH_4/H_2	10/40
16G1001	c-Si, SiO_2/c-Si, Ni/c-Si Ni/ SiO_2/c-Si	0.014	0.4	800	20	450	CH_4/H_2	7/20
16G1201	c-Si, SiO_2/c-Si, Ni/c-Si Ni/ SiO_2/c-Si	0.010	0.4	900	20	450	CH_4/H_2	7/20
16G1301	c-Si, SiO_2/c-Si, Ni/c-Si Ni/ SiO_2/c-Si	0.004	0.4	550	20	450	CH_4/H_2	7/20
16G1401	c-Si, SiO_2/c-Si, Ni/c-Si Ni/ SiO_2/c-Si	0.004	0.4	700	10	400	CH_4/H_2	7/20
16G1501	c-Si, SiO_2/c-Si, Ni/c-Si Ni/ SiO_2/c-Si, SS304	0.001	0.4	900	20	400	CH_4/H_2	10/15
16G1502	Cu foil, Ni foil, SS304, c-Si, SiO_2/c-Si, Ni/c-Si, Ni/ SiO_2/c-Si	0.003	0.4	850	20	400	CH_4/H_2	10/15
16G1901	c-Si, SiO_2 /c-Si,Ni/c-Si, Ni/ SiO_2/c-Si, Cu foil, Fe foil ,SS304	0.003	0.4	800	15	400	CH_4/H_2	10/15
16G2001	c-Si, SiO_2 /c-Si,Ni/c-Si, Ni/ SiO_2/c-Si, Cu foil, Fe foil ,SS304	0.008	0.4	700	15	400	CH_4/H_2	10/15
16G2101	c-Si, SiO_2 /c-Si,Ni/c-Si,	0.004	0.2	650	15	400	CH_4/H_2	10/15

Substrate	Sample	Previous pressure (Torr)	Reactor pressure (Torr)	Temperature (ºC)	Time (min)	Plasma power (W)	Gas	Gas flow (sccm)
	Ni/ SiO_2/c-Si, Cu foil, Fe foil ,SS304							
16I1301	SiO_2/c-Si, c-Si,Cu foil, Fe foil	0.006	0.2	800	20	400	CH_4/H_2	10/15
16I1401	Cu foil, Ni foil, Fe foil, SiO_2/c-Si, c-Si,	0.007	0.4	800	20	450	CH_4/H_2	10/15
16I1601	c-Si, SiO_2/c-Si, Cu foil, Ni foil,	0.006	0.2	700	20	450	CH_4/H_2	10/15
16I1901	Cu foil, Ni foil, c-Si, SiO_2/c-Si	0,001	0.4	800	10	450	CH_4/H_2	10/15
16I2001	Cu foil, Fe foil, c-Si, SiO_2/c-Si	0.015	0.2	750	10	450	CH_4/H_2	10/15
16I2201	Cu foil, Fe foil, c-Si, SiO_2/c-Si	0.007	0.3	750	5	450	CH_4/H_2	10/15
16I2202	Cu foil, Fe foil, c-Si, SiO_2/c-Si	0.007	0.3	800	5	450	CH_4/H_2	10/15
16I2301	Cu foil, Ni foil, c-Si, SiO_2/c-Si	0.002	0.3	900	10	450	CH_4/H_2	10/15
16I2602	Cu foil, Ni foil, c-Si, SiO_2/c-Si	0.008	0.4	900	10	420	CH_4/H_2	10/15
16I2801	Cu foil, c-Si, SiO_2/c-Si	0.005	0.2	900	10	420/1	CH_4/H_2	10/15
16I2901	c-Si, SiO_2/c-Si, Cu foil	0.005	0.36	750	10	420/5	CH_4/H_2	10/15
16I2902	Cu foil, c-Si, SiO_2/c-Si	0.008	0.37	800	10	420	CH_4/H_2	10/15
16J0301	c-Si, SiO_2/c-Si, Cu foil	0.01	0.27	810	10	440	CH_4/H_2	10/15
16J0302	c-Si, SiO_2/c-Si, Cu foil	0.0015	0.5	800	10	440	CH_4/H_2	10/15
16J0401	c-Si, SiO_2/c-Si, Cu foil	0.001	0.5	750	10	440	CH_4/H_2	10/15

Substrate	**Sample**	**Previous pressure (Torr)**	**Reactor pressure (Torr)**	**Temperature (ºC)**	**Time (min)**	**Plasma power (W)**	**Gas**	**Gas flow (sccm)**
16J0601	c-Si, SiO_2/c-Si, Cu foil	0.004	0.5	750	10	440	CH_4/H_2	10/15
16J0701	c-Si, SiO_2/c-Si, Cu foil	0.001	0.4	750	20	440	CH_4/H_2	10/15
16J1001	c-Si, SiO_2/c-Si, Cu foil	0.001	0.5	750	30	440	CH_4/H_2	10/15
16J1002	c-Si, SiO_2/c-Si, Cu foil	0.01	0.3	750	30	440	CH_4/H_2	10/10
16J1101	c-Si, SiO_2/c-Si, Cu foil	0.01	0.5	750	40	440	CH_4/H_2	10/15
16J1901	c-Si, SiO_2/c-Si, Cu foil	0.012	0.4	750	50	440	CH_4	10
16J2001	c-Si, SiO_2/c-Si, Cu foil	0.006	0.5	750	60	440	CH_4	10
16J2101	c-Si, SiO_2/c-Si, Cu foil	0.004	0.4	750	80	440	CH_4	10
16J2601	c-Si, SiO_2/c-Si, Cu foil	0.002	0.4	750	40	440	CH_4	10
16J2701	c-Si, SiO_2/c-Si, Cu foil	0.007	0.5	750	40	440	CH_4/H_2	10/15
16K0201	c-Si, SiO_2/c-Si, Cu foil	0.001	0.4	750	40	440	CH_4	10
16K0202	c-Si, SiO_2/c-Si	0.004	0.4	750	10	440	CH_4	10
16K0301	c-Si, SiO_2/c-Si	0.007	0.4	750	20	440	CH_4	10
16K0401	c-Si, SiO_2/c-Si	0.007	0.4	750	40	440	CH_4	10
16K0701	c-Si, SiO_2/c-Si	0.006	0.4	750	30	440	CH_4	10
16K0901	c-Si, SiO_2/c-Si	0.009	0.4	750	40	440	CH_4/H_2	10/15

Substrate	**Sample**	**Previous pressure (Torr)**	**Reactor pressure (Torr)**	**Temperature (ºC)**	**Time (min)**	**Plasma power (W)**	**Gas**	**Gas flow (sccm)**
16K1001	c-Si, SiO_2/c-Si	0.009	0.4	750	30	440	CH_4/H_2	10/15
16K1002	c-Si, SiO_2/c-Si	0.01	0.4	750	30	440	CH_4	15
16K1501	c-Si, SiO_2/c-Si	0.01	0.4	750	30	440	CH_4	20
16K1502	c-Si, SiO_2/c-Si	0.01	0.3	750	30	440	CH_4	20
16K1701	c-Si, SiO_2/c-Si	0.01	0.4	750	30	440	CH_4	5
16K1801	c-Si, SiO_2/c-Si	0.006	0.4	750	80	440	CH_4	10
16K2101	c-Si, SiO_2/c-Si	0.01	0.4	750	40	440	CH_4	10
16K2102	c-Si	0.01	0.4	750	80	440	CH_4	10
16K2301	c-Si, SiO_2/c-Si	0.01	0.4	750	20	440	CH_4	10
16K2302	c-Si	0.01	0.4	550	80	440	CH_4	10
16K2401	c-Si, SiO_2/c-Si	0.008	0.4	650	80	440	CH_4	10
16K2801	c-Si	0.01	0.4	750	5	440	CH_4	10
16K2802	c-Si	0.01	0.4	750	10	440	CH_4	10
16K2901	c-Si	0.01	0.4	650	80	440	CH_4	10
16L0101	c-Si	0.006	0.4	750	20	440	CH_4	10
16L1901	c-Si	0.01	0.4	750	30	440	CH_4	10

Substrate	**Sample**	**Previous pressure (Torr)**	**Reactor pressure (Torr)**	**Temperature (ºC)**	**Time (min)**	**Plasma power (W)**	**Gas**	**Gas flow (sccm)**
17A2301	c-Si	0.008	0.4	750	30	440	CH_4	10
17A2401	c-Si	0.008	0.4	750	40	440	CH_4	10
17A2402	c-Si	0.003	0.6	750	30	440	CH_4	10
17A3001	c-Si	0.01	0.5	750	50	440	CH_4	10
17A3002	c-Si	0.01	0.5	750	30	440	CH_4	10
17A3101	c-Si	0.010	0.4	750	80	440	CH_4	10
17B0201	c-Si, SiO_2/c-Si , Fe foil, Cu foil	0.009	0.4	750	40	440	CH_4	10
17B0202	c-Si	0.009	0.4	850	30	440	CH_4	10
17B0301	c-Si	0.002	0.4	800	30	440	CH_4	10
17B0302	c-Si	0.002	0,4	750	30	440	CH_4	10
17B0601	c-Si	0.005	0.4	700	30	440	CH_4	10
17B0701	c-Si	0.01	0.4	850	30	440	CH_4	10
17B0901	Quartz	0.005	0.4	750	50	440	CH_4	10
17B1501	c-Si	0.01	0.4	750	30	440	CH_4	10
17B1701	c-Si	0.01	0.4	750	30	440	CH_4	10
17B2101	c-Si	0.01	0.4	750	30	440	CH_4	10

Substrate	**Sample**	**Previous pressure (Torr)**	**Reactor pressure (Torr)**	**Temperature (ºC)**	**Time (min)**	**Plasma power (W)**	**Gas**	**Gas flow (sccm)**
17B2301	c-Si	0.006	0.4	750	50	440	CH_4	10
17C0202	c-Si	0.009	0.4	750	30	440	CH_4	10
17C0301	c-Si	0.1	0.4	750	30	440	CH_4	10
17C0302	c-Si, SS350, Cu foil, Papex® Gr	0.01	04	750	40	440	CH_4	10
17C0701	c-Si, SS304, SS304/CNT	0.01	0.4	750	40	440	CH_4	10
17C0802	SS-304	0.02	0.4	600	40	440	CH_4	10
17C1501	c-Si	0.003	0.4	750	30	440	CH_4	10
17E0301	c-Si	0.009	0.5	750	30	440	CH_4	10
17E0302	c-Si	0.01	0.4	750	50	440	CH_4	10
17E0303	c-Si, CNT/c-Si, CNT/SS304	0.01	0.4	750	40	440	CH_4	10
17E0401	c-Si, Cu foil	0.006	0.4	750	60	440	CH_4	10
17E0402	c-Si	0.003	0.6	750	20	440	CH_4	10
17E0403	c-Si	0.007	0.3	750	30	440	CH_4	10
17E0501	c-Si	0.01	0.6	750	40	440	CH_4	10
17E0801	Cu grid	0.02	0.4	750	40	440	CH_4	10
17E0901	c-Si, Cu grid	0.005	0.6	750	40	440	CH_4	10

Substrate	**Sample**	**Previous pressure (Torr)**	**Reactor pressure (Torr)**	**Temperature (ºC)**	**Time (min)**	**Plasma power (W)**	**Gas**	**Gas flow (sccm)**
17E0902	c-Si	0.01	0,4	750	40	440	CH_4/A_2	10/7
17E1001	c-Si	0.01	0.4	750	40	440	CH_4	10
17E1101	Cu grid	0.02	0.4	750	30	440	CH_4	10
17E1201	c-Si	0.03	0.7	750	50	440	CH_4	10
17E1202	c-Si	0.01	0.6	750	50	440	CH_4	10
17E1501	c-Si	0.01	0.6	750	50	440	CH_4	10
17E1601	CNT/SS304, CNT/c-Si	0.01	0.4	750	30	440	CH_4	10
17E1801	Cu grid	0.006	0.4	750	20	440	CH_4	10
17E1802	Cu grid	0.008	0.3	750	50	440	CH_4	10
17E1901	c-Si, Cu foil	0.004	0.4	750	40	440	CH_4	10
17E2401	c-Si	0,01	0.2	750	50	440	CH_4/ A_2	10/12
17E2402	c-Si	0.02	0.3	750	50	440	CH_4/ A_2	10/21
17E2601	Ni foil, Fe foil, SS-304, Cu foil	0.006	0.4	750	60	440	CH_4/ A_2	10/33
17E2901	Cu grid, TEM	0.02	0.4	750	50	440	CH_4/ A_2	10/33
17E3001	Cu grid, TEM	0.02	0.4	750	50	440	CH_4/ A_2	10/33
17F1301	CNT/SS304	0.02	0.4	750	40	450	CH_4	10

Substrate	**Sample**	**Previous pressure (Torr)**	**Reactor pressure (Torr)**	**Temperature (ºC)**	**Time (min)**	**Plasma power (W)**	**Gas**	**Gas flow (sccm)**
17F1401	c-Si	0.03	0.4	750	50	450	CH_4	10
17F1501	c-Si	0.004	0.5	750	50	450	CH_4/ A_2	10/9
17F1502	c-Si	0.020	0.4	750	50	450	CH_4/H_2	10/15
17F2701	CNT/SS304	0.01	0.4	750	50	450	CH_4	10
17F2802	CNT/Si, CNT/SS304	0.06	0.4	750	50	450	CH_4	10
17G0401	SS-304,CNT/ SS304	0.03	0.4	750	50	450	CH_4	10
17G1002	c-Si,CNT/SS-304, SS-304	0.02	0.4	750	30	450	CH_4	10
17G1101	c-Si	0.008	0.4	850	40	440	CH_4	10
17G1201	c-Si	0.004	0.4	750	30	440	CH_4	10
17G1301	c-Si	0.008	0.4	750	20	450	CH_4	10
17G1401	c-Si	0.05	0.4	750	50	440	CH_4	10
17I1901	CNT/c-Si	0.002	0.4	750	40	440	CH_4	10
17I2201	c-Si, c-Si/CNT	0.03	0.4	750	40	440	CH_4	10
17I2701	c-Si, CNT/ c-Si, Cu foil	0.03	0.4	750	40	440	CH_4	10
17J0901	c-Si	0.009	0.4	750	10	440	CH_4	10
17J0902	CNTs/ c-Si	0.01	0.4	750	50	440	CH_4	10

Substrate	Sample	Previous pressure (Torr)	Reactor pressure (Torr)	Temperature (ºC)	Time (min)	Plasma power (W)	Gas	Gas flow (sccm)
17J1801	Cu, c-Si	0.02	0.4	750	30	440	CH_4	10
17J2401	c-Si	0.02	0.4	750	50	460	CH_4	10
17J2601	c-Si	0.02	0.4	750	40	440	CH_4	10
17K0201	CNT/c-Si	0.020	0.4	750	40	440	CH_4	10
17K0301	CNT/c-Si	0.02	0.4	750	50	440	CH_4	10
17K0701	c-Si	0.02	0.4	750	5	440	CH_4	10
17K0901	c-Si	0.020	0.4	750	60	440	CH_4	10
17K1401	CNT/c-Si	0.03	0.4	750	40	440	CH_4	10
17K1501	Water patterned CNTs/c-Si	0.02	0.4	750	40	440	CH_4	10
17K2201	c-Si	0.03	0.4	750	30	440	CH_4	10
17K2202	CNWs/c-Si	0.1	0.1	RT	0.36	400	O_2	9.8
17L0101	Cu foil	0.02	0.4	750	40	440	CH_4	10
17L0102	SS304	0.02	0.4	750	40	440	CH_4	10
17L0501	Cu foil	0.02	0.4	750	40	440	CH_4	10
17L0502	Papyex® graphite	0.02	0.4	750	40	440	CH_4	10
17L1801	c-Si	0.02	0.4	750	40	440	CH_4	10

Substrate	Sample	Previous pressure (Torr)	Reactor pressure (Torr)	Temperature (ºC)	Time (min)	Plasma power (W)	Gas	Gas flow (sccm)
17L1901	SS-304	0.02	0.4	750	40	440	CH_4	10
17L1902	SS-304	0.02	0.1	RT	0.36	40	O_2	9
17L2002	Papyex graphite	0.02	0.4	750	40	440	CH_4	10
17L2101	SS304	0.02	0.4	750	40	440	CH_4	10
17L2201	GNWs/SS304	0.03	0.1	RT	0.08	40	O_2	9
18A0801	SS-304	0.02	0.4	780	40	440	CH_4	10
18A1001	CNT/Papyex Gr, Papyex Gr, SS304	0.02	0.4	750	40	440	CH_4	10
18A1002	c-Si, Gr, SS304, Cu foil,	0.004	0.4	500	40	440	CH_4	10
18A1601	c-Si, Gr, SS304, Cu foil,	0.01	0.4	750	40	440	CH_4	10
18A1602	c-Si	0.01	0.4	750	40	440	CH_4	10
18A1701	Cu foil	0.01	0.4	650	40	440	CH_4	10
18A1801	Cu foil	0.02	0.4	700	40	440	CH_4	10
18A1901	Gr	0.02	0.4	700	40	440	CH_4	10
18A2301	Gr	0.02	0.4	700	40	440	CH_4	10
18A2401	Gr , SS-304	0.02	0.5	700	30	440	CH_4	10
18A2402	G_2	0.02	0.4	750	40	440	CH_4	10

Substrate	**Sample**	**Previous pressure (Torr)**	**Reactor pressure (Torr)**	**Temperature (ºC)**	**Time (min)**	**Plasma power (W)**	**Gas**	**Gas flow (sccm)**
18A2601	Gr	0.003	0.4	700	30	440	CH_4	10
18A2602	DLC/ Gr	0.01	0.4	700	30	440	CH_4	10
18A2901	c-Si, Gr, SS304, Cu foil	0.01	0.4	550	40	440	CH_4	10
18A2902	c-Si, Gr, SS-304, Cu foil	0.02	0.4	800	40	440	CH_4	10
18A2903	c-Si, Gr, SS-304, Cu foil	0.01	0.4	650	40	440	CH_4	10
18A3101	Gr, c-Si, Cu, SS304	0.02	0.4	750	40	440	CH_4	10
18B0801	SS304	0.04	0.4	750	60	440	CH_4	10
18B0802	SS304	0.004	0.4	750	80	440	CH_4	10
18B0901	SS304, Cu foil, c-Si, Gr,	0.007	0.4	600	40	440	CH_4	10
18B0902	SS304, Cu foil, c-Si, Gr,	0.02	0.4	700	40	440	CH_4	10
18B0903	SS304, Cu foil, c-Si, Gr,	0.02	0.4	750	40	440	CH_4	10
18B1201	SS304	0,002	0,4	750	40	440	CH_4	10
18B1401	SS304, Cu foil, c-Si, Gr,	0.007	0.4	750	10	440	CH_4	10
18B1402	SS304, Cu foil, Gr,	0.006	0.4	750	20	440	CH_4	10
18B1501	SS304, Cu foil, Gr,	0.008	0.4	750	10	440	CH_4	10
18B1502	SS304, Cu foil, Gr,	0.02	0.4	650	40	440	CH_4	10
18B1601	SS304, Cu foil,	0.016	0.4	650	50	440	CH_4	10

Substrate	**Sample**	**Previous pressure (Torr)**	**Reactor pressure (Torr)**	**Temperature (ºC)**	**Time (min)**	**Plasma power (W)**	**Gas**	**Gas flow (sccm)**
	Gr ,							
18B1901	SS304, Cu foil, Gr ,	0.005	0.4	750	40	440	CH_4	10
18B2201	SS304, Cu foil, Gr ,	0.007	0.4	650	5	440	CH_4	10
18B2202	SS304, Cu foil, Gr ,c-Si	0.009	0.4	750	5	440	CH_4	10
18B2601	SS-304	0.003	0.4	750	30	440	CH_4	10
18B2602	SS-304	0.002	0.4	650	20	440	CH_4	10
18B2701	CNT/DLC/ SS304 (patterned)	0.009	0.4	650	20	440	CH_4	10
18B2702	SS304	0.002	0.4	650	40	440	CH_4	10
18B2703	SS304	0.002	0.4	650	10	440	CH_4	10
18C0501	CNTs/c-Si (patterned)	0.004	0.4	750	40	440	CH_4	10
18C0701	SS304,Cu foil,Gr,c-Si	0.002	0.4	750	40	440	CH_4	10
18C0702	SS304, Cu foil, Gr ,	0.002	0.4	560	40	440	CH_4	10
18C0703	SS304, Cu foil, Gr ,	0.003	0.4	900	40	440	CH_4	10
18C0901	Gr	0.001	0.4	650	40	440	CH_4	10
18C1601	CNT/c-Si (patterned)	0.001	0.4	650	40	440	CH_4	10
18C1901	SS304	0.001	0.4	750	40	440	CH_4	10
18C2001	CNTs/ G_2	0.01	0.4	750	40	440	CH_4	200

Substrate	Sample	Previous pressure (Torr)	Reactor pressure (Torr)	Temperature (ºC)	Time (min)	Plasma power (W)	Gas	Gas flow (sccm)
18C2002	SS-304	0.02	0.4	750	40	400	CH_4	200